UNIVERSITY OF NOVI SAD

FACULTY OF TECHNICAL SCIENCES

POSSIBILITIES OF SUNFLOWER HUSK ASH UTILIZATION AS AN ALTERNATIVE ACTIVATOR FOR SLAG-BASED ALKALI-ACTIVATED MATERIALS

DOCTORAL DISSERTATION

Supervisors:

Asst. Prof. Suzana Draganić

Assoc. Prof. Marijana Serdar

Candidate:

Olivera Bedov

Novi Sad, 2026

УНИВЕРЗИТЕТ У НОВОМ САДУ

ФАКУЛТЕТ ТЕХНИЧКИХ НАУКА

МОГУЋНОСТИ ПРИМЕНЕ ПЕПЕЛА СУНЦОКРЕТОВЕ ЉУСКЕ КАО АЛТЕРНАТИВНОГ АКТИВАТОРА ЗА АЛКАЛНО АКТИВИРАНЕ МАТЕРИЈАЛЕ НА БАЗИ ЗГУРЕ

ДОКТОРСКА ДИСЕРТАЦИЈА

Ментори:

Доц. др Сузана Драганић

Проф. др Маријана Сердар

Кандидат:

Оливера Бедов

Нови Сад, 2026. године

УНИВЕРЗИТЕТ У НОВОМ САДУ
ФАКУЛТЕТ ТЕХНИЧКИХ НАУКА **ОБРАЗАЦ – 5а**

КЉУЧНА ДОКУМЕНТАЦИЈСКА ИНФОРМАЦИЈА[1]

Врста рада:	Докторска дисертација
Име и презиме аутора:	Оливера Бедов
Ментор 1 (титула, име, презиме, звање, институција):	др Сузана Драганић, доцент, Факултет техничких наука, Универзитет у Новом Саду
Ментор 2 (титула, име, презиме, звање, институција):	др Маријана Сердар, ванредни професор, Грађевински факултет, Универзитет у Загребу
Наслов рада:	Могућности примене пепела сунцокретове љуске као алтернативног активатора за алкално-активиране материјале на бази згуре
Језик и писмо рада:	Енглески (латиница)
Физички опис рада:	Страница: 210 Поглавља: 5 Референци: 198 Табела: 30 Слика: 98 Прилога: 10
Научна област:	Грађевинско инжењерство
Ужа научна област (научна дисциплина):	Грађевински материјали, процена стања и санација конструкција
Кључне речи / предметна одредница:	алкално-активирани материјали, алтернативна везива, валоризација, алтернативни активатор, пепео биомасе, пепео сунцокретове љуске, једнофазна алкална активација, одрживост, декарбонизација, циркуларна економија
Апстракт на језику рада:	Производња цемента спада међу најзначајније изворе антропогених емисија CO_2, са учешћем од приближно 7% у укупним глобалним емисијама. Смањење његове употребе стога представља једну од кључних стратегија декарбонизације. Последњих деценија, истраживања су усмерена ка развоју везива с нижим угљеничним отиском. Алкално-активирани материјали (енг. *alkali-activated materials*, AAM) представљају алтернативу цементу, јер се синтетишу реакцијом аморфних алумосиликата (најчешће индустријских нуспроизвода, као што су згура и летећи пепео) са алкалним активаторима. Међутим, конвенционални хемијски активатори који се користе у AAM системима значајно доприносе CO_2 отиску и цени тих система, због енергетски захтевне

[1] Аутор докторске дисертације потписао је и приложио следеће Обрасце:
5б – Изјава о ауторству;
5в – Изјава о истоветности штампане и електронске верзије докторског рада и дозвола за објављивање личних података;
5г – Изјава о коришћењу.
Ове Изјаве се чувају у институцији у штампаном и електронском облику и не кориче се са радом.

	производње. Ова дисертација истражује могућност валоризације пепела љуске сунцокрета (енгл. *sunflower husk ash*, SHA), локално доступног пољопривредног отпада богатог калијумом, који настаје сагоревањем љуске сунцокрета, као алтернативног активатора за ААМ на бази згуре. Истраживање је спроведено кроз четири експерименталне фазе: карактеризацију материјала, оптимизацију састава алкално-активираног бетона са смањеним уделом конвенционалних активатора (натријум-хидроксид и натријум-силикат), развој и оптимизацију везива активираног са SHA и евалуацију система активираних са SHA и конвенционалним силикатним активатором на нивоу бетона. Докторска дисертација представља прву свеобухватну карактеризацију утицаја SHA - и пепела биомасе богатог калијумом уопште - употребљеног као хидроксидни активатор на физичка, механичка и трајносна својства, алкално-активираног везива на нивоу бетона, уз идентификацију механизама који управљају његовим понашањем. Резултати истраживања потврђују да SHA представља одржив хидроксидни активатор за производњу алкално-активираних малтера и бетона на бази згуре, уз допринос валоризацији локално доступног пољопривредног отпада.
Датум прихватања теме од стране надлежног већа:	10.10.2024.
Датум одбране: (Попуњава накнадно институција)	
Чланови комисије: (титула, име, презиме, звање, институција)	**Председник:** др Нина Штирмер, редовни професор, Грађевински факултет, Универзитет у Загребу **Члан:** др Снежана Вучетић, ванредни професор, Технолошки факултет Нови Сад, Универзитет у Новом Саду **Члан:** др Весна Булатовић, ванредни професор, Факултет техничких наука, Универзитет у Новом Саду **Члан:** др Владимир Вукобратовић, ванредни професор, Факултет техничких наука, Универзитет у Новом Саду **Члан, ментор:** др Маријана Сердар, ванредни професор, Грађевински факултет, Универзитет у Загребу
Напомена:	

UNIVERSITY OF NOVI SAD
FACULTY OF TECHNICAL SCIENCES

KEY WORD DOCUMENTATION[2]

Document type:	Doctoral dissertation
Author:	Olivera Bedov
Supervisor 1 (title, first name, last name, position, institution)	dr. Suzana Draganić, Assistant Professor, Faculty of Technical Sciences, University of Novi Sad
Supervisor 2 (title, first name, last name, position, institution)	dr. Marijana Serdar, Associate Professor, Faculty of Civil Engineering, University of Zagreb
Thesis title in English:	Possibilities of sunflower husk ash utilization as an alternative activator for slag-based alkali-activated materials
Language and script:	English (latin)
Physical description:	Pages: 210 Chapters: 5 References: 198 Tables: 30 Illustrations: 98 Appendices: 10
Scientific field:	Civil Engineering
Scientific subfield (scientific discipline):	Building materials, assessment and repair of structures
Subject, Key words:	alkali-activated materials, alternative binders, valorisation, alternative activator, biomass ash, sunflower husk ash, one-part alkali-activation, sustainability, decarbonisation, circular economy
Abstract in English:	Cement production ranks among the largest sources of anthropogenic CO_2 emissions, accounting for approximately 7% of total global emissions. Reducing its use represents one of the key decarbonisation strategies. Over the past decades, research has focused on the development of binders with a lower carbon footprint. Alkali-activated materials (AAMs) represent a promising alternative, as they are synthesised from amorphous aluminosilicates (most commonly industrial by-products such as slag and fly ash) with alkaline activators. However, conventional chemical activators used in AAM systems account for a significant share of both the environmental footprint and the overall cost of these systems, due to their energy-intensive production. This thesis investigates the possibility of valorising sunflower husk ash (SHA), a locally available potassium-rich waste generated through the combustion of sunflower husks, as an alternative activator for slag-based AAMs.

[2] The author of the doctoral dissertation has signed the following Statements:
5б – Statement on the authorship,
5в – Statement that the printed and e-version of the doctoral dissertation are identical and authorization to use personal data,
5г – Copyright statement.
The paper and e-versions of Statements are held at the institution and are not included into the printed thesis.

	The research was conducted in four experimental phases: material characterisation, optimisation of alkali-activated concrete mix design with reduced conventional activator content (sodium hydroxide and sodium silicate), development and optimisation of the binder activated with SHA and evaluation of the systems activated with SHA and conventional silicate activator at the concrete level. The presented doctoral dissertation provides the first comprehensive characterisation of the influence of SHA - and potassium-rich biomass ash in general - when used as an alkali hydroxide activator, on the physical, mechanical, and durability properties of alkali-activated binder at a concrete level, together with the identification of mechanisms governing its performance. The research results demonstrate that SHA is a viable alkali hydroxide activator for the production of slag-based alkali-activated mortars and concretes, contributing to the valorisation of locally available agricultural waste.
Date of endorsement by the scientific board:	October 10, 2024
Date of defense: (Filled in by the institution)	
Thesis defence board: (title, first name, last name, position, institution)	**Chair:** dr. Nina Štirmer, Full Professor, Faculty of Civil Engineering, University of Zagreb **Member:** dr. Snežana Vučetić, Associate Professor, Faculty of Technology Novi Sad, University of Novi Sad **Member:** dr. Vesna Bulatović, Associate Professor, Faculty of Technical Sciences, University of Novi Sad **Member:** dr. Vladimir Vukobratović, Associate Professor, Faculty of Technical Sciences, University of Novi Sad **Member, supervisor:** dr. Marijana Serdar, Associate Professor, Faculty of Civil Engineering, University of Zagreb
Note:	

Possibilities of sunflower husk ash utilization as an alternative activator for slag-based alkali-activated materials

by

Olivera Bedov

INTERNATIONAL DUAL DOCTORATE

University of Novi Sad, Faculty of Technical Sciences

University of Zagreb, Faculty of Civil Engineering

A dissertation submitted to the

Faculty of Technical Sciences

University of Novi Sad

April 2026

ACKNOWLEDGEMENT

First and foremost, I would like to express my deepest appreciation to my supervisors, Associate Professor Marijana Serdar and Assistant Professor Suzana Draganić. To Professor Serdar I am particularly indebted - her trust, generosity, and scientific vision gave me the extraordinary opportunity to pursue a joint doctoral degree, an experience that has shaped not only this thesis but also my broader academic path. I am equally grateful to Professor Draganić, whose mentorship, patience, and encouragement have been a constant source of motivation.

I owe the deepest gratitude to my advisor, Professor Mirjana Malešev, for guidance in the first years of doctoral studies, support and inspiration for the dissertation topic.

My sincere thanks go to my colleagues at the Department of Civil Engineering and Geodesy at the Faculty of Technical Sciences for creating a collaborative and stimulating working environment and for their willingness to share their knowledge and time whenever needed.

I am deeply grateful to the colleagues at the Department of Materials at the Faculty of Civil Engineering, University of Zagreb, for welcoming me with open arms during my research stay, especially the team at Sveti Duh and the LATOM research group. The professionalism, friendliness, and generosity I encountered there made my time in Zagreb not only scientifically enriching but also personally rewarding. I feel fortunate that what began as a research collaboration has grown into lasting connections that I continue to cherish.

A special word of gratitude is due to the laboratory staff at both institutions, whose help and support were essential for carrying out the extensive experimental programme.

Finally, I would like to thank my family and friends for their love, patience, and encouragement throughout these years. Their ever-present support has made even the most demanding moments of this journey easier.

ABSTRACT

Decarbonisation of the construction sector plays a significant role in achieving the Sustainable Development Goals. Cement production ranks among the largest sources of anthropogenic CO_2 emissions, accounting for approximately 7% of total global emissions. Reducing its use represents one of the key decarbonisation strategies. Over the past decades, research has focused on the development of binders with a lower carbon footprint.

Alkali-activated materials (AAMs) are binders synthesised from amorphous aluminosilicates (most commonly industrial by-products such as slag and fly ash) and alkaline activators. They are cement-free binders that represent a promising alternative to Portland cement because of their lower CO_2 emissions. However, conventional chemical activators used in AAM systems account for a significant share of both the environmental footprint and the overall cost of these systems, due to their energy-intensive production. This thesis investigates the possibility of valorising sunflower husk ash (SHA), a locally available potassium-rich agricultural waste, as an alternative activator for slag-based AAMs.

The research was conducted in four experimental phases: material characterisation, optimisation of alkali-activated concrete mix design with reduced conventional activator content (sodium hydroxide and sodium silicate), development and optimisation of SHA-activated binder, and evaluation of the influence of SHA on binder properties at the concrete level. Material characterisation confirmed that SHA possesses suitable chemical and physical properties for alkali activation, with the reaction between SHA and ground granulated blast furnace slag (GGBFS) producing C-S-H and C-A-S-H gels characteristic of alkali-activated slag systems. The optimisation of the binder through systematic assessment of water-to-binder ratio, SHA content, mixing procedures and curing regimes established the parameters for producing a waste-based binder using SHA as received, with minimal technological requirements. The highest 28-day compressive strength of 55 MPa was attained with 25 wt% GGBFS of SHA, cured at ambient temperature.

At the concrete level, the combination of SHA with sodium silicate (Ms=0.42) was used as an activator, resulting in the compressive strength of 50 MPa, after 28 days. To assess the influence of SHA on the concrete system, a set of physical, mechanical, and durability properties was tested and compared to the developed reference concrete mix with reduced chemical activator content (n(Na_2O=4%), Ms=0.42), attaining a 28-day compressive strength of 46 MPa. Using only SHA as an activator was not viable because of significant workability challenges. Two alkali-activated concrete mixes exhibited comparable mechanical properties. Despite the higher compressive strength, the introduction of SHA resulted in a 12-17% lower

modulus of elasticity. Replacing sodium hydroxide with SHA increased capillary pore content without affecting total porosity, the critical pore diameter, or the threshold diameter. Introducing SHA into the mix doubled drying shrinkage, driven by two concurrent mechanisms: greater moisture loss from the coarser capillary pore network and lower elastic stiffness of the K^+-modified matrix. However, the same compliance that increased total shrinkage simultaneously enabled stress relaxation, preventing surface cracking despite the substantially higher deformation.

Durability properties were not compromised by the addition of SHA. For all examined durability indicators - carbonation resistance, chloride migration, and water absorption - the dominant role of chemically controlled mechanisms, specifically hydrotalcite-facilitated CO_2 uptake and chloride binding, mitigated the negative impact of the coarser pore structure. These findings demonstrate that pore structure refinement alone cannot be considered a reliable predictor of durability in AAMs containing SHA.

The presented thesis provides the first comprehensive characterisation of the influence of SHA - and potassium-rich biomass ash in general - when used as an alkali hydroxide activator, on the physical, mechanical, and durability properties of alkali-activated binder at a concrete level, together with the identification of mechanisms governing its performance. The results demonstrate that SHA is a viable alkali hydroxide activator for the production of slag-based alkali-activated mortars and concretes, contributing to the valorisation of locally available agricultural waste. However, future research is needed to address the two main challenges - workability and shrinkage.

Key words: alkali-activated materials, alternative binders, valorisation, alternative activator, biomass ash, sunflower husk ash, one-part alkali-activation, sustainability, decarbonisation, circular economy

ПРОДУЖЕНИ ИЗВОД НА СРПСКОМ ЈЕЗИКУ

Декарбонизација грађевинског сектора има значајну улогу у остваривању циљева одрживог развоја. Производња цемента спада међу најзначајније изворе антропогених емисија CO_2, са учешћем од приближно 7% у укупним глобалним емисијама. Смањење његове употребе стога представља једну од кључних стратегија декарбонизације. Последњих деценија, истраживања су усмерена ка развоју везива с нижим угљеничним отиском.

Алкално-активирани материјали (енг. *alkali-activated materials*, AAM) су везива без цемента која се синтетишу реакцијом аморфних алумосиликата (најчешће индустријских нуспроизвода, као што су згура и летећи пепео) са алкалним активаторима. Конвенционални хемијски активатори који се користе у AAM системима - алкални хидроксиди и силикати - обезбеђују неопходну алкалну средину за растварање прекурсора, полимеризацију и формирање продуката реакције активације. AAM су предмет опсежних истраживања током последњих неколико деценија, захваљујући знатно нижим емисијама CO_2 у поређењу са бетонима на бази Портланд цемента. Ово се првенствено приписује одсуству цементног клинкера и употреби отпадних материјала и индустријских нуспроизвода као прекурсора, чиме се испуњавају захтеви стратегија одрживог развоја. Обим смањења емисија CO_2 у значајној мери зависи од врсте и доступности употребљених прекурсора и активатора. Истраживање утицаја алкално-активираних бетона (енгл. *alkali-activated concrete*, AAC) са различитим прекурсорима на животну средину показало је да се смањење емисија CO_2 од 57%, 42% и 39% може постићи код алкално- активираних бетона на бази згуре летећег пепела и метакаолина, респективно.

Упркос томе што је знатно нижи од бетона на бази Портланд цемента, готово целокупан еколошки отисак AAM приписује се неизбежном присуству синтетичких хемијских активатора. Процес њихове производње је енергетски интензиван и повлачи за собом и друге изазове по животну средину, попут оштећења озонског омотача и екотоксичности. Иако алкални хидроксид по правилу чини тек 1-5%, а алкални силикат 3-10% масе AAC, активатори чине 13% до 33% укупног потенцијала глобалног загревања AAM, у зависности од састава мешавине. Њихова висока цена, као и безбедносни проблеми проистекли из руковања високо каустичним раствором активатора, додатно ограничавају ширу примену AAM у грађевинском сектору. У научној литератури, ови изазови су разматрани кроз пројектовање AAM мешавина са смањеним садржајем активатора уз очување задовољавајућих перформанси, као и кроз замену конвенционалних хемијских

активатора алтернативним изворима алкалија и силицијума. Међу индустријским нуспроизводима истраженим као замена за силикатне активаторе налазе се силикатна прашина и стаклени отпад, док се црвени муљ предлаже као извор алкалија. Пепели настали сагоревањем пољопривредне биомасе се такође сматрају перспективним алтернативним активаторима, будући да су богати калијумом, калцијумом и силицијумом, у зависности од биљне врсте од које потичу.

На глобалном нивоу, термоенергетска постројења на биомасу производе 480 милиона тона пепела годишње, а процењује се да би биомаса као алтернативни извор енергије могла да замени 33-50% светских енергетских резерви до 2050. године. У зависности од хемијског састава, ови пепели могу имати различите примене у разним индустријским гранама, као што су употреба у својству минералних додатака (енгл. *supplementary cementitious materials*, SCM) у грађевинарству или побољшање квалитета земљишта употребом у својству ђубрива, односно средстава за рекултивацију и ремедијацију у пољопривреди и рударству. Међутим, значајне количине ових пепела и се и даље одлажу на депонијама, узрокујући загађење животне средине. Потенцијално проширење њихове примене као алтернативног активатора у технологији ААМ може смањити допринети остваривању циљева циркуларне економије засноване на концепту „нула отпада", уз истовремено унапређење одрживости ААМ.

Потреба за истраживањем

Пољопривредне активности широм света годишње производе приближно 140 милијарди тона остатака биомасе. Значајан удео међу овим остацима чини биомаса сунцокрета - широко распрострањене индустријске биљне културе која се примењује у прехрамбеној и хемијској индустрији, као и у производњи биодизела. Светска производња сунцокрета у 2025. години износила је приближно 54,8 милиона тона.

Сунцокрет је доминантна биљна култура међу индустријским биљем у Републици Србији, при чему 45,2% укупних пољопривредних површина под индустријским биљем чине усеви сунцокрета. Од тога, 88,5% засејано на територији Аутономне Покрајине Војводине.

Сунцокретове љуске представљају нуспроизвод процеса прераде семена сунцокрета. Ниска природна влажност (9%) и повољне топлотне карактеристике (у просеку 18 $MJ \cdot kg^{-1}$) чине их погодним извором енергије. Поједини произвођачи сунцокретовог уља на територији Аутономне Покрајине Војводине у одређеној мери их користе као гориво. Љуска сунцокрета се такође користи као енергент за систем даљинског грејања града Сремске Митровице. Пепео сунцокретове љуске (енгл. *sunflower husk ash*, SHA) настаје као отпад при сагоревању сунцокретове љуске. Према извештајима двеју компанија -

произвођача уља Викториа Оил из Шида и топлане ТЕТО у Сремској Митровици - у овим процесима годишње настаје 960 тона SHA. Карактерише га висок садржај калијума, а најчешће се одлаже на депоније без практичне примене. Иако је доказано да се поједини пепели пољопривредне биомасе могу успешно користити као SCM, употреба SHA у конвенционалним цементним композитима ограничена је управо због високог садржаја алкалија.

Докторска дисертација истражује могућност валоризације локално доступног отпада, SHA, као алтернативног активатора за AAM системе. Смањење удела или потпуна замена хемијских активатора истовремено би смањили емисије CO_2 и материјалне трошкове, унапредили примену принципа циркуларне економије и одрживог развоја у грађевинском сектору и омогућили да се SHA уместо одлагања - најнижег степена хијерархије управљања отпадом - усмери ка превенцији.

Предмет, циљ и хипотезе истраживања

Предмет истраживања су AAM на бази гранулисане згуре високих пећи (енгл. *ground granulated blast furnace slag*, GGBFS), активиране:

- конвенционалним хемијским алкалним активаторима, натријум-хидроксидом и натријум-силикатом,
- алтернативним активатором SHA,
- комбинацијом SHA и натријум-силиката.

Циљ предложеног истраживања је валоризација локално доступног отпадног материјала, SHA, његовом применом у грађевинском сектору као алтернативног активатора за AAM на бази GGBFS са смањеним еколошким отиском. Валоризација ће се спровести кроз:

- замену конвенционалног алкалног хидроксидног активатора у AAM мешавинама са SHA,
- утврђивање утицаја SHA на процес активације и својства AAM на бази GGBFS,
- упоредну анализу перформанси AAC активираних смањеним садржајем конвенционалног активатора и AAC активираних алтернативним активатором,
- пројектовање AAM на бази згуре са везивом заснованим искључиво на отпадним материјалима и/или везивом заснованим на комбинацији отпадног материјала и конвенционалног активатора.

Истраживање се заснива на следећим хипотезама:

- Хипотеза 1: SHA се може користити као алтернативни активатор за синтезу ААМ на бази згуре.
- Хипотеза 2: Употреба искључиво алтернативног активатора у ААМ неће значајно умањити механичка и трајносна својства ААМ на бази згуре.
- Хипотеза 3: Могуће је произвести алкално ААС на бази згуре искључиво од отпадних материјала - згуре и SHA.

Експериментално истраживање

Експериментално истраживање је организовано у четири фазе. Програм је структуриран тако да закључци добијени у једној експерименталној фази представљају основу за наредну.

Циљ прве фазе је карактеризација компонентних материјала - GGBFS и SHA. Карактеризација је спроведена испитивањем хемијског и минералошког састава, функционалних група, расподеле величине честица, специфичне површине и специфичне запреминске масе. За SHA су додатно одређени морфологија површине, облик честица и растворљивост у води.

Циљ друге фазе је оптимизација ААС са смањеним садржајем активатора ради побољшања њихове одрживости. Планом експерименталног истраживања омогућена је систематска оптимизација кроз варирање садржаја алкалија, силикатног модула (*енгл. silicate modulus*, Ms) и водовезивног односа (енгл. *water-to binder-ratio*, w/b) у десет ААС мешавина. За даље испитивање изабране су три мешавине које су показале оптималну обрадивост и чврстоћу при притиску. На одабраним мешавинама су испитивани порозност, дубина продора воде под притиском, отпорност на карбонатизацију и продор хлорида како би била одабрана крајња референтна мешавина.

Циљ треће експерименталне фазе је развој и оптимизација обрадивости и чврстоће при притиску везива активираног SHA. На нивоу малтера варирани су следећи параметри: w/b однос (0,42; 0,45; 0,5), садржај SHA (15, 25 и 35 мас.% GGBFS), режим неге (амбијентална температура и неговање на 65˚C током 5 дана) и време растварања SHA пре мешања (0 ч, 1 ч, 6 ч и 24 ч). Додатно, праћено је излуживање калијума и pH вредност SHA суспензије. Утицај садржаја SHA и режима неге на промене функционалних група и продуката реакције испитиван је на узорцима пасте коришћењем ФТИР и ТГА анализа.

Циљ четврте експерименталне фазе био је испитивање утицаја SHA на свежа и очврсла физичка, механичка и трајносна својства на нивоу бетона. Упоређиване су три ААС мешавине: референтна мешавина са конвенционалним хемијским активаторима

(изабрана у фази 2), мешавина активирана SHA и натријум силикатом и мешавина активирана само SHA. Оптималан садржај SHA одређен је на основу резултата из фазе 3. Испитивања су обухватила својства у свежем стању (време везивања одговарајућих пасти, температура, конзистенција, садржај ваздуха, запреминска маса), физичка својства у очврслом стању (запреминска маса, порозност, фазни састав, капиларно упијање воде, скупљање), механичка својства (чврстоћа при притиску, чврстоћа при савијању, модул еластичности) и трајносна својства (продор воде под притиском, отпорност на карбонатизацију, отпорност на продор хлорида).

Резултати и закључци истраживања

Резултати карактеризације материјала (**Фаза 1**) анализирани су по релевантним физичким и хемијским својставима GGBFS и SHA. Главни оксиди идентификовани у GGBFS су SiO_2, CaO и MgO, што је класификује као неутрално-базну згуру. SHA превасходно садржи K_2O, CaO, SO_3 и MgO, при чему је калијум у SHA углавном присутан у облику арканита. Анализа слика добијених скенирајућом електронском микроскопијом показала је да честице SHA нису порозне и да имају неправилане облике са храпавим површинама. За разлику од SHA, који има крупније честице и ширу расподелу величина честица, GGBFS је значајно финији материјал са уједначенијом гранулацијом. Растворљивост SHA у води повећава се са повећањем времена и температуре растварања. Карактеризација материјала потврдила је да SHA има задовољавајућа хемијска и физичка својства за употребу као алтернативни хидроксидни активатор у AAM, без претходне обраде.

У Фази 2, резултати су анализирани кроз утицај варираних параметара на својства бетона (мешавине R1-R10). Уочено је да обрадивост AAC бетона зависи од међусобно зависних утицаја w/b односа, садржаја алкалија и Ms, при чему је Mc идентификован као најзначајнија појединачна променљива. При веома малом садржају активатора, w/b има умерен утицај на слегање. Садржај алкалија изнад приближно 4 мас.% има већи утицај на слегање од w/b, али само за Ms ≥ 1,0. Чврстоћа при притиску у AAC бетону углавном зависи од садржаја Na_2O и силикатног модула, при чему w/b има секундарну, али конзистентну улогу када је састав активатора константан. Испод Mc = 1,0, садржај Na_2O је доминантан параметар за чврстоћу, док код Ms ≥ 1,0 силикатни модул постаје пресудан. На основу ових резултата, за даље испитивање изабране су три мешавине: две са ниским садржајем активатора (R2, R5) и једна са умереним садржајем активатора (R7). Испитивања порозности и трајности показала су да смањен садржај активатора омогућава не само задовољавајућа механичка, већ и трајносна својства AAC. Закључено је да су оптималан садржај алкалија и Ms за овај систем 4 мас.% GGBFS и 0,42,

респективно. Мешавина са овим параметрима (R5) изабрана је као референтни ААС за Фазу 4.

Резултати Фазе 3 анализирани су у контексту утицаја варираних параметара на својства три пасте (P15, P25 и P35) и три малтерске мешавине (M15, M25 и M35). Повећање w/b односа довело је до повећања слегања малтерских мешавина. Задовољавајућа обрадивост за употребу кварцног песка постигнута је при w/b од 0,45, док је увођење дробљеног доломитног агрегата захтевало w/b од 0,5. Уочено је да већи садржај SHA смањује обрадивост, што је у складу са морфологијом честица SHA. Међутим, већи садржаји SHA утицали су на формирање веће количине гелова калцијум-силикат-хидрата (енгл. *calcium silicate hydrate*, C-S-H) и калцијум-алумо-силиката-хидрата (енгл. *calcium aluminosilicate hydrate*, C-A-S-H), што је уочено анализом узорака пасти. Неговање на 65°C утицало је на бржи развој ране чврстоће при притиску (постигнуто је 89-98% у односу на чврстоћу након 28 дана), али је резултирало нижом чврстоћом при притиску након 28 дана у поређењу са неговањем на амбијенталној температури. Потапање SHA у воду пре мешања побољшало је растварање калијумових јона и довело до повећања чврстоће при притиску до 14,7%, у зависности од трајања потапања, али је негативно утицало на обрадивост мешавина. Највећа чврстоћа при притиску након 28 дана од 55 MPa постигнута је мешавином са 25% SHA (M25), без претходне обраде SHA и растварања у води пре мешања, негованом на амбијенталној температури.
Избор параметара мешавине за наредна испитивања заснован је на постигнутим оптималним својствима и минималним техничким захтевима за потенцијалну примену (режим неге и растварање SHA). Овакав систематичан приступ омогућио је ефикасну евалуацију бројних утицајних параметара и својстава, што је на крају довело до идентификације оптималне малтерске мешавине активиране SHA и дефинисања састава мешавине за ААС на бази SHA за последњу фазу истраживања. Поред тога, варијација поступка мешања представља нови аспект истраживања који раније није обрађен у доступној литератури.

Резултати Фазе 4 анализирани су компаративно са аспекта типа активатора. На основу закључака из Фазе 3, пројектоване су две ААС мешавине које садрже SHA: једна активирана искључиво SHA (SHA25) и друга активирана комбинацијом SHA и силикатног активатора (SHA-S), у складу са саставом референтне мешавине. Ове мешавине упоређене су са референтном из Фазе 2 (R). Анализа је спроведена кроз свеобухватна испитивања својстава у свежем стању и механичких, физичких и трајносних својстава бетона, праћена оценом промена у микроструктури, продуктима реакције активације и порозности, изазваним додатком SHA.

Резултати су показали да SHA значајно смањује обрадивост када се комбинује са дробљеним агрегатом. Мешавина SHA25 (активирана са 25% SHA у односу на масу GGBFS) је имала слабо пластичну конзистенцију, што је довело до неадекватне уградње, па су њена својства даље испитивана само у погледу чврстоће при притиску. Замена натријум-хидроксида са SHA није утицала на механичка својства мешавине SHA-S, при чему је чврстоћа при притиску након 28 дана неговања достигла приближно 50 MPa , у поређењу са 46 MPa код референтне R мешавине. Након 90 дана неговања, обе мешавине постигле су исту чврстоћу при притиску од 57 MPa. Чврстоћа при савијању пратила је сличан тренд након 56 дана.

Увођење K^+ јона кроз SHA довело је до смањења уређености гела, услед разлике у величини и густини наелектрисања између K^+ и Na^+. То је резултирало 12% и 17% нижим модулом еластичности након 28 и 56 дана, респективно, у поређењу са R мешавином. Мешавина SHA-S такође је показала 25,6% већи садржај капиларних пора у односу на R узорке након 28 дана неговања, док су кумулативна порозност, критични пречник пора и гранични пречник пора били исти.

Понашање обе мешавине у погледу упијања воде одступало је од стандардног билинеарног модела прописаног за бетон на бази Портланд цемента, што је очекивано за AAC заснован на згури. Брзина упијања за мешавину са SHA била је два пута већа него за референтну мешавину, иако је коначна апсорпција воде била слична. Увођење SHA у мешавину удвостручило је скупљање због већег губитка воде и веће деформабилности матрице, што је потврђено нижим модулом еластичности. Већа деформабилност је, међутим, имала позитиван утицај на смањење појаве прслина услед сушења.

Упркос већем садржају капиларних пора и упијању воде, SHA није нарушио трајност. Отпорност на карбонатизацију током свих дана изложености била је суштински идентична за обе мешавине. MgO у SHA допринео је формирању веће количине хидроталцита који делује као апсорбент CO_2. Повећање укупне порозности мешавине SHA-S након карбонатизације било је мање него у референтној мешавини (2,9% у односу на 4,9% за R), као и повећање критичног и граничног пречника пора. То указује да додатни хидроталцит делимично ублажава микроструктурна оштећења изазвана декалцификацијом C-A-S-H, што доводи до мање израженог укрупњавања мреже пора. Термогравиметријска анализа потврдила је овај механизам: SHA-S показује и већи почетни садржај хидроталцита и веће повећање губитка масе повезаног са хидроталцитом након карбонатизације.

Мешавина SHA-S је имала већи продор хлорида након 28 дана неге, у складу са већим садржајем капиларних пора. Међутим, након 56 дана неге надмашила је референтну мешавину, постижући 20% нижи коефицијент миграције упркос знатно већем садржају

капиларних пора. Раздвајање утицаја структуре пора и транспорта хлорида указује да је хемијско везивање доминантан механизам који управља отпорношћу на хлориде у систему SHA-S. Већи садржај хидроталцита омогућио је већу способност везивања хлорида кроз анјонску замену у слојевима хидроталцита. Смањење коефицијента миграције за 52% између 28 и 56 дана у односу на 10% код референтне мешавине указује да SHA поспешује формирање хидроталцита и након 28 дана неговања.

На основу резултата експерименталног истраживања, изведени су следећи закључци:

1. Својства материјала SHA

SHA поседује задовољавајућа хемијска и физичка својства за примену као активатор у AAM, без потребе за претходном обрадом.

2. Оптимизација референтних AAC мешавина

Оптималан садржај алкалија и силикатни модул Ms за референтну AAC мешавину са ниским садржајем активатора износе 4 мас.% GGBFS и 0,42, респективно. Овим се обезбеђују одрживе AAC мешавине са смањеним садржајем хемијских активатора, без нарушавања обрадивости, чврстоће при притиску и трајности.

3. Развој и оптимизација везива активираног SHA

Реакција између SHA и GGBFS доводи до формирања C-S-H и C-A-S-H гелова карактеристичних за алкално-активиране системе засноване на згури.

SHA смањује обрадивост малтерских мешавина услед неправилног облика и храпаве површине честица. На основу експерименталних резултата препоручени су следећи параметри мешавине:

- Оптималан w/b однос од 0,45 при садржају SHA од 25 мас.% GGBFS, чиме се постиже равнотежа између обрадивости и чврстоће при притиску.
- За малтере са дробљеним агрегатом фракције 0-4 mm, обрадивост и чврстоћа при притиску оптимизоване су повећањем w/b на 0,5 и додавањем натријум-силиката ради постизања Ms = 0,42.

SHA се може користити самостално као активатор за AAM-е засноване на згури, на нивоу малтера. Најважнији закључци обухватају:

- Неговање на 65°C поспешује развој ране чврстоће, при чему се у првим данима достиже 89-98% чврстоће при притиску након 28 дана. Међутим, повишена температура неговања смањује чврстоћу након 28 дана у односу на неговање на амбијенталној температури.

- Претходно растварање SHA у води повећава ослобађање K^+ јона и доводи до повећања чврстоће при притиску до 14,7%, у зависности од трајања растварања, али истовремено смањује обрадивост услед убрзане реакције активације у почетном периоду.

4. Својства бетона активираног са SHA

Обрадивост - SHA се не може користити као једини активатор на нивоу бетона, услед значајног смањења обрадивости. Додавање натријум-силиката ради постизања Ms = 0,42 побољшава слегање и омогућава адекватно уграђивање и збијање бетона.

Механичка својства - Замена NaOH са SHA не утиче на смањења механичких својстава.

- Мешавина са 25 мас.% GGBFS SHA и Ms = 0,42 достигла је чврстоћу при притиску од 50 MPa након 28 дана (референтна мешавина: 46 MPa). Мала разлика може бити последица филер ефекта нерастворених пепела.
- Након 90 дана, обе мешавине су достигле исту чврстоћу при притиску од 57 MPa, при чему чврстоћа при затезању показује сличан тренд након 56 дана.
- Додавање K^+ јона путем растварања SHA доводи до смањења модула еластичности након 28 и 56 дана, што се објашњава слабијим везама у међуслојевима C-A-S-H гела услед присуства K^+ јона.

Физичка својства - Замена NaOH са SHA не утиче значајно на укупну порозност и капиларно упијање воде, али значајно повећава скупљање.

- Кумулативна отворена порозност је била иста за обе мешавине бетона. Замена NaOH са SHA довела је до повећања удела капиларних пора, без утицаја на укупну отворену порозност, критични и гранични пречник пора.
- Капиларно упијање воде код обе мешавине одступа од стандардног билинеарног модела прописаног за PC бетон, што је уобичајено за алкално-активиране системе засноване на згури. Додавање SHA повећава почетну брзину упијања услед веће капиларне порозности. Коначна вредност упијања воде је само незнатно већа код мешавине са SHA, што потврђује сличну укупну порозност две мешавине.
- Скупљање услед сушења код AAC се удвостручује увођењем SHA. Условљено је већим губитком влаге из мреже крупнијих капиларних пора и већом деформабилношћу матрице модификоване K^+ јонима. Међутим, нижи модул еластичности, који доприноси већем скупљању, истовремено омогућава већу релаксацију напона услед течења, чиме се спречава појава површинских прслина услед сушења, упркос знатно већим укупним деформацијама.

Трајносна својства - Замена NaOH са SHA не утиче негативно на трајност.

- Продор воде под притиском је био исти за обе мешавине.
- Брзина карбонатизације код оба бетона је приближна за свако време трајања изложености. Мешавина са SHA показује само благо повећање брзине карбонатизације. Упркос грубљој структури пора и очекивано већој дубини карбонатизације, повећан садржај хидроталцита, као последица додатног MgO из SHA, делује као апсорбент CO_2 и ублажава декалцификацију C-A-S-H гела.
- Иако мешавина са SHA има већи продор хлорида након 28 дана неге, овај тренд се мења након 56 дана неговања, када продор постаје мањи у односу на референтну мешавину. Смањење дубине продора хлорида при додавању SHA приписује се већем капацитету везивања хлорида услед повећаног садржаја хидроталцита.

Замена NaOH са SHA доводи до промена физичких и хемијских карактеристика продуката реакције активације. У оквиру испитиваних трајносних својстава, резултати указују да хемијски механизми имају доминантан утицај у односу на физичке, као што су промене у структури пора.

Предложени правци даљих истраживања укључују одређивање садржаја калијума који учествује у реакцији активације, испитивање потенцијалнпог континуалног растварања калијума у систему, утицај на течење и релаксацију напона у бетону, побољшање обрадивости и смањење скупљања бетона.

Ова дисертација представља прву свеобухватну карактеризацију утицаја SHA - и пепела биомасе уопште - употребљеног као хидроксидни активатор на физичка, механичка и трајносна својства, алкално-активираног везива на нивоу бетона, уз идентификацију механизама који управљају његовим понашањем. Резулттати потврђују да се SHA може употребити као одржив хидроксидни активатор за производњу малтера и бетона на бази згуре, уз допринос валоризацији локално доступног полуопривредног отпада.

Кључне речи: алкално-активирани материјали, алтернативна везива, валоризација, алтернативни активатор, пепео биомасе, пепео сунцокретове љуске, једнофазна алкална активација, одрживост, декарбонизација, циркуларна економија

Table of Contents

LIST OF FIGURES

LIST OF TABLES

LIST OF ABBREVIATIONS

AAM	alkali-activated material
PC	Portland cement
FA	fly ash
BFS	blast furnace slag
MK	metakaolin
SCM	supplementary cementitious material
SF	silica fume
GW	glass waste
SHA	sunflower husk ash
GGBFS	ground granulated blast furnace slag
N, K-A-S-H	alkali-aluminosilicate hydrate
C-A-S-H	calcium-aluminosilicate hydrate
AFm	Alumina-Ferric oxide-monosulfate
C-S-H	calcium silicate hydrate
w/b	water-to-binder ratio
n	alkali content
Ms	silica modulus
AAS	alkali-activated slag
AAC	alkali-activated concrete
ABA	agricultural biomass ashes
WSA	wheat straw ash
RHA	rice husk ash
SCBA	sugarcane bagasse ash
SCSA	sugarcane straw ash
POFA	palm oil fuel ash
OBA	olive stone biomass ash
OBFA	olive stone biomass fly ash
OBBA	olive stone biomass bottom ash
ASA	almond biomass ash
HBA	hazelnut biomass ashes
SSA	sunflower stalk ash

SSFA	sunflower shell fly ash
TA	ambient curing
T65	curing at 65ºC
XRF	X-ray fluorescence
EDX	energy-dispersive X-ray spectroscopy
FTIR	Fourier-transform infrared
XRD	X-ray diffraction
PSD	particle size distribution
TGA	thermogravimetric analysis
DTG	derivative thermogravimetry
MIP	mercury intrusion porosimetry

Chapter 1
INTRODUCTION

1. INTRODUCTION

The effort to address the issues of climate change and sustainable development marked decarbonisation of the construction industry as one of the primary strategies for achieving the global goal of net-zero carbon dioxide emissions by 2050 [1,2]. Changes in the cement industry are necessary to achieve this goal, as cement production of 4.2 billion tonnes annually is responsible for approximately 7% of anthropogenic CO_2 emissions [3]. Cement is primarily used to produce concrete, the most widely used construction material worldwide, whose reliability has been demonstrated over more than 150 years of application and research. Given its proven performance, durability, cost-effectiveness, and broad applicability, no alternative material is expected to replace concrete in the near future. Additionally, cement production is highly resource and energy-intensive, with energy supply costs accounting for 50-60% of total production expenses [4]. This makes concrete unable to meet contemporary requirements for efficient, sustainable construction and circular economy practices. Considering that the cement production rates are comparable to global food production, and that demand increases with rapid urbanisation [5], several pathways toward sustainable concrete have been proposed [1,3], including the development of alternative binders [6].

1.1 Alkali-activated materials - definition, history, contemporary application, and challenges

Alkali-activated materials (AAMs) are cement-free binders synthesised from amorphous aluminosilicate-rich precursors and alkaline activators in liquid or solid form. The most common precursors are coal fly ash (FA), blast furnace slag (BFS), and calcined clays or metakaolin (MK). Alkaline activators are usually solutions of potassium or sodium hydroxides and silicates, while carbonates and sulphates can also be used, depending on the type of precursor [7]. The activation reaction is initiated and catalysed by activators through the dissolution of Si and Al from the precursors by raising the pH, enabling their polymerisation and the formation of reaction products [8].

AAMs have been extensively researched over the last few decades due to their significantly lower CO_2 emissions compared to PC concrete production. This is mainly attributed to the absence of cement clinker and the use of waste and industrial by-products as precursors, thus complying with sustainable development strategies [9]. The extent of CO_2 emissions reduction strongly depends on the type and availability of used precursors and activators [10]. A study on the environmental impact of alkali-activated concretes with different precursors [11] showed that CO_2 emissions reductions of 57%, 42%, and 39% can be achieved with BFS-, FA-, and MK-based alkali-activated concretes, respectively, compared to PC concrete.

AAMs can also be designed to have mechanical and durability properties comparable to or superior to those of PC concrete. The literature reports excellent mechanical properties, higher resistance to elevated temperatures than PC concrete, and higher resistance to chloride attack as well as chemical resistivity [12,13]. Their potentially good long-term durability is further evidenced by structures built in the former Soviet Union, China, and Northern Europe during the 1950s to 1980s, North America and Netherlands in 1990s, as well as structures constructed in Australia in more recent times [9]. Therefore, interest in AAMs is being renewed, although alkali-activation has been extensively researched and applied on a large scale at varying degrees since the 1950s [6].

Despite their advantages, AAMs also exhibit several performance limitations, including low workability retention, fast setting, inconsistent consistency, and high total shrinkage. Freeze-thaw resistance seems to be an important challenge, and the published research is not always consistent on the AAMs' performance [14,15,16]. Given the wide range of possible precursors and activators, the properties of AAMs can vary considerably, making it difficult to generalize about their properties [17].

It should be noted that the terminology in the field of alkali-activation can be complicated, since there were a lot of different names in research applied for the group of binders synthesized by this chemical process. Some of them are “mineral polymers,” “inorganic polymers”, “inorganic polymer glasses”, “alkali-bonded ceramics”, “alkali ash material”, “soil cements”, “soil silicates”, “F-concrete”, “hydroceramics”, “zeocemen”, etc [17]. The recent consensus in the research community proposed that “AAM” should serve as the broad umbrella term for all binders produced by reacting aluminosilicate precursors with alkaline solutions, while “geopolymer” should refer specifically to the low-calcium subgroup activated by hydroxide or silicate solutions [17,18]. Comparison of AAMs and other PC based binders in respect to Ca, Al and alkali content is shown in Figure 1.

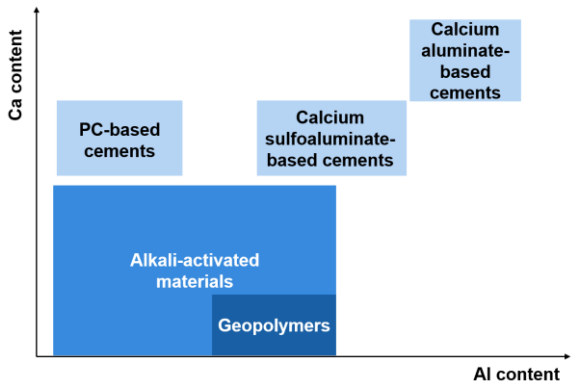

Figure 1. Classification of AAMs compared to different cements based on Ca, Al content and alkali content (darker shading indicates higher alkali content). Adapted from [17]

The first documented investigation of slag activation dates to Kuhl (1930), who studied the setting behaviour of slag mixed with potassium hydroxide solution. Shortly after, Chassevent (1937) quantified the reactivity of slag when activated with both potassium hydroxide and sodium hydroxide solutions [14,17]. The first systematic study of cement-free binders based on alkali-activation of blast furnace slag was carried out by Purdon (1940), who demonstrated that caustic alkalis - including sodium hydroxide and alkalis generated in situ from a base and an alkaline salt - could effectively activate slag to produce cementitious materials [14]. Building on this work, Purdon later developed the commercial product "Purdociment", which was applied during the 1950s in the construction of several residential, public, and industrial buildings in Belgium [19].

In 1957, Glukhovsky introduced the concept of "soil binders" - based on the alkali-activation of low-calcium or calcium-free aluminosilicate materials - laying the foundation for what would later be termed geopolymer chemistry [17]. From the 1960s onward, significant industrial-scale production of alkali-activated slag was established in the former Soviet Union and subsequently in China [14,17]. A further milestone in the field was the development by Davidovits of binders produced from a burnt mixture of kaolinite, limestone, and dolomite activated by alkalis. Davidovits termed these materials "geopolymers" on account of their polymeric molecular structure, and filed several trademarks for related products, including Pyrament, Geopolycem, and Geopolymite [14,17]. A broader chronological overview of significant research contributions to alkali-activated concrete in the 2000s is presented in Amer et al. [4].

Even though there is a significant number of AAM structures, the studies examining their long-term behaviour remain relatively scarce. However, existing field investigations of structures built decades earlier generally revealed good protection of embedded steel reinforcement from corrosion and high strength retention [17]. Some of the examples of the AAMs application in the past decades are presented in the Figure 2 - Figure 5. The viability of the AAMs contemporary application can be seen through some of the recent projects: 763 m^3 alkali-activated concrete as part of the London power tunnels project [20], heavy-duty pavements at Toowoomba Wellcamp Airport in 2014 and the foundations for the Chatham railway station in 2021, cycle bridge in Wageningen (2020) and a 17-meter deep concrete barrette at the Grand Port Maritime du Havre in France [21].

Figure 2. High-rise building made from alkali carbonate-activated slag, Lipetsk, Russia [17]

Figure 3. Residential building - precast blocks made from alkali hydroxide-activated slag, Mariupol, Ukraine [17]

Figure 4. Na_2SO_3-activated Portland-BFS-steel slag cement concrete beams in a workshop, Ukraine [17]

Figure 5. The “Parking 58”, Brussels, Belgium – parts of the first six floors are built from Purdociment [17]

Beyond building construction, AAMs have been applied across a range of specialised fields. These include refractory concrete for high-temperature applications, concrete designed for

chemically aggressive environments, oil well cementing, the stabilisation and solidification of hazardous and radioactive waste materials, and rapid structural repair works [14].

Because of differences in reaction mechanisms and products, standards and regulations for PC concrete cannot be directly adopted for AAMs, which is one of the reasons for the hindered large-scale, unified application. For further commercialisation, it is necessary to develop a set of performance-based standards and regulations for the quality of diverse component materials and supply chains, production technology, and the validation of different AAMs' properties [7,22]. This can be achieved with comprehensive experience in these matters, which is why there is a great need for further research in this field. To date, the most significant achievements in AAM standardisation have been made in Australia, particularly in structural design. Australia adopted a technical specification developed specifically for AAMs, which is applied in conjunction with existing standards for concrete structures and supplementary cementitious materials (SCMs) [23]. Within the American standardisation framework, ASTM International has published two dedicated standards for "alkali-activated cementitious materials". ASTM C1928/C1928M-23 prescribes a standard test method for the compressive strength of AAM mortars [24]. A full material performance specification covering AAMs for both general and special applications, with no restrictions imposed on binder composition or constituent materials, is given in the standard ASTM C1948/C1948M-24 [25]. Furthermore, the performance-based British code of practice BSI Flex 350 v2.0 describes a method by which concrete produced with a lower-carbon, non-standardized binder can be assessed for use in structures [26].

Even though it is significantly lower than that of PC concrete, almost the entire ecological footprint of AAMs is assigned to the inevitable presence of synthetic chemical activators [17]. Their production process is energy-intensive and poses other environmental challenges, such as ozone layer depletion and ecotoxicity [11]. Although alkali hydroxide typically constitutes only 1-5% and alkali silicate 3-10% by mass of AA concrete [22], activators are collectively responsible for between 13% and 33% of the total global warming potential of AAMs, depending on the mix design [11]. Their high cost and safety issues due to handling the highly caustic activator solution additionally limit the widespread application of AAMs in the construction sector [27,28]. While standardisation is primarily a policy issue, the other challenges have been addressed in the scientific literature by designing AAM mixes with reduced activator content, while maintaining satisfactory performance, and by replacing conventional chemical activators with alternative alkali and silicon sources [29]. Industrial by-products investigated as replacements for silicate activators include silica fume (SF) and glass waste (GW) [30,31], while red mud is proposed as an alkali source [30]. Biomass ashes are also considered promising alternative activators, as they are rich in potassium, calcium, and

amorphous silica, depending on the plant species from which they originate [32]. These waste materials are generated during the combustion of biomass, including woody, herbaceous, and agricultural biomass [32].

In addition to replacing chemical activators in AAMs, using biomass ashes can also mitigate other environmental problems, such as ash landfilling. Worldwide, biomass-fired power plants produce 480 million tonnes of ash per year [33], and it is estimated that biomass as an alternative energy source could replace 33-50% of the global energy deposit by 2050 [34]. Depending on their chemical composition, the biomass ashes can have different applications across industries, such as SCMs (construction) or soil quality improvement as fertilisers, reclamation and remediation agents (agriculture and mining) [34]. However, a significant amount of biomass ashes is still landfilled, causing environmental problems [35]. Potential upscaling as an alternative activator in AAM technology could be a promising pathway to achieving “zero waste” circular economy goals while enhancing the sustainability of AAMs [29,36,37].

1.2 Motivation for the research

Globally, approximately 140 billion tonnes of biomass residues are generated each year through agricultural activities [38]. Among these residues, sunflower biomass constitutes a significant fraction, as sunflower is a widely cultivated industrial crop used in the food and chemical industries and for biodiesel production. The total world production of sunflower in 2025 was 54.8 million tons [39]. The average annual production and harvested area from 2016 to 2025 worldwide are presented in Figure 6.

Sunflowers are a dominant crop among industrial plants in the Republic of Serbia, accounting for 45.2% of the total agricultural area under their cultivation. In 2022, sunflowers were planted on 251,155 ha of agricultural land, of which 88.5% is planted in the Region of the Autonomous Province of Vojvodina. From 2013 to 2022, the area of agricultural land planted with sunflowers increased annually by 3.3% on average [40]. During the sunflower seed processing, a significant amount of sunflower husk is generated [41]. Their low natural moisture (9%) and good thermal properties (average 18 MJ·kg-1) make them suitable as a biomass energy source [42].

Some sunflower oil producers in the Autonomous Province of Vojvodina, Serbia, have been using sunflower husks as a fuel, to a certain extent. Sunflower husks are also used as an energy source for the city of Sremska Mitrovica's heating supply. Significant quantities of waste, i.e., sunflower husk ash (SHA), are generated due to these processes. According to the reports from two companies, oil producer Victoria Oil in Šid and heat and electrical plant TETO

in Sremska Mitrovica, 960 t/y of SHA is generated in these processes and disposed of in landfills. Other potential sources for collecting the sunflower husk ash in the Vojvodina Region are industrial complexes for processing sunflower are:

- Oil industry „Dijamant“, Zrenjanin,
- Oil and plant fat factory „Vital“, Vrbas,
- Oil industry „Sunce“, Sombor and
- Plant oils and fats production company „Banat“, Nova Crnja.

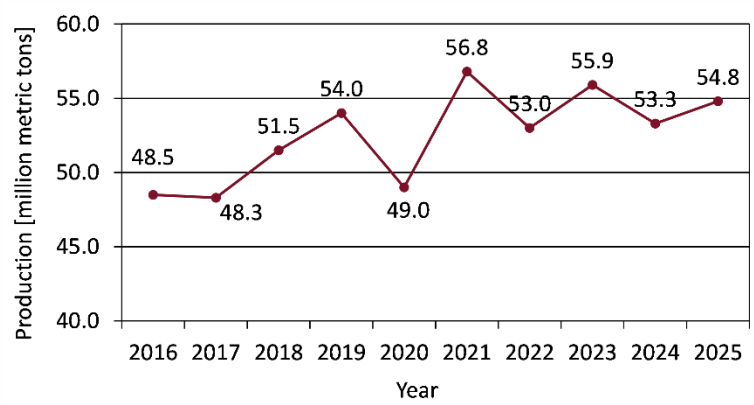

Figure 6. Average annual production of sunflower seed (million tons) from 2016 to 2025 [39]

SHA is rich in potassium and therefore has potential for application in AAMs as an alternative alkali source. Local availability of SHA makes it suitable for use as a component material of AAMs.

Valorising agricultural waste through construction materials production has been established as an effective waste management strategy aligned with circular economy principles [43]. Extensive research in Serbia has confirmed that most agricultural ashes are viable as SCMs [44,45], though SHA has proven inefficient for this purpose due to its low silica and high alkali content [46,47].

However, this same high alkali content makes SHA a promising alternative activator for AAMs. The use of alternative activators has been shown to reduce CO_2 emissions by 60-99% [48]. A study on alkali-activated slag (AAS) grouting slurries activated with sunflower stalk ash instead of industrial KOH reported a 83.5% reduction in CO_2 emissions [49]. Nevertheless, this field of research requires further development. There is a significant gap in the literature regarding reaction degree, setting time, shrinkage and durability properties of AAMs synthesised with alternative activators [50,51], with a notable scarcity on waste-derived hydroxide activators such as SHA on a concrete level.

The proposed research, therefore, investigates locally available SHA as an alternative alkali activator for cement-free AAMs, with the dual aim of reducing the carbon footprint of the binder system and promoting the valorisation of agricultural by-products in line with circular economy principles. It is important to emphasise that not all mix designs of AAMs can provide a lower CO_2 footprint and that the local (non)availability of the component materials can be the decisive factor in the justification of their potential application. The availability of SHA in the region is an advantage for introducing it as an alternative alkali activator in AAM technology. Since AAMs in general can have very different properties, the new synthesised material must be tested for a set of fresh-state and hardened-state mechanical and durability properties.

Reduction or replacement of the chemical activators would simultaneously reduce CO_2 emissions and material costs, advance circular economy principles in the construction sector, and elevate SHA management from disposal - the lowest level of the waste hierarchy - towards prevention. Considering the national cement production of 2.73 million tonnes [52], this approach creates the potential to partially substitute conventional binders with local materials, while simultaneously reducing SHA landfilling.

1.3 Subject, aim and methodology of the research

The subjects of the proposed research are AAMs based on ground granulated blast furnace slag (GGBFS) activated with:

- conventional chemical alkali activators, sodium hydroxide and sodium silicate,
- an alternative activator SHA,
- SHA and sodium silicate.

The aim of the proposed research is to valorise the locally available waste material, SHA, by applying it in the construction sector as an alternative, bio-based activator for GGBFS-based AAMs with a reduced ecological footprint. The valorisation will be conducted through:

- replacing conventional alkali hydroxide activator in AAM mixes with SHA,
- determination of the SHA influence on the activation process and properties of slag-based AAM,
- comparative analysis of the performance of AACs activated with reduced content of conventional activator and AACs activated with alternative activator,
- design of slag-based AAMs with a binder based only on waste materials and/or with a binder based on a combination of waste material and conventional activator.

- The valorisation of SHA as an activator in AAM systems and its influence on fresh- and hardened-state properties will be conducted based on the results of the original experimental research. Using SHA in AAMs can address the environmental issues by:
- reduction of the ecological footprint of AAMs,
- increasing the sustainability of AAMs,
- reduction of production costs of AAMs,
- improvement of waste management by preventing the landfill of SHA,
- development of the cement-free alkali-activated mortar/concrete based only on waste materials.

1.4 Hypothesis

The following hypothesis will be tested:

H1: The sunflower husk ash can be used as an alternative activator for synthesising slag-based alkali-activated materials

H2: Utilisation of only the alternative activator in AAMs will not significantly reduce the mechanical and durability properties of slag-based alkali-activated materials.

H3: It is possible to produce slag-based alkali-activated concrete derived only from waste materials - slag and sunflower husk ash.

1.5 Brief description of the research programme

The research conducted within the framework of the doctoral dissertation was carried out in the following stages:

I Description and defining the subject and problem of the research

II Literature review

III Validation of hypothesis through the following activities:

1. Systematisation and analysis of data collected in the literature review.

2. Experimental research of the fresh-state and hardened-state properties of SHA-activated and conventionally activated GGBFS-based alkali-activated mortars.

3. Analysis of the collected data and experimental results to find an optimal mix design for concretes with reduced activator content and for attaining the slag-based alkali-activated concrete activated with SHA as alkaline source.

IV Results, discussion, and conclusions

V Final remarks, contribution, and future perspectives

The first chapter of the doctoral thesis defines the subject, aim, motivation, and hypothesis of the research.

The second chapter provides a literature review of the critical parameters relevant for designing AAM mixtures, as well as their key properties. It also provides a review of studies on alternative activators for AAMs, with particular emphasis on ABA as a replacement for alkaline hydroxides.

The third chapter outlines the experimental programme.

Chapter four presents the results of each experimental phase, followed by analysis, discussion and conclusions for every stage, which subsequently serve as input parameters for the next phase of the study.

Chapter five provides final remarks, scientific contribution of the doctoral thesis and future research perspectives.

Chapter 2
LITERATURE REVIEW

2. LITERATURE REVIEW

This chapter provides an overview of relevant research on the chemistry, reaction mechanisms, and component materials of AAMs, as well as a summary of the key parameters influencing the mix design of alkali-activated concretes. Furthermore, it provides a review of the mechanical and durability properties of AAMs. This is followed by a review of studies examining alternative activators, with particular emphasis on replacing alkaline hydroxides with agricultural biomass ashes (ABA).

2.1 Chemistry and reaction products of alkali-activated materials

The structural development of AAMs is set off by an activation reaction, where alkalis induce the dissolution of the amorphous aluminosilicates from the precursors, which is then followed by the rearrangement, condensation, and resolidification processes, i.e., formation of reaction products [17,48,53], as presented in Figure 7.

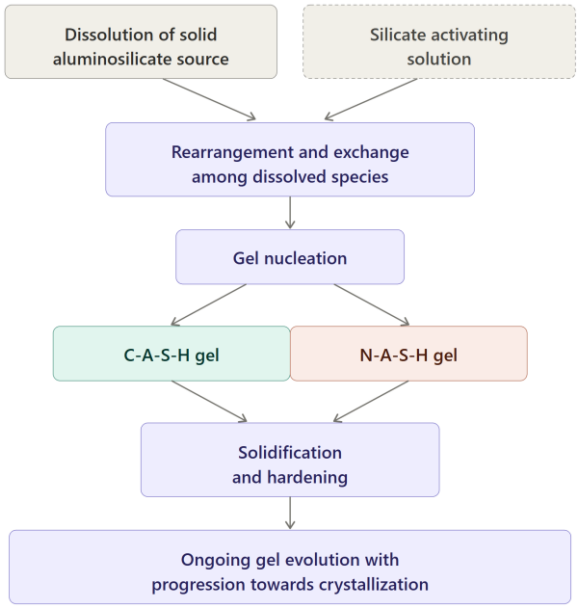

Figure 7. Phases of the activation process. Adapted from [8]

The AAMs, as previously mentioned, can be distinguished into two different categories based on the final phase assemblage: low-calcium (Ca) and high-Ca systems. Low-Ca systems are based on the activation of a precursor, such as fly ash or MK, in which the main reaction product is a three-dimensional alkali-aluminosilicate hydrate (N,K-A-S-H) type gel [17,14]. Aluminium and silicon atoms with tetrahedral coordination to oxygen are bonded to form a highly cross-linked structure, an aluminosilicate ‘framework’, with alkali metal cations [54].

High-Ca systems are based on the activation of a precursor with high Ca content, such as slag. The main reaction product is calcium-aluminosilicate hydrate (C-A-S-H) type gel [17,14].

Furthermore, hybrid systems combining precursors with both high and low-Ca content are also being developed [17,14,8]. The threshold value for this classification based on the Ca content can be adopted as 10 wt% [21].

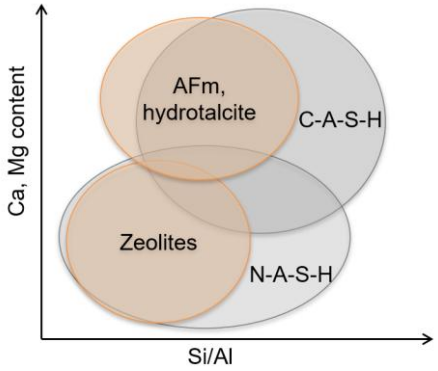

Figure 8. Primary (grey) and secondary (orange) reaction products formed in AAMs, depending on the Ca content of the precursor and Si/Al ratio. Adapted from [54]

In the slag-activated systems, the aluminium-substituted C-A-S-H type gel has a disordered tobermorite-like type structure. This is accompanied by the formation of secondary reaction products such as Alumina-Ferric oxide-monosulfate (AFm) type phases (mainly identified in alkali hydroxides-activated binders), Si-containing AFm phase strätlingite in silicate-activated binders, hydrotalcite (identified in activated slag with relatively high contents of MgO) and zeolites (formed in activated slag binders with high Al_2O_3 and low MgO content) [17,55,56]. A simplified representation of the main and secondary reaction products that form in slag systems is presented in Figure 8.

The structure and composition of the C-A-S-H type product forming upon activation of slag is strongly dependent on the nature of the activator used. The C-A-S-H product formed in alkali hydroxide-activated slag presents a higher Ca/Si ratio and a more ordered structure than the C-A-S-H type gel formed in silicate-activated slag binders [17]. In the systems activated with NaOH, chemically bound Ca^{2+} ions can be replaced with alkalis from the activator, forming C-(N)-A-S-H gel [17].

2.2 Technology and component materials

The technology for producing AAMs differs from the PC concrete technology. AAMs can be produced from different raw materials as precursors and different alkali activators by grinding, blending, or directly mixing in concrete. They can be applied as ready-mix concrete or precast concrete; hence, it is hard to prescribe these materials in the same compositional and

procedural way as for PC concrete. RILEM Technical Committee for Alkali-Activated materials is conducting comprehensive research in developing recommendations for future performance-based standards, which are the key to unlocking the wider industry application of AAMs [17].

There are two procedures for producing AAMs, depending on how the component materials are mixed:

- one-part alkali-activation and
- two-part alkali-activation.

The difference is whether the alkali activator is added in solid form or as a solution. The precursor and solid activator can be dry mixed, followed by the addition of water and aggregate. Alternatively, the alkali activator can be prepared as a concentrated water solution, added to dry mixed precursor and aggregates, along with additional water, to obtain satisfactory workability. The first approach, in which a solid activator is premixed with the precursor, is called one-part alkali activation. The second approach, where the activator solution is added to mix is two-part alkali-activation. Although most of the research is focused on the two-part alkali activation due to the better mechanical properties of the obtained concrete, one-part alkali activation is gaining increased attention [17]. Schematic representations of two alkali-activation processes are shown in Figure 9. A two-part activation process could be associated with practical, health and safety issues because, for example, the dissolution of alkali hydroxides is an exothermic reaction and concentrated alkali solutions obtained in two-part activation are highly caustic [27]. Furthermore, the activator solutions must be prepared at least 24 hours before mixing, due to their high temperature resulting from the exothermic reaction.

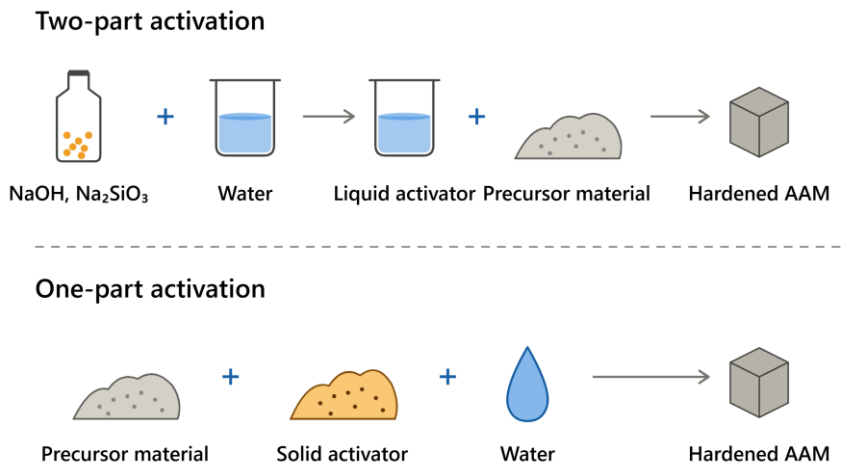

Figure 9. One-part and two-part alkali-activation. Adapted from [57]

2.2.1 Precursors

Raw materials that can be used as precursors for AAMs production include slag, fly ash, metakaolin and fly ash. Silica fume, rice husk ash, red mud, ferrochrome ash, mine tailings, natural pozzolans, have also been researched as a partial substitution for standard precursors. The selection of precursors is generally influenced by their chemical composition, water demand, availability, cost, and the specific type of AAM application [31]. BFS is one of the most widely used precursors in AAMs [58,59,49] mostly due to its high CaO and SiO_2 content. Slag is a non-metallic by-product generated during the production of pig iron in a blast furnace, where temperatures typically reach approximately 1500 ˚C to 1600 ˚C [60]. Slag forms when iron ore, coke (as a fuel and reducing agent), and limestone or dolomite (as fluxing agents) react in the furnace. The primary function of the flux is to lower the viscosity of the impurities - largely silicates and aluminates from the ore and coke ash - to separate them from the molten iron. Due to its lower density, the molten slag floats on the surface of the liquid iron and is periodically tapped off for processing [60,61].

The reactivity of the slag depends on the cooling rate applied during its solidification. When molten slag is cooled slowly in the atmosphere, it forms air-cooled blast furnace slag, composed of stable mineral phases with low reactivity. To produce SCM or reactive precursor for alkali activation, the molten slag must undergo rapid quenching to prevent the formation of a crystalline lattice. This process is known as granulation, which involves the sudden cooling of molten slag from over 1400 ˚C to below its glass transition temperature using water, air, or mechanical means [60].

GGBFS consists primarily of silicates, aluminosilicates, and calcium-alumina-silicates. The dominant oxides in chemical composition are calcium oxide (CaO), silicon oxide (SiO_2), aluminium oxide (Al_2O_3), and magnesium oxide (MgO). They are present in the form of a vitrified glass phase, which often exceeds 95% of the slag's total volume in high-quality precursors [14].

Fly ash is the fine-grained residue captured from the flue gases of coal-fired power plants. It is primarily composed of spherical, glassy particles containing silica, alumina, iron, and calcium.

The reactivity of fly ash in AAMs is generally lower than that of slag, leading to slower setting times and lower early-age strength. The spherical morphology of fly ash particles improves the workability and flow of fresh concrete [62].

MK is produced by the calcination of kaolinite clay, a process known as dehydroxylation, at temperatures typically between 550 °C and 800 °C. This thermal treatment expels hydroxyl ions, transforming the crystalline clay into an amorphous aluminosilicate [62].

While fly ash and MK-based systems usually require curing at elevated temperatures to enhance their dissolution, alkali-activated systems with slag do not require this type of curing.

GGBFS and fly ash already have a use-value through application in blended cements, but the usual clinker substitution is up to 50% for slag and 25% for fly ash, while higher substitutions are used for specific types of concretes, with specific mix design and performance [63], a more appropriate application of GGBFS, for example, could be in AAMs [9].

2.2.2 Chemical activators

The most widely used activators in AAMs technology are sodium-based, due to their availability and lower price, compared to potassium activators [14,64]. It is reported that the most reliable sodium activators for GGBFS are sodium hydroxide (NaOH) and sodium silicate ($Na_2O \cdot nSiO_2$) [14,64]. NaOH is available commercially in the form of pellets and flakes (Figure 10 and Figure 11). In the AAM technology, it is usually used as 50% water solution.

Figure 10. Sodium hydroxide pellets

Figure 11. Sodium hydroxide flakes

Sodium silicate, or sodium water glass, is used in AAM technology as a commercially available solution. It is derived from silica and carbonate salts. In the commercial solutions, the mass ratios of SiO_2 to Na_2O range from 1.6 to 3.85. Given the variety of this ratio, the properties of sodium silicates can also be different [14,64]. Although the alkalis induce the slag activation degree, silica content is also essential for producing the AAMs with good engineering properties, which is why the combination of alkalis and silicates is the most common activator. An increase in silica content leads to the formation of a dense binder matrix and higher polymerisation of gels, thus enhancing the mechanical properties of the binder [64]. This is explained in literature by the slower slag hydration due to the addition of silica, which in turn results in a more uniform distribution of hydration products [56,65,66]. The fast initial reaction of the NaOH-activated slag results in a denser gel with less chemically bound water, leading

to increased coarse porosity at later ages. Volume of hydration products and bound water content were found to be higher in sodium silicate-activated GGBFS samples [56].

In comparison to the sodium silicate activated system, the NaOH activated system exhibits faster decrease of coarse porosity and reaction kinetics during the first days of hydration, a more crystalline type of calcium-silicate hydrate C-S-H, higher coarse porosity for similar hydration degree, lower volume of hydration products and amount of bound water and lower compressive strength for similar hydration degree [56].

The use of potassium activators is limited mostly to laboratory-scale experiments [14,67], although Davidovits explains in his patent [68] that potassium silicate is highly satisfactory in obtaining alkali-activated binder: it does not develop efflorescence and displays higher solubility and compatibility with other additives than sodium silicate. According to his work, mixtures of potassium and sodium silicates can also be used. As suggested in [14,69], the properties of sodium and potassium-activated systems can be very similar, but the potassium-activated systems are generally referred to as more thermally stable than sodium-activated systems [70]. The combination of potassium hydroxide and sodium silicate instead of sodium hydroxide and sodium silicate was found beneficial for 28 days of compressive strength [71], but there is a scarcity in research on the mixed alkali use. Furthermore, sodium hydroxide and silicates activating blended slag/fly ash systems induced the development of early strengths, while the 28-day strength of samples activated with potassium activators was higher [72]. However, due to high material demand, high cost of potassium activators is a limiting factor for application in the activation of AAMs produced for the construction sector [70].

Alkali activators are the primary contributors to the environmental footprint of AAMs. A comparison across various studies reveals that sodium silicate generally has a higher carbon dioxide emission factor than NaOH, though reported values vary based on the data source: one review reporting on global databases cites a range of 1.222 $kgCO_2/kg$ to 1.514 $kgCO_2/kg$ compared to NaOH, ranging from 0.504 $kgCO_2/kg$ to 1.893 $kgCO_2/kg$ [11,73]. Conversely, NaOH can be more energy-intensive to produce, with reported embodied energy ranging from 3.5 MJ/kg [73] to 9.5 MJ/kg [74], compared to 5.371 MJ/kg for sodium silicate [73,74]. Furthermore, the dissolution of NaOH and other alkali hydroxides in water is a highly exothermic reaction; the solution is caustic, and therefore, the safety of the person handling the dissolution process could be compromised [4].

2.3 Mix design parameters

The most important parameters characterizing AAM mixes are water-to binder-ratio (w/b), the total alkali content in the activator/s and the amount of SiO_2 in the activator, expressed as modulus, or silica modulus (Ms), i.e., the SiO_2 and M_2O content ratio ($Ms = n(Si_2O)/n(MO_2)$),

where M is alkaline metal depending on the type of activator, as well as precursor content [75,76,77]. Other important parameters are the type of activator, the chemical and physical properties of slag and the amount of paste in concrete [75,76].

The w/b ratio, or water-to-solids ratio (w/s), as often referred to in the literature, is the ratio of total water to total solids (precursor and solid activator components) in AAMs. In two-part alkali activation, the total water is the sum of water in alkali hydroxide solution, alkali silicate, and additional water needed to achieve the desired w/b ratio. Total binder is calculated as the sum of slag content, solids in alkaline hydroxide solution and solids in alkaline silicate solution [75,77,78]. It influences workability and compressive strength of AAMs by the same mechanisms as in PC concrete [14,79]. Nevertheless, it is difficult to establish a single parameter directly affecting the compressive strength, as multiple factors interact to influence its value and development in time, and it depends on alkali content and Ms as well [75,21]. To attain the desired Ms of the AAM mixture, the combination of alkaline hydroxides and silicates is often used [17,14,72]. The modulus of alkali silicates is restricted to the interval 1.6 to 3.85 due to their instability out of this range [14]. However, to attain the desired properties of basic alkali-activated slag (AAS), the Ms should usually be in the range 0.6-1.5 [75]. Therefore, the alkalis are added to the mix in the hydroxide form. An example of mix design of sodium hydroxide and sodium silicate activated slag-based concrete is presented in the Table 1.

Table 1. An example of a mix design for slag-based alkali-activated concrete

w/b	Slag [kg/m^3]	NaOH* [kg/m^3]	Na-silicate* [kg/m^3]	Na_2O [wt% slag]	Ms	Water [kg/m^3]	m_a [kg/m^3]
0.42	375.0	11.6	17.0	4.1	0.72	139.3	1762.0

*solid

Due to the potential alkali leaching, it is generally not recommended for AAMs to be cured in water as PC concrete, although this depends on the precursor used (e.g., fly ash-based AAMs are more prone to alkali leaching than slag-based AAMs). To prevent the excessive moisture loss, they are usually cured sealed in polymeric films instead [78]. Furthermore, AAMs based on slag gain high strength cured at ambient temperature whilst requiring relatively low activator dosage, unlike fly ash-based AAMs, which usually require high alkali dosage (6-10% Na_2O or K_2O) and elevated curing temperatures (40-100 °C) to achieve suitable mechanical properties [80].

2.4 Properties of alkali-activated materials

2.4.1 Workability and setting time

One of the challenges of the AAM's technology, based on slag precursors, is reduced workability and fast setting time. It is a complicated issue that depends on different factors. Unlike in the PC concrete systems, workability is not only dependent on the w/b ratio. The Na_2O content and Ms significantly affect the workability of the AAM mix [14,75,81]. Increased liquid consistency (i.e. higher slump) can be achieved by increasing the alkali content, but its effectiveness depends on w/b ratio and Ms as well [75,76,80]. The literature reports that for w/b<0.5, the %Na_2O content to attain S3 slump class as defined in EN 12350-2 [82] is 7.5%. For w/b>0.5, the same slump class can be attained with 4% of Na_2O [75]. An example of the influence of Ms and alkali content on the slump of slag-based AAM with w/b=0.43 is presented in Figure 12. Higher Ms will also result in a higher slump of AAC mix [75,77]. This is more dominant for a higher w/b ratio, i.e. 0.55, while for a lower w/b ratio, Na_2O content has more impact, according to [75]. In [75] it is also stated that for attaining S3 slump class, for w/b=0.47, Ms has to be at least 1.0. For higher w/b=0.55, S3 slump class can be attained for Ms=0.45. Some research reported that an excessive increase in Ms (1.5 or higher) can result in a decrease in slump due to increased viscosity of the entire AAC mix [81,83].

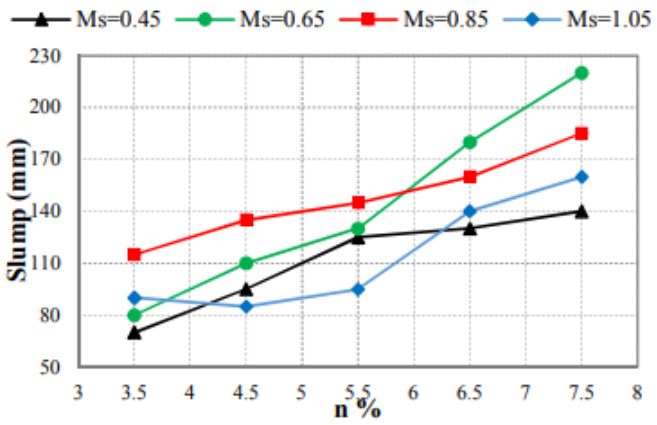

Figure 12. Slump values of slag-based AAM, depending on the Ms and alkali content (n%) [77]

Slag-based AAMs are prone to fast setting [17,80]. The influence of Ms and alkali content on the initial and final setting times of AAC are presented in Figure 13 and Figure 14.

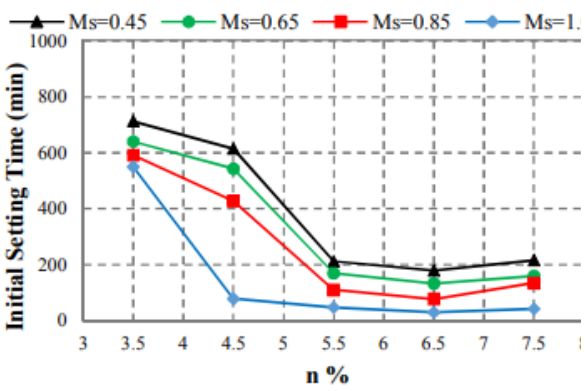

Figure 13. Initial setting time of slag-based AAM, depending on the Ms and alkali content (n%) [77]

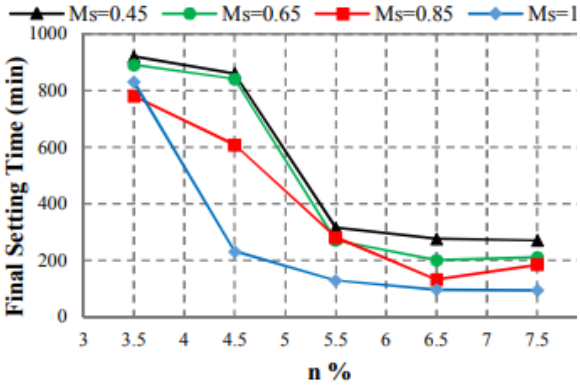

Figure 14. Final setting time of slag-based AAM, depending on the Ms and alkali content (n%) [77]

Since the setting is controlled by reaction kinetics, the setting time can be adjusted. However, high activator concentrations are often necessary to achieve the desired strength, which can lead to a short setting time, sometimes only 10 minutes long [81]. An increase in alkali content reduces setting time by enhancing the rate and total amount of heat released, thereby increasing the degree of hydration [77]. Increased silica in sodium silicate-activated slag cement mixtures can increase setting time and induce the development of high strengths.

Water-reducing admixtures, which are usually applied to PC concrete, have proven ineffective. The high pH in AAMs can cause structural degradation of superplasticisers and surface charge repulsion. It can also compromise their solubility and induce agglomeration due to high ionic strength from high alkali concentration. Due to these reasons, is not recommended to use them in AAM mixes, while admixtures specifically designed for AAMs are still under development. The general recommendation is that they should be tailored to a specific precursor and even activators [84]. Some researchers reported improvements in the rheology of slag-based AAMs when air-entraining admixtures were added to the mix [81].

2.4.2 Compressive strength

Alkali content (n) is calculated as the sum of Na_2O in sodium hydroxide and sodium silicate solution. The alkali content increases compressive strength, due to the higher degree of slag activation and the formation of more C-A-S-H gel. However, excessive alkali content can lead to efflorescence and brittleness. This content limit depends on slag type, activator and curing conditions [76]. Although there are studies reporting both lower and higher n applied in the AAMs, taking into account the above-stated, economic factors and the fact that for stable activation, the recommended Na_2O content is 2-8%, the optimal interval of alkali content is 3-

5% [75] or 3-5.5% [76]. This will also affect the optimal w/b ratio required to attain the desired compressive strength. Li et al. [80] developed a model to determine the w/b ratio and alkali content for targeted compressive strengths (Figure 15). According to this research, compressive strength up to 40 MPa can be reached for 4% of Na_2O and w/b ratio in the range of 0.35-0.50. Higher compressive strengths demand higher alkali content (5%) and w/b ratio between 0.35 and 0.45. Raising alkali content up to 6% and 7% can result in compressive strengths of 60-80 MPa or higher, depending on the w/b ratio (0.35-0.50).

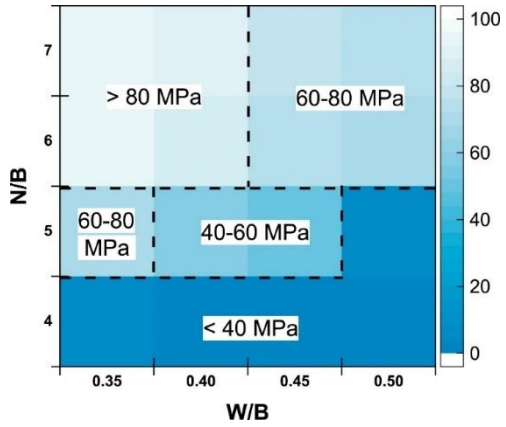

Figure 15. Optimal w/b ratio and alkali content (N/B) for targeted compressive strength [80]

The modulus of the mix is calculated as the SiO_2/Na_2O ratio, where SiO_2 is the total silica content in the activator and Na_2O is the total alkali content, as stated previously. An increase in Ms increases compressive strength due to the formation of more silica gel [76]. The Ms range that provides applicable AA concrete is 0.6-1.5, depending on the type of slag [75,77]. For basic slags, the Ms will provide the highest compressive strengths in the 1.0-1.5 range, while for neutral and acidic slags, the ranges are 0.9-1.3 and 0.75-1.25, respectively [75]. Higher Ms will result in lower early age compressive strengths, with later high propagation, and longer curing period needed [75].

Increasing Ms above 1.5 for Na_2O% below 5% could result in a decrease in compressive strength, due to the system's low alkalinity, which limits the degree of reactivity [75]. When Na_2O content is constant, the effect of alkali activation is constant - an increase in Ms (Si_2O) will increase compressive strength. If the solids in sodium silicates are constant, higher Ms will decrease Na_2O content, and the degree of alkali activation might be too low. When alkali activation is insufficient for slag hydration, it is better to use lower Ms; otherwise, higher Ms will result in higher compressive strength [76]. It should be noted that increasing Ms and n beyond a certain value will have no effect on increasing compressive strength [77]. These values depend on the slag type, the activator, and the curing conditions [76]. In the experimental study by Ben HaHa et al [56], NaOH-activated GGBFS-based pastes showed high 1-day

compressive strength. The sodium silicate-activated pastes had no measurable compressive strength after 1 day, but the compressive strength after 7 days is higher than for the NaOH-activated slags. The sodium silicate-activated samples gained 70-80% of compressive strength between 7 and 28 days. Their 180-day compressive strength increased more than double, compared to 7-day strength. The NaOH-activated samples do not exhibit a significant increase in compressive strength during ageing.

2.4.3 Shrinkage

High levels of shrinkage in slag-based AAMs can result from internal moisture loss due to hydration (autogenous shrinkage) or as a result of evaporation (drying shrinkage). It depends on the component materials' properties, i.e., slag and activators, their dosage, water-to-slag ratio, and degree of hydration [81]. Furthermore, curing temperature and conditions, and relative humidity, affect drying shrinkage as well [14].

Slag-based AAMs are generally more susceptible to shrinkage than the PC concretes - it has been found that it can be 1.5 to 2.5 times higher [77]. Shrinkage in slag-based AAMs manifests differently than in hydrated Portland cement (Figure 16), due to the differences in hydration products [81]. The generally higher shrinkage, compared to PC, is explained by pore size refinement, causing higher capillary pressures and lower elastic modulus in AAMs than in PC systems [85]. The high viscoelastic deformation results in high drying shrinkage [86]. Furthermore, AAMs are more prone to moisture loss than PC concrete [87].

However, there are also reports on AAM mixes with lower drying shrinkage than PC, depending on the w/b ratio and aggregate grading. Furthermore, inadequate curing conditions will almost certainly result in high drying shrinkage. Prolonged sealed curing of AAMs has been found beneficial in terms of reducing the shrinkage [78].

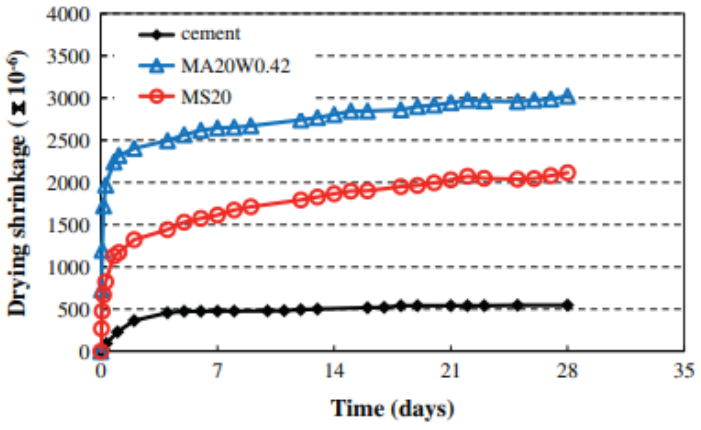

Figure 16. Drying shrinkage of AAMs compared to PC concrete [88]

The type and dosage of the activator have a significant influence: several studies show that increasing the activator content and silica modulus results in higher shrinkage [17]. It is also reported that alkali silicates tend to induce higher drying shrinkage than alkali hydroxide activators. Increased content of both types of activators will promote shrinkage, but the alkali concentration will have the most effect on shrinkage in early stages, while silicates will have more impact on the final amount of shrinkage [14]. Several parameters affect shrinkage, workability, and compressive strength, but they do not affect these properties equally. Additionally, these parameters also depend on slag content, curing, etc. A study by Taghvayi et al. [77] shows that alkali concentrations up to 5.5% and a sodium silicate modulus less than 0.85 were optimal to prevent rapid setting, loss of compressive strength, and high drying shrinkage in slag-based AAC [77].

2.4.4 Elastic modulus

The elastic modulus of AA concrete reported in existing studies varies between 10-40 GPa [89,90]. However, due to the numerous possibilities for synthesising AAMs, the results vary depending on the component materials.

The elastic modulus of AAS concrete activated with sodium silicate at 28 days is most commonly reported between 20 and 30 GPa. Robayo-Salazar et al. [91] measured 30.51 GPa for 100% slag concrete with sodium silicate activation. Adesanya et al. [92] reported 25 GPa for a 50/50 copper slag/GGBS one-part AAS with sodium metasilicate at 75 MPa compressive strength. This range is 10-30% lower than PC concrete at comparable compressive strength, a finding that is well established. Prinsse et al. [4] documented that AAC elastic moduli are up to 30% lower than conventional concrete. The lower modulus reflects the fundamentally different gel structure: C-A-S-H in AAS has a lower Ca/Si ratio, higher Al incorporation, and different nano structural organisation than C-S-H in PC [93].

Existing models that accurately predict the relationship between compressive strength and elastic modulus in PC are often not applicable to AAC. In addition to the type and content of coarse aggregate, microstructure, composition, and degree of hydration also play a significant role in the elastic modulus of AAC. Like the compressive strength development, an increase in alkali and silica content promotes an increase in elastic modulus [90].

2.4.5 Porosity and water permeability

Porosity and transport characteristics are essential for the durability of concrete, since they affect the ingress of water and chlorides as well as the carbonation process [17].

Although porosity can vary depending on the used precursors and activators, AAMs in general have a lower content of capillary pores (0.01-10 μm) than PC concrete. Since the capillary pores have a main role in water transport, it can be expected that the AAMs will have lower water permeability [17]. The increase in w/b ratio governs the capillarity in the same way as in PC systems, but it also dilutes the activators [14]. The use of a higher Ms or a lower water content in alkali-activated BFS systems reduces the rate of water uptake, and sorptivity decreases with increasing curing time under moist conditions [17].

Despite the finer pore structure, experimentally measured sorptivity of alkali-activated slag (AAS) concrete is often higher than that of PC concrete at comparable strength levels [94,95]. This apparent contradiction has been attributed to drying-induced surface microcracking, to which AAS systems are particularly susceptible [95,96]. Ismail et al. [97] observed that high water absorption of AAMs (especially slag-based systems) did not result in high chloride permeability, as can be expected, suggesting that the high water uptake is primarily a surface phenomenon related to microcracking rather than an indication of a highly permeable bulk matrix. Standard sorptivity test methods developed for PC concrete may therefore overestimate the permeability of AA slag systems [96].

2.4.6 Carbonation resistance

During service life, concrete structures are inevitably exposed to the carbonation process along with other environmental factors. The CO_2 in the atmosphere reacts with the hydration products and leads to the decalcification of the calcium-rich hydration products, the decrease of the alkalinity of the pore solution, and the acceleration of the corrosion of the steel reinforcement [17].

AAMs have been reported to be more susceptible to carbonation than PC concrete [98], due to fundamental differences in the chemistry of hydration products.

The pore solution in PC concrete has a high pH (12.5-13.5), mostly due to portlandite, or calcium hydroxide ($Ca(OH)_2$). When atmospheric CO_2 diffuses through the pore network and dissolves in the pore solution, it forms carbonic acid (H_2CO_3), which dissociates to produce bicarbonate (HCO_3^-) and carbonate (CO_3^{2-}) ions. The carbonation of PC concrete develops mainly through carbonation of portlandite, forming calcite ($CaCO_3$). Only after portlandite is substantially carbonated does the decalcification of C-S-H begin. The formation of $CaCO_3$ can partially fill pores in the carbonated zone, and the porosity of the carbonated region decreases. [99].

The chemistry of AAM changes the carbonation mechanism. Portlandite is not formed in AAMs, and therefore, CO_2 first lowers the pH of the pore solution and then reacts with C-S-H and C-A-S-H, causing their direct decalcification [100]. In high Ca systems, C-A-S-H structure becomes more cross-linked due to decalcification [101]. Calcium is removed from the silicate chains and the residual gel becomes a highly polymerised, disordered aluminosilicate that provides much less binding capacity. This gel decomposition can cause significant strength loss and increased porosity [102]. Hydrotalcite-like phases (Mg-Al layered double hydroxides), which form as secondary products in AAS when the slag has a high MgO content, play an important mitigating role [65,103]. Previous studies have shown that higher magnesium content in slag reduces the susceptibility of AAS to carbonation and improves resistance to C-(A)-S-H decalcification by absorbing CO_2 and partially compensating for the absence of portlandite. The calcium carbonate polymorph formed during carbonation of AAS is mainly the vaterite [101], while high CO_2 concentration induces the formation of aragonite [104]. Under natural carbonation conditions, however, calcite may become the stable end product over longer time frames [105].

The susceptibility of AAMs to carbonation is especially pronounced under accelerated carbonation conditions with high CO_2 concentration at controlled relative humidity [65,106]. However, their high pore solution pH after natural carbonation may be promising with respect to reinforcement corrosion [12]. Accelerated test protocols designed for PC, without questioning whether the tests replicate the chemistry and mechanisms observed in AAMs in service [107].

The AAMs' resistance to carbonation depends mainly on the properties of hydration products, pore structure, and pore solution chemistry, which are determined by the chemistry of the precursor and the dosage and type of activator [65,98,108]. Conflicting results have been reported regarding which type of activator best promotes carbonation resistance [66]. Despite the increasing scientific and commercial interest in AAMs for decades, there are still open questions regarding the mix design of AAMs to achieve satisfactory carbonation resistance.

It is reported that higher alkali content (%Na_2O) and higher Ms of the mix (i.e., SiO_2/Na_2O) improve the carbonation resistance [65,109,110]. A higher alkali content may result in a higher activation degree of the slag, while a higher Ms results in a denser matrix and lower permeability due to slower slag hydration, which in turn results in a more uniform distribution of hydration products [65,56,66]. It is believed that the volumetric expansion of hydrotalcite during hydration decreases matrix porosity of AAMs and CO_2 diffusion [111]. It has been reported that slag activation with higher alkali dosage results in the formation of more hydrotalcite-like phases, which can absorb more CO_2 [65,103,112]. However, when the alkali

dosage is too high (e.g., 10%), not all alkalis contribute to the activation reaction and may increase the carbonation depth due to carbonation-induced cracking [112].

2.4.7 Resistance to chloride penetration

The penetration of chloride ions is detrimental to the passive oxide film that protects embedded steel in concrete from corrosion, by keeping high pH (>12.5). When free chloride ions accumulate at the steel-concrete interface and reach a critical threshold concentration, they locally break down the passive film, initiating pitting corrosion [113]. Once corrosion is initiated, the iron dissolution products occupy a volume 2-4 times greater than the original steel, generating expansive internal stresses. This leads to cracking and spalling of the concrete cover, which further accelerates the degradation process by creating additional pathways for aggressive agents [114]. This deterioration mechanism is critical for coastal structures and regions where de-icing salts are used.

The main chloride transport mechanisms are diffusion, capillary absorption and, for submerged structures, permeation [115,116]. The diffusion occurs due to a chloride concentration gradient between the external environment and the internal pore solution. Capillary absorption becomes the predominant transport process when unsaturated concrete is exposed to a chloride-bearing solution. In this case, capillary pore suction draws the chloride-rich water into the pore network. In practice, chloride transport rarely occurs through a single mechanism in isolation. In most exposure conditions, diffusion and capillary suction act simultaneously, producing a coupled transport mode.

AAMs have significantly higher resistance to chloride penetration compared to PC concrete, due to the finer pore structure, higher tortuosity and chloride binding capacity [14,117]. The C-(N-)A-S-H gel produced in AA slag systems, combined with secondary phases such as hydrotalcite, creates a more refined pore network with a greater proportion of gel pores and fewer interconnected capillary pores [97]. The critical pore entry radius and threshold pore radius are identified by Runci et al. [117] as important and reliable microstructural indicators of chloride diffusion.

In PC systems, chloride binding relies primarily on Friedel's salt formation, which does not form in AAMs. Instead, chlorides in AAM systems are bound by physical adsorption on the gel surface and chemically by hydrotalcite [117], through the interlayer anion exchange [118]. The pore solution chemistry is also an important parameter. It reduces penetration of chlorides by creating denser hydration products, but it can also increase penetration by limiting the material's chemical ability to bind chloride ions [117].

The most important parameters for chloride ingress are the type of precursor (calcium content), the alkali content, silica modulus, and the curing conditions [119]. High-calcium systems, such as BFS, form dense C-A-S-H gels that provide a superior physical barrier compared to the more porous N-A-S-H gels found in low-calcium systems [97]. The MgO content of the slag is particularly important because it controls the formation of hydrotalcite. Studies have shown that slags with MgO content above approximately 5% produce significant quantities of hydrotalcite, while lower MgO content combined with higher Al_2O_3 content (above approximately 16%) tends to favour the formation of zeolites instead [120,101].

Increasing the alkali content in the mix accelerates the activation reaction and formation of more hydration products, including hydrotalcite. Higher values lead to reduced total porosity and smaller average pore sizes, which improve the physical barrier against chloride ingress [117,119] and increased chloride binding capacity [75]. However, increasing alkali content could have an adverse effect, since OH^- can reduce the chloride binding capacity [117].

2.5 Potential of biomass ash in alkali-activated materials technology

Biomass ash is defined as the solid byproduct remaining after the thermochemical transformation of biological materials through processes such as combustion, gasification, or pyrolysis [32,36,34]. These residues are complex inorganic-organic mixtures characterised by high chemical heterogeneity. The phase-mineral composition typically includes a dominant inorganic fraction composed of amorphous and crystalline minerals, a subordinate organic fraction containing char and organic minerals, and fluid matter comprising gas-liquid inclusions and moisture. Over 229 distinct mineral species have been identified in biomass ashes, including silicates, oxides, hydroxides, sulphates, and carbonates [32].

Chemically, biomass ash is dominated by SiO_2, CaO, K_2O and phosphorus pentoxide (P_2O_5). While rich in essential plant nutrients like magnesium and sulphur, these ashes also frequently concentrate hazardous trace elements, including lead, cadmium, chromium, and mercury. Physically, these materials are distinguished between bottom ash, which remains in the furnace, and fly ash, the lighter fraction captured from flue gases [32,34].

Agricultural biomass ashes (ABA) are specifically derived from the combustion of agricultural byproducts [48,121,50,122]. A defining characteristic of agricultural ashes is their high content of water-soluble components, which averages approximately 14.3%, significantly exceeding the 5.8% mean yield found in wood-derived ashes. This soluble fraction is highly enriched in mobile nutrients such as chlorine, sulphur, nitrogen, phosphorus, and potassium [123].

Existing studies demonstrate that, besides industrial by-products such as SF and GW, biomass ashes can serve both as partial precursor replacements and as partial or full substitutes for

alkaline activators, due to their high content of silicon, potassium, and calcium, depending on the type of crop [32].

2.6 Biomass ashes as precursors

The possibility of using wheat straw ash (WSA), rice husk ash (RHA), sugarcane bagasse ash (SCBA), sugarcane straw ash (SCSA), and palm oil fuel ash (POFA) as a precursor due to their higher silicon content was tested. Mixes were activated using conventional sodium hydroxide and silicate activators. Replacement of BFS with SCBA by replacing 15% and 25% resulted in a minor increase in 7-day compressive strength compared to samples with 100% BFS and a decrease in 28-day compressive strength. Replacement of BFS with a maximum of 25% of SCSA resulted in higher compressive strengths than reference mixes. BFS and FA replacement with up to 35% of RHA also increased compressive strength, as well as 30% BFS replacement with POFA. Mixes with higher levels of replacement resulted in a strength decrease [124].

Alkali-activated concrete samples with 25% K, 25% FA, and 50% WSA as precursor outperformed the Portland cement-based system in terms of 7-day compressive strength after ambient curing (51.3 MPa vs. 32.4 MPa) [125].

In a study by Yurt and Bekar [126], hazelnut-shell biomass ash was used as a 5, 10 and 15% replacement for BFS in a sodium hydroxide and sodium silicate-activated concrete. Tested properties were curing regime (60 ˚C for the first 18h, followed by curing in air, water at 25 and water 60 ˚C), compressive strength after 3, 7 and 28 days and abrasion. The increase in ash content generally reduced the compressive strength up to 10%, depending on the curing regime. The highest strength after 28 days was observed for the samples cured in water at 60 ˚C. Hazelnut-shell ash did not affect the sorptivity of the reference AAC. However, the abrasion resistance was lower.

FA (pulverised fuel fly ash) and wood ash with high calcium content (61% CaO) and moderate potassium content (12% K2O) were used, in different ratios, to synthesise alkali-activated pastes [127]. The compressive strength after 7 days was 12 MPa and 16 MPa after 28 days. The significantly lower strength compared to other referenced research is due to the lower potassium content, as suggested by the authors. Considering the high CaO content, wood ash would possibly be more effective as a replacement for the precursor.

The application of biomass ashes as precursors has been investigated as a partial or complete replacement of MK (25-100%) for the production of geopolymer bricks [128]. The ashes originated from the combustion of mixed olive pruning, forest residues, and energy crops. The study showed that replacing 50% of the MK increased the compressive strength of the

geopolymer, due to the formation of the mixed (N, C)–A–S–H gel. It was also concluded that the biomass ash contributes to the binder as an activator due to the presence of soluble alkaline salts. In his PhD thesis, Prochon evaluated the properties of alkali-activated coal fly ash, biomass ash, and co-combusted coal and biomass fly ashes cured at ambient temperature [129]. It was concluded that the biomass ash cannot be used as a precursor to produce stable AAM. However, it was shown to be an activator.

2.7 Agricultural biomass ashes as alternative activators

Replacing the conventional activators with alternative alkali and silica sources has been investigated in several past years [48,121,50]. Activation of precursors with complete or partial replacement of conventional activators has proven viable for RHA [130,122], SCSA, or olive stone biomass ash (OBA) [121]. Literature review showed that the other biomass ashes (cotton, maize, almond, olive stone ashes) have been investigated as precursors or activators for AAMs, because of the high calcium or potassium content [131,132,58,121,133]. Their use as SCMs is not possible because they do not exhibit pozzolanic activity [134].

2.7.1 Alternative silica sources

Bernal et al. [130] tested the RHA potential to act as a silica source in the activation of BFS pastes. Rice husks were burnt in the laboratory at 600˚C and ground to the desired particle size distribution. The obtained RHA had 68% of amorphous silica. RHA-activated pastes showed higher 7-day (>40 MPa) and 28-day (> 100 MPa) compressive strengths than reference samples (75 MPa) activated with commercial sodium silicate. Authors also investigated thermal stability, where RHA activated retained measurable compressive strength after exposure to 800˚C, while the reference mix did not.

The use of RHA as a replacement for water glass was proven viable for BFS, FA and FA-BFS pastes [135]. BFS and blended systems were cured at 95% of relative humidity and ambient temperature, while FA pastes were cured at 80 ˚C, for 24 hours. Although the reference mix with conventional sodium silicate had compressive strength of 75 MPa after 7 days, RHA-activated systems showed promising results at the same age, reaching approximately 41 MPa for BFS-activated pastes, 49 MPa for FA, and 39 MPa for the blended system.

RHA and SCSA were investigated as activators for BFS mortars by Moraes et al. [136]. Two activator solutions were prepared by dissolving RHA and SCSA in NaOH. After curing at 65 °C for 3 days and at 20 °C for 28 days, the RHA-activated samples achieved compressive strengths of 49.7 MPa and 59.7 MPa, respectively, while the SCSA-activated samples reached 45.0 MPa and 54.9 MPa, respectively. However, neither of the alternative activators

outperformed the reference samples, which achieved 62.9 MPa and 78.8 MPa under the same curing conditions.

Furthermore, FA was activated with RHA and SCSA to produce alkali-activated pastes in the work of Gomonsirisuk and Thavorniti [137]. After curing at ambient temperature for 7 days, samples synthesised with RHA exhibited the highest compressive strength of approximately 23 MPa, whereas those synthesised with SCBA achieved a maximum strength of approximately 16 MPa.

MK-based alkali-activated pastes were successfully synthesised with RHA as silica source [138,139,140]. After 20 hours of curing at 72 °C and ambient curing up to 28 days, the achieved compressive strength is reported to be approximately 40MPa [140]. For samples cured only at ambient conditions, 28-day compressive strengths were reported as 36.29 MPa [139] and 29.9 MPa, which increased to 32.8 MPa after 56 days of curing [138]. Similar results were reported for the activation of MK with SCBA [141].

Blended MK-BFS pastes activated with RHA were analysed by Bernal et al. [122]. Authors varied the BFS content and the silicon-to-alumina ratio, resulting in 7-day compressive strengths ranging from 12 MPa to almost 60 MPa. The conducted curing regime was as follows: ambient conditions (25-30°C) for 24 h, then thermal curing at 60°C and >90% relative humidity for 24 h. The samples were then stored at ambient temperature and 90% relative humidity until testing.

FA-BFS blended mortars were also activated with RHA in the work of Tong et al. [142]. RHA-activated samples reached almost 60 MPa after 28 days of ambient curing, which is the same as the reference mix.

2.7.2 Alternative alkali sources

Several research groups have reported the one-part alkali-activation with OBA. De Moraes Pinheiro et al. [26] investigated OBA as an alkaline activator for BFS mortars. The first set of mortar samples was made with the replacement of BFS by OBA from 15 to 35 wt% BFS. The second set was made with the addition of OBA from 5% to 25% wt BFS. Samples were cured in a thermal bath at 65 ^{0}C, for 7 days. The highest 7-day compressive strength was obtained for samples with the addition of 25% of OBA (38.38 MPa).

Similar results were obtained in another study by this research group [58]. Mortar samples were cured at 65^{0}C and 100% relative humidity until the day of testing. The results showed that OBA activated mix had higher 3 and 7-day compressive strength than KOH activated mix

(OBA: 29.9 MPa at 7 days and 45% strength gain with respect to 3-day strength; KOH: 16.9 MPa, 33% of strength gain).

The feasibility of OBA fly ash (OBFA) and OBA bottom ash (OBBA) application as activators for BFS was also evaluated by Alonso et al. [134]. Paste samples made with 70 wt % BFS and 30 wt % of OBFA or OBBA cured at 45 °C or 85 °C, had 28-day compressive strength of 33 MPa to 18 MPa. The OBFA activator induced the development of higher strength than the OBBA activator. In pastes prepared with 30 % wt. OBFA, strength values were comparable to those developed by BFS pastes activated with a commercial KOH.

To activate BFS and produce mortars made only from waste materials, Font et al. [143] used OBA as alkali and RHA as a silica source. The biomass ashes were dissolved in water 24 hours prior to mixing. Authors investigated the influence of curing regime and use of OBA as addition (15, 20 and 25%) or replacement (20%) by mass of BFS. The highest 7-day compressive strength was attained for 25% addition of OBA and curing at 65 ^{0}C, which accelerated the early strength development, resulting in up to 58.1 MPa for the addition of 25% of OBA. Curing at elevated temperature. Mixes with both replacement and addition of 20% of OBA, 7-day compressive strength was 52.1 MPa for elevated temperature curing, 35.0 MPa for ambient temperature, and 100% RH curing. These mixes, cured at ambient temperature, were also tested for 3, 28, 60, and 90 days, reaching 7.8, 46.2, 61.5, and 67.4 MPa, respectively.

Almond shell biomass ash has also been studied as a replacement and addition to BFS (from 15% to 35% and 5% to 25% in respect to BFS mass, respectively) [131]. Mortar samples were cured for 7 days at 65^{0}C, and the obtained compressive strength values were in the range 25-45 MPa. These compressive strengths were higher than those obtained by activation with 4M and 8M KOH solutions.

The same research group investigated the potential use of nutshell ashes, mango seed-bark ashes, and hazelnut biomass ashes (HBA) as an alkaline activator for BFS [133]. Alkali-activated pastes exhibited 26 MPa compressive strength after 28 days. The first 7 days, samples were cured at 65 ^{0}C, after which the samples were kept at 20 ^{0}C until the testing.

Hazelnut was also shown to be an efficient BFS activator in the study by Omur et al. [144]. The experimental testing of pastes cured at 22 ^{0}C and 50% RH showed that the compressive strength reached 26.8 MPa at 28 days, which was equivalent to that of reference mixtures activated with 2.0 M NaOH and 2.2 M KOH.

SSA was used as an alternative activator for BFS to form grout slurries, reaching approximately 24 MPa [145]. BFA and black RHA-based grouts were successfully activated with SSA and SHA reaching 24.31 MPa, 22 MPa, respectively, after 28 days of curing at ambient temperature

and 95% RH (both exceeding the reference KOH-activated grout) [49]. In this study, WSA was also tested as an alternative alkali activator, but did not exhibit good performance (9 MPa).

Peys et al. [132] investigated the possibility of using maize cob and maize stalk ashes to activate MK. The pastes were prepared by two-part and one-part activation. However, the MK binder produced with ash solutions as activators exhibited instability in water and low strengths. The application of maize ashes as an activator in powder form for producing one-part pastes was successful. Tested compressive strengths at 7 days were in the interval between 27 MPa and 40 MPa, depending on the ash-to-MK ratio (0.9-1.2) and curing regime (open: 48h at 60^0C and 80^0C; wrapped: 48h at 80^0C; pre-cured 24h at 20^0C and then opened for 48h at 80^0C).

Despite the Peys et al. conclusion that ash solutions are not suitable for producing AAMs, the work conducted to extract potassium hydroxide from biomass ash for biodiesel production suggests that optimal extraction conditions may vary [146]. Therefore, it could be of interest for the development of AAMs activated with biomass ash to evaluate the different ash dissolution conditions and then compare the effectiveness of one-part and two-part activation technologies. Key parameters for the potassium extraction in water that should be investigated are the ash-to-water ratio, the extraction duration and the temperature at which the extraction is conducted [134,146]. Furthermore, in a study on activating BFS with olive stone biomass ash (alkali source) and rice husk ash (silica source), it was confirmed that AAMs can be produced from water solutions of these ashes. The compressive strength at 28 days and 90 days was 46 MPa and 67 MPa, respectively, under a curing regime with elevated temperature [143].

There are several advantages of one-part over two-part alkali-activation with biomass ashes. Avoiding the dissolution of ashes in water makes the processing easier by removing one step in activator preparation. Furthermore, potential health and safety issues due to working with highly caustic alkaline solutions are avoided. Finally, because the dissolution of ashes and polymerisation reactions occur simultaneously, the dissolved ions are consumed immediately, and it can be expected that this will increase the rates of both dissolution and polymerisation to achieve system equilibrium. However, the influence of the undissolved fraction may influence the mechanical properties [132]. To the author's knowledge, this has not been addressed yet in the literature for this specific case, although it is discussed as a filler effect of undissolved ash in [58].

According to the literature review, ABA was identified as the most effective activator for BFS compared to other precursors (fly ash and MK). The performance of these AAMs has been tested on paste and mortar samples.

The AAMs were usually mixed by one-part alkali-activation [58,69,131], i.e., without previous dissolution of ABA in water [28]. However, some authors reported using dissolved ABA for the preparation of AAMs with [147] and without [144] filtering the suspension. To the best of the author's knowledge, there are no studies on the optimal dissolution time of the ABA activator prior to mixing and its influence on the AAMs properties. Some studies reported drying and/or milling as ash pretreatments [58,69,131,144,148], while there is no research on untreated ABA in AAMs.

The chemical composition of the examined ashes revealed high contents of K_2O, e.g., 61.78% in CHA [149], 32.16% in OBA [58], 31.81% [133] and 19.88% [144] in HBA, 36.67% in SSA [145] and 21.37% in SHA [148]. Furthermore, some of the ABA analyses showed the moderate to high CaO content (12-18% in SHA and SSA [148], 27.77% in OBA [58,69]). In the published research, the ash content was usually determined as an addition (5-30%) [147,69,144] and as a partial replacement (15-35%) by mass of precursor [147,69,134]. Alternatively, ABA was added to reassemble different molarities of activator solutions [58]. A range of liquid-to-solid (l/s) ratios was used for paste formulations (0.32-0.45) [134,144]. In mortar formulations, w/b ratio was 0.40 [69,150].

The curing regimes varied across studies, with curing temperatures in the first 24 hours ranging from 20°C to 85°C (typically 65°C for most studies) and durations between 4 to 48 hours [58,69]**,** followed by post-curing (after demoulding) at either ambient (18-23°C, 55-100% RH) [58,134,144,149] or elevated (65°C) conditions for 7 days [69,133,131]. Therefore, **t**he reported compressive strengths are various, from 22.1 MPa at 28 days of ambient curing [144] to 45.2 MPa after 7 days of curing at 65°C [131]. The ABA-activated AAMs exhibited comparable or superior performance to the reference mixes, which were activated with commercial KOH or NaOH [58,134,150,131,149]. For example, OBA-activated BFS paste samples resulted in compressive strength of 29 MPa after 7 days of curing and outperformed the reference mixes activated with the 4M water solution of commercial KOH (16.9MPa) [58]. Summarised findings on the use of ABA in AAMs technology are presented in Figure 17.

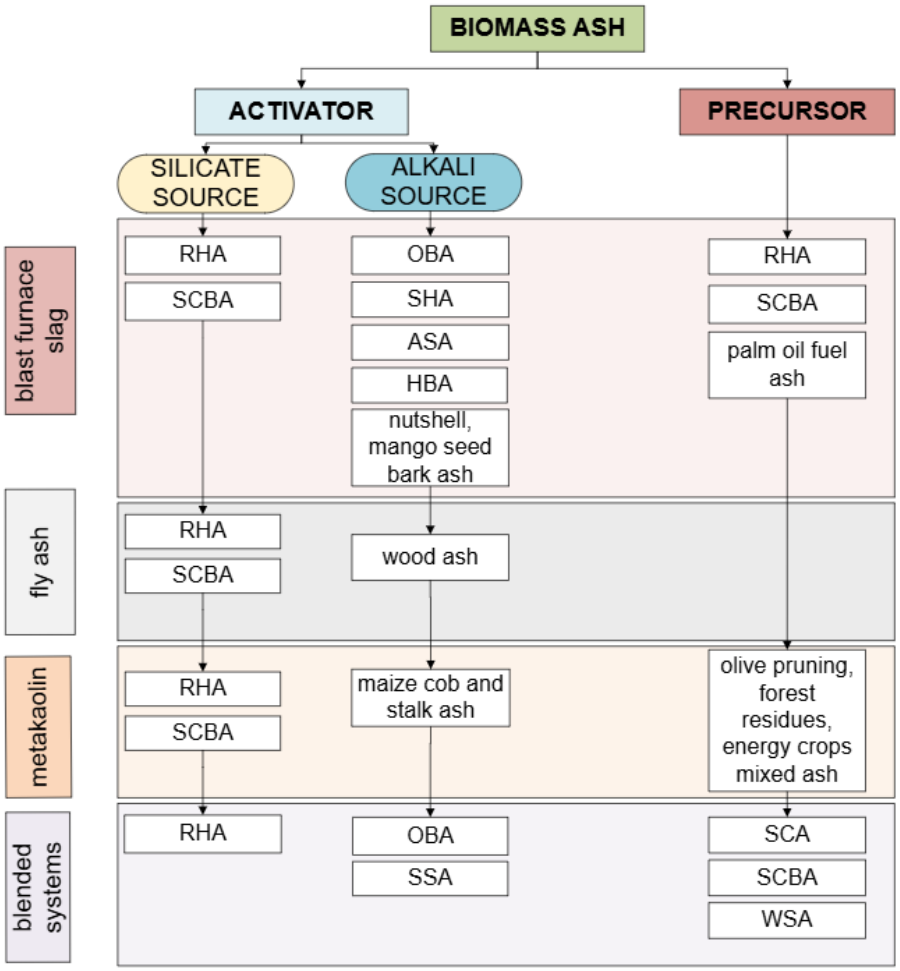

Figure 17. ABA in the AAM technology - summarised findings of the literature review

2.7.2.1 Sunflower husk ash as alkali source

The published research on sunflower-originated biomass ashes includes sunflower stalk ash (SSA), sunflower hull or husk ash (SHA), also denoted as sunflower shell fly ash (SSFA) [148,145,49,151,152]. Several papers are focused on the development of grouting slurries by activating BFS [148,145,49]. Grouting mixes with SSA and SHA were cured at 20°C and 95%RH, reaching higher 28-day compressive strength than reference mixes as well (24.88 MPa - SSA, 21.27MPa - SHA, 9.58 MPa - KOH and 11.59 MPa - NaOH) [148]. SSA was also successfully used for the activation of the BFS and black rice hull ash grouts [49]. The obtained results met the requirements of grouting engineering [49], with SSA-activated samples demonstrating significantly higher compressive strength compared to the samples activated with conventional activators (KOH, NaOH). The same group of authors tested changes in setting time and workability of the slurries [49,148], as well as microstructure by X-ray diffraction (XRD) [49,148,145] and pore structure by mercury intrusion porosimetry [145]. The

analysis of heavy metal leaching from slurries after 28 days of curing indicated that formed hydration products can promote the immobilisation of heavy metals with the formed C-(A)-S-H gel [49].

SSFA was also used to produce paste samples by activating ladle slag in the research of Nikolov et al. [152]. The results showed that the compressive strength of 30 MPa can be achieved by adding 10% of SSFA, by mass of ladle slag, while higher contents resulted in a decrease in compressive strength.

2.8 Conclusions and definition of research gap

Based on the literature review, it can be concluded that the properties of AAMs activated with ABA have predominantly been investigated on pastes or mortars. Previous studies have examined reaction kinetics, microstructural development, setting time, fresh-state behaviour, mechanical performance, and durability-related properties such as porosity and water absorption. Additionally, five scientific publications analysing SHA as an activator were identified. Although different curing regimes have been explored, these investigations were mostly limited to early ages, typically up to 7 days, unless ambient curing was applied. No studies were found on concrete mixtures of this type, nor any assessment of the durability properties of alkali-activated systems incorporating SHA. The following experimental programme was designed to address the existing research gap.

Chapter 3
EXPERIMENTAL RESEARCH

3. EXPERIMENTAL RESEARCH

The experimental research was designed to achieve the objectives of the doctoral thesis and address the defined research gap. An experimental programme was established, comprising the selection, procurement, preparation, and characterisation of the component materials; the determination of mix designs for pastes, mortars, and concretes; the selection of mortar and concrete properties used to assess the feasibility of applying alkali-activated composites with a reduced activator content and with SHA as a replacement for hydroxide activators; and the definition of the shape, dimensions, and number of samples for testing.

Experimental testing was predominantly conducted in the Laboratory of Materials and Laboratory for Advanced Testing of Materials, Faculty of Civil Engineering, University of Zagreb (Phase 1 and Phase 2), Croatia, and the Laboratory for Testing of Construction Materials, Department of Civil Engineering (Phase 1, 3 and 4), Faculty of Technical Sciences, University of Novi Sad, Serbia. FTIR analysis was conducted in the Laboratory for Materials in Cultural Heritage, Faculty of Technology Novi Sad, University of Novi Sad, Serbia (Phase 4). Chloride migration tests were performed in the Laboratory for Concrete, The Centre for Materials, IMS Institute, Belgrade, Serbia. Resistance to accelerated carbonation of concrete was tested in the Laboratory for Materials, Faculty of Civil Engineering, University of Belgrade (Phase 4).

Raw materials were obtained as donations or provided by the Laboratory at the Faculty of Civil Engineering, University of Zagreb and the Laboratory at the Faculty of Technical Sciences, University of Novi Sad.

3.1 Experimental programme

The experimental programme was divided into four phases:

Phase 1: Material characterisation (GGBFS and SHA),

Phase 2: Design of the reference concrete mix with reduced activator content,

Phase 3: Development and optimisation of sunflower-husk ash-activated binder,

Phase 4: Comparative analysis of the performance of concrete activated with conventional and alternative alkaline activators.

The results and conclusions from each phase were used as input for the next one.

The first phase of the experimental research was the characterisation of component materials GGBFS and SHA, in terms of their physicochemical and physical properties.

The second phase of experimental research focused on designing reference alkali-activated concrete (AAC) mixes with a lower ecological footprint, using GGBFS and conventional chemical activators – sodium hydroxide and sodium silicate.

Ten AAC mixes with lower to moderate activator content were prepared, and the influence of critical parameters on slump and compressive strength was analysed. The varied critical parameters were:

- w/b ratio (0.42, 0.44, 0.45, 0.47),
- alkali content (2.5 - 5.0),
- silica modulus (0.15 - 1.14).

Three optimal reference mixes were selected based on satisfactory workability and achieved compressive strength classes of C25/30, C30/37, and C40/50. To assess the influence of lower activator content of AAC, selected mixes were additionally tested for durability properties (water penetration under pressure, resistance to chloride penetration, and carbonation resistance). Finally, the reference mix for the comparative analysis with SHA-activated concrete was selected (mix R5).

The third phase aimed to assess the feasibility of using SHA as an alternative alkali hydroxide activator for GGBFS and obtain the mix design for concrete activated with SHA and sodium silicate. The first set of mortar mixes was designed to optimise SHA content, curing conditions, and mixing technology. The following parameters were varied:

- w/b ratio (0.42, 0.45, 0.5),
- SHA content (15, 25, 35 wt% GGBFS),
- Curing regime (ambient curing and curing at 65˚C),
- Mixing technology (one-part alkali activation - no immersion of SHA in water, two-part alkali-activation with immersion durations of 0h, 1h, 6h and 24h).

Optimal w/b ratios were selected for further research based on workability and compressive strength. Mortar mixes with selected w/b ratios were then further tested to evaluate the influence of SHA content and curing regimes on consistency and compressive strength at 7 and 28 days of curing, as well as on phase assemblage and reaction products in the paste samples. Finally, the optimal mix based on SHA content and curing regime was selected and tested across different mixing procedures to optimise the mixing process.

Trial mortar mixes containing SHA or SHA and sodium silicate and crushed limestone aggregate (0-4 mm) were designed. The mixes were prepared to test the Phase 4 mix design

for workability and compressive strength. This was achieved by the determination of Ms to reassemble the reference concrete mix and by varying the w/b ratio (0.45, 0.47, 0.5) to account for the potential changes in workability due to the use of aggregate with a high content of small particles.

The flowchart of the experimental Phase 3 is given in Figure 18.

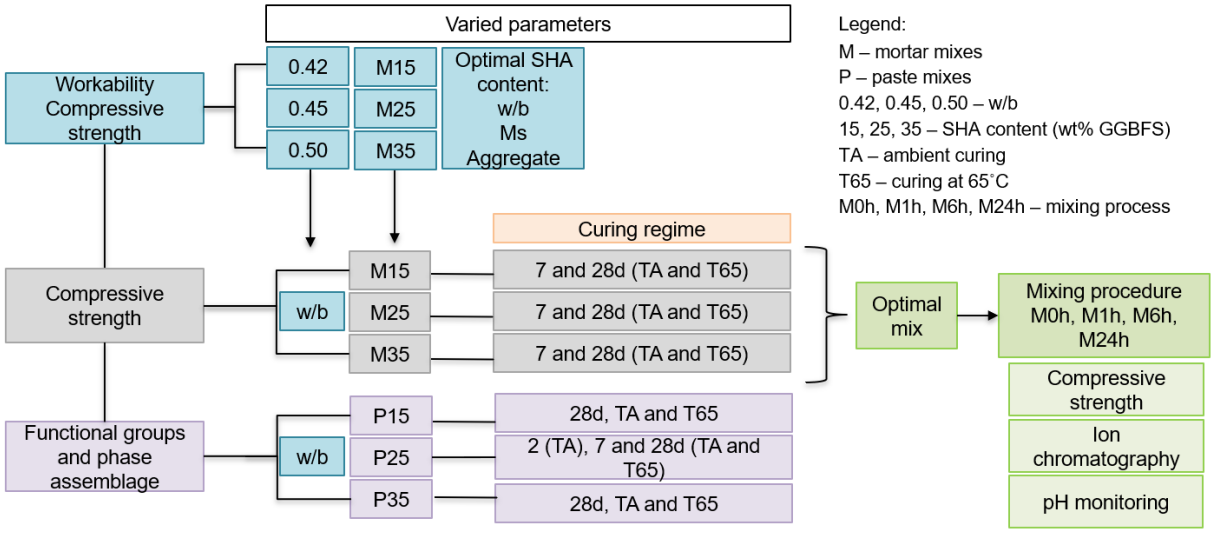

Figure 18. Flowchart of experimental Phase 3

The fourth phase investigated the effect of replacing sodium hydroxide with SHA in concrete activated with alkaline hydroxide or hydroxide and silicate on the following mechanical and durability properties:

- setting time on pastes with a mix design corresponding to concretes,
- compressive strength after 2, 7, 28, 56 and 90 days of curing,
- tensile strength after 28 and 56 days of curing,
- modulus of elasticity after 28 and 56 days of curing,
- water permeability under pressure after 28 days of curing,
- capillary sorption after 28 days of curing,
- porosity,
- shrinkage,
- carbonation resistance,
- resistance to chloride penetration.

3.2 Materials

3.2.1 Phase 1 - Characterisation of component materials

The component materials tested in Phase 1 included:

- Precursor: GGBFS, supplied by:
  - Lafarge, Serbia (Phase 3 and 4);
- SHA, supplied by VictoriaOil, Sid, Serbia.

GGBFS provided by Ecocem, Benelux, for application in Phase 2 is commercial slag, provided ready for use and extensively characterised in the literature [117,119]. GGBFS used in Phases 3 and 4 was received untreated and therefore air-dried, and milled in a laboratory mill to obtain the specific surface area of approximately 500 m^2/kg (Figure 19). SHA was used as received (Figure 19), without any pretreatment.

Figure 19. GGBFS after milling and SHA as received

3.2.2 Phase 2 - Optimisation of the reference concrete mix with reduced activator content

The following component materials were used:

- GGBFS, Ecocem, Benelux, Netherlands;
- Sodium hydroxide pellets, p.a., Gram-mol, Croatia;
- Sodium silicate, GEOSIL 34417, produced by Woellner, Germany;
- Crushed limestone (dolomite) aggregate, Holcim, quarry Očura, Croatia.

The sodium hydroxide pellets were of analytical grade, used as a water solution at a ratio of 50-50%. The commercially available sodium silicate solution Geosil 34417 had a molar ratio of 1.7 and the following chemical composition: Na_2O=16.7%, SiO_2=27.5%, H_2O=55.8%. The real densities of the component material are presented in Table 2. The grading and water absorption of the aggregate fractions are given in Appendix 1.

Table 2. Real densities of component materials used in Phase 2

Material	Real density [kg/m3]
GGBFS	2830.0
Sodium hydroxide pellets	2130.0
Geosil 34417	1550.0
Limestone aggregate	2650.0

3.2.3 Phase 3 - Development and optimisation of sunflower husk ash-activated binder

The materials used in this phase are:

- SHA, provided by VictoriaOil, Sid, Serbia,
- GGBFS, provided by Lafarge, Serbia,
- Sodium silicate, GEOSIL 34417, produced by Woellner, Germany
- Quartz sand
- Crushed limestone aggregate, fraction 0/4, Iva Agrar, quarry Ostres, Serbia.

Characterisation of GGBFS and SHA is provided within the results of Phase 1.

Table 3. Real densities of component materials used in Phase 3

Material	Real density [kg/m3]
Geosil 34417	1550.0
Quartz aggregate	2650.0
Limestone aggregate	2700.0

3.2.4 Phase 4 - Comparative analysis of the performance of concrete activated with conventional and alternative alkaline activators

The following materials were used to produce AACs:

- GGBFS, Lafarge, Serbia;
- SHA, VictoriaOil, Šid, Serbia;
- Sodium hydroxide pellets, p.a., Betahem, Serbia;
- Sodium silicate, GEOSIL 34417, produced by Woellner, Germany;
- Crushed limestone (dolomite) aggregate, Iva Agrar, quarry Ostreš, Serbia.

Properties of GGBFS and SHA are provided within the results of Phase 1, while the properties of sodium silicate are the same as in Phase 2. Real densities of sodium hydroxide and aggregate are presented in Table 4. The grading and water absorption of the aggregate fractions are given in Appendix 1.

Table 4. Real densities of component materials used in Phase 4

Material	γ [kg/m3]
Sodium hydroxide pellets	2130.0
Limestone aggregate	2700.0

3.3 Mix design

3.3.1 Phase 1 - Characterisation of component materials

The characterisation was conducted on powder samples of GGBFS and SHA.

3.3.2 Phase 2 - Optimisation of the reference concrete mix with reduced activator content

The mix proportion was calculated based on the absolute volume of 1m^3 of the AAC mix, with a constant slag content of 375 kg/m^3 for each mix and different w/b ratios. The total amount of water was calculated as the sum of water from activators and extra fresh water added. The total amount of binder in the w/b ratio represents the sum of GGBFS and solid compounds of activators.

Ten mix designs are presented in Table 5. The mixes are denoted as R (reference), numbered 1-10. The alkali content was calculated as the sum of Na_2O in NaOH and sodium silicate, expressed as weight per cent (wt%) of GGBFS. The Ms was calculated as the molar ratio of Na_2O from NaOH and sodium silicate and SiO_2 in sodium silicates. Solid components in the activators were calculated as the sum of NaOH pellets and the sodium silicate's solid component.

Four of the ten mix designs were developed based on the RILEM Round Robin test mix SN3 [24], with modified w/b ratios (R1 and R2) or with modified w/b ratios along with Na_2O content and Ms (R3 and R4). In other mixes, these parameters were chosen as potential thresholds for slump and compressive strength, based on the literature [23]. R5, R6, and R7 mixes with w/b=0.42 were designed to test the impact of varying Ms from 0.42 to 1.03, coupled with Na2O content below and above 4%. Furthermore, mixes R8, R9 and R10 had constant w/b=0.45, Ms=1.03 and Ms=1.14, along with different Na_2O contents – from 3.5%- 5%- to investigate the effect of >4% with Ms≥1 and higher w/b=0.45. The aggregate grading curve was defined according to the EMPA curve, with a fine-to-coarse aggregate ratio of 1:1.5 for each mix and a maximum aggregate size of 16 mm. The water correction was conducted based on the aggregate's humidity and absorption.

Mixes R1-R6 are considered to have lower activator content, while mixes R7-R8 have moderate activator content and were designed as references to assess the influence of critical parameters for Ms=1.

Table 5. Mix design of AAC mixes with conventional activators

Mix	GGBFS [kg/m^3]	NaOH[a] [kg/m^3]	Sodium silicate[b] [kg/m^3]	Additional water [kg/m^3]	w/b	Na_2O[c]	SiO_2[c]	Ms	Aggregate [kg/m^3]			
									0/4	4/8	8/16	Total
R1	375	15.0	10.09	153	0.44	3.5	0.7	0.22	732	344	689	1766
R2	375	15.0	10.09	133	0.42	3.5	0.7	0.22	728	479	612	1819
R3	375	11.25	5.03	157	0.44	2.5	0.4	0.15	739	348	696	1784
R4	375	11.25	5.03	169	0.47	2.5	0.4	0.15	726	342	684	1753
R5	375	15.0	22.82	140	0.42	4.1	1.7	0.42	734	346	691	1746
R6	375	6.65	47.73	136	0.42	2.8	1.9	0.69	730	344	688	1764
R7	375	8.17	25.92	143	0.42	4.1	4.1	1.03	740	349	697	1787
R8	375	6.65	47.73	148	0.45	3.5	3.5	1.03	718	338	676	1732
R9	375	8.17	58.64	143	0.45	4.3	4.3	1.03	710	335	669	1713
R10	375	8.03	75.0	137	0.45	5.0	5.5	1.14	701	331	661	1693

*a - solid (pellets); b - solution; c - wt% GGBFS

3.3.3 Phase 3 - Development and optimisation of sunflower husk ash-activated binder

Mortar mixes were designed with constant GGBFS content, while SHA content was varied: 15, 25 and 35 wt% GGBFS. All mixes had a w/b ratio of 0.45, and the binder was calculated as the sum of the precursor and the soluble fraction of the SHA, assuming that the entire potassium oxide content was dissolved and contributed to the alkali activation. The mass of the soluble SHA content was previously determined by dissolving SHA in water. The aggregate-to-binder ratio was 3, with the undissolved fraction of SHA included in the total aggregate mass. The mass proportions of the individual fractions were adopted in accordance with those used for a standard cement mortar.

Paste mixes were prepared with the same material ratios as mortar mixes, with the omission of the aggregates.

A detailed mix design for w-b=0.45 is provided in Table 6. The mixtures were labelled based on their composition. The paste mixtures were designated as P15, P25, and P35 - the letter “P” denotes pastes, while the numbers 15, 25, and 35 represent the added SHA content wt% GGBFS. Similarly, the letter “M” denotes mortar mixtures, following the same numerical convention, resulting in designations such as M15, M25, and M35.

Table 6. Mix design of pastes and mortars for Phase 3 of the experimental research

Mix	GGBFS (g)	SHA (g)	SHA’ (g)	SHA’’ (g)	Water (g)	Quartz sand fraction (mm)			
						0.008-0.16 (g)	0.16-0.5 (g)	0.5-1.0 (g)	1.0-2.0 (g)
Pastes									
P15	400	60	27	33	192	-	-	-	-
P25	400	100	45	55	200	-	-	-	-
P35	400	140	63	77	208	-	-	-	-
Mortars									
M15	400	60	27	33	192	277	139	416	416
M25	400	100	45	55	200	285	142	427	427
M35	400	140	63	77	208	292	146	438	438

SHA’ - SHA dissolved in water; SHA’’ - mass of SHA undissolved in water

3.3.4 Phase 4 - Comparative analysis of the performance of concrete activated with conventional and alternative alkaline activators

The AAC mix chosen as the reference mix for this phase in Phase 2, based on the performance, was denoted as R (reference) mix. AAC mix with the substitution of NaOH with SHA was denoted as SHA-S. The mix containing only SHA as an activator was labelled SHA25, where 25 denotes the SHA content, by mass of GGBFS.

The mix design of the mix R was calculated as for the mixes in Phase 2.

Mix SHA-S was designed to reassemble the mix R, i.e., it had the same amount of GGBFS (375 kg/m^3), w/b ratio, and targeted alkali content and silica modulus. Alkali content was calculated as the sum of dissolved K_2O from SHA and Na_2O sodium silicate, expressed as wt% GGBFS, assuming that the dissolved portion of SHA is K_2O. The Ms was calculated as the molar ratio of K_2O in SHA and Na_2O from sodium silicate to SiO_2 in sodium silicate. The total amount of water was calculated as the sum of water from activators and extra fresh water added. Solid components in the activators for the binder calculation were calculated as the sum of dissolved K_2O from SHA and solids from sodium silicate. The undissolved fraction of the SHA was included in the fine aggregate fraction (0-4 mm). Based on the results of the SHA dissolution in water conducted in Phase 1 and the restraint on the fine particle content in concrete, this fraction was 42.5%. The aggregate grading curve was designed to match that of the aggregate used in Phase 2, with a fine-to-coarse ratio of 1:1.5 and a maximum aggregate size of 16 mm. The water correction was conducted in accordance with the aggregate's humidity and absorption.

The w/b ratio was 0.5 in all mixes, due to the low workability of mixes with SHA at lower w/b ratios. Mix designs of the mixes R, SHA-S and SHA25 are presented in Table 7.

Table 7. Mix design of AAC R, SHA25, and SHA-S

Mix	GGBFS [kg/m^3]	NaOH[a] [kg/m^3]	SHA [kg/m^3]	Sodium silicate[b] [kg/m^3]	Add. water [kg/m^3]	w/b	Na_2O[c]	K_2O[c]	SiO_2[c]	Ms	Aggregate [kg/m^3]			
											0/4	4/8	8/16	Total
R1	375	15.0	-	22.82	172	0.5	4.1	-	1.7	0.42	909	224	593	1726
SHA-S	375	-	93.75	23.0	189	0.5	1.0	4.0	1.7	0.42	860[d]	212	561	1683
SHA25	375	-	93.75	-		0.5	-	4.0	-	-	842[d]	207	549	1650

a-solid; b – solution, c – wt% GGBFS, d-undissolved ash: 51kg/m^3

3.3.4.1 Mix design calculations

An example of the mix design calculation for the AAC with a conventional alkaline activator is presented for the mix R5.

Mass proportions of aggregate fractions were chosen so that the grading curve of the aggregate mix represents the EMPA grading curve:

- Fraction 0/4 mm – $X_{0/4}$=41%
- Fraction 4/8 mm - $X_{4/8}$=20%
- Fraction 8/16 mm - $X_{8/16}$=39%

Aggregate mass was calculated from the absolute volumes of the component materials in 1 m^3 of concrete.

$$\frac{m_z}{\gamma_{z,s}} + \frac{m_{SH}}{\gamma_{SH,s}} + \frac{m_{SS}}{\gamma_{SS,s}} + \frac{m_w}{\gamma_{w,s}} + \frac{m_a}{\gamma_{a,s}} + \Delta p = 1$$

$$\frac{375}{2730} + \frac{30}{1560} + \frac{22.82}{1550} + \frac{140}{1000} + \frac{m_a}{2650} + 0.01 = 1$$

$$m_a = 1746 \text{ kg/m}^3$$

Mass of each aggregate fraction:

- Fraction 0/4 mm - $m_{0/4}$ = 724 kg/m^3
- Fraction 4/8 mm - $m_{4/8}$ = 341 kg/m^3
- Fraction 8/16 mm - $m_{8/16}$ = 681 kg/m^3

Designed fresh-state density:

375 + 30 + 22.82 + 140 + 1746 = 2313 kg/m^3

The grading curve for the aggregate mix is presented in Figure 20.

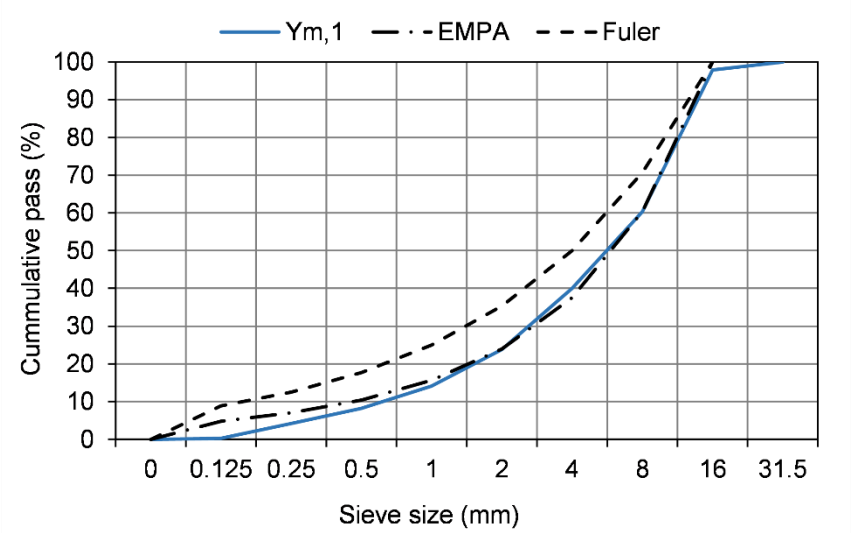

Figure 20. Grading curve of the aggregate (Ym) and reference curves (EMPA and Fuler)

AAC mixed with SHA as a hydroxide activator is presented in the following section.

Mass proportions of aggregate fractions were chosen so that the grading curve resembles the curve from Phase 2:

- Fraction 0/4 mm - $X_{0/4}$=53%
- Fraction 4/8 mm - $X_{4/8}$=13%
- Fraction 8/16 mm - $X_{8/16}$=34%

Aggregate mass was calculated from the absolute volumes of the component materials in 1 m^3 of concrete.

$$\frac{m_z}{\gamma_{z,s}} + \frac{m_{SHA}}{\gamma_{SHA,s}} + \frac{m_{SS}}{\gamma_{SS,s}} + \frac{m_w}{\gamma_{w,s}} + \frac{m_a}{\gamma_{a,s}} + \Delta p = 1$$

$$\frac{375}{2730} + \frac{93.75}{2200} + \frac{23}{1550} + \frac{189}{1000} + \frac{m_a}{2650} + 0.01 = 1$$

$$m_a = 1650 \text{ kg/m}^3$$

Mass of each aggregate fraction:

- Fraction 0/4 mm - $m_{0/4}$ = 869 kg/m^3
- Fraction 4/8 mm - $m_{4/8}$ = 214 kg/m^3
- Fraction 8/16 mm - $m_{8/16}$ = 567 kg/m^3

Designed fresh-state density:

375 + 93.75 + 23 + 189 + 1650 = 2330 kg/m^3

The grading curve of the aggregate mix is presented in Figure 21.

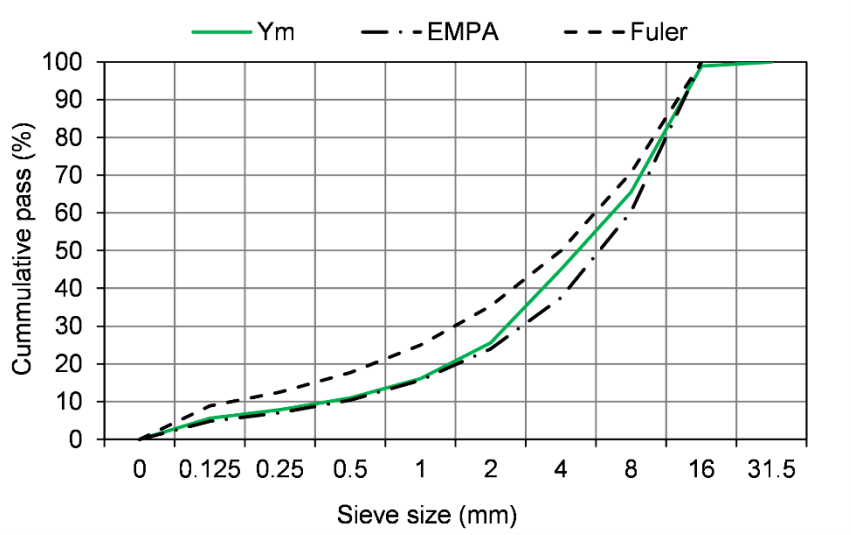

Figure 21. Grading curve of the aggregate for the AAC mixes R and SHA-S (Ym) and reference curves (EMPA and Fuler)

The sieving and humidity of the aggregate used for concrete mixes were determined during the characterisation phase, while the real density was provided by the manufacturer.

3.4 Mixing, casting and curing

3.4.1 Paste and mortar mixes

The reference mixing procedure involved using dry SHA, without prior immersion of SHA in water. In this procedure, GGBFS and SHA were manually dry-mixed and added to aggregates. Three solid components were then manually homogenised, after which they were added to water and mixed in the mixer at high speed for five minutes. The same procedure was followed for paste preparation, but without the addition of the aggregate. Additionally, several procedures were applied, varying the immersion time of SHA in water, to assess the influence of alkali (primarily potassium) pre-dissolution from SHA on the workability and compressive strength of the resulting mortars. The first step in these procedures was to immerse the SHA and keep it in the water for a different period. The GGBFS and aggregates were dry-mixed and then mixed with SHA and water suspension immediately (0h) and after 1, 6, and 24 hours of immersion. The mixing procedures for assessing the influence of activator preparation on mortar properties are summarised in Table 8. Procedures are marked as Mx,y where x denotes the SHA content in the mix chosen for testing, based on the optimal workability and compressive strength performance. The duration of SHA immersion in water is denoted by y.

Table 8. Mixing procedures for assessing the influence of activator preparation on the mortar properties

Procedure	Step 1: immersion	Step 2: dry-mixing, manual	Step 3: mixing, manual	Step 4: mixer
Mx,0h	SHA immersed just before binder mixing	GGBFS + aggregate	GGBFS + aggregate + SHA suspension	GGBFS + aggregate + SHA suspension
Mx,1h	SHA was immersed in water for 1h			
Mx,6h	SHA was immersed in water for 6h	GGBFS + aggregate	GGBFS + aggregate + SHA suspension	
Mx,24h	SHA was immersed in water for 24h			

The mortar samples were cast in prism metal moulds (40x40x160mm) and kept in sealed in polymeric films to prevent moisture loss for 24 hours. Paste samples for testing microstructure were cast in metal moulds with dimensions 5x5x60mm and also cured sealed.

The influence of elevated-temperature curing was assessed on mortar mixes with different SHA content, used dry without immersion in water. After 24 hours in moulds, samples were subjected to two different curing regimes. One set of samples was demoulded and cured at an ambient temperature (TA). In contrast, the other set was cured in moulds for 5 days at 65˚C (T65), then demoulded and cured at ambient temperature until the day of testing, to investigate the influence of elevated-temperature curing on compressive strength at 7 and 28 days. The two regimes were conducted for samples tested for microstructure analysis (TGA and FTIR) and compressive strength at 7 and 28 days. Samples tested at 2 days of age were not subjected to the elevated temperature. Summarised curing regimes are given in Table 9.

Table 9. Curing regimes of paste and mortar samples

Day of testing	Curing regime	First 24h	5 days	Until the day of testing
2, 7, 28	TA	sealed, ambient temperature		
7, 28	T65	sealed, ambient temperature	sealed, 65ºC	sealed, ambient temperature

3.4.2 Concrete mixes

The mixing procedure and curing were conducted according to the recommendations in the RILEM Round Robin tests [78] and the specification PAS 8820:2016, Construction materials. Alkali-activated cementitious material and concrete, published by the British Standards Institution [153]. Aggregates and GGBFS were mixed for 1 minute. After that, sodium silicate and sodium hydroxide were continuously added, respectively, and mixed for 2 minutes in a 50 l concrete mixer. Water was added next and mixed for 4 minutes.

After casting, the samples were covered with plastic sheets to prevent excessive drying of the top surface. After 24h, samples were demoulded, wrapped in polymeric films to prevent moisture loss, and cured sealed in laboratory conditions until testing.

The mixing procedure for the reference mix was the same as described in Phase 2 of the experimental programme, with one additional step prior to mixing. Before adding the binder components to the mixes SHA25 and SHA-S to enhance workability due to the high proportion of small particles in the aggregate, the aggregate was saturated with water calculated based on the absorption of the aggregate and mixed for 3 minutes. After that, aggregates stayed in the closed mixer for 10 minutes to absorb the water.

Mix SHA-S was further mixed the same way, but the SHA was added at the beginning of the process, along with GGBFS, to the aggregates, and mixed for 1 minute. After that, sodium silicate was added and mixed for 2 minutes in a 50 L concrete mixer. Water was added next and mixed for 4 minutes. The same mixing procedure was followed for SHA25, without the addition of sodium silicate.

Examples of cast concrete samples in moulds and samples sealed for curing are presented in Figure 22 and Figure 23, respectively.

The samples were demoulded and cured sealed, as described in Phase 2, until the day of testing.

Figure 22. Example of the sealed curing of the concrete samples

Figure 23. Samples in the moulds after casting

3.5 Testing methods

3.5.1 Characterisation of component materials

To characterise GGBFS and SHA in Phase 1, the following properties were tested:

- Physicochemical properties:
  - Chemical composition,
  - Functional groups,
  - Mineralogical composition,

- Solubility of SHA in water.

- Physical properties:
  - Particle morphology and shape of SHA,
  - Particle size distribution (PSD),
  - Specific surface area,
  - Real density.

The chemical compositions were obtained by X-ray fluorescence (XRF) and energy-dispersive X-ray spectroscopy (EDX). The samples for XRF were prepared according to the standard method. EDX analysis was conducted in the Biosense Institute laboratory with a scanning electron microscope Apreo 2C, Thermo Fisher Scientific, USA, using an accelerating voltage of 20 kV and a probe current of 0.4 pA.

Chemical compositions and functional groups were analysed by Fourier-transform infrared (FTIR) spectroscopy. The FTIR analysis was conducted on a powder sample using a mobile Alpha Bruker Optics (BRUKER OPTICS, Germany) FTIR device in ATR (Attenuated Total Reflection) mode with a diamond crystal. The wavenumber range was between 400 and 4000 cm^{-1}. The obtained spectra were analysed using the Spectragryph software.

Mineralogical composition was determined by X-ray diffraction (XRD) of powder, in the laboratory of Lafarge BFC d.o.o., Serbia, using Bruker D4 Endeavour.

Scanning electron microscopy (SEM) was conducted in the Biosense Institute laboratory with a scanning electron microscope Apreo 2C, Thermo Fisher Scientific, USA. SEM imaging was performed using an in-lens T1 detector in OptiPlan mode at an accelerating voltage of 1 kV and a probe current of 0.1 pA. Micrographs were acquired at magnifications 5000×, 10000×, and 25000×.

PSD was determined in the Lafarge laboratory in Serbia using a Mastersizer 2000 (Malvern Panalytical, United Kingdom).

The real density of GGBFS and SHA is determined by Method A, described in SRPS 1936:2009 [154]. Specific surface area was measured with the Blaine air permeability method, in accordance with SRPS EN 196-6: 2019 [155].

The solubility of the ash was determined by immersing SHA in water at a 1:2 ratio for 5 minutes at ambient temperature, while stirring to simulate mixing. To determine the influence of higher temperature and longer dissolution period, SHA was also immersed for two hours at 65˚C. The sample was filtered, and the insoluble fraction was dried at 105 °C to a constant mass and expressed by mass of SHA.

3.5.2 Paste and mortar mixes

The following properties were tested on mortar samples:

- fresh-state properties:
  - consistency;
- hardened-state properties:
  - compressive strength;
- influence of immersion time on SHA dissolution:
  - potassium leaching;
  - alkalinity.

Paste samples were used to analyse:

- functional groups;
- reaction products. Fresh-state properties

The consistency of mortar mixes was tested using the flow table test, in accordance with the standard procedure described in SRPS EN 1015-3:2008 [156]. After mixing the components and preparing the mortar, the mean flow diameter was determined as the arithmetic average of the spread diameters measured in two perpendicular directions. The flow table test is shown in Figure 24 and individual measurements are given in Appendix 5.

Figure 24. Measurement of the consistency of mortars by the flow table test

3.5.2.1 Hardened-state properties

The compressive strength of mortar mixes was tested at 2, 7, and 28 days, in accordance with SRPS EN 196-1:2017 [157], for three samples per batch. The example of a compressive strength test is shown in Figure 25. Individual measurements of the compressive strengths of mortars are given in Appendix 6.

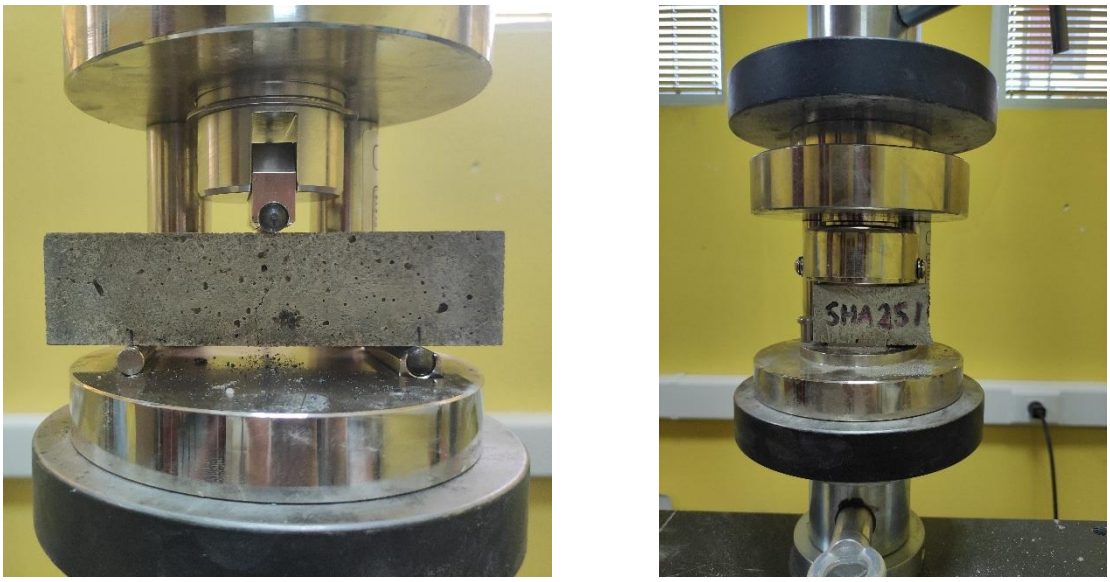

Figure 25. Testing of compressive strength of mortar samples

Phase composition and reaction products

Paste samples with varying SHA content and two curing regimes were used to determine phase composition and reaction products after 28 days of curing. Phase composition in pastes was analysed using thermogravimetric analysis (TGA), derivative thermogravimetric (DTG) analysis and FTIR spectroscopy. TGA and DTG were performed on pastes, using the Labsys evo DTA/DSC1150 (Setaram). To prepare samples, the paste prisms were crushed and dried in an oven for 2 hours at 65°C. After cooling to an ambient temperature, pastes were ground to a fine powder in an agate mortar and immediately tested. Approximately 30 mg of the sample was heated from 30^0C to 1000^0C at a constant rate of 10^0C/min under an argon atmosphere. The samples were tested at 2, 7 and 28 days of age, according to the curing regimes described in Table 9. FTIR spectroscopy was conducted on paste samples at 2, 7, and 28 days of age. The analysis was conducted using a mobile Alpha Bruker Optics (BRUKER OPTICS, Germany) FTIR device in ATR (Attenuated Total Reflection) mode with a diamond crystal. The wavenumber range was between 400 and 4000 cm− 1. The obtained spectra were analysed using the integrated OPUS software developed by BRUKER.

Influence of immersion time on SHA dissolution

The influence of the immersion time on SHA dissolution was analysed by monitoring pH of SHA solution and by analysing the potassium leaching. Alkalinity of the SHA solution was measured after immersion of the SHA in water to resemble the different mixing procedures given in Table 8. The water-to-SHA ratio was the same as that for the mortar chosen for optimal performance. After the immersion, the solutions were filtered, and their pH values were measured by pH meter Edge HI2020-02 (Hanna Instruments, Woonsocket, RI, USA). The dependence of the potassium leaching on the described immersion times of SHA was quantified by an ion chromatograph Thermo Scientific DIONEX ICS-5000+, by dissolving 20g of SHA in 200ml of water.

3.5.3 Concrete mixes

The following properties were tested on AAC mixes:

- fresh-state properties:
  - setting time of the corresponding pastes (Phase 4),
  - temperature (Phase 2, Phase 4),
  - consistency (Phase 2, Phase 4),
  - air content (Phase 2, Phase 4),
  - density (Phase 2, Phase 4);
- hardened-state properties:
  - physical properties
    - density (Phase 2, Phase 4);
    - porosity (Phase 2, Phase 4);
    - phase assemblage (Phase 4);
    - water absorption (Phase 4);
    - shrinkage (Phase 4);
  - mechanical properties:
    - compressive strength after 2, 7, 28 (Phase 2 and 4), 56, and 90 days (Phase 4) days of curing,
    - flexural strength after 28 and 56 days of curing (Phase 4);

- modulus of elasticity (Phase 4)

- durability properties:
  - water permeability under pressure (Phase 2, Phase 4);
  - carbonation resistance (Phase 2, Phase 4);
  - resistance to chloride penetration (Phase 2, Phase 4).

3.5.3.1 Fresh-state properties

To investigate the influence of SHA on setting time, paste specimens of identical binder composition as AAC (without aggregates) were prepared and tested for initial and final setting time, in accordance with SRPS EN 196-3:2017 [158].

The temperature of the concrete mixes was measured after mixing using a thermometer, in accordance with SRPS EN 12350-1:2019 [159].

Consistency was measured by the slump test (Figure 26), following the procedure described in SRPS EN 12350-2:2019 [160].

Air content was determined by the pressure method (Figure 27) defined in SRPS EN 12350-7:2019 [161]. A known volume of fresh concrete was placed into a calibrated air-meter container, the lid was clamped and pressurised, and the resulting pressure drop after equalisation was used to calculate the percentage of entrapped air in the concrete.

The density of fresh concrete was determined by measuring the mass of concrete in a container of known volume in accordance with SRPS EN 12350-6:2019 [162].

Measurements of fresh-state properties are given in Appendix 2 (Phase 2) and Appendix 7 (Phase 4).

Figure 26. Example of a slump test of concrete

Figure 27. Determination of the air content of concrete by the pressure method

3.5.3.2 Hardened-state properties

Physical properties

Density

The density of hardened concrete was determined in accordance with SRPS EN 12390-7:2019 [163]. The mass of hardened samples was weighed, and their volume was obtained by geometric measurement. The density was calculated as the ratio of mass to the corresponding volume.

Porosity

Mercury intrusion porosimetry (MIP) analysis was performed using the AutoPore IV 9500 2.03.00 instrument (Micromeritics Instrument), with a capacity of 206 MPa. MIP was used to qualitatively compare the porosity and pore size distribution of three AAM mixes. The selected concrete mixes were tested after 28 days of sealed curing and an additional 14 days under laboratory conditions.

Phase assemblage

Hydration products of two mixes were analysed by TGA and DTG, using the Labsys evo DTA/DSC1150 (Setaram). Parts of the samples used for compressive strength tests at 28 days of curing were taken, and the hydration of the samples was stopped by immersion in isopropanol for 7 days, followed by drying under vacuum and kept in a desiccator until the day

of testing. Prior to testing, samples were crushed into powder and then immediately tested. Approximately 30 mg of the sample was heated from 30^0C to 1000^0C at a constant rate of 10^0C/min under an argon atmosphere.

Water absorption

Capillary water absorption of concrete was tested on cylindrical specimens with a diameter of approximately 100 mm and a height of approximately 50 mm, in accordance with ASTM C1585 [164]. The samples were preconditioned for 3 days, at 50 ˚C and RH 80%. After this period, the samples were placed in separate sealed containers for an additional 15 days. Before starting the test, the side sample surfaces were covered with sealing material. Samples were then placed on the supports in the pan, filled with water so that the water level is 1-3mm above the sample height. The sample mass was recorded at 60s, 5, 10, 20, 30 and 60 minutes, followed by measurement every hour. After 6 hours, the mass was recorded each day by the end of testing. Individual water-absorption measurements are given in Appendix 9.

Shrinkage

Total shrinkage of concrete was determined in accordance with SRPS 12390-16:2019 [165] using three prismatic samples measuring 100 × 100 × 500 mm. The length changes were measured over stud gauges along the principal axis by using a digital length comparator (Insize, China) with a measurement accuracy of 0.001 mm. Tests were conducted after 1, 3, 7, 14, 28, 42, 46 and 90 days of age. The representative value of the length change was calculated as the arithmetic mean of the results obtained from three prisms. During testing, the samples were kept in a humidity chamber at 20-22 ˚C and a relative air humidity of 53–60%. Additionally, length changes were measured on the sample surface using 50 mm long strain gauges. After demoulding, one of the specimens' surfaces perpendicular to the trowelled side was mechanically roughened, prior to bonding of the gauges. Samples after preparation for testing and testing setup are presented in Figure 28 and Figure 29, respectively. Measured length changes and mass losses are presented in Appendix 9.

Figure 28. Concrete samples prepared for shrinkage testing - mix R

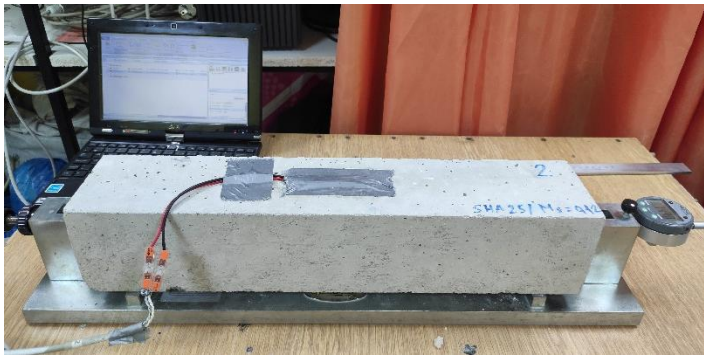

Figure 29. The setup for the shrinkage test - mix SHA-S

Mechanical properties

Compressive strength

The compressive strength was determined following the standard SRPS EN 12390-3:2019 [166], for the set of three cubic samples d=150 mm, per batch, after 2, 7, 28, 56 and 90 days of sealed curing. The tests were carried out using a hydraulic press with a capacity of 3000 kN, and the loading rate was 0.4 Mpa/s. Before testing, the dimensions and mass of the specimens were measured. The compressive strength test is shown in and the measurement results of are provided in Appendix 3 (Phase 3) and Appendix 8 (Phase 4).

Flexural strength

The flexural strength test was conducted in accordance with SRPS EN 12390-5:2019 [167], prismatic samples with dimensions of 100 × 100 × 400 mm after 28 and 56 days of curing. Tests were performed using a hydraulic testing machine manufactured by VEB Werkstoffprüfmaschinen, with a capacity of 400 kN. The prisms were placed on two supporting rollers with a diameter of 40 mm, positioned 50 mm from each end of the specimen, resulting in a span of 300 mm. A loading roller with a diameter of 30 mm was placed on the top surface, through which the load was applied as a concentrated force at mid-span. The load was increased at a constant rate of 0.04 MPa/s. The testing setup is shown in Figure 30.

Modulus of elasticity

The static modulus of elasticity of concrete was determined in accordance with SRPS EN 12390-13:2021, on cylindrical concrete specimens at the 28 and 56 days of age. The test was conducted under uniaxial compressive loading using a calibrated hydraulic testing machine and a digital length comparator system to measure axial deformation. The loading was applied

at a rate of 0.6±0.2 MPa/s. Prior to testing, the specimens' dimensions were measured to determine the loaded cross-sectional area. According to method A, the preload stress was 0.5 MPa, the lower stress $0.1f_c$, and the upper stress $f_c/3$. The testing setup is presented in Figure 31. The measured tensile strength and modulus of elasticity are presented in Appendix 9.

Figure 30. Set up for testing the flexural strength of concrete samples

Figure 31. Set up for testing the modulus of elasticity of concrete samples

Durability properties

Individual measurements of durability properties are given in Appendix 4 and Appendix 10, for the Phase 2 and Phase 4, respectively.

Water permeability under pressure

The water permeability pressure was tested in accordance with SRPS EN 12390-8:2019 [168]. Three cubic samples, d=150 mm, were tested after 28 days of curing. Specimens were placed in the testing apparatus (Figure 20), and water pressure was applied to one face of each specimen, perpendicular to the concrete pouring direction. A constant water pressure of 0.5 MPa was maintained for 72 hours. After the test period, the specimens were split perpendicular to the pressurised surface, and the maximum depth of water penetration was measured from the wetted front. The highest measured penetration depth was taken as the test result for each specimen. The experimental setup and an example of the samples after testing are presented in Figure 32 and Figure 33, respectively.

Figure 32. Set up for testing the water permeability under pressure of the concrete samples

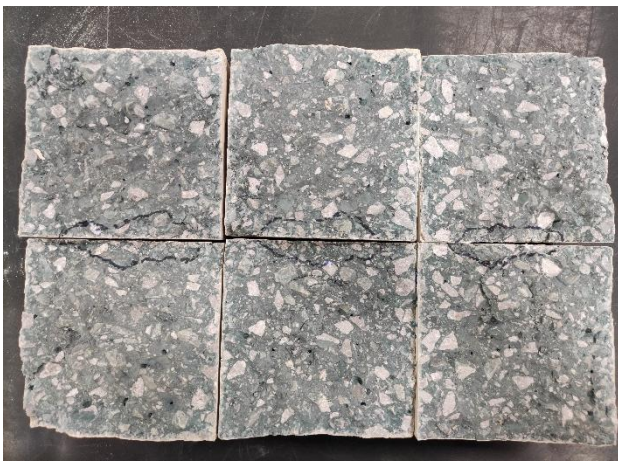

Figure 33. Example of the samples after exposure to water under pressure

Carbonation resistance

Resistance to carbonation was tested by the accelerated carbonation method, as described in SRPS EN 12390-12 [169]. After 28 days of curing, prior to placing in the carbonation chamber, unsealed samples were stored under laboratory conditions (i.e., 18-25°C and 50-65% RH) for 14 days. Carbonation depth was determined by the phenolphthalein spray method on two samples of each mix after they were exposed to accelerated carbonation conditions for 7, 28 and 56 days, i.e., 3% CO_2 at 20°C and RH 57%. The samples were split and sprayed with phenolphthalein. The samples in the carbonation chamber and the samples after 28 days of exposure to accelerated carbonation are presented in Figure 34 and Figure 35.

Figure 34. Concrete samples in the carbonation chamber

Figure 35. Concrete samples after 28 days of exposure to accelerated carbonation

Resistance to chloride penetration

Resistance to chloride penetration was determined by measuring the chloride migration coefficient from non-steady-state migration after 28 and 56 days of curing, in accordance with NT BUILD 492 [170]. Concrete specimens are cast in cylindrical moulds (diameter 100 mm and height 200 mm), and after demoulding, they are stored sealed until testing. From each cylinder, a 50 ± 2 mm thick slice was cut using a water-cooled diamond saw. Prior to testing, samples were pretreated by placing them in the vacuum container under approximately 5 kPa for 3 hours. While maintaining a vacuum, the $Ca(OH)_2$ solution was poured into the container to fully cover the samples. The vacuum was then released, and the samples were kept immersed for 18 hours. This set of three samples was placed in test cells and exposed to a NaCl solution under an applied current. The voltage and duration of the test were determined at the beginning of the test. After testing, the samples are split in half, sprayed with $AgNO_3$ and the penetration depth is measured. While the NT BUILD 492 standard specifies a value of c_d coefficient 0.07 N for PC concrete, a value of 0.21 N was used to account for pore solution chemistry of AAMs and its effect on the chloride concentration at which the colour changes during the colorimetric spray test [117]. The experimental setup is presented in Figure 36.

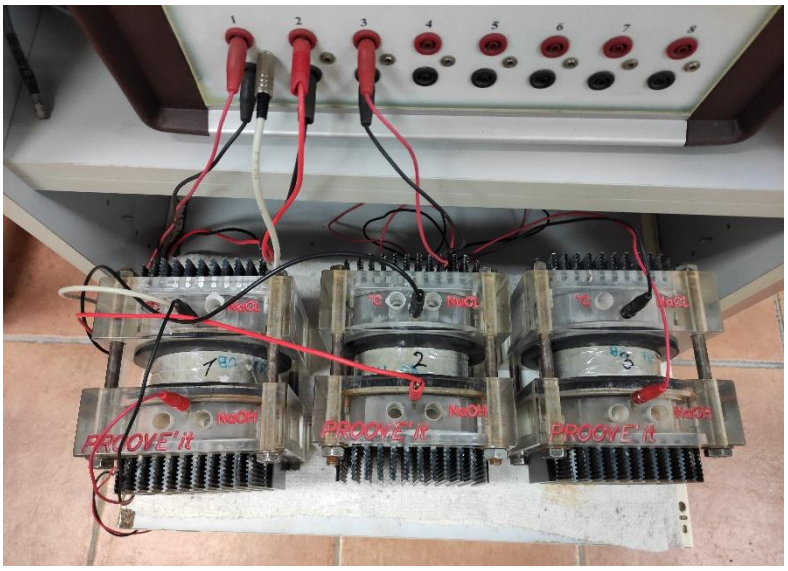

Figure 36. Set up for testing resistance to chloride penetration by non-steady-state migration

Chapter 4
RESULTS, DISCUSSION, AND CONCLUSIONS

4. RESULTS, DISCUSSION AND CONCLUSIONS

4.1 Phase 1 - Characterisation of component materials

Phase 1 of the experimental research was designed to assess the possibility of using SHA as an alternative activator for GGBFS, by its characterisation. It corresponds to hypothesis 1:

H1: *"The sunflower husk ash can be used as an alternative activator for synthesising slag-based alkali-activated materials."*

4.1.1 Results

The chemical composition of GGBFS and SHA obtained by XRF is presented in Table 10. Chemical composition of GGBFS indicates that it is a neutral slag with high content of SiO_2, (38.69%), CaO (37.19%) and 10.52% of MgO (Kb=(%CaO+%MgO)/(%SiO_2+Al_2O_3)=0.99) [76]. Slags with >5% MgO are considered to have moderate to high MgO content [171]. SHA exhibited a very high K_2O content (38%). Other dominant oxides in the SHA are CaO (14.29%), SO_3 (13.53%), and MgO (10.46%). SHA also contains chlorine in a smaller percentage (1.74%).

Table 10. Chemical composition of GGBFS and SHA

Material	Oxide (%)								
	SiO_2	CaO	Al_2O_3	Fe_2O_3	MgO	SO_3	K_2O	Na_2O	Cl^-
GGBFS	38.69	37.19	9.51	0.47	10.52	2.17	0.83	0.41	-
SHA	1.75	14.29	0.59	0.21	10.46	13.53	38.00	0.07	1.74

Elemental composition of SHA determined by EDX analysis at 20kV accelerating voltage and 0.4 nA probe current is presented in Figure 37. It confirms the XRF results: the dominant element is K, followed by Ca, Mg, S. The spectrum also shows the presence of P and Cl.

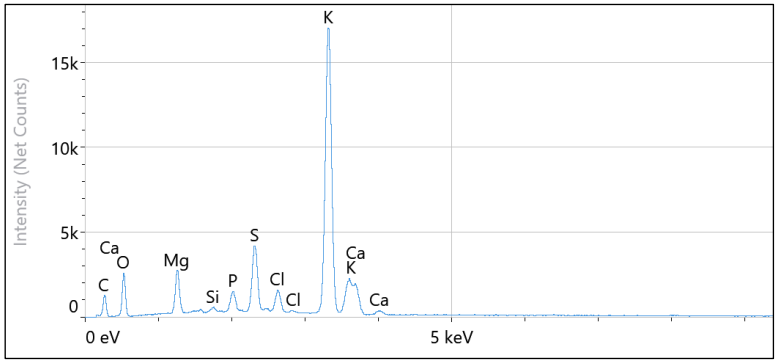

Figure 37. EDX spectrum of SHA

SEM image of SHA at a magnification of 25000x is presented in Figure 38. SHA particles exhibited a rough surface and an irregular shape, with no signs of porosity.

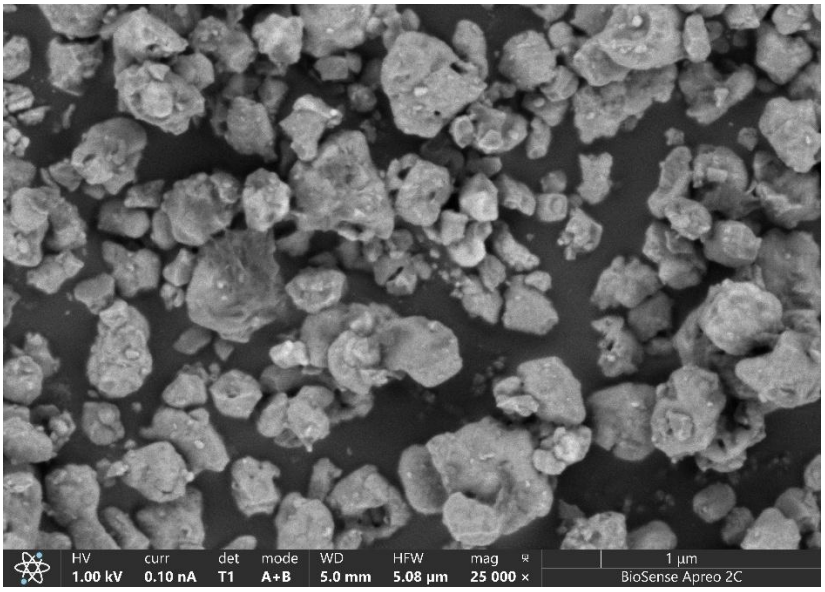

Figure 38. SEM image of SHA at a magnification of 25000x

XRD and FTIR spectra of GGBFS and SHA are presented in Figure 39, Figure 40 and Figure 41.

The XRD pattern of GGBFS (Figure 39) indicates an amorphous phase, with dominant melilite peaks and smaller calcite and ferrite peaks. The Si-O-Si bonds at 924 cm^{-1} and 478 cm^{-1} are visible in the FTIR spectra (Figure 41).

The XRD analysis of SHA (Figure 40) showed strong peaks of arcanite (A), sylvite (S), calcite (C), chamosite (CH) and magnesium oxide (M), and less pronounced peaks of quartz (Q), lime (L) and hematite (H).

The presence of arcanite can be confirmed by high peaks in the FTIR spectra of SHA (Figure 41) at the wavelengths 1110 cm^{-1} and 617 cm^{-1} [152]. The absorption bands at 1401 cm^{-1} and 881 cm^{-1} represent C-O symmetric stretching and out-of-plane bending vibrations, respectively.

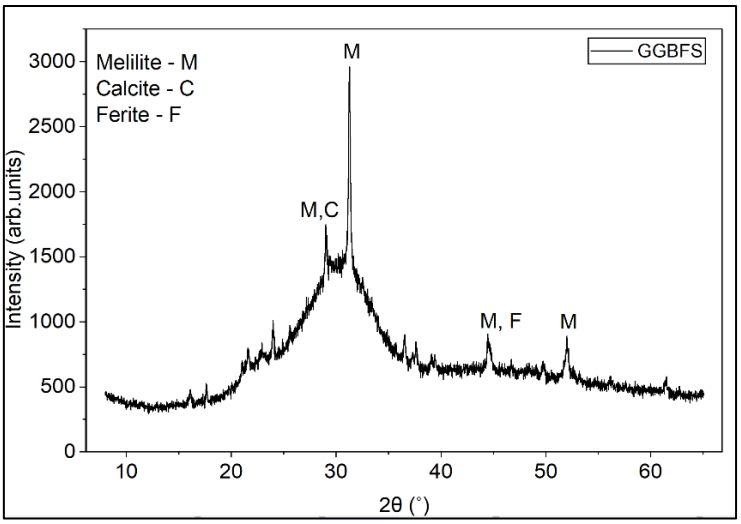

Figure 39. XRD pattern of GGBFS

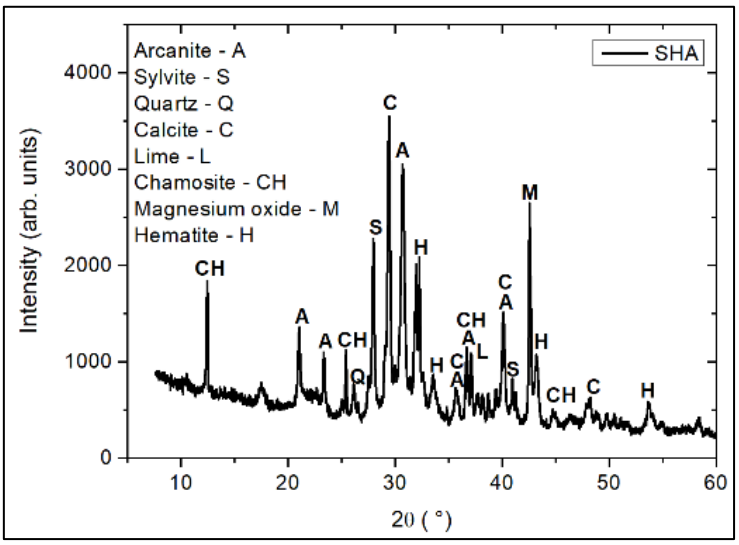

Figure 40. XRD pattern of SHA

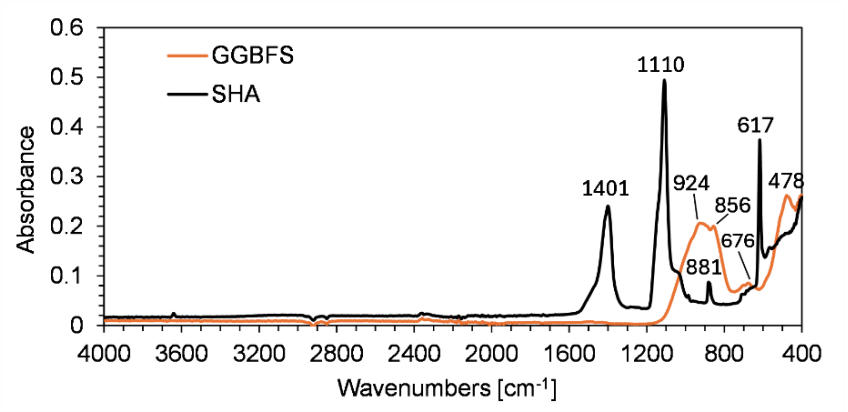

Figure 41. FTIR spectra of GGBFS and SHA

Absolute peak intensities and integrated peak areas at the main absorbance bands of the GGBFS and SHA FTIR spectra are presented in Table 11.

Table 11. Absolute peak intensities and integrated peak areas at the main absorbance bands of the GGBFS and SHA FTIR spectra

	Wavelength [cm^{-1}]	**924**	**856**	**676**	**478**
GGBFS	Absolute peak intensity [a.u.]	0.206	0.200	0.085	0.262
	Integrated peak area [a.u.]	17.750	5.158	1.653	0.704
	Wavelength [cm^{-1}]	**1401**	**1110**	**881**	**617**
SHA	Absolute peak intensity [a.u.]	0.240	0.494	0.087	0.371
	Integrated peak area [a.u.]	15.920	21.750	0.407	6.333

The results of real density and specific surface area are shown in Table 12.

Table 12. Real density and specific surface area of GGBFS and SHA

Material	**Real density [kg/m^3]**	**Specific surface area [m^2/kg]**
GGBFS	2831.0	517.8
SHA	2200.0	610.0

Table 13. Particle size percentiles D10, D50 and D90 for GGBFS and SHA

Material	Particle size percentiles [µm]		
	D10	D50	D90
GGBFS	1.02	5.50	51.33
SHA	1.06	10.50	110.58

The results of the PSD of GGBFS and SHA are presented in Figure 42. Based on the percentile particle sizes (D10, D50, D90), the two materials show clear differences in fineness and particle size spread. GGBFS exhibits significantly finer particles, with D10 = 1.02 µm and D50 = 5.50 µm. Therefore, the median particle size of SHA is twice that of GGBFS. SHA has a much broader particle size distribution (D90 = 110.58 µm vs. D51 = 33.33 µm), indicating it contains a larger fraction of coarse particles.

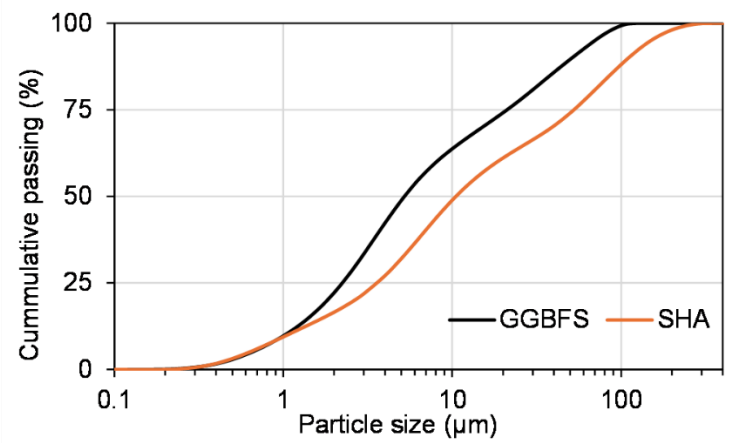

Figure 42. Particle size distribution of GGBFS and SHA

The results on the solubility of SHA, presented as mass loss after dissolution in water, are given in Table 14. After 5 minutes of immersion in water at ambient temperature, the mass loss was 16%. Extending the immersion duration to 2 hours at 65°C increased the mass loss to 42.5%.

Table 14. Mass loss of SHA after dissolution in water under different conditions

Dissolution conditions	5 minutes, TA	2 hours, T65
Mass loss [%]	16%	42.5%

4.1.2 Discussion

The XRF analysis of SHA showed a high potassium content of 38% by mass. Published research on the activation of slag with sunflower-originated ashes reported a potassium content of 36.67% [145], 21.37% [148], and the highest of 45.1%, 49.8% and 61.34% [152]. The XRD pattern and FTIR spectra showed that SHA is dominantly in the form of arcanite, a moderately soluble salt. The presence of CaO corresponds with the formation of calcite, which has low solubility in water. The MgO content of 10.46% could be beneficial for the durability properties of AAMs.

The presence of chlorine is typical for biomass ashes [152]. Therefore, its content should be taken into account when designing AAMs activated with the SHA to be within the prescribed limit (total Cl- content < 0.4 by mass of cement/binder).

The PSD results show that GGBFS has a finer, more uniform particle size distribution (D50 = 5.5 μm), which provides a higher specific surface area favourable for early-age reactivity. SHA exhibits a significantly broader distribution with a larger median particle size (D50 = 10.5 μm) and D90 exceeding 100 μm. The coarser fraction in SHA may reduce its dissolution rate. However, when blended, the contrasting PSDs of SHA and GGBFS could complement each other, with the finer GGBFS particles filling voids between coarser SHA particles, potentially improving overall packing density.

The dissolution results indicate that SHA releases its soluble components gradually, with only 16% of mass dissolving within 5 minutes at ambient temperature. It can be concluded that when SHA is added directly during mixing - where the effective contact time with water is limited to the mixing duration - a significant portion of SHA remains undissolved at the time of casting. At 65°C, the mass loss more than doubles to 42.5%, demonstrating that elevated temperature significantly accelerates SHA dissolution.

4.1.3 Conclusions

Based on the analysis, the following conclusions on the characteristics of component materials can be drawn:

- The main oxides detected in the analysed materials are:
  - GGBFS: SiO_2, (38.69%), CaO (37.19%), and a relatively high content of MgO (10.52); it is a neutral-to-basic slag (Kb=0.99).
  - SHA: K_2O (38%), CaO (14.29%), SO_3 (13.53%), and MgO (10.46%).

- The chemical composition of SHA is suitable for alkali-activation.
- Potassium oxide is dominantly in the form of arcanite (K_2SO_3), according to the XRD pattern. Other significant peaks present calcite, sylvite, chamosite, and MgO.
- The presence of arcanite was confirmed by absorption peaks 1110 cm^{-1} and 617 cm^{-1} and of calcite1401 cm^{-1} and 881 cm^{-1} in FTIR spectra.
- SHA particles have an irregular shape and rough surface and show no signs of porosity.
- GGBFS is significantly finer and more uniformly graded than SHA, while SHA shows a coarser and much broader particle size distribution.
- The solubility of SHA in water increases by more than double with increasing the dissolution duration and temperature of the water.

Material characterisation confirmed that SHA has satisfactory chemical and physical properties to be used as an alternative potassium-rich activator in AAMs.

4.2 Phase 2 - Optimisation of the reference mix with reduced activator content

The objective of Phase 2 was to design AAC mixes with reduced activator content and satisfactory workability and compressive strength. The w/b ratio, alkali content up to 5%, and Ms up to 1.14 were varied across 10 mix designs. Three mixes with optimal performance were further tested for durability properties. The best-performing mix was chosen as the reference mix for Phase 4.

4.2.1 Results

4.2.1.1 Critical parameters for workability and compressive strength of alkali-activated concretes with reduced activator content

The measured slump values and mix design parameters of mixes R1-R10 are presented in Figure 43.

The results varied significantly, ranging from 27 mm (mix R2) to 212 mm (mix R10), within a relatively narrow range of w/b ratios (w/b = 0.42-0.47). The mixes may be grouped into four workability classes based on their slump values, according to SRPS EN 206 [172]. Mixes R2 and R3 had the lowest slump values (27 mm and 30 mm, respectively). Mixes R4, R5, R6, and R7 fell within the S2-S3 range (50-78 mm), representing stiff-to-plastic consistency. Mixes R1

and R8 attained slump class S3 (130 mm and 120 mm, respectively), while mixes R9 and R10 achieved the highest workability, with R9 at 157 mm (S4) and R10 at 212 mm (S4).

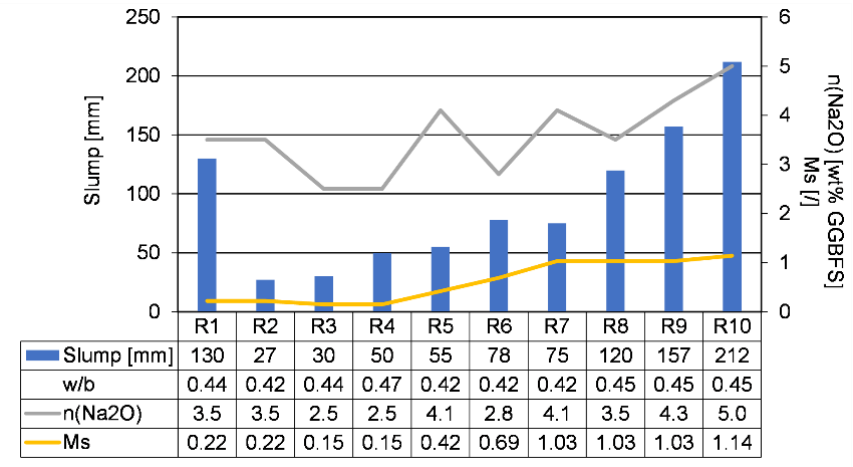

	R1	R2	R3	R4	R5	R6	R7	R8	R9	R10
Slump [mm]	130	27	30	50	55	78	75	120	157	212
w/b	0.44	0.42	0.44	0.47	0.42	0.42	0.42	0.45	0.45	0.45
n(Na2O)	3.5	3.5	2.5	2.5	4.1	2.8	4.1	3.5	4.3	5.0
Ms	0.22	0.22	0.15	0.15	0.42	0.69	1.03	1.03	1.03	1.14

Figure 43. Slump values and mix design parameters of AAC mixes

Mixes R1-R4, characterised by low silicate modulus (Ms ≤ 0.22) and n(Na_2O) ≤ 3.5 wt%, exhibited slump values ranging from 27 to 130 mm. Mixes R2 (w/b = 0.42, slump = 27 mm) and R3 (w/b = 0.44, slump = 30 mm) produced virtually identical and very low slump values despite differing in w/b, n(Na_2O) content (3.5 vs 2.5 wt%), and Ms (0.22 vs 0.15). Mix R4 (w/b = 0.47, n(Na_2O) = 2.5 wt%, Ms = 0.15) recorded a slump of 50 mm, 20 mm higher than R3, despite having the same activator composition. Mix R1 had a significantly higher slump than mix R2 (130mm vs 27 mm), even though they had identical activator parameters (n(Na_2O) = 3.5 wt%, Ms = 0.22).

Mixes R2, R5, R6, and R7 had w/b ratio of 0.42, Ms ranging from 0.22 to 1.03 and n(Na_2O) from 2.8 to 4.1 wt%. Within this group, slump values were 27 mm (R2), 55 mm (R5), 78 mm (R6), and 75 mm (R7). Mix R6, with the lowest n(Na_2O) content in the group (2.8 wt%) but the second highest Ms (0.69), recorded the highest slump (78 mm). Mix R7, with the highest Ms (1.03) and equal n(Na_2O) to R5 (4.1 wt%), recorded a slump of 75 mm - marginally lower than R6 despite both higher Ms and higher n(Na_2O) content.

Mixes R8, R9, and R10, all designed at w/b = 0.45 and Ms ≥ 1.03, recorded the three highest slump values in the experimental programme: 120 mm (R8), 157 mm (R9), and 212 mm (R10). Within this group, slump increased consistently with increasing Na_2O content at approximately constant Ms and w/b. Mix R8 and mix R7 share the same Ms (1.03) but differ in w/b (0.45 vs 0.42) and n(Na_2O) content (3.5 vs 4.1 wt%); R8 recorded a slump 45 mm higher than R7.

The compressive strength results at 2, 7 and 28 days are shown in Figure 44.

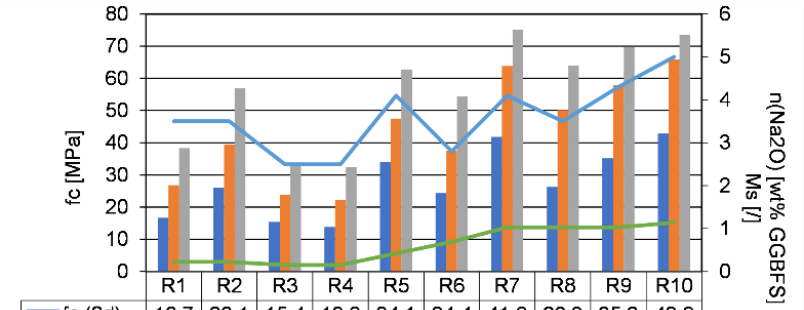

	R1	R2	R3	R4	R5	R6	R7	R8	R9	R10
fc (2d)	16.7	26.1	15.4	13.8	34.1	24.4	41.8	26.3	35.2	42.9
fc (7d)	26.8	39.4	23.9	22.2	47.5	37.5	63.8	50.1	58	65.9
fc (28d)	38.3	56.9	33.3	32.5	62.8	54.4	75.1	64	69.7	73.5
w/b	0.44	0.42	0.44	0.47	0.42	0.42	0.42	0.45	0.45	0.45
n(Na2O)	3.5	3.5	2.5	2.5	4.1	2.8	4.1	3.5	4.3	5.0
Ms	0.22	0.22	0.15	0.15	0.42	0.69	1.03	1.03	1.03	1.14

Figure 44. Results of 2, 7 and 28 days compressive strength test of AAC mixes

When activator content was held constant, lower w/b produced higher compressive strength at all ages: R2 (w/b = 0.42) recorded 28-day strength of 56.9 MPa compared to 38.3 MPa for R1 (w/b = 0.44), and R3 (w/b = 0.44) outperformed R4 (w/b = 0.47) at all ages (33.3 vs 32.5 MPa at 28 days).

Within the w/b = 0.42 group, Na_2O content was the primary determinant of strength at Ms < 1.0. Mix R5 (Na_2O = 4.1 wt%, Ms = 0.42) recorded higher strength than R6 (Na_2O = 2.8 wt%, Ms = 0.69) at all ages despite R6 having a higher Ms, with 7-day strengths of 47.5 and 37.5 MPa respectively and 28-day strengths of 62.8 and 54.4 MPa respectively.

Raising Ms from 0.42 to 1.03 at constant w/b = 0.42 and Na_2O = 4.1 wt% (R5 vs R7) increased 28-day strength from 62.8 to 75.1 MPa and 7-day strength from 47.5 to 63.8 MPa. Mix R7 recorded the highest 28-day strength in the dataset.

Mixes R8–R10 (w/b = 0.45, Ms = 1.03 - 1.14) achieved higher 7-day and 28-day strengths than R5 and R6 (w/b = 0.42, Ms < 1.0), despite the higher w/b. Within R8–R10, increasing Na_2O from 3.5 to 5.0 wt% raised 28-day strength from 64.0 to 73.5 MPa.

The gain in compressive strength between 2 and 7 days was 22–23 MPa for high-Ms mixes (R7–R10, Ms ≥ 1.03), compared to 8–13 MPa for lower-Ms mixes (R1–R6).

Based on the analysis of the results, three selected AAC mixes for testing durability and porosity are R2, R5, and R7.

4.2.1.2 Durability and porosity of selected mixes

Porosity

The results of MIP analysis are summarised in Table 15. Cumulative intrusion and differential curves are presented in Figure 45 and Figure 46, respectively. The pore size classification [173] is also presented in Figure 46.

Table 15. Porosity, critical and threshold pore diameter of mixes R2, R5 and R7

Mix	Porosity [%]	$d_{crit,1}$ [µm]	$d_{crit,2}$ [µm]	d_{tr} [µm]
R2	8.8	0.017	-	0.03
R5	10.6	0.006	0.011	0.02
R7	6.1	0.006	-	0.01

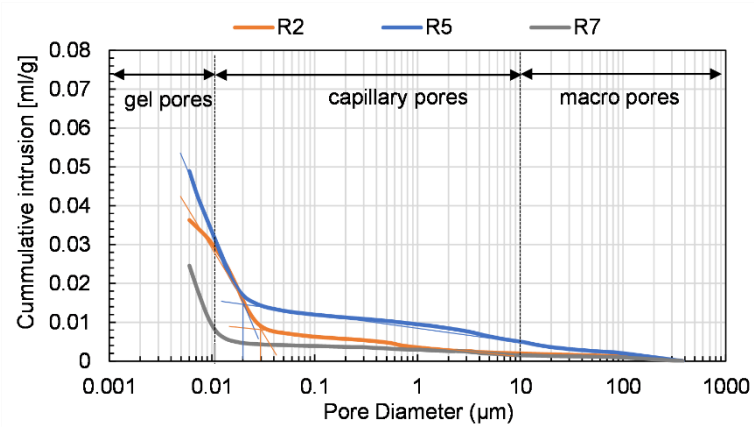

Figure 45. Cumulative intrusion curves of mixes R2, R5 and R7

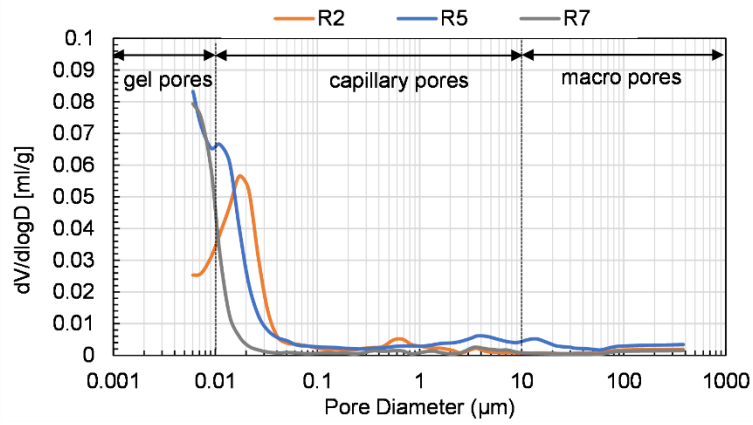

Figure 46. Differential curves of mixes R2, R5 and R7

Mix R5 had the highest porosity (10.6%), followed by R2 (8.8%) and R7 (6.1%). Differential curves showed that mix R2 exhibited a unimodal distribution with a single broad peak at a critical pore diameter of 0.017 µm and a threshold diameter of 0.03 µm. Mix R5 showed a bimodal distribution with a primary peak at 0.006 µm and a secondary peak at 0.011 µm, and

a threshold diameter of 0.02 μm. Mix R7 had a unimodal distribution with the sharpest and narrowest peak at 0.006 μm and the smallest threshold diameter of 0.01 μm. The cumulative intrusion curves confirm that R7 has the lowest total pore volume, while R5 has the highest.

Water penetration under pressure

The results of water penetration under pressure are presented graphically in Figure 47. According to the Croatian national requirements [174], mixes R2 and R5 attained resistance classes VDP2 and VDP3, respectively, while mix R7 had significantly higher water penetration front than the maximum value of class VDP1 (up to 50 mm).

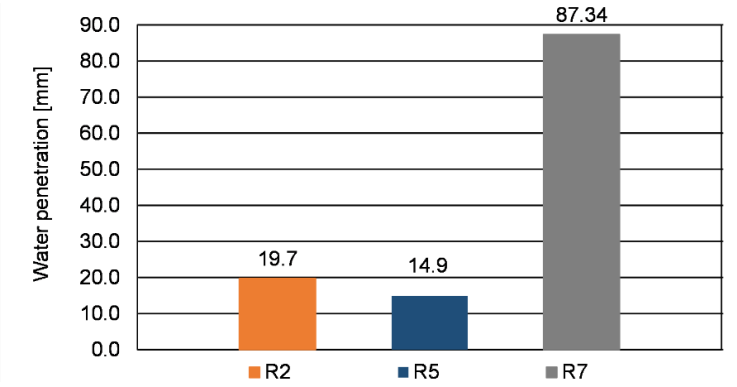

Figure 47. Graphical presentation of depth of water penetration under pressure: concrete mixes R2, R5, and R7

Carbonation resistance

Carbonation depth (d_k) after 7 and 28 days of exposure to 3% CO_2, as well as carbonation rates (K_{AC}) and coefficients of determination (R^2) of concrete mixes, are presented in Table 16 and in Figure 48.

Table 16. Carbonation resistance of concrete mixes R2, R5 and R7: carbonation depths after 7 and 28 days of exposure, carbonation rates and coefficients of determination

Mix	d_k [mm]		K_{AC} [mm/days$^{0.5}$]	R^2
	7d	28d		
R2	9.1	19.1	3.6156	0.9991
R5	6.7	17.0	3.2053	0.9861
R7	8.1	19.4	3.6583	0.9914

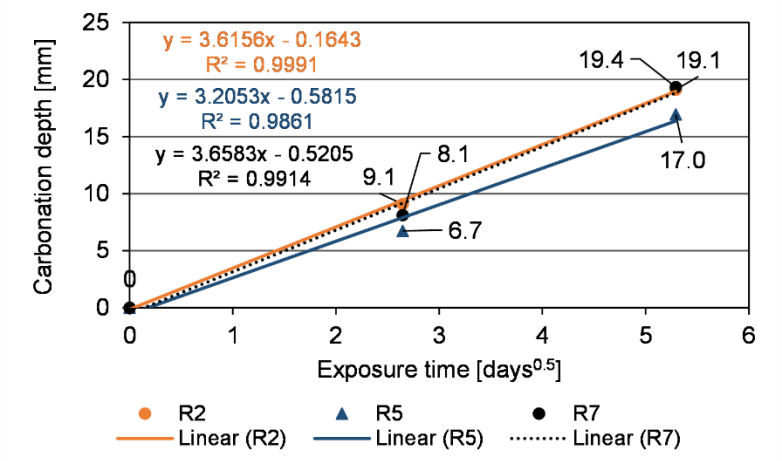

Figure 48. Carbonation depth versus the square root of exposure time

After 7 days of accelerated carbonation exposure, mix R2 exhibited the highest carbonation depth (9.1 mm), followed by mix R7 (8.1 mm) and mix R5 (6.7 mm). After 28 days of exposure, R5 had the lowest carbonation depth, while the carbonation depths of R2 and R7 were the same. Mix R7 had a similar carbonation rate to mix R2. All mixes showed a strong linear correlation between carbonation depth and the square root of exposure time (R^2>0.98 for all mixes).

Resistance to chloride penetration

Chloride migration coefficients after 28 days of curing for the selected concrete mixes are presented in Figure 49.

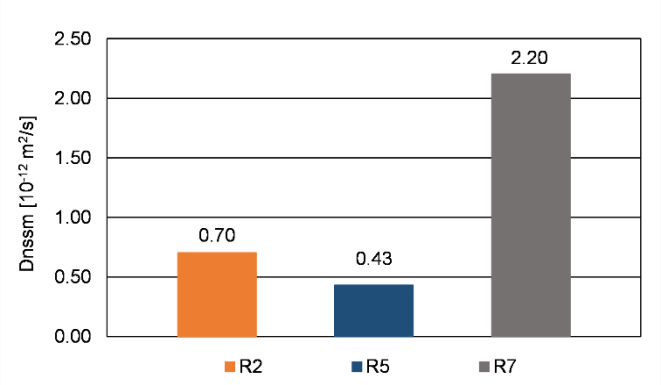

Figure 49. Migration coefficients for selected AAC mixes after 28 days of curing

An increase in alkali content and silica modulus in the mix R2 compared to R1 resulted in the reduction of the migration coefficient. However, a further increase in sodium silicate content had an adverse effect.

4.2.2 Discussion

4.2.2.1 Critical parameters for workability and compressive strength of alkali-activated concretes with reduced activator content

Workability

The slump results indicate that w/b ratio, n(Na_2O) content, and silicate modulus Ms all influence AAS concrete workability, but their effects are interdependent and conditional on threshold values of the other parameters, consistent with findings reported in the literature [75,83].

When Ms and n(Na_2O) are low (R2-R4, Ms ≤ 0.22, n(Na_2O) ≤ 3.5 wt%), slump values are uniformly low regardless of w/b variations in the range 0.42-0.47, suggesting that at low activator content, the free water available is insufficient to overcome the inherent stiffness of the paste. Within this low-Ms group, mixes R3 and R4 share identical activator composition but differ in w/b (0.44 and 0.47, respectively), recording slump values of 30 and 50 mm, confirming that w/b exerts a positive effect on workability when activator composition is held constant, in a manner consistent with the reported behaviour of the w/b ratio in hydroxide-dominated AAS systems [14]. Mixes R1 and R2 share identical n(Na_2O) = 3.5 wt% and Ms = 0.22 but differ in w/b (0.44 and 0.42, respectively), recording slump values of 130 and 27 mm. This is consistent with the same w/b effect, though the magnitude of the difference is disproportionate relative to the R3/R4 comparison and likely reflects additional factors, including possible batch variability or differences in the effective free water contribution of the activator solutions. Within the constant w/b = 0.42 group, increasing Ms from 0.22 (R2, 27 mm) to 0.69 (R6, 78 mm) produced a substantial slump increase, while a further increase to Ms = 1.03 (R7, 75 mm) produced no additional gain despite higher n(Na_2O), indicating that the workability benefit of increasing Ms reaches a practical ceiling at w/b = 0.42. At the higher w/b of 0.45 (R8-R10, Ms ≥ 1.03), n(Na_2O) content above 4 wt% had a greater impact on slump than the w/b variations within this study, similarly to the findings of Bondar et al. [75].

Compressive strength

The compressive strength results follow the same conditional parameter hierarchy identified for workability. Lowering the w/b ratio resulted in higher compressive strengths, consistent with its role in controlling matrix porosity and density [14]. However, activator composition dominates over w/b when parameters vary simultaneously, as demonstrated by R8-R10 (w/b = 0.45) outperforming R5 and R6 (w/b = 0.42) in compressive strength despite the higher water content.

Below Ms = 1.0, Na_2O content has the dominant effect on compressive strength. The higher strength of R5 relative to R6 - despite R6 having higher Ms - confirms that Na_2O content governs the degree of slag reaction and consequently the volume of C-A-S-H gel formed when the silicate modulus is insufficient to compensate for lower alkali dose [75,56]. For Na_2O content of 4% or higher, this effect becomes dominant over the w/b ratio, as demonstrated by the 7-day strengths of mixes R5, R7, R8, R9 and R10.

At Ms ≥ 1.0, the silicate modulus becomes the decisive strength variable. The R5/R7 comparison provides the clearest evidence for this: w/b and Na_2O are identical in both mixes, and Ms alone increases from 0.42 to 1.03, producing a 28-day strength gain of 12.3 MPa. This is consistent with the reported role of dissolved silicate in promoting a denser and more cross-linked C-A-S-H gel structure at higher silicate modulus values [75].

The higher absolute strength gain between 2 and 7 days in high-Ms mixes R7-R10 (22-23 MPa) compared to lower-Ms mixes (8-13 MPa) reflects more active reaction in this period, with R7 and R10 reaching 85% and 90% of their 28-day strength by day 7 respectively. The Na_2O content modulates this behaviour: at Ms = 1.03, reducing Na_2O from 4.1 wt% (R7, 56% of 28-day strength at 2 days) to 3.5 wt% (R8, 41% of 28-day strength at 2 days) produces the slowest early-age development in the dataset, confirming that insufficient Na_2O limits the initial reaction rate even at high Ms. Continued strength development beyond 28 days is expected for high-Ms mixes, with 28-day strength typically representing 80–90% of 90-day strength in silicate-activated slag systems [75].

The results indicated that slump class S2 is attainable at substantially lower activator content, representing a balance between workability and activator economy. On this basis, mixes R2, R5, and R7 were selected for durability testing, spanning the range from hydroxide-dominated to moderate silicate activation. From a compressive strength perspective, the selected mixes span a representative range: R2 achieved 56.9 MPa at 28 days under hydroxide-dominated activation, R5 achieved 62.8 MPa at moderate activator content, and R7 achieved the highest 28-day strength in the experimental programme (75.1 MPa) at Ms = 1.03, providing a basis for assessing the relationship between activator composition, strength, and durability across three distinct activation regimes.

4.2.2.2 Durability and porosity of selected mixes

Porosity, water permeability under pressure and chloride penetration

The MIP results reveal that increasing the silicate modulus progressively refines the critical pore diameter (from 0.017 µm in R2 to 0.006 µm in R5 and R7) and reduces the threshold diameter (from 0.03 to 0.02 to 0.01 µm), reflecting the formation of a denser C-A-S-H gel with higher Ms and alkali content.

The durability results reveal that despite having the finest and most refined pore structure, mix R7 exhibited by far the worst performance in both water penetration and chloride migration. This contradicts the conventional expectation that pore refinement improves impermeability. This behaviour could be explained by microcracking induced by the high silicate modulus activation. AAS systems are prone to microcracking, depending on the drying conditions [87,14] The microcracks provide preferential pathways for both water and chloride ion transport, explaining the dramatically higher penetration and migration values.

Carbonation resistance

The highest carbonation depth of mix R2 is consistent with its lower alkali content (n=3.5%) and lower silicate modulus (Ms=0.22) compared to mixes R5 (n=4.1%, Ms=0.42) and R7 (n=4.1%, Ms=1.0), both of which are known to improve carbonation resistance through higher pore solution alkalinity and denser matrix formation [65,109,110]. An increase in Ms is expected to provide the best performance in terms of carbonation resistance as it leads to a less porous matrix structure [110]. However, the comparison between R5 and R7 reveals that increasing Ms to 1.0 does not necessarily improve carbonation resistance when alkali dosage is similar. Despite having the highest Ms and comparable alkali content, R7 was more susceptible to carbonation than R5, suggesting that alkali dosage has a more dominant positive influence on carbonation resistance than silicate modulus within this range. This is consistent with findings by Shi et al. [65], who reported that for Ms=1, alkali dosage significantly influences carbonation depth, while this influence diminishes at higher moduli (Ms=1.5-2.0), where mixes with 6% and 8% alkali dosage exhibited nearly identical carbonation depths. The present results indicate that the beneficial effect of increased alkali content on carbonation resistance is most pronounced for Ms up to 1.0.

Based on the mechanical and durability properties, mix R5 was selected as a reference mix for Phase 4, and is denoted as R in the following text.

4.2.3 Conclusions

The experimental research presented in this phase aimed to investigate the effects of critical parameters on achieving the targeted slump and compressive strength, and to identify an optimal mix design with reduced activator content for reference AACs for further experimental testing. Analysing the results obtained by varying w/b ratio, alkali content and Ms, the following can be concluded:

- At low activator content (Ms ≤ 0.22, n(Na_2O) ≤ 3.5 wt%), w/b variations in the range 0.42-0.47 produced modest slump changes of 27-50 mm;
- Increasing Ms from 0.22 to 0.69 at constant w/b = 0.42 produced a substantial slump increase (27 to 78 mm), demonstrating that Ms is the most influential single variable within this w/b range. At higher w/b (0.45), the positive effect of Ms continues beyond Ms = 1.0, suggesting that the optimal Ms for workability is conditioned by the free water content of the mix;
- The sensitivity of workability to w/b increases with the silicate modulus of the activator, indicating that free water content becomes a more effective workability lever as silicate content increases;
- n(Na_2O) content above approximately 4 wt% has a greater marginal impact on slump than the w/b variations studied, but only when Ms ≥ 1.0; at low Ms the Na_2O effect on workability is limited within the range investigated;
- Slump class S2 is achievable at relatively low activator content (n(Na_2O) = 4.1 wt%, Ms = 0.42, w/b = 0.42, mix R5, slump = 55 mm), representing a balance between workability and activator economy relevant to the objectives of this research;
- When activator composition is held constant, lower w/b ratio produces higher compressive strength at all ages, consistent with its role in controlling matrix density and porosity;
- For mixes with similar w/b and Ms, higher Na_2O content produces higher compressive strength at all ages, attributable to a higher degree of slag reaction and greater C-A-S-H gel formation;
- Below Ms = 1.0, Na_2O content is the dominant strength variable;
- Increasing Ms from 0.42 to 1.03 at constant w/b and Na_2O (R5 vs R7) produced a 28-day strength increase from 62.8 to 75.1 MPa;

- igh-Ms mixes (Ms ≥ 1.03) exhibit a concentrated strength gain between 2 and 7 days, reaching 83–90% of their 28-day strength by day 7.
- A 7-day compressive strength above 47 MPa is achievable at moderate activator content (Na_2O = 4.1 wt%, Ms = 0.42, w/b = 0.42).

The results of porosity and durability testing showed that the mix R5 had an optimal performance, with alkali content and silica modulus are 4 wt% GGBFS and 0.42, respectively. The reduced activator content can result in satisfactory mechanical and durability properties of AAC. The mix R5 exhibited the lowest water permeability under pressure, migration coefficient and carbonation rate. It was chosen as a reference mix for the Phase 4 and denoted as the mix R.

4.3 Phase 3 - Development and optimisation of the sunflower husk ash-activated binder

The objective of Phase 3 was to develop a SHA-activated binder and optimise its workability and compressive strength by varying w/b ratio, SHA content, curing regime and mixing technology. Characterisation of materials in Phase 1 partially confirmed hypothesis 1 by analysing the chemical and physical properties of the SHA. Phase 3 aimed to confirm it and test hypothesis 2 through analysis of the mortar mixes.

H1: *“The sunflower husk ash can be used as an alternative activator for synthesising slag-based alkali-activated materials.”*

H2: *“Utilisation of only the alternative activator in AAMs will not significantly reduce the mechanical and durability properties of slag-based alkali-activated materials. “*

4.3.1 Results

4.3.1.1 Variation of water-to-binder ratio to optimise workability and compressive strength

To optimise the workability and compressive strength, w/b ratios of 0.42, 0.45, and 0.5 were varied across the mixes with SHA content of 15, 25, and 35 wt% GGBFS. An example of mortar mixes after the flow table test is presented in Figure 50. The results of the slump flow test and 7-day compressive strengths of mortar mixes with different SHA content and w/b ratios are presented in Figure 51 and Figure 52, respectively.

Figure 50. Mortar mixes with w/b=0.45 after the flow table test

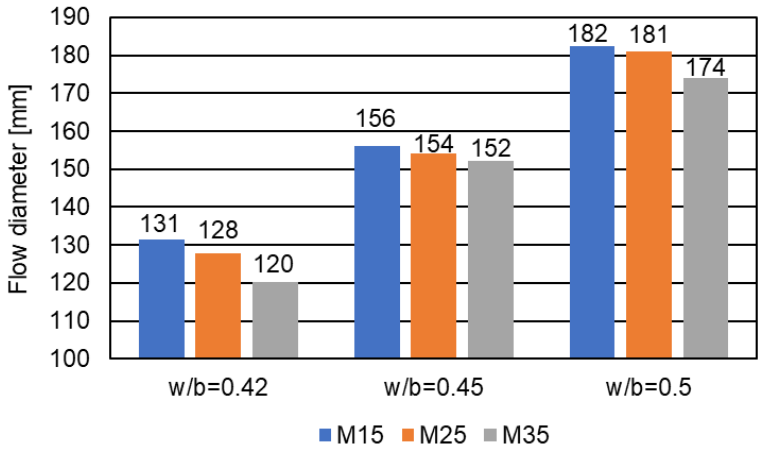

Figure 51. Slump flow of mortar mixes with different SHA content and w/b ratios

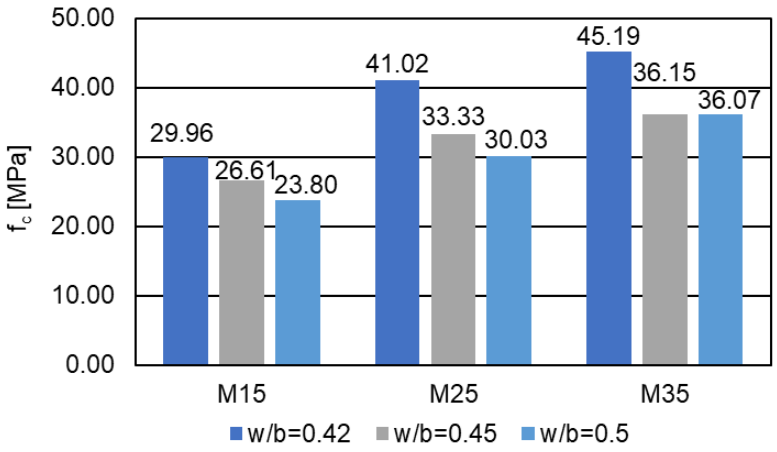

Figure 52. The 7-day compressive strengths of mortar mixes with different SHA content and w/b ratios

Higher w/b ratios resulted in approximately 15% increases in slump flow for each SHA content. The highest difference of 12% was observed for the mix SHA35 when w/b ratio was increased from 0.42 to 0.45. The lowest flow diameter was 120 mm, for the w/b=0.42 and SHA content of 35%. The highest flow diameter of 182 mm was observed for the mix with the lowest SHA content (15%) and w/b=0.5.

Compressive strength increased gradually with increasing SHA and decreasing w/b ratio. The highest attained compressive strength was 45.19 MPa, for the mix M35 and w/b=0.42. Mix SHA15 with w/b=0.5 had the lowest compressive strength of 23.8 MPa.

Based on the workability and compressive strength, mix M25 was chosen for further testing.

To assess the effect of the crushed aggregate that will be used in concrete, mortar mixes with chosen SHA content were designed to optimise workability, taking into account the high content of fine particles in aggregate. The summarised results are presented in Figure 53.

Due to the decrease in slump flow after the addition of crushed aggregate, the chosen w/b ratio was 0.5, i.e., mix SHA-S/0.5, with 7-day compressive strength of 36.56 MPa.

The results on slump flow and 7-day compressive strength are given in Figure 53. Mixes activated with SHA are denoted as SHA25 (25 wt% GGBFS), while the mortars activated with 25 wt% GGBFS and sodium silicate are denoted as SHA-S. The Ms=0.42 (as for the reference concrete mix selected in Phase 2) was calculated under the assumption that the entire 16% of dissolved SHA is alkali.

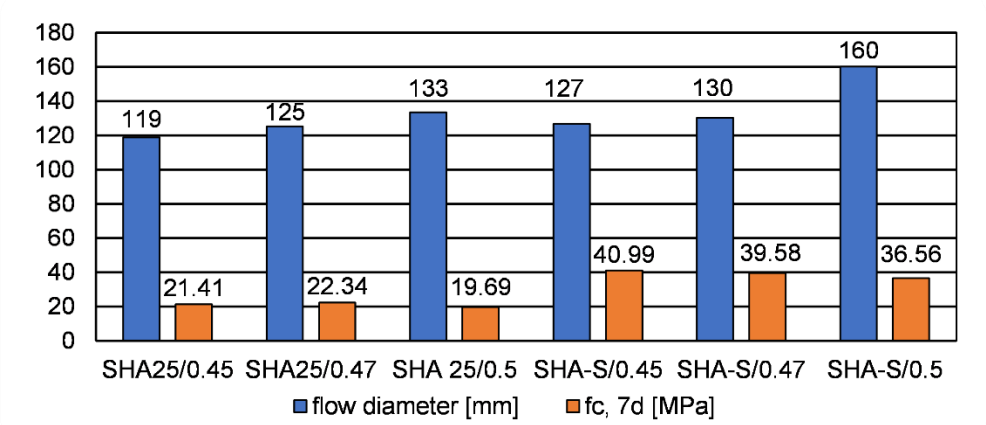

Figure 53. Flow diameter and 7-day compressive strength of trial mortar mixes activated with SHA and SHA and sodium silicate

Mixes activated only with SHA exhibited stiff consistency. The addition of sodium silicate to achieve an Ms of 0.42 increased the slump flow and compressive strength at all w/b ratios. Sodium silicate increased the compressive strength significantly, even for w/b=0.5 (from 19.69 MPa to 36.56 MPa).

4.3.1.2 Variation of curing regime to optimise compressive strength

To assess the effects of ambient (TA) and elevated-temperature (T65) curing, mortar mixes with selected w/b=0.45 and varied SHA content were tested for 7- and 28-day compressive strengths. Examples of hardened samples before and after testing are presented in Figure 54 and Figure 55, respectively.

Figure 54. Example of hardened samples before compressive-strength testing

Figure 55. Example of a sample cross-section after testing of the compressive strength

The results on compressive strength of samples under both curing regimes after 7 days of curing are presented in

Figure 56 and after 28 days in Figure 57.

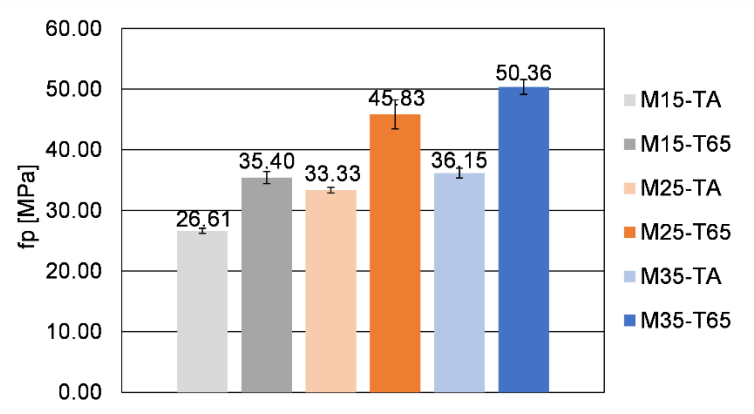

Figure 56. Compressive strength of mortar mixes with different SHA content cured at TA and T65 curing regime, tested at 7 days

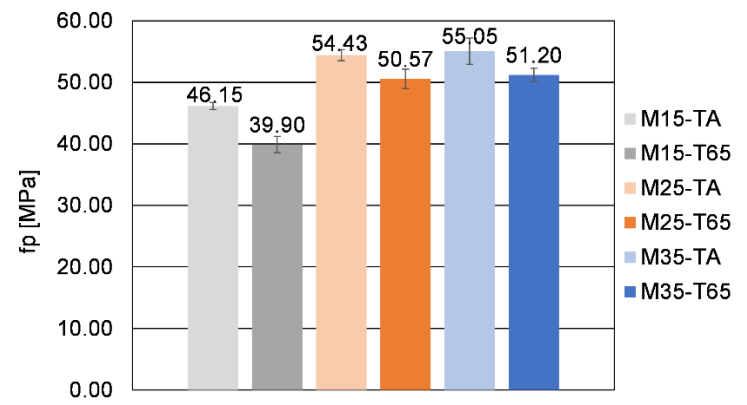

Figure 57. Compressive strength of mortar mixes with different SHA content cured at TA and T65 curing regime, tested at 28 days

The increase in SHA content has led to an increase in compressive strength at both 7 and 28 days. Compared to the TA regime, curing at elevated temperature altered the 7-day compressive strength of mixes M15, M25, and M35, reaching 35.4 MPa, 45.83 MPa, and 50.36 MPa, respectively (for 33%, 37.5%, and 39%). Furthermore, after 7 days, mortars M15, M25, and M35 achieved 89%, 91%, and 98% of their respective 28-day compressive strengths.

Higher compressive strength at 28 days was obtained for the TA than the T65 curing regime (Figure 57). The highest difference of 15.7% was observed for the mix M15 (39.9 MPa vs 46.15 MPa), while mixes M25 and M35 showed a similar increase of approximately 7.5%. For these two mixes, compressive strength at both TA and T65 was practically the same after 28 days (50.57 MPa vs 51.20 MPa and 54.43 MPa vs 55.05 MPa).

The differences in compressive strength were further investigated through phase assemblage analysis using FTIR and TGA.

The FTIR analysis of pastes with different SHA content after 28 days of curing at the two described regimes is presented in Figure 58. The influence of the curing duration and regime on the FTIR spectra is shown in Figure 59., for the samples with 25% of SHA. The distinct absorbance bands in all tested samples are 3389/3398 cm^{-1}, 1641 cm^{-1}, 1401-1412 cm^{-1}, 1104-1109 cm^{-1}, between 1000 and 800 cm-1, 941/942 cm^{-1}, 615 cm^{-1} and 430/441 cm^{-1}. The band at 871 cm^{-1} is present in the spectra of samples tested at an early age (2 and 7 days).

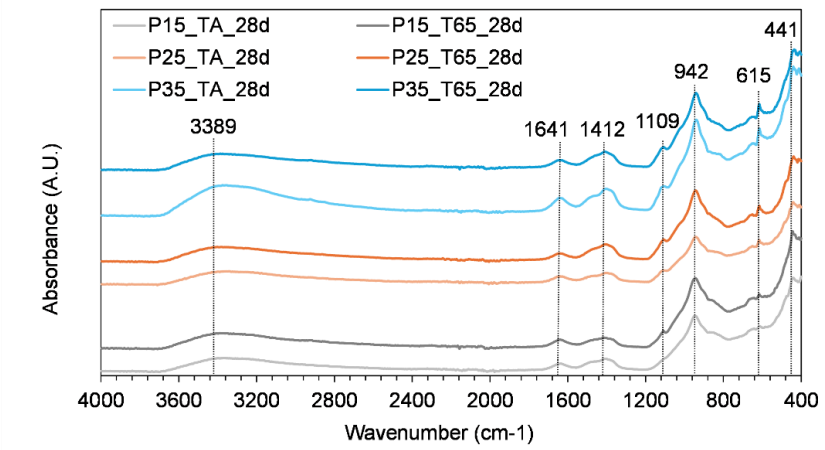

Figure 58. FTIR spectra of paste samples with different SHA content cured at two different regimes, tested at 28 days

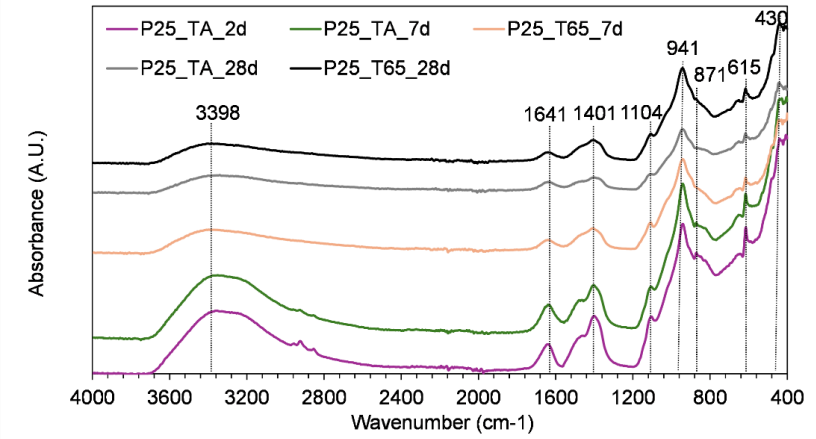

Figure 59. FTIR spectra of paste with 25% of SHA, cured at two different regimes, tested at 2, 7 and 28 days

The absorbance bands at 3389/3398 cm^{-1} and 1641 cm^{-1} correspond to the O-H stretching and bending vibrations, respectively. They can be seen in all tested samples and present weakly bonded water [175].

The wavelengths 1401 cm^{-1} and 1412 cm^{-1} indicate the C-O asymmetric stretching vibration. The absorption band at 871 cm^{-1} corresponds to C-O out-of-plane bending vibrations [149,176]. The peak at 1104/1109 cm^{-1} (Figure 58) represents symmetric stretching vibrations associated with the sulphate group SO_4^{2-} [46], and it increases with the addition of the SHA. The main band at 941 cm^{-1} represents asymmetrical Si-O-Si(Al) stretching vibrations [175,176] and Si-O-M (M-alkali or alkali earth metal) [177]. This absorption band is related to the SiQ^n, where n=2, according to [176], typical for slag-based AAMs. The band represents C-A-S-H and C-S-H. Some research on BFS alkali-activation by CHA and SHA combined FTIR with SEM/EDS analysis, concluding that these gels could also incorporate potassium (C-(K)-A-S-H gels) [149,49]. The addition of SHA resulted in higher peak intensity and integrated peak area

of the main band representing C-A-S-H and C-S-H gels, as presented in Table 17 for the samples P15, P25, P35, cured at T65 regime. Samples cured at T65 curing regime exhibited decreased integrated peak areas, compared to samples cured at TA. The absorption band at 615 cm^{-1} are Al-O and Mg-O bending modes, possibly from hydrotalcite [178]. Peaks in the range 430-441 cm^{-1} are characteristic of flexural vibrations of Si-O-Si [179].

Table 17. Peak intensities and integrated peak areas at the main absorbance band for the samples P15, P25 and P35, cured at TA and T65, tested at 28 days of age

Sample	Absolute peak intensity at 941 cm^{-1} [a.u.]	Integrated peak area [a.u.]
P15_TA	0.164	25.541
P15_T65	0.153	22.41
P25_TA	0.176	25.396
P25_T65	0.175	24.826
P35_TA	0.222	31.951
P35_T65	0.179	25.764

TG curves and differential thermogravimetric (DTG) curves of the tested pastes are presented in Figure 60, Figure 61 and Figure 62. All samples exhibit DTG peaks commonly formed in the alkali-activated slag systems, such as peaks indicating C-S-H, C-A-S-H and hydrotalcite [65], which is in line with FTIR analysis and research on SSA and SHA slurries [145] . The peak between 30°C and 200°C corresponds to the loss of structurally unbound water from the C-S-H. This peak overlaps with the one between 140°C and 240°C, associated with the dehydration of C-A-S-H [180]. In studies on OBA [58,69] and ABA [150] activated slags, these peaks are also attributed to the C-(K)-S-H and C-(K)-A-S-H gels. The formation of hydrotalcite is also confirmed by the peak between 300°C and 400°C [58,69]. However, due to its layered structure, it is possible that it contributes to the peak around 200 °C [56]. The peaks between 440°C and 550°C [181] and 600°C and 700°C [144,180] present decomposition of $CaCO_3$.

The influence of SHA content and curing regimes after 28 days of curing can be seen in Figure 60. Table 18 presents the mass loss percentages for peaks representing main hydration products, C-A-S-H, C-S-H (Peak 1) and hydrotalcite (Peak 2). The intensity of the peaks and mass loss percentage of samples cured at T65 increase with the addition of SHA, suggesting the formation of more hydration products due to the higher alkali content [58,69]. Although the difference in the Peak 1 between the TA and T65 curing regimes for samples P15 and P35 appears small - and the T65 regime even shows slightly sharper peaks - the mass loss results indicate otherwise. Specifically, the TGA analysis shows that the T65-cured samples exhibit

lower mass loss in the region associated with C-A-S-H and C-S-H decomposition, suggesting that less hydration products are formed under the T65 regime. In DSC curves of the sample P25, it is clearly visible that the T65 curing regime resulted in less prominent peaks 1 and 2 than TA, as confirmed by higher mass loss of the samples cured at TA (6.790 and 2.055) compared to those at T65 (5.458 and 1.767). The exception was sample P35, cured at T65; it had a higher Peak 2 than the sample cured at TA. However, this could be the consequence of analysing a very small sample of heterogeneous material.

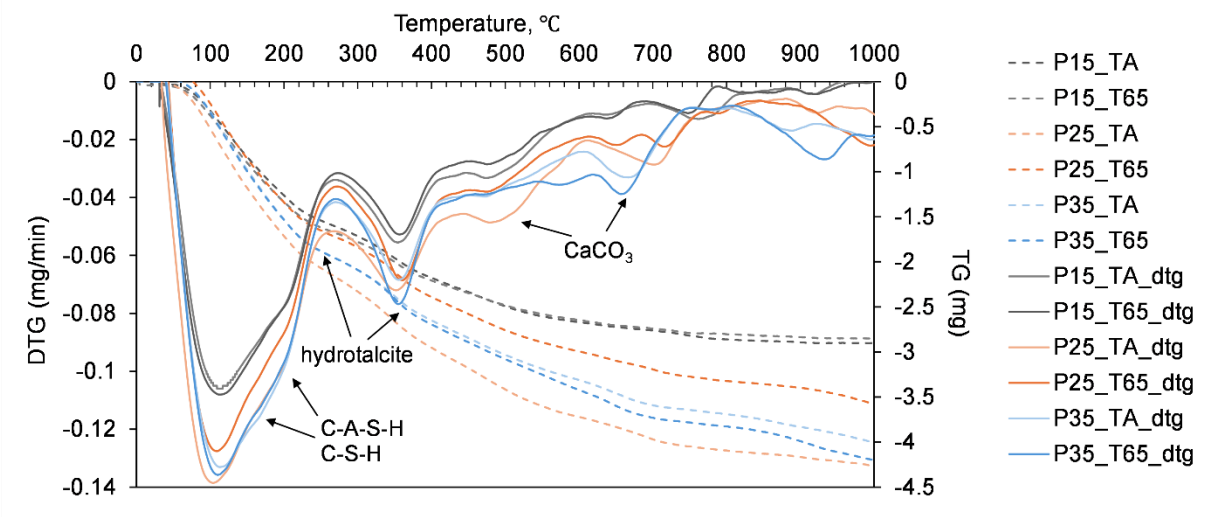

Figure 60. TG and DTG curves of paste samples with different SHA content cured at two different regimes, tested at 28 days

Table 18. Mass loss between 30-240 ˚C and 300-400 ˚C of samples P15, P25 and P35, after 28 days of curing at TA and T65 regimes

	Mass loss [%]					
Sample	P15		P25		P35	
Curing regime	TA	T65	TA	T65	TA	T65
Peak 1 (30-240 ˚C)	4.777	3.386	6.790	5.458	6.145	5.942
Peak 2 (300-400 ˚C)	1.472	0.963	2.055	1.767	1.563	1.851

The influence of curing duration at the TA and T65 curing regimes is presented for the pastes with 25% of SHA, in Figure 61 and Figure 62, respectively. The mass losses after 2 and 7 days of curing at both regimes are presented in Table 19. The longer curing time led to greater mass loss and sharper characteristic peaks, which is also explained by the increase in hydration degree over time [147,58]. Curing at 65˚C altered only the peak formation at 7 days but did not

have a positive effect on gel formation after 28 days of curing, as mentioned in the previous section.

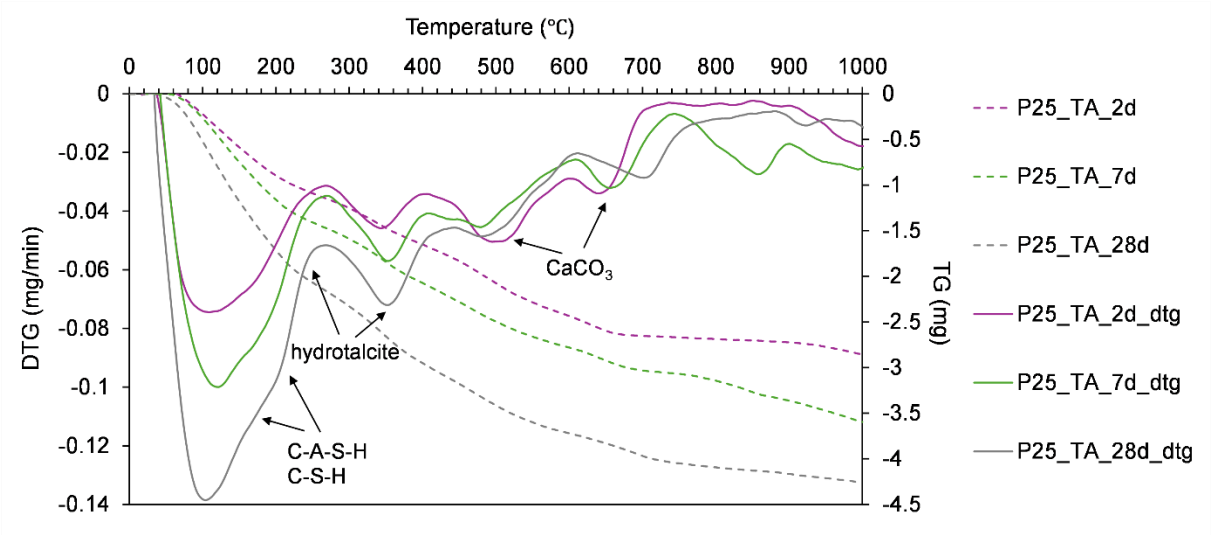

Figure 61. TG and DTG curves of paste with 25% of SHA, cured at TA, tested at 2, 7 and 28 days

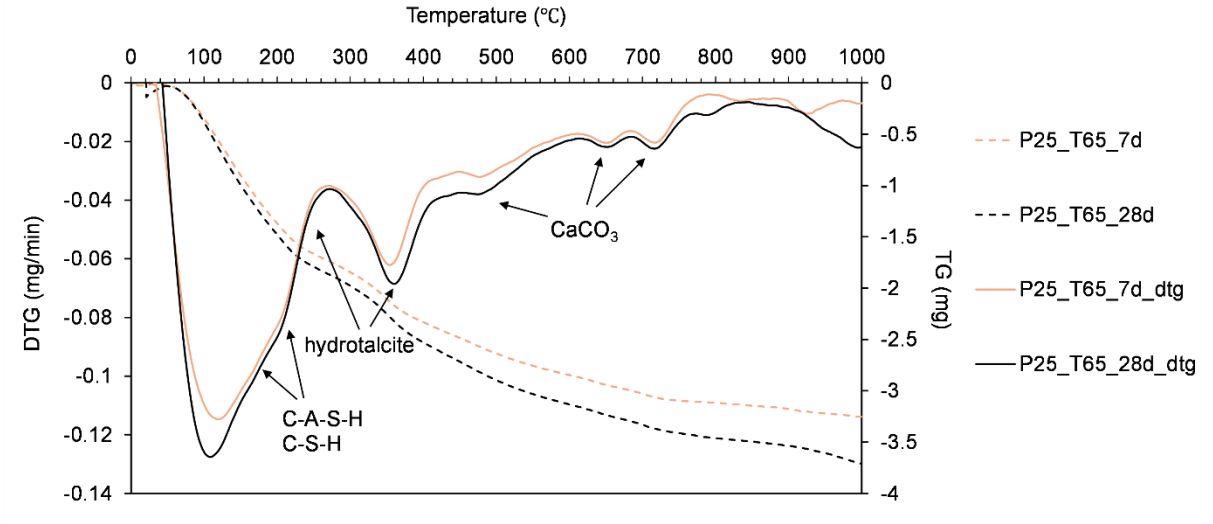

Figure 62. TG and DTG curves of paste with 25% of SHA, cured at T65, tested at 7 and 28 days

Table 19. Mass loss between 30-240 ˚C and 300-400 ˚C of samples P25, after 2 days of curing at TA, and 7 days of curing at TA and T65 regimes

	Mass loss [%]		
Curing time	2d	7d	
Curing regime	TA	TA	T65
Peak 1 (30-240 ˚C)	3.437	4.487	5.277
Peak 2 (300-400 ˚C)	1.289	1.545	1.593

4.3.1.3 Variation of SHA dissolution time to optimise compressive strength

This section provides insight into the effect of the duration of SHA immersion in water before mixing the M25 mortar. This mix was selected as optimal based on the slump flow and compressive strength.

Figure 63 presents the slump flow for the mortars mixed with no immersion of the SHA (M25), followed by the immersion procedures described in Table 8 (M25/0h, M25/1h, M25/6h and M25/24h). Mixes with prolonged immersion times of up to 6 hours resulted in a decrease in slump flow, while the mix M25/24h exhibited a higher slump than the mix M25/6h.

The compressive strengths (Figure 64) of the mixes M25, M25/0h, and M25/1h after 7 days of ambient curing were similar. Mixes M25/6h and M25/24h showed a mild increase in compressive strength. However, the difference between the lowest and the highest was approximately 5 MPa.

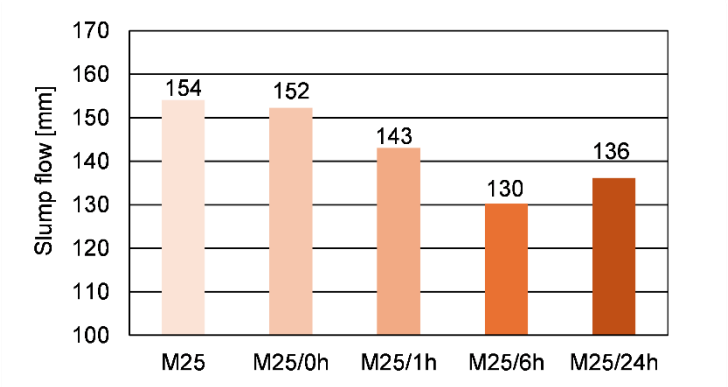

Figure 63. Influence of the mixing procedure on the workability of the mix M25

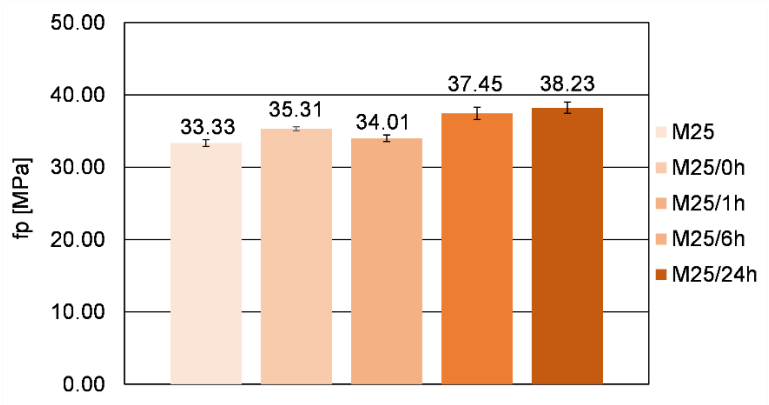

Figure 64. Influence of the mixing procedure on the compressive strength of the mix M25 at 7 days of age

Changes in the potassium content in water after different times of SHA immersion are presented in Figure 65. Over time, potassium content increases, as reflected in the altered pH

shown in Figure 66. The immersion time up to 24 hours and pH value of the suspension have a strong linear correlation (R^2=0.9561).

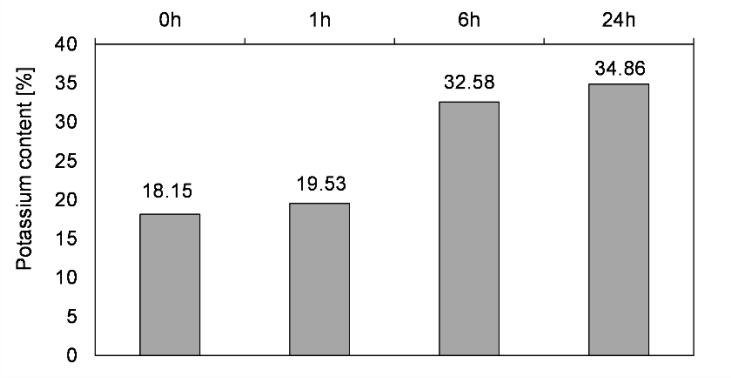

Figure 65. Potassium content in the leachate of SHA after different immersion times

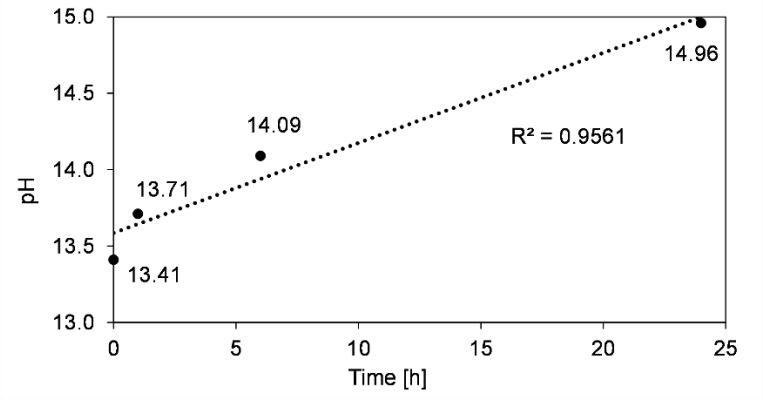

Figure 66. Changes in the alkalinity of the SHA suspension depending on the duration of the SHA immersion in water

The increase in pH of the SHA suspension increases with immersion time, which correlates with the increase in compressive strength for 14.7 % compared to the mortar with undissolved SHA (Figure 64).

4.3.2 Discussion

4.3.2.1 Variation of water to binder ratio to optimise workability and compressive strength

An increase in solid particle content increases yield stress and reduces the workability [182]. Irregular shape and rough surface of SHA particles, observed by SEM, increase inter-particle friction [183,49]. The shape and texture can increase water demand for particle surface wetting and reduce available water in the mix.

The compressive strength increases with an increase in SHA content, providing more alkali for the slag dissolution and enhanced formation of hydration products. Lower w/b ratios provide less excess water in the mix and less porosity, resulting in higher compressive strength.

Based on the results the chosen optimum mix for further testing of the SHA influence on the properties of AAS was SHA25 with w/b ratio 0.45.

The addition of sodium silicate resulted in higher slump flow and a general increase in 7-day compressive strength, compared to SHA-activated samples. This is consistent with the literature findings on the improvement of mechanical properties with the addition of silicates.

4.3.2.2 Variation of curing regime to optimise compressive strength

Curing at elevated temperatures was found to be beneficial for early strength development, which is in line with other studies with different biomass ashes [69,58,147]. This is also consistent with results on dissolution of the SHA at TA and T65 where higher mass loss was observed after dissolution at T65. Elevated temperature may induce dissolution of Ca and Mg besides K, accelerating the slag reaction and formation of more hydration products. Contrary to expectations and findings in the literature on AAMs with biomass ashes [134], higher compressive strength at 28 days was obtained for the TA than the T65 curing regime (Figure 57). Although the reduced strength with T65 regime was not pronounced, it may be attributed to the accelerated reaction kinetics induced by elevated temperatures. This rapid reaction can lead to the early formation of dense hydration products, which inhibit further gel development by limiting ion diffusion and promoting microstructural inhomogeneity [184]. An additional explanation found in the literature is that exposure to elevated curing temperatures can lead to significant water evaporation, thereby reducing the amount of free water available for subsequent hydration reactions [185,95].

The interpretation of the compressive strength results is supported by TGA analysis (Figure 60 and Figure 61 which shows that more hydration products are formed at 28 days under the TA curing regime compared to T65. This is also confirmed by the lower integrated peak areas in FTIR spectra for the samples with the same amount of SHA cured at T65, compared to TA (Table 17). Overall, elevated-temperature curing appears to be more effective in enhancing early-age strength.

The higher SHA content has led to an increase in compressive strength at both 7 and 28 days (Figure 56 and Figure 57), due to the formation of more hydration products; however, mixes M25 and M35 at 28 days exhibited essentially the same strengths. This can also be explained by the fast initial reaction in the presence of more alkalis, hindering the development of compressive strength at 28 days. The increase in SHA content also resulted in higher DTG and FTIR peaks that represent the C-S-H, C-A-S-H, and possibly C-(K)-S-H and C-(K)-A-S-H gel (Figure 60, Table 17 and Table 18).

The formation of the gels could also be altered by the CaO in the SHA [145]. The increase in biomass ash content was followed by higher compressive strengths in the works of other authors as well [69,144,148]. The contribution to compressive strength could also be attributed to the filler effect of undissolved SHA [145,144]. However, Moraes Pinheiro et al. [69] found that the filler effect in the OBA-activated slag was negligible, compared to the OBA contribution to the slag activation.

The 7-day compressive strengths obtained under the T65 curing regime are comparable to or higher than those reported in the literature. The highest 7-day compressive strengths previously reported were 38.38 MPa for mortars with the addition of 25% of OBA [69] and 45.2 MPa for those incorporating almond biomass ash [131], both cured at 65 °C, for 7 days. Mortar samples in this study achieved 35.4 MPa (15% SHA), 45.83 MPa (25% SHA) and 50.36 MPa (35% SHA) (Figure 56). Furthermore, the published data shows that mortars activated with 10, 20 and 30 wt% BFS of HBA exhibited 28-day compressive strength from 22.1 MPa to 26.8 MPa, at ambient temperature, corresponding to 1.7 M, 1.9 M, and 2.0 M NaOH, and 1.8 M, 2.0 M and 2.2 M KOH molarities, respectively [144]. In another study, mortars based on BFS and CHA yielded 29.9 MPa and 40.9 MPa after 7 and 28 days of curing at ambient temperature and 95% RH, respectively [149]. Under the TA curing regime, the results of this research show similar compressive strengths for 7 days of curing (Figure 56) and significantly higher 28-day compressive strengths by up to 15 MPa (Figure 57).

Although strength development depends on multiple factors, such as the chemical composition of the biomass ash and GGBFS, mix design, and curing regime, the comparison leads to the

conclusion that the use of SHA in alkali activation can result in compressive strengths of the same order of magnitude as those reported in the literature for other biomass ashes.

4.3.2.3 Variation of SHA dissolution time to optimise compressive strength

The increase in compressive strength can be attributed to the higher dissolution degree of potassium from SHA over time, confirmed by ion chromatography, thus increasing the pH and altering alkali activation. Although the pH of the SHA suspension is notably higher after 6 hours of immersion and compressive strength improved by up to 14.7%, the mixing procedure without SHA immersion is selected. Using SHA as received, without previous dissolution in water, considerably simplifies its potential practical application, as the binder can be produced by pre-mixing solid components and subsequently adding water. Immersion of the SHA for 6 hours reduces workability. Most importantly, the compressive strength results without SHA dissolution prior to mixing (33 MPa) are notably good, comparable to conventional systems and other literature results on AAMs with biomass ashes as activators.

4.3.3 Conclusions

The influence of w/b ratio, SHA content, curing regime (ambient and elevated temperature), and mixing procedure was evaluated on paste and mortar mixes activated with 15, 25, and 35% SHA by mass of GGBFS. The following conclusions can be drawn:

- An increase in the w/b ratio also resulted in an increase in the slump of mortar mixtures across all ash contents. For mortar mixtures prepared with quartz aggregate, the optimal w/b ratio with respect to consistency was determined to be 0.45. In the case of mortar mixtures containing crushed aggregate, the w/b ratio was increased to 0.50 in order to achieve satisfactory workability. Similarly, a w/b ratio of 0.50 was adopted for mixtures incorporating silicate-based activators.
- Increasing the SHA content leads to a minor reduction in workability and alters gel formation, consequently increasing compressive strength. FTIR and TGA analyses confirmed that the reaction between SHA and GGBFS results in the formation of C-S-H and C-A-S-H gels, characteristic of alkali-activation of slag. The optimal SHA content was 25 wt% GGBFS, considering the workability and compressive strength.
- Curing at 65 °C promotes early strength development (attaining 89-98% of 28-day compressive strength) but results in lower 28-day compressive strength compared to ambient curing.

- Immersion of SHA in water before mixing enhances the dissolution of potassium ions and results in higher compressive strength up to 14.7%, depending on the immersion duration; however, it negatively impacts workability.
- The highest 28-day compressive strength of 55 MPa (25% SHA) is attained with minimal technological requirements, without SHA pretreatment and dissolution in water before mixing, cured at ambient temperature. This is 15 MPa higher than reported in the literature, highlighting the novelty for mortar mixes with similar component materials, mix designs, and curing conditions.

Research further confirmed the conclusions from Phase 1: SHA can be used as an alternative activator in slag-based AAMs. Furthermore, hypothesis 2 was also partially confirmed - based on the mechanical properties, SHA can be used as only activator for slag-based AAMs.

4.4 Phase 4 - Properties of alkali-activated concrete activated with SHA and sodium silicate

This experimental phase aimed at investigating the influence of SHA on mechanical and durability properties at the concrete level. Three AAC mixes were compared: reference mix with conventional chemical activators, mix activated with SHA and sodium silicate and mix activated only with SHA. Tested hypotheses are:

H2: *"Utilisation of only the alternative activator in AAMs will not significantly reduce the mechanical and durability properties of slag-based alkali-activated materials."*

H3: *"It is possible to produce slag-based alkali-activated concrete derived only from waste materials - slag and sunflower husk ash."*

4.4.1 Results

4.4.1.1 Fresh-state properties

The results of the tested fresh-state properties of concrete mixes are presented in Table 20, Figure 67, and Figure 68.

Both concrete mixes exhibited cohesive behaviour, and no segregation was observed during the slump test. The reference mix had an average slump of 66 mm (Figure 69), attaining a slump class of S2 [172]. This value was expected, given the previous consistency results from Phase 2 and the increase in w/b ratio. Mix SHA-S had an average slump of 27 mm (Figure 70), corresponding to a very stiff consistency (slump class S1) [172]. However, the concrete

was placed and compacted adequately. The SHA25 mixture showed very stiff consistency, corresponding to slump class S1, with a slump value of only 10 mm. Due to its very dry and stiff nature, the mixture was difficult to place and compact into the moulds. After demoulding, these specimens exhibited visible defects (honeycombs), resulting from inadequate compaction.

Table 20. Fresh-state properties of concrete mixes (averages of measurements for individual concrete batches)

Mix	Temperature [˚C]	Δp [%]	Δh [mm]	Slump class	γ [kg/m³]
R	25.2	1.2	66	S2	2348
SHA-S	23.2	1.3	27	S1	2352
SHA25	21.7	1.7	10	S1	2234

Δp - entrained air; Δh - slump, ρ_{fc} - density of fresh concrete

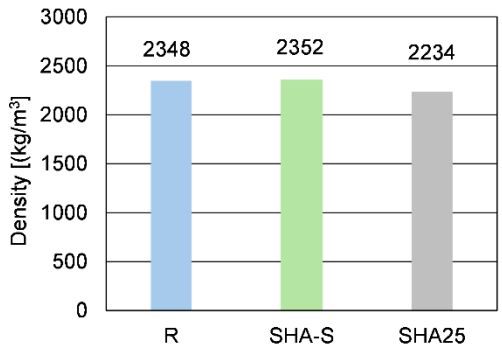

Figure 67. Density of fresh AAC

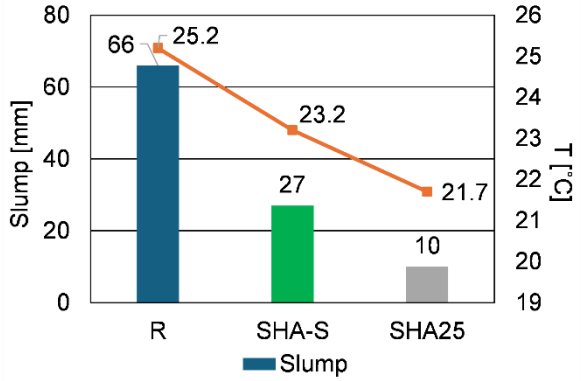

Figure 68. Slump and temperature values of the AAC mixes R, SHA-S and SHA25

Figure 69. Slump test of the reference mix

Figure 70. Slump test of the mix SHA-S

The temperature of the reference mix was approximately 2 ˚C higher than that of the concrete containing SHA. The mix activated only with SHA had the lowest temperature (21.7 ˚C).

The initial and final setting times of pastes corresponding to mix R and SHA-S are presented in Table 21. Mix SHA-S exhibited a 112-minute longer initial setting time than mix R, and the final setting time exceeded 10 hours and was not recorded.

Table 21. Initial and final setting times of the pastes corresponding to the AAC mixes R and SHA-S

Paste	Initial setting time [min]	Final setting time [min]
R	306	375
SHA-S	418	>600

4.4.1.2 Mechanical properties

Graphical representation of the compressive strength after 2, 7, 28, 56 and 90 days of curing are presented in Figure 71 at 2 and 90 days are identical. Compressive strengths at 7, 28, and 56 days are higher for the SHA-S concrete mixture, although this difference decreases with an increase in curing time. Tensile strength and modulus of elasticity of the mixes after 28 and 56 days of curing are presented in Figure 72 and Figure 73, respectively. The development of tensile strength is similar to compressive strength, reaching the same values after 56 days of curing. The reference mix had a higher modulus of elasticity than the SHA-S at both 28 and 56 days, by approximately 12% and 14%, respectively. Both mixes exhibited a decline in elastic modulus from 28 to 56 days of curing (R for 4.5% and SHA-S for 7%), despite the increase in compressive strength.

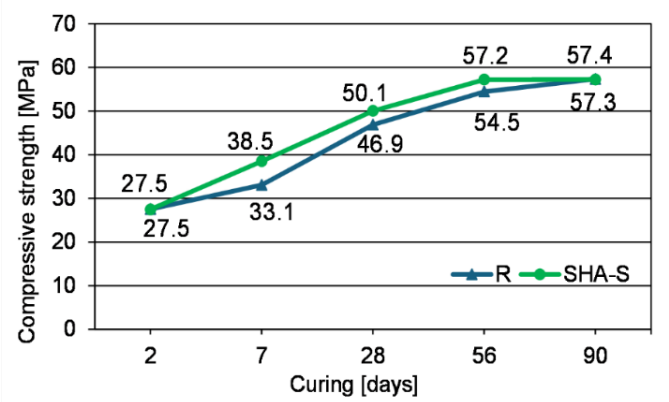

Figure 71. Compressive strength of concrete mixes R and SHA-S after 2, 7, 28, 56 and 90 days of curing

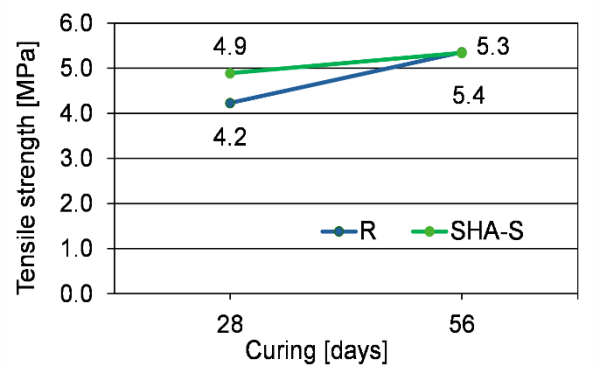

Figure 72. Tensile strength of the mixes after 28 and 56 days of curing

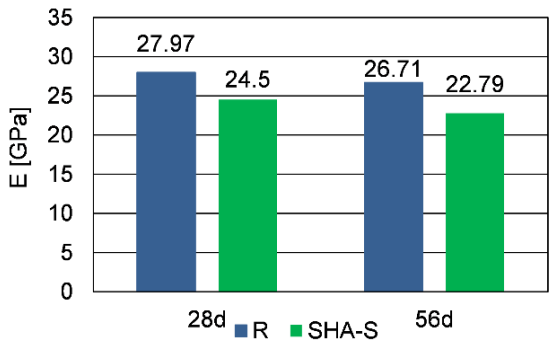

Figure 73. Modulus of elasticity of the mixes R and SHA-S, after 28 and 56 days of curing

4.4.1.3 Physical properties

Density and porosity

The results of the density of hardened concrete, open porosity, critical pore diameter (d_{crit}) and threshold pore diameter (d_{tr}) after 28 days of curing are presented in Table 22. All mixes exhibited hardened concrete densities typical of normal concrete (>2000 kg/m^3 <2600 kg/m^3) [172], as shown in Figure 74.

Table 22. Physical properties of AAC mixes: density, porosity, critical pore diameter and threshold diameter

Mix	ρ_{hc} [kg/m^3]	Porosity [%]	d_{crit} [µm]	d_{tr} [µm]
R_28d	2353	9.4	0.0056	0.0120
SHA-S_28d	2348	9.9	0.0056	0.0117

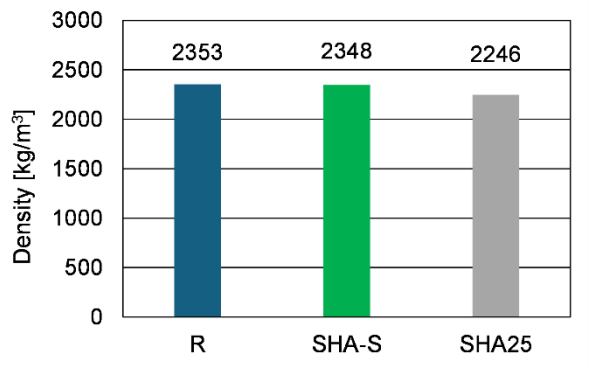

Figure 74. Density of hardened AAC mixes

The results of MIP analysis of mixes R and SHA-S after 28 days of curing are presented in Figure 75, Figure 76 and Figure 77. Mixes R and SHA-S had the same open porosity (9.4%

and 9.9%, respectively). However, the replacement of NaOH with SHA resulted in a higher content of capillary pores (0.01µm - 10 µm) and a lower content of gel pores (<0.01µm) [173], which can be seen in the cumulative intrusion curves (Figure 75) and pore size distribution diagram (Figure 77). Cumulative intrusion curves were used to graphically determine the threshold pore diameter, also known as the entry size, because it allows a high volume of mercury to intrude. The threshold pore diameter is determined as a diameter at which the slope of the cumulative intrusion curve increases steeply and is defined as the tangent intersection of the initial and inflexion slopes [186]. Both mixes had essentially the same d_{th} of 0.012 µm after 28 days of curing.

Derivatives of the pore distribution curves (dV/dP) or differential curves after 28 days of curing (Figure 76) show that the dominant pores in both concretes are gel pores. The higher gel pore content was in the reference mix. Critical pore diameter - the pore size corresponding to the most probable pore throat size that controls the transport - can be determined from the diagram as the peak of the log differential curves [186]. This diameter was the same for mixes R and SHA-S (0.0056 µm).

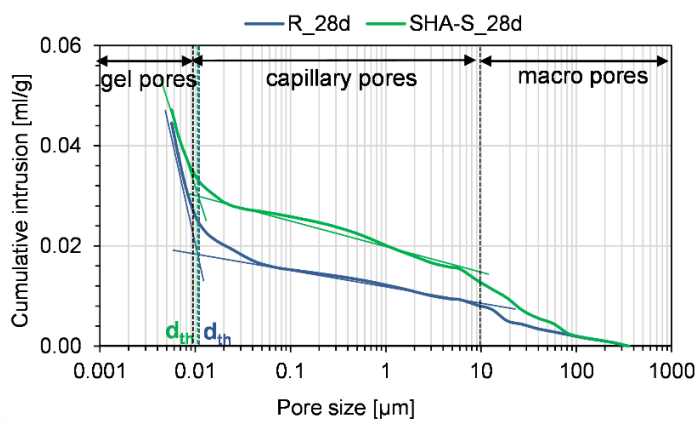

Figure 75. Cumulative intrusion curves and graphical determination of threshold pore diameter of the mixes R and SHA-S after 28 days of curing

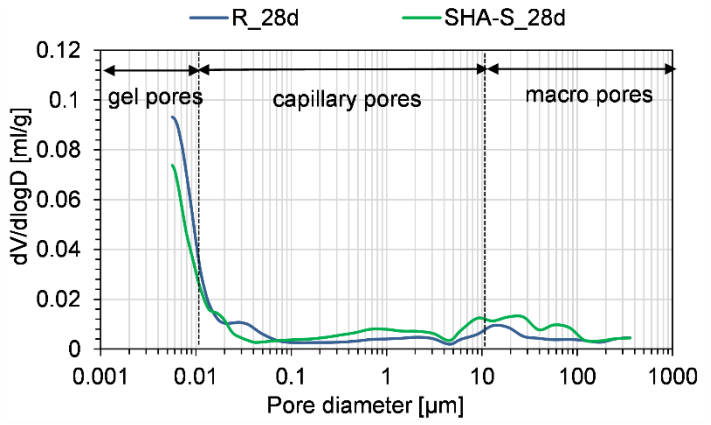

Figure 76. Log differential curves of the mixes R and SHA-S after 28 days of curing

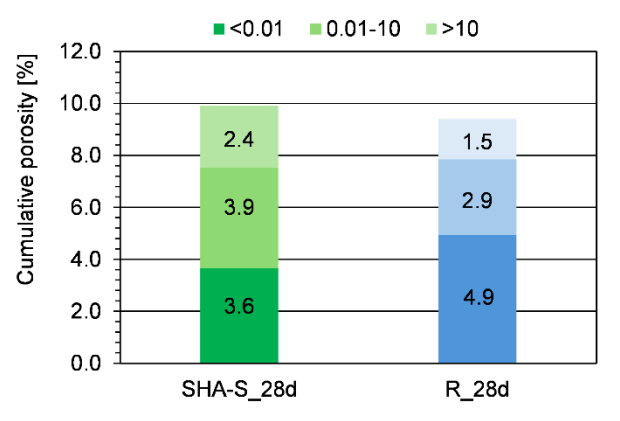

Figure 77. Pore size distribution of the mixes R and SHA-S, according to the pore diameter, after 28 days of curing

Water absorption

The results on cumulative water absorption after 8 days of testing are presented in the Figure 78, while Figure 79 shows a diagram of water absorption through the testing period. Initial and secondary absorption equations are shown in Table 23.

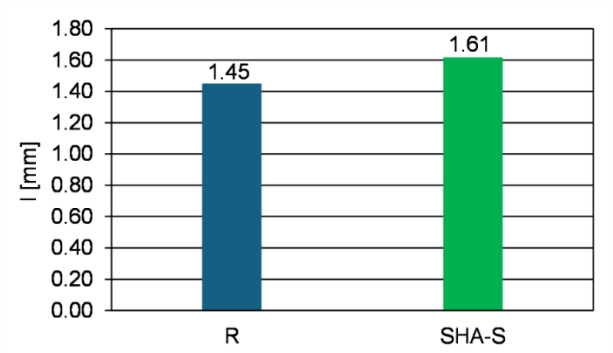

Figure 78. Cumulative water absorption after concrete mixes after 8 days of testing

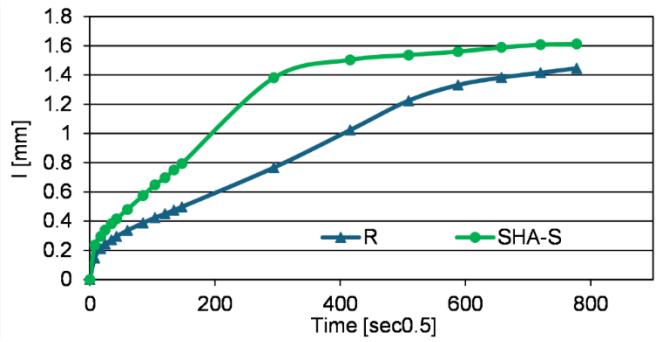

Figure 79. Diagram of water absorption throughout the testing period

Table 23. Absorption equations of mixes R and SHA-S

Mix	Initial absorption			Secondary absorption		
	Absorption equation	R^2	S_i [mm/s$^{0.5}$]	Absorption equation	R^2	Ss [mm/s$^{0.5}$]
R	y=0.0023x + 0.2365	0.9684	-	y=0.0014x+0.434	0.9323	-
SHA-S	y=0.0039x+0.2365	0.9948	0.0039	y=0.004x+1.2878	0.9107	-
R*	y=0.002x + 0.1980	0.9958	0.002	y=0.0005x+1.0342	1.0	0.0005
SHA-S*	y=0.0039+0.2352	0.9982	0.0039	y=0.0003x+1.4094	0.9841	0.0003

R^2 - coefficient of determination; S_i – initial rate of absorption; S_s - secondary rate of absorption.

The mix SHA-S exhibited higher cumulative water absorption than the reference mix (1.63 mm and 1.49 mm, respectively), although the difference was not prominent.

The standard ASTM C 1584-04 [164] defines the initial rate of absorption as the slope of the line obtained by linear regression of the mass change data recorded between 1 minute and 6 hours. The secondary rate of absorption is determined the same way, using the data points between 1 and 7 days (Figure 29). Table 23 shows the absorption equations and the corresponding correlation coefficients for the initial and secondary absorption phases. Only the initial absorption of the mix SHA-S followed the linear relationship (correlation coefficient higher than 0.98).

However, the mix R showed linear behaviour when considering data points from 1 minute to 7 days, yielding a correlation coefficient of 0.9845. The highest correlation coefficient can be obtained for the data points from 1 minute to 4 days (0.9958). The second part of the sorptivity curve (points from 5 to 7 days) then exhibits an ideal linear behaviour (R^2=1). Mix SHA-S shows linear behaviour up to 1 day of testing, with a correlation coefficient of 0.9982, while the secondary sorptivity also shows a linear correlation for the measurement points from 2 to 7 days (R^2=0.9841).

In this case, mixes R and SHA-S can be compared based on the linear part of each curve. The absorption rate for the mix with SHA is twice that of the reference mix (0.0039 vs 0.002). In the secondary absorption area, the reference mix had a higher rate than mix SHA-S (0.0005 vs 0.0003, respectively).

As water absorption did not reach equilibrium by the seventh day, the measurement period was extended until the mass stabilised. No further mass increase was recorded after the tenth day of immersion, when the cumulative water absorption for the mixes R and SHA-S were 1.49 mm and 1.63 mm, respectively.

Shrinkage

The results of total shrinkage after testing up to 90 days by stud gauges ($\varepsilon_{cs,1}$) and strain gauges ($\varepsilon_{cs,2}$) and cumulative mass loss are given Table 24 and Table 25 for the mix R and in Table 26 and Table 27 for the mix SHA-S. The total shrinkage after 90 days of testing in accordance with SRPS EN 12390-16:2019 is presented in Figure 80. The results of total shrinkage measured with strain gauges are presented in Figure 81. The relationships between shrinkage and cumulative mass loss for measurements with stud and strain gauges are shown in Figure 82 and Figure 83, respectively.

Table 24. Shrinkage of the AAC mix R after 90 days

	Testing time [days]									
	t_0	t_{0+1}	t_{0+3}	t_{0+7}	t_{0+14}	t_{0+21}	t_{0+28}	t_{0+42}	t_{0+56}	t_{0+90}
$\varepsilon_{cs,1}$ [mm/m]	0	-0.329	-0.623	-0.718	-0.879	-0.994	-1.036	-1.098	-1.194	-1.397
$\varepsilon_{cs,2}$ [mm/m]	0	-0.210	-0.287	-0.356	-0.457	-0.508	-0.552	-0.577	-0.641	-0.716

Table 25. Cumulative mass loss of the R mix samples

	Mass loss [kg]									
	t_0	t_{0+1}	t_{0+3}	t_{0+7}	t_{0+14}	t_{0+21}	t_{0+28}	t_{0+42}	t_{0+56}	t_{0+90}
avg. cumulative	0	0.045	0.068	0.090	0.111	0.124	0.131	0.145	0.157	0.174

Table 26. Shrinkage of the AAC mix SHA-S after 90 days

	Testing time [days]									
	t_0	t_{0+1}	t_{0+3}	t_{0+7}	t_{0+14}	t_{0+21}	t_{0+28}	t_{0+42}	t_{0+56}	t_{0+90}
$\varepsilon_{cs,1}$ [mm/m]	0	-0.878	-1.536	-2.014	-2.270	-2.474	-2.606	-2.738	-2.829	-3.112
$\varepsilon_{cs,2}$ [mm/m]	0	-0.395	-0.747	-0.928	-1.104	-1.225	-1.311	-1.412	-1.482	-1.586

Table 27. Cumulative mass loss of the SHA-S mix samples

	Mass loss [kg]									
	t_0	t_{0+1}	t_{0+3}	t_{0+7}	t_{0+14}	t_{0+21}	t_{0+28}	t_{0+42}	t_{0+56}	t_{0+90}
avg. cumulative	0	0.125	0.171	0.202	0.231	0.252	0.265	0.281	0.292	0.314

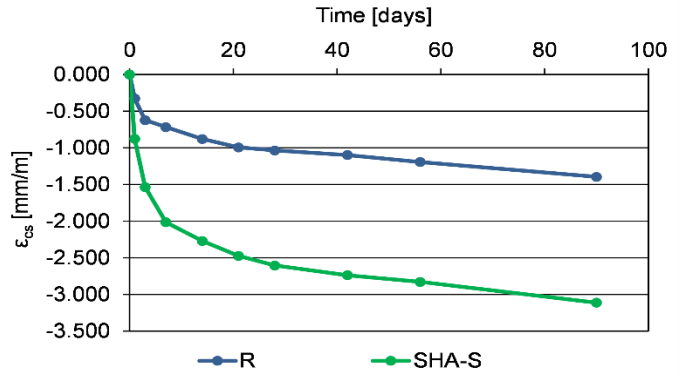

Figure 80. Total shrinkage of mixes R and SHA-S after 90 days, measured along the principal axis, over stud gauges

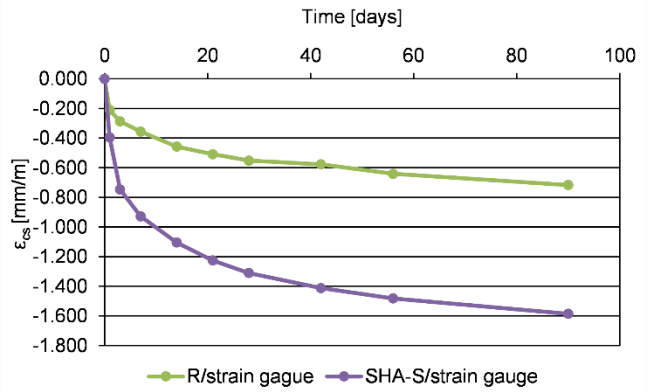

Figure 81. Total shrinkage of mixes R and SHA-S after 90 days, measured at the surface of the samples, with strain gauges

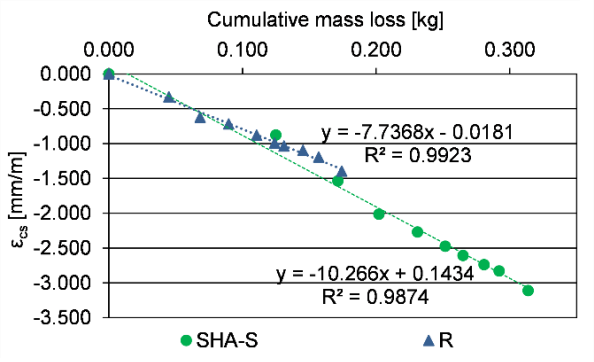

Figure 82. The correlation between cumulative mass loss and shrinkage measured over stud gauges, for mix R and SHA-S

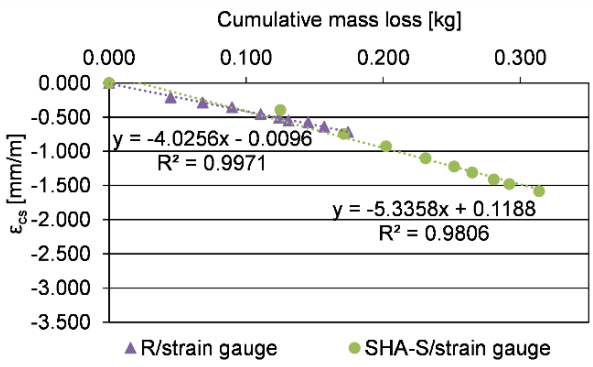

Figure 83. The correlation between cumulative mass loss and shrinkage measured with strain gauges, for mix R and SHA-S

Total shrinkage of the mix R was 1.397 mm/m. In the first 7 days of testing, mix R reached 51% of total shrinkage at 90 days and mix SHA-S 65%. The total shrinkage of the mix SHA-S

was 3.112 mm/m, 2.23 times that of the reference mix. Mix SHA-S lost 1.8 times more water than R over 90 days (0.314 kg vs 0.174 kg).

The same trend of 2.22 times higher shrinkage of the mix SHA-S was also observed for the length changes at the surface, measured with strain gauges (Figure 81). Furthermore, both mixes show a consistent ratio of approximately 0.52 between strain gauge readings and gauge stud readings, with $R^2 > 0.98$ for both mixes (Figure 84).

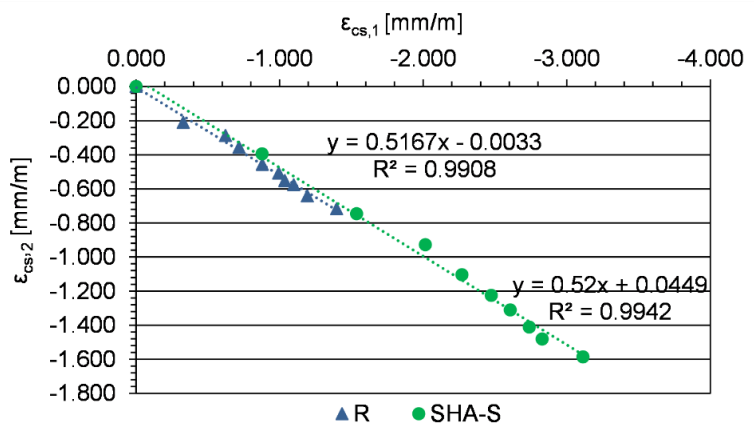

Figure 84. Relationship between stud gauges (εcs,1) and strain gauge measurement (εcs,2) of the shrinkage for the mixes R and SHA-S

Despite the almost double shrinkage compared to the reference mix, samples of SHA-S had much less surface cracking, which can be observed in Figure 85.

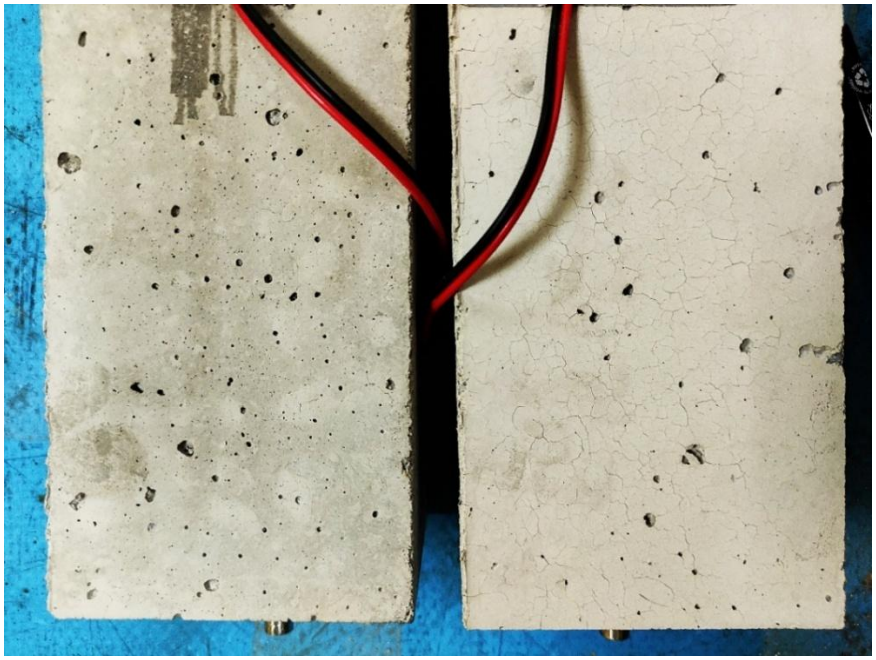

Figure 85. Surface cracking (crazing) of the AAC samples: SHA-S (left) and R (right)

4.4.1.4 Durability properties

Penetration of water under pressure

The results on depth of water penetration under pressure for mixes R and SHA-S, after 28 days of curing, are presented in Figure 86. Mix SHA-S the highest penetration depth of 35.3 mm, which is not significantly higher than the 33 mm penetration of the mix R. According to the Croatian national requirements [174], both concretes attained class VDP1 of resistance to water penetration (maximum depth <50mm).

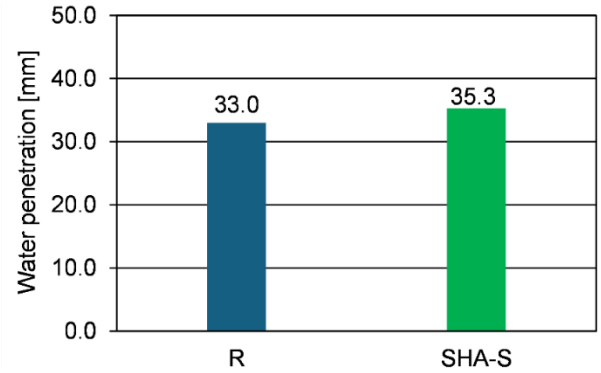

Figure 86. Graphical presentation of depth of water penetration under pressure: concrete mixes R and SHA-S

Carbonation resistance

Samples after 7, 28 and 56 days of exposure to 3% CO_2 are presented in Figure 87. Carbonation depth (d_k), carbonation rates (K_{AC}) and coefficients of determination (R^2) of concrete mixes R and SHA-S are presented in Table 28. The graphical representation of the results is presented in Figure 88.

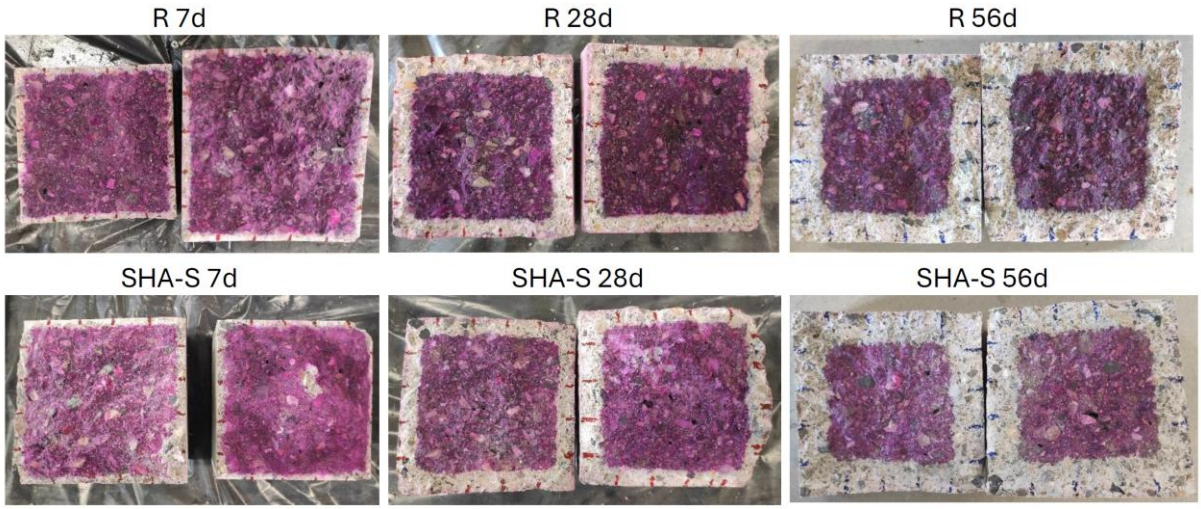

Figure 87. Samples of the mixes R and SHA-S after 7, 28 and 56 days of accelerated carbonation

Table 28. Carbonation resistance of concrete mixes: carbonation depths after 7, 28 and 56 days of exposure, carbonation rates and coefficients of determination

Mix	d_k [mm]			K_{AC}	R^2
	7d	28d	56d	[mm/days$^{0.5}$]	
R	6.9	15.3	24.6	3.263	0.9889
SHA-S	7.7	17.0	26.2	3.4915	0.994

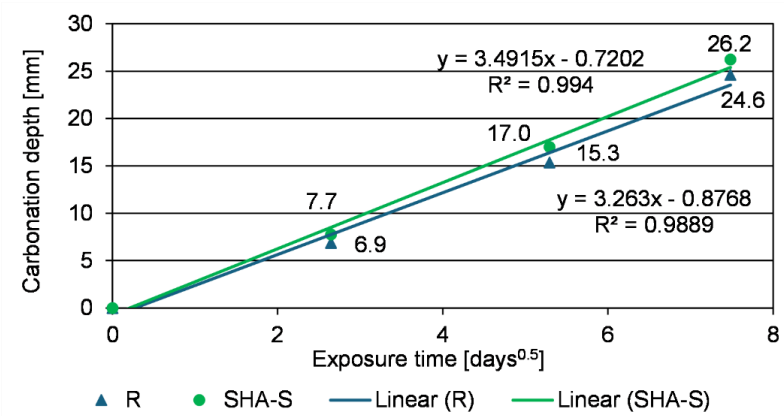

Figure 88. Carbonation depth versus the square root of exposure time

Both mixes exhibited similar resistance to carbonation. The SHA-S mix showed slightly higher carbonation depths (7.7, 17.0 and 26.2 mm after 7, 28 and 56 days) and a marginally higher carbonation rate (K_{AC}=3.4915 mm/days$^{0.5}$) than the reference mix (6.9, 15.3 and 24.6 mm; K_{AC}=3.263 mm/days$^{0.5}$), indicating a small reduction in carbonation resistance. In both cases, carbonation depth increased linearly with the square root of time (R^2 > 0.98).

TGA was conducted to reveal changes in phase assemblage after carbonation. TG and DTG curves of carbonated and non-carbonated samples are presented in Figure 89 and Figure 90. Dominant peaks and mass loss of the samples before and after exposure to carbonation are given in Table 29. Mass losses in the temperature ranges 30-240 ˚C and 300-400 ˚C correspond to the decomposition of hydration products: C-S-H, C-A-S-H, and hydrotalcite, respectively. Mass loss between 450 ˚C and 700˚C corresponds to carbonates. Before and after exposure to carbonation, mix SHA-S had higher mass losses across all distinct temperature ranges, indicating the formation of more hydration and carbonation products.

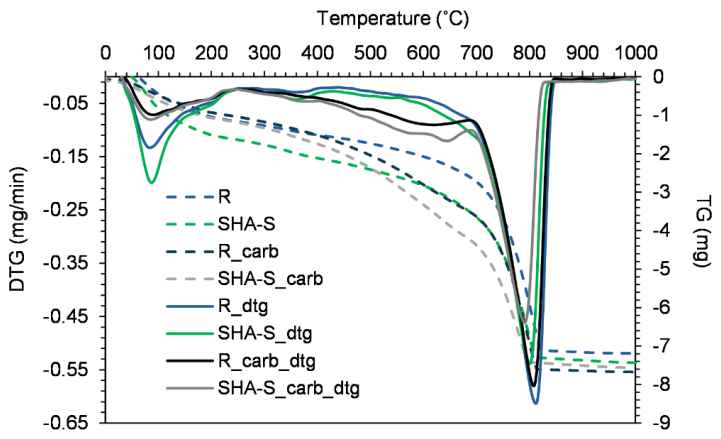

Figure 89. TG and DTG curves of mixes R and SHA-S before and after 56 days of exposure to accelerated carbonation

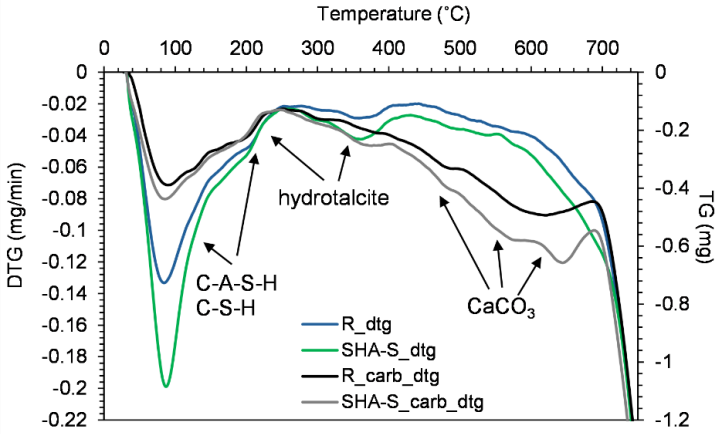

Figure 90. TG and DTG curves of mixes R and SHA-S before and after 56 days of exposure to accelerated carbonation - temperature range up to 700 ˚C

Table 29. Mass loss obtained by TGA for AAC mixes before and after carbonation

	R	SHA-S	R_carb_56d	SHA-S_carb_56d
Temperature range	**Mass loss [%]**			
30-240 ˚C	4.263	5.719	2.990	3.346
300-400 ˚C	0.808	1.136	1.069	1.295
450-500 ˚C	0.675	0.945	1.63	1.951
500-600 ˚C	-	-	2.403	3.074
600-700 ˚C	1.928	2.528	2.561	3.554

After exposure to carbonation, the C-S-H and C-A-S-H peaks decreased due to decalcification of the gels [65]. Consequently, the peaks corresponding to carbonates increased. The broad mass loss between 450°C and 700°C encompasses the decomposition of amorphous and crystalline $CaCO_3$ polymorphs [65]. The mass loss between 450 ˚C and 640 ˚C usually

corresponds to amorphous $CaCO_3$, while the peak between 640 ˚C and 700 ˚C are attributed to its crystalline form [187]. Even though the carbonation front i.e., carbonation rate, was very similar, the highest peaks of the mix SHA-S in this region indicate the formation of more carbonates, i.e., a higher degree of carbonation. This is supported by the greater reduction in the peaks of C-S-H and C-A-S-H compared with the mix R. The large peak from 700˚C to 850˚C represents carbonates in the aggregate. After carbonation, hydrotalcite peaks also increased and became diffused.

To assess the effect of SHA on this process, MIP analysis of samples after 56 days of exposure to accelerated carbonation was conducted. The results are shown in Table 30.

Table 30. Porosity, critical pore diameter and threshold diameter of the mixes R and SHA-S after 56 days of exposure to accelerated carbonation

Mix	Porosity, carb [%]	$d_{cr1,c}$ [µm]	$d_{cr2,c}$ [µm]	$d_{th,c}$ [µm]
R	14.3	0.0071	0.0241	0.051
SHA-S	12.8	0.0065	0.0103	0.031

Cumulative intrusion and differential curves of carbonated and non-carbonated samples are plotted in Figure 91 and Figure 92, respectively. The pore size distribution of samples before carbonation (28 days of curing) and after is presented in Figure 93.

The carbonation process increased the cumulative porosity of both mixes: for the reference mix from 9.4% to 14.3% and for the mix SHA-S from 9.9 to 12.8%.

The coarsening of the pores can be observed in both mixes in the differential curves (Figure 92) through an increase in total porosity in both mixes, with increases in both gel and capillary pore ranges for SHA-S, and predominantly in the capillary range for R. After carbonation, the differential pore size distribution became bimodal - a secondary peak was formed in the capillary region, and therefore, two critical pore diameters can be observed. Critical pore diameter $d_{cr1,c}$ increased from 0.0056 µm to 0.0071 µm for mix R, and to 0.0065 µm for the mix SHA-S. Secondary critical pore diameter ($d_{cr2,c}$) was 0.0241 µm and 0.0103 µm for R and SHA-S mix, respectively. Furthermore, the threshold diameter increased significantly, which can be observed by the shift of the cumulative intrusion curves in Figure 91. For the mix R, it increased to 0.051 µm, and for the mix SHA-S, it increased to 0.031 µm.

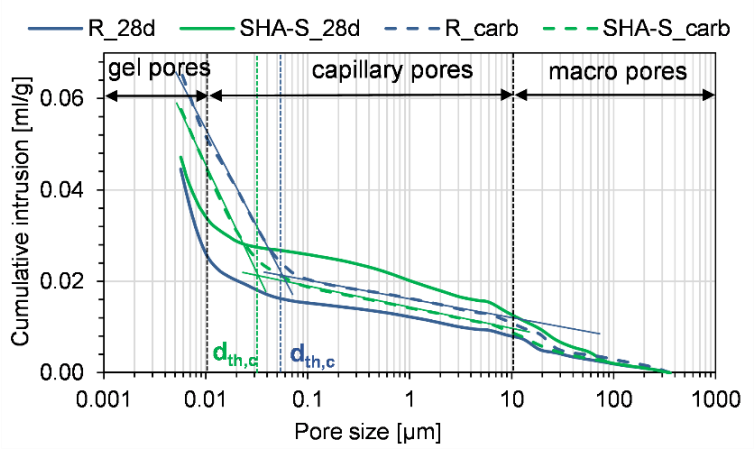

Figure 91. Cumulative intrusion curves of the non-carbonated and carbonated AAC mixes and graphical determination of the threshold pore diameter of carbonated mixes

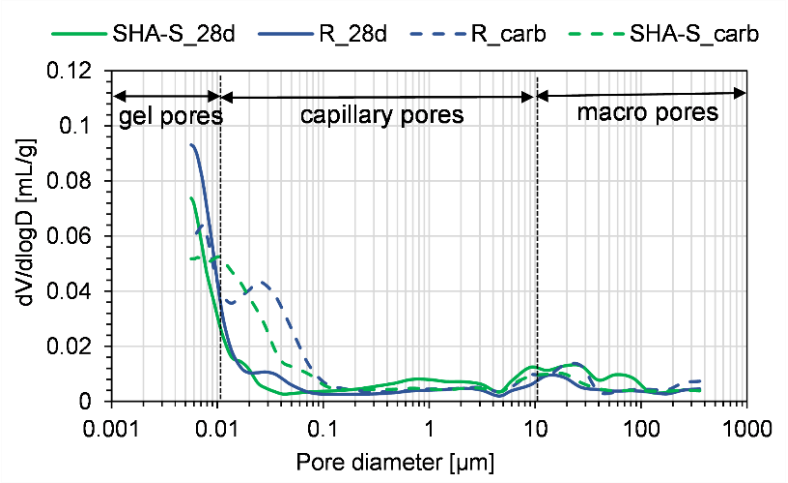

Figure 92. Differential curves of the non-carbonated and carbonated AAC mixes

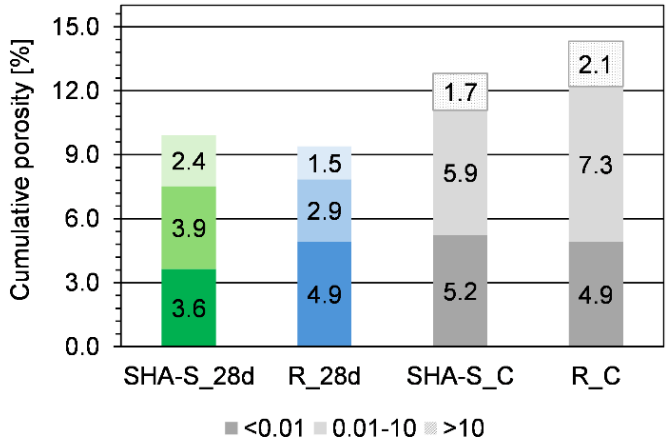

Figure 93. Pore size distribution of the non-carbonated and carbonated samples, according to the pore diameter

Resistance to chloride penetration

The chloride migration coefficients (Dnssm) after 28 and 56 days of curing are presented in Figure 94. The samples after the chloride migration test, after 28 and 56 days of curing, are presented in Figure 95, Figure 96, Figure 97 and Figure 98.

After 28 days of curing, mix R exhibited higher resistance to chloride penetration than mix SHA-S. However, the reduction of the migration coefficient of this mix at 56 days was approximately 10%, while the mix SHA-S had 52% of reduction, resulting in a lower migration coefficient than mix R.

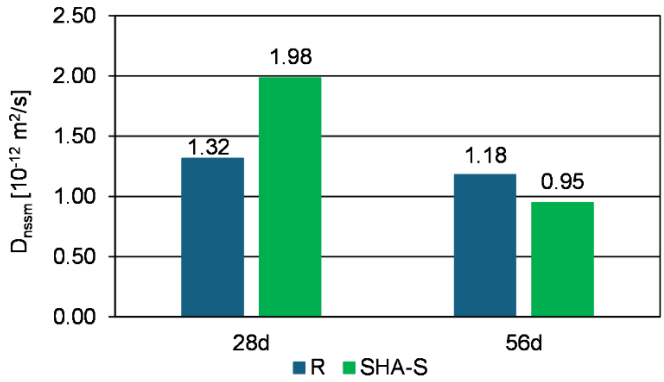

Figure 94. Graphical representation of migration coefficients for concrete mixes R and SHA-A, after 28 and 56 days

Both mixes showed a reduction in the chloride migration coefficient after 56 days of curing (1.18, mix R and 0.95, mix SHA-S) compared to 28 days (1.32, mix R and 1.98, mix SHA-S), due to an increase in matrix density over curing time. The discrepancy between the relatively high water absorption and the low chloride migration coefficients of the tested mixes is consistent with findings that AAS systems can have higher sorptivity due to microcracking, but low chloride permeability of the bulk matrix [97].

Figure 95. Chloride penetration of the samples R, after 28 days of curing

Figure 96. Chloride penetration of the samples SHA-S, after 28 days of curing

Figure 97. Chloride penetration of the samples R, after 56 days of curing

Figure 98. Chloride penetration of the samples SHA-S, after 56 days of curing

4.4.2 Discussion

4.4.2.1 Fresh-state properties

The replacement of NaOH with SHA in concrete did not have a significant influence on the mix temperature. The difference was 2˚C, consistently throughout the series of concrete batches. This can be attributed to the greater hydration reaction that occurs with sodium hydroxide compared to potassium hydroxide. In addition, this difference is influenced by the fact that sodium was introduced as a pure chemical, whereas potassium was released from the biomass ash; consequently, the reaction proceeded more slowly [49], resulting in a lower concrete temperature. However, the difference and individual temperatures are not high since the activator content in the mixes are at the lower limit of the usual range. Mix SHA25 had a lower temperature than mix SHA-S by 2˚C.

The reduction in slump of mix SHA-S compared to the reference mixture was expected, considering the addition of SHA to the mix. In mix R, the alkali activator (NaOH) is dissolved in the mixing water and added to the mixer. In mix SHA-S, the activator is provided as solid SHA particles at 25 wt% of slag, increasing the total solid content and yield stress while reducing the workability [182]. Furthermore, the irregular shape and rough surface texture of SHA particles, as observed by SEM, increase inter-particle friction [183]. It is possible that there is a secondary contribution of shape and texture to the reduction in workability, through particle surface wetting and a reduction in available water in the mix. Additionally, the aggregate fraction 0-4 mm had a significant portion of fine particles, which also contributed to the decrease in slump in both mixes.

The SHA25 mixture showed very stiff consistency, corresponding to slump class S1, with a slump value of only 10 mm. Due to its very dry and stiff nature, the mixture was difficult to place and compact into the moulds. After demoulding, these specimens exhibited visible defects (honeycombs), resulting from inadequate compaction. This led to the conclusion that SHA alone cannot be used as an activator in this research because of the poor workability and compactability of the concrete. Therefore, this mixture was not tested further for durability properties. The reason is the omission of sodium silicate, which increases workability up to a certain content, as concluded in Phase 2 of the research. The effect of the fine aggregate particles played a significant role in this mix as well.

The increase in initial setting time of SHA-S paste is attributed to the slower activation kinetics of SHA, in which K^+ ions dissolve more gradually compared to Na^+ from a chemical activator [49]. The setting times of the pastes should be interpreted comparatively rather than as absolute values. The SRPS EN 196-3 standard [158] prescribes measuring setting time on

cement paste of standard consistency; however, no equivalent standard consistency is defined for AAMs. Therefore, the test was performed on pastes with w/b = 0.5, matching the ratio used in the corresponding concrete mixes. Since the pastes lack aggregate, their effective water content is considerably higher than in concrete of the same w/b ratio, which delays setting. Consequently, the measured setting times are expected to be longer than those of the corresponding concrete mixes, and the results are best used to compare the relative effects of SHA versus NaOH activation rather than as representative setting times of the concretes. However, these results are promising, as the excessively rapid setting of AAMs remains a technological challenge, and the use of SHA demonstrates potential to extend the workable time of alkali-activated slag systems.

4.4.2.2 Mechanical properties

Higher compressive strength of SHA-S over the curing period may reflect contributions from both the filler effect of the undissolved SHA fraction [144,145] and potentially ongoing slag activation by progressively released K^+ throughout the hardening period, resulting in a higher alkali content than calculated in the mix design. The higher increase of compressive strength of mix R after 7 days of curing could be due to the dissolution of silicon from sodium silicate. However, contributions from other SHA-derived species (CaO, MgO, SO_3) and their interaction with the sodium silicate system are also possible.

The lower modulus of elasticity of SHA-S compared to R, despite higher compressive strength, can be attributed to the incorporation of K^+ ions from SHA dissolution into the C-A-S-H gel interlayer. K^+ has a larger ionic radius (1.38 Å) and lower charge density than Na^+ (1.02 Å), forming weaker bonds with silicate oxygens and reducing the stacking regularity of C-A-S-H layers, which results in a more compliant matrix [188,189,190].

4.4.2.3 Physical properties

Porosity

Higher content of capillary pores in SHA-S compared to R after 28 days of curing can be attributed to the dissolution of the soluble fraction of SHA particles during hydration. SEM imaging of raw SHA confirmed dense particle morphology without visible internal porosity, while dissolution tests showed 16% of the ash dissolves in water, almost immediately, with an increase up to 42.5% after 2 hours of water dissolution at 65 ˚C. The void space potentially created by this dissolution is consistent with the capillary-range porosity observed in MIP.

Water absorption

The higher initial absorption rate of SHA-S is consistent with its coarser pore size distribution (more capillary porosity), which allows faster water uptake by capillary suction. Conversely, the higher secondary absorption rate of R could reflect the slower filling of its predominantly gel-sized porosity. The similar final absorption values (1.49 mm and 1.63 mm) are consistent with the comparable total porosity of both mixes measured by MIP.

The deviation from the standard bilinear absorption model is consistent with observations reported for AA slag systems. The drying-induced microcracking has been shown to increase water sorptivity and changes in absorption behaviour [95,96]. It should be noted that standard sorptivity test methods developed for PC concrete may not be directly applicable to AAM systems, as the conditioning protocol can induce microcracking that affects absorption behaviour [191].

Shrinkage

Despite an increased w/b ratio, lowering Ms was beneficial for the shrinkage of the reference mix. Similar mix designs of concrete and mortar samples showed higher shrinkage. Cartwright et al. [85] reported shrinkage of 2,0 mm/m after 28 days of drying at RH 50%, for the mortar samples. Studies on similar mix designs reported 90-days shrinkage of 1.750 mm/m with w/b=0.5 [192], and 1.125 mm/m with w/b=0.43 [77].

High early shrinkage observed in mix R and SHA-S was also reported by Thomas et al. [193], and explained by the delayed formation of the reaction products and rapid water loss.

A 2.23 times higher total shrinkage of the mix SHA-S compared to the reference mix can be explained by the higher total moisture loss of the mix SHA-S (0.314 kg, compared to 0.174 kg in the mix R) and the higher shrinkage per unit mass loss. MIP data at 28 days shows that while total porosity is similar for both mixes, the pore size distribution is different. Mix SHA-S has fewer gel pores but more porosity distributed across the capillary range, where water is less tightly retained and evaporates more rapidly, compared to mix R, where porosity is mostly in the gel range, where water evaporates slowly [173].

The slope of the shrinkage vs. mass loss relationship is 33% steeper for SHA-S (10.266 mm/m per kg) than for R (7.7368 mm/m per kg) (Figure 82). This means that even at the same amount of water loss, SHA-S would have higher total shrinkage than mix R. SHA-S has a coarser pore size distribution than R (3.9% vs 2.9% in the capillary range), but both mixes retain significant gel porosity (3.6% and 4.9%, respectively). SHA-S could generate lower capillary pressure per unit of water lost and lower shrinkage, according to the Kelvin-Laplace equation, as indicated by its lower elastic modulus (24.5 GPa vs 28.0 GPa) and consistent with the high viscoelastic

compliance characteristic of AAS systems. However, the SHA-S mix had a lower modulus of elasticity than mix R (24.5 GPa vs 28.0 GPa for R at 28 days). This indicates that steeper shrinkage-to-cumulative mass loss is primarily due to the higher deformability of the SHA-S matrix and may be consistent with the pronounced viscoelastic compliance reported for AAS systems as an important factor contributing to drying shrinkage [86,190].

If SHA continues to dissolve and release K^+, as indicated by the compressive strength results, and additional reaction occurs during the drying period, it implies that it consumes water, thereby causing self-desiccation. This could add internal capillary stress to the drying-induced capillary stress, increasing total shrinkage of the mix SHA-S [190,189]. However, the distinction between these two mechanisms should be further researched, and the dominant factor is the higher deformability of the SHA-S matrix, as evidenced by its lower elastic modulus.

The identical ratio between strain gauge readings and gauge stud readings for both mixes confirms that the higher shrinkage of SHA-S is a volumetric material property, not a measurement artefact. The difference in drying shrinkage at the surface and in the core of the samples occurs due to the moisture gradient, causing non-uniform strain distribution across the cross-section of the sample [194]. As the surface dries faster than the core, the restrained surface develops tensile stress, leading to microcracking. These microcracks partially relieve the compressive shrinkage strain at the surface, reducing the strain gauge reading relative to the gauge stud measurement, which captures the volume-averaged deformation over the full cross-section [195].

As discussed, a higher content of capillary pores in the mix SHA-S could induce lower capillary pressures than in the mix R, which is why stress intensity per unit volume of drying is lower, resulting in less cracking as observed in Figure 85. Another explanation could be that under sustained capillary stress; a more deformable matrix is expected to exhibit greater stress relaxation through creep before reaching the tensile cracking threshold [86,190]. The stiffer R matrix has less capacity for stress relaxation, allowing capillary stresses to accumulate and exceed the tensile strength, causing surface crazing. Li et al. [196] demonstrated that AAS concrete shows lower shrinkage-induced stress and later cracking onset than PC despite higher shrinkage, due to pronounced stress relaxation from high viscoelastic compliance.

4.4.2.4 Durability properties

Carbonation resistance

The accelerated carbonation results show that both mixes exhibited similar carbonation rates, with SHA-S carbonating slightly faster than R (3.49 vs 3.26 mm/day$^{0.5}$). The slightly higher

carbonation rate of SHA-S is consistent with its coarser pore size distribution, which may facilitate CO_2 diffusion into the matrix. However, the small difference between the two mixes suggests that pore structure is not the dominant factor, and that both mixes have comparable resistance to carbonation.

The similar carbonation resistance may be attributed to the higher MgO content in the system, due to the presence of SHA. The high MgO content (GGBFS+SHA) resulted in the formation of more hydrotalcite, which acts as a CO_2 absorbent [65,103]. The higher hydrotalcite content in the mix SHA-S is confirmed by TGA and DTG curves of the samples before and after 56 days of exposure, as shown in Figure 89 and Figure 90. Hydrotalcite peaks in both mixes increase and broaden after carbonation, due to CO_2 absorption [104,171], with the intensity of the SHA-S peak being higher, because initially more hydrotalcite has been formed and has a higher capacity to uptake CO_2. The increased formation of amorphous $CaCO_3$ in each mix and in SHA-S relative to R, is characteristic of slags with higher MgO content and could be beneficial. McCaslin and White [197] observed a lower extent of decalcification of C-(N)-A-S-H gel, because amorphous $CaCO_3$ has a higher solubility than crystalline calcium carbonate phases; its presence maintains a higher calcium concentration in the pore solution, decreasing the decalcification.

This further reflected on the porosity of the carbonated samples. Carbonation induces decalcification of C-S-H and C-A-S-H gels, resulting in increased porosity and coarsening of the pores in AAM systems [65]. Critical pore diameter also increased, and the secondary critical pore diameter formed in a capillary range for both mixes. Mix R exhibited a higher increase in cumulative porosity and coarsening of the pores, as well as threshold pore diameter.

The replacement of NaOH with SHA in the AAC resulted in a slightly higher carbonation rate and it had a positive effect on pore structure, resulting in a smaller increase in capillary porosity and in critical pore diameter and threshold pore diameter than in the reference mix.

Resistance to chloride penetration

The discrepancy between the relatively high water absorption and the low chloride migration coefficients of the tested mixes is consistent with findings that AAS systems can have higher sorptivity due to microcracking, but low chloride permeability of the bulk matrix [97].

Despite retaining higher capillary porosity at 56 days (4.2% vs 0.9% for R), SHA-S achieved a lower chloride migration coefficient (0.95 vs 1.18 $\times 10^{-12}$ m²/s). This contradiction between pore structure and chloride transport can be explained by the higher formation of hydrotalcite, confirmed by TGA (Figure 90), which chemically binds chloride ions [117,171]. Ye et al. published that hydrotalcite and AFm-type phases can contribute with 40-70% of total chloride

binding capacity in AAS systems and that they are higher in AAMs activated with potassium [198].

This can further indicate that chloride binding is the dominant mechanism governing chloride resistance in SHA-S, not pore refinement. The fact that the improvement of the chloride migration coefficient of the mix SHA-S over curing time was greater than for the mix R could add up to the theory of continued formation of hydrotalcite, i.e., continued dissolution of SHA. The significantly higher capillary porosity of mix SHA-S at 56 days of curing could be due to continued dissolution, and therefore the prevalence of the formation of additional hydration products or increased capillarity should be further studied.

4.4.3 Conclusions

Based on the analysed experimental results, the following conclusions can be drawn:

- SHA compromises the workability of the mix. This can be explained by increased total solid content in the mix, reduced available water, and increased interparticle friction due to the shape and texture of SHA particles.
- The concrete mix activated only with SHA was hard to place due to its stiff consistency. Therefore, the SHA cannot be used as the sole activator without the addition of a silicate solution to improve workability.
- Replacing NaOH with SHA did not compromise mechanical properties. AAC mix activated with 25 wt% GGBFS of SHA and Ms=0.42 attained approximately 50 MPa at 28 days of curing, compared to 46 MPa of the reference mix. After 90 days of curing, mixes had the same compressive strength of 57 MPa. Tensile strength tends to follow the same trend at 56 days of curing. The incorporation of K^+ ions via SHA resulted in a reduced degree of regularity in the gel, due to the size and charge density differences between K+ and Na+. This resulted in 12% and 17% lower modulus of elasticity after 28 and 56 days, respectively, compared the mix R.
- Mix with SHA exhibited 25.6% higher capillary pore content than R samples, after 28 days of curing. It did not influence the cumulative porosity, critical pore diameter and threshold diameter.
- The absorption behaviour of both mixes deviates from the standard bilinear model prescribed for PC concrete. This is characteristic of AAS systems, where the conditioning protocol (drying at 50°C) can induce microcracking that alters the capillary network and disrupts the expected absorption kinetics. The rate of absorption for the

mix with SHA was twice that of the reference mix, but in the secondary absorption area, the reference mix had a higher rate than the mix with SHA-S. Final water absorption was only slightly higher for the mix SHA-S, due to the higher capillary pore content and the same open porosity obtained by MIP.

- The shrinkage of AAC doubled with the addition of the SHA. This is explained by two mechanisms: higher total moisture loss due to the coarser capillary pore network and greater matrix deformability, as evidenced by a lower elastic modulus compared to the mix R. This compliance also had a positive effect on drying-induced cracking. It enables stress relaxation through creep and prevents capillary stresses from reaching the tensile cracking threshold.
- The carbonation resistance at all exposure days was essentially the same for both mixes, where the mix SHA-S exhibited a minor increase in carbonation rate. Even though it was expected that higher SHA-S permeability would lead to lower carbonation resistance, the addition of SHA reduced pore coarsening during carbonation. High MgO content in SHA contributed to the formation of more hydrotalcite, which acted as a CO_2 absorbent. The increase in total porosity of the SHA-S after carbonation was lower (2.9% vs 4.9% for R), and the critical and threshold pore diameters increased less than in R. This suggests that the additional hydrotalcite in SHA-S partially buffers the microstructural damage caused by C-A-S-H decalcification, resulting in a less severe coarsening of the pore network. The DTG data confirmed this mechanism: SHA-S shows both higher initial hydrotalcite content and a greater increase in hydrotalcite-related mass loss after carbonation.
- SHA-S initially shows higher chloride permeability at 28 days, consistent with its coarser pore structure. However, it surpasses the reference mix by 56 days, achieving a 20% lower migration coefficient despite retaining significantly more capillary porosity. The decoupling of pore structure from chloride transport performance can provide evidence of significant chemical binding as the dominant mechanism governing chloride resistance in the SHA-S system. The higher hydrotalcite content in SHA-S provides greater chloride binding capacity through anion exchange in the hydrotalcite interlayer. The 52% reduction in migration coefficient between 28 and 56 days versus 10% reduction in mix R - suggests that hydrotalcite formation continues beyond 28 days in SHA-S. This favours the potential progressive dissolution of SHA.

Hypotheses 1 and 2 were not proven at a concrete level due to technological issues related to the workability of the mix activated only with SHA. However, using SHA instead of NaOH in

combination with sodium silicate did not compromise the mechanical and durability properties of AAC.

SHA, as an alternative hydroxide activator, modified both the physical and chemical characteristics of the hydration products. Across the tested durability properties - carbonation resistance, chloride migration and water absorption - the results suggest that chemically governed mechanisms surpass the influence of the coarser physical pore structure of SHA-S. The extent to which chemical mechanisms prevail over physical ones is likely to depend on the SHA dosage, mixing procedure, and overall mix design, and requires further investigation.

Chapter 5
FINAL REMARKS, CONTRIBUTIONS, AND FUTURE PERSPECTIVES

5. FINAL REMARKS, CONTRIBUTION, AND FUTURE PERSPECTIVES

5.1 Final remarks

This research investigated the possibilities of using SHA as an alternative potassium-rich activator in slag-based AAMs, through four experimental phases from material characterisation to concrete-level performance. Furthermore, results demonstrated that mixes with reduced content of conventional chemical activators can have satisfactory mechanical and durability properties, providing the baseline for comparison with SHA-activated mixes.

The main conclusions of the thesis are:

1. SHA has satisfactory chemical and physical properties for use as an activator in AAMs. The reaction between SHA and GGBFS produces C-S-H and C-A-S-H gels characteristic of alkali-activated slag systems.
2. Optimal alkali content and silicate modulus for the reference AAC mix with low activator content are 4 wt% of GGBFS and 0.42, respectively.
3. SHA reduces the workability of mortar mixes, due to its irregular shape and rough surface. The experimental research resulted in the following conclusions and recommendations:
    - The optimal w/b ratio was found to be 0.45 with an optimal SHA content of 25 wt% of GGBFS, considering both workability and compressive strength.
    - For mortars with crushed 0-4 mm aggregate that was used, workability and compressive strength were optimised by increasing w/b ratio to 0.5 and by adding sodium silicate so that Ms is 0.42, based on the research in Phase 2.
4. Based on mechanical properties, SHA can serve as the only activator for slag-based AAMs.
    - Curing at 65°C promotes early strength development, with specimens attaining 89–98% of the 28-day compressive strength within the first days. However, elevated-temperature curing results in lower 28-day compressive strength than ambient curing.
    - Pre-dissolution of SHA in water before mixing enhances the release of potassium ions and increases compressive strength by up to 14.7%, depending on immersion duration. However, this pre-treatment negatively affects workability due to accelerated early reaction.

5. SHA cannot be used as the only activator at the concrete level, due to the significant reduction in workability. However, adding sodium silicate to achieve Ms=0.42 in the mix increases slumps and alters the concrete's ability to be placed and compacted.
6. Replacing NaOH with SHA did not compromise the mechanical properties of AAC with sodium silicate activator.
    - The mix activated with 25 wt% GGBFS of SHA and Ms=0.42 attained a 28-day compressive strength of 50 MPa and can be compared to the compressive strength and mix design of 46 MPa, n=4%, Ms=0.42. The small difference in compressive strength may arise from the filler effect of undissolved ash or higher alkali content from both SHA and sodium silicate.
    - After 90 days, both mixes converged to the same compressive strength of 57 MPa, with tensile strength following a similar trend at 56 days.
    - The incorporation of K^+ ions through SHA dissolution resulted in a 12% and 17% lower modulus of elasticity after 28 and 56 days, respectively, attributed to the weaker interlayer bonding of K^+ within the C-A-S-H gel.
7. The replacement of NaOH with SHA resulted increases capillary pore content, without affecting the cumulative open porosity, critical pore diameter or threshold diameter.
8. The capillary absorption behaviour of both mixes deviated from the standard bilinear model prescribed for PC concrete, which is common for AAS systems. SHA has a higher initial absorption due to the higher capillary porosity. Final water absorption was only marginally higher for SHA-S, confirming the comparable total porosity of both mixes.
9. The drying shrinkage of AAC doubled with the incorporation of SHA. It is governed by the higher moisture loss from the coarser capillary pore network and the higher deformability of the K^+-modified matrix. However, the lower modulus of elasticity, which contributed to greater shrinkage, simultaneously enabled greater stress relaxation through creep, preventing drying-induced surface cracking despite the substantially higher total deformation.
10. Durability properties were not compromised by the addition of SHA.
    - Carbonation rates of both concretes were essentially comparable at all exposure ages, with SHA-S exhibiting only a minor increase. Despite the coarser pore structure of SHA-S and the expected higher depth of carbonation, the higher hydrotalcite content resulting from the additional MgO introduced by SHA acted as a CO_2 absorbent, buffering the decalcification of the C-A-S-H gel.

- Similarly, the chloride migration coefficient of SHA-S was lower than that of the reference mix at 56 days, attributed to the greater chloride binding capacity of the higher hydrotalcite content.

Overall, replacing NaOH with SHA modified the physical and chemical characteristics of the hydration products. The increased capillary porosity induced by SHA had the highest negative effect on shrinkage. For all examined durability indicators - carbonation resistance, chloride migration, and water absorption - the dominant role of chemically controlled mechanisms, specifically hydrotalcite-facilitated CO_2 uptake and chloride binding, mitigated the negative impact of the coarser pore structure. However, the extent to which chemical mechanisms prevail over physical ones depends on the SHA dosage, mixing procedure and overall mix design, and needs further investigation.

5.2 Contribution

The original scientific contribution of the doctoral thesis is reflected in:

1. Valorisation of SHA, a locally available waste material in the construction sector, by using it as an alternative activator for slag-based AAMs.

2. Optimisation of the binder activated with SHA through assessing the influence of w/b ratio, SHA content, mixing procedures and curing regimes on workability and compressive strength. The optimisation resulted in defining these parameters to use SHA as received and produce waste-based binder with minimal technological requirements.

3. Determination of the influence of SHA on the activation process and properties of slag-based AAM by understanding the mechanisms through which it changes the chemical and physical properties of the binder. For the first time in the literature, a set of physical, mechanical, and durability properties was tested on AAC with SHA and biomass ash in general, rather than the chemical alkali-hydroxide activator. The results offer insight into the mechanisms by which SHA influences a wide range of AAC properties, as well as the technological challenges that arise.

5.3 Future perspectives

The presented doctoral thesis opened several questions and future research perspectives. The main recommendations for future investigations are:

1. Quantification of potassium content available for activation at the mortar and concrete level.
2. Investigation of the potential continuous dissolution of K^+ ions and decouple its effect from the filler effect on the properties of mortar and concrete.
3. Understanding the coupled effect of K^+ and Na^+ on the hydration products of concrete activated with SHA and sodium silicate.
4. Improvement of workability of concrete activated solely with SHA by using river aggregate and superplasticisers compatible with AAMs, and testing of its durability properties.
5. Assessment of the potential to reduce shrinkage by pre-dissolving SHA in water prior to mixing, thereby reducing the capillary porosity created by in-situ dissolution of SHA particles during the curing period.
6. Further understanding of the influence of SHA on the viscoelastic behaviour of AAC, including creep and stress relaxation.
7. Assessment of the suitability of SHA-activated slag mortar as a repair material, given its adequate compressive strength, the lower modulus of elasticity of potassium-activated systems, and the potential high stress relaxation capacity. The compatibility between the repair mortar and the concrete substrate should be investigated, with an emphasis on reducing differential shrinkage, testing bond strength, and ensuring long-term durability.

REFERENCES

REFERENCES

[1] Marsh Alastair, Dillon Thomas, Bernal Susan: Cement and concrete decarbonisation roadmaps – a meta-analysis within the context of the United Kingdom. *RILEM Technical Letters*, Vol. 8, 94–105, 2023, doi: 10.21809/rilemtechlett.2023.163

[2] European Commission: A new Circular Economy Action Plan: For a Cleaner and More Competitive Europe. Brussels: European Commission, 2020, Available at https://environment.ec.europa.eu/topics/circular-economy-topics/first-circular-economy-action-plan_en

[3] Building Materials and the Climate: Constructing a New Future. *United Nations Environment Programme*, Paris, France, 2023

[4] Amer Ismail, Kohail Mohamed, El-Feky M. S., Rashad Ahmed, Khalaf Mohamed A.: A review on alkali-activated slag concrete. *Ain Shams Engineering Journal*, Vol. 12, No. 2, 1475–1499, 2021, doi: 10.1016/j.asej.2020.12.003

[5] Habert G., Miller S. A., John V. M., Provis J. L., Favier A., Horvath A., Scrivener K. L.: Environmental impacts and decarbonization strategies in the cement and concrete industries. *Nature Reviews Earth & Environment*, Vol. 1, No. 11, 559–573, 2020, doi: 10.1038/s43017-020-0093-3

[6] Provis John L., Van Deventer Jannie S.J.: Geopolymers and Other Alkali-Activated Materials. In *Lea's Chemistry of Cement and Concrete*, ed. Peter C. Hewlett, p. 779-805, Oxford, United Kingdom: Butterworth-Heinemann, 2019.

[7] Provis John L.: Alkali-activated materials. *Cement and Concrete Research*, Vol. 114, 40–48, 2018, doi: 10.1016/j.cemconres.2017.02.009

[8] Juenger M. C. G., Winnefeld F., Provis J. L., Ideker J. H.: Advances in alternative cementitious binders. *Cement and Concrete Research*, Vol. 41, No. 12, 1232–1243, 2011, doi: 10.1016/j.cemconres.2010.11.012

[9] Provis John L., Bernal Susan A.: Geopolymers and Related Alkali-Activated Materials. *Annual Review of Materials Research*, Vol. 44, No. 1, 299–327, 2014, doi: 10.1146/annurev-matsci-070813-113515

[10] Provis J. L.: Green concrete or red herring? – future of alkali-activated materials. *Advances in Applied Ceramics*, Vol. 113, No. 8, 472–477, 2014, doi: 10.1179/1743676114Y.0000000177

[11] Komkova Anastasija, Habert Guillaume: Environmental impact assessment of alkali-activated materials: Examining impacts of variability in constituent production processes and transportation. *Construction and Building Materials*, Vol. 363, 129032, 2023, doi: 10.1016/j.conbuildmat.2022.129032

[12] Wang Aiguo, Zheng Yi, Zhang Zuhua, Liu Kaiwei, Li Yan, Shi Liang, Sun Daosheng: The Durability of Alkali-Activated Materials in Comparison with

Ordinary Portland Cements and Concretes: A Review. *Engineering*, Vol. 6, No. 6, 695–706, 2020, doi: 10.1016/j.eng.2019.08.019

[13] Zhang Jian, Shi Caijun, Zhang Zuhua, Ou Zhihua: Durability of alkali-activated materials in aggressive environments: A review on recent studies. *Construction and Building Materials*, Vol. 152, 598–613, 2017, doi: 10.1016/j.conbuildmat.2017.07.027

[14] Shi Caijun, Krivenko Pavel V., Roy Della: Alkali Activated Cements and Concretes. *Taylor&Francis*, Oxon, UK, 2006

[15] Cyr Martin, Pouhet R: Chapter 11 - The frost resistance of alkali-activated cement-based binders.

[16] Bilek Vlastimil, Hurta Jan, Done Petra, Zidek Libor: Development of alkali-activated concrete for structures – Mechanical properties and durability. *Perspectives in Science*, Vol. 7, 190–194, 2016, doi: 10.1016/j.pisc.2015.11.031

[17] Alkali Activated Materials - State of the Art Report TC 224-AAM. *Springer Netherlands*, Dordrecht, 2014

[18] Deventer Jannie S. J. van, Provis John L., Duxson Peter, Brice David G.: Chemical Research and Climate Change as Drivers in the Commercial Adoption of Alkali Activated Materials. *Waste and Biomass Valorization*, Vol. 1, No. 1, 145–155, 2010, doi: 10.1007/s12649-010-9015-9

[19] Buchwald Anja, Vanooteghem Maarten, Gruyaert Elke, Hilbig Harald, De Belie Nele: Purdocement: application of alkali-activated slag cement in Belgium in the 1950s. *Materials and Structures*, Vol. 48, No. 1–2, 501–511, 2015, doi: 10.1617/s11527-013-0200-8

[20] Blake Helen: National Grid completes record-breaking pour of cement-free concrete at London Power Tunnels.

[21] Rossi Laura, Lima Luiz Miranda de, Sun Yubo, Dehn Frank, Provis John, Ye Guang, Schutter Geert De: Future perspectives for alkali-activated materials: from existing standards to structural applications. *RILEM Technical Letters*, Vol. 7, 159–177, 2022, doi: 10.21809/rilemtechlett.2022.160

[22] Pol Segura Isabel, Ranjbar Navid, Juul Damø Anne, Skaarup Jensen Lars, Canut Mariana, Arendt Jensen Peter: A review: Alkali-activated cement and concrete production technologies available in the industry. *Heliyon*, Vol. 9, No. 5, e15718, 2023, doi: 10.1016/j.heliyon.2023.e15718

[23] Kriven Waltraud M., Leonelli Cristina, Provis John L., Boccaccini Aldo R., Attwell Cyril, Ducman Vilma S., Ferone Claudio, Rossignol Sylvie, Luukkonen Tero, Deventer Jannie S. J. van, Emiliano José V., Lombardi Jérôme E.: Why geopolymers and alkali-activated materials are key components of a sustainable world: A perspective contribution. *Journal of the American Ceramic Society*, Vol. 107, No. 8, 5159–5177, 2024, doi: 10.1111/jace.19828

[24] ASTM C1928/C1928M-23: Standard Test Method for Compressive Strength of Alkali Activated Cementitious Material Mortars (Using 2-in. [50 mm] Cube Specimens).

[25] ASTM C1948/C1948M-24: Standard Specification for Alkali-Activated Cementitious Materials. *ASTM International*, West Conshohocken, PA, USA, 2024.

[26] BSI Flex 350 v2.0:2024-09 - Alternative binder systems for lower carbon concrete - Code of practice. *BSI Standards Limited*, 2024

[27] Segura Isabel Pol, Luukkonen Tero, Yliniemi Juho, Sreenivasan Harisankar, Damø Anne Juul, Jensen Lars Skaarup, Canut Mariana, Kantola Anu M., Telkki Ville-Veikko, Jensen Peter Arendt: Comparison of One-Part and Two-Part Alkali-Activated Metakaolin and Blast Furnace Slag. *Journal of Sustainable Metallurgy*, Vol. 8, No. 4, 1816–1830, 2022, doi: 10.1007/s40831-022-00606-9

[28] Luukkonen Tero, Abdollahnejad Zahra, Yliniemi Juho, Kinnunen Paivo, Illikainen Mirja: One-part alkali-activated materials: A review. *Cement and Concrete Research*, Vol. 103, 21–34, 2018, doi: 10.1016/j.cemconres.2017.10.001

[29] Alnahhal Mohammed Fouad, Kim Taehwan, Hajimohammadi Ailar: Waste-derived activators for alkali-activated materials: A review. *Cement and Concrete Composites*, Vol. 118, 103980, 2021, doi: 10.1016/j.cemconcomp.2021.103980

[30] Mendes Beatryz C., Pedroti Leonardo G., Vieira Carlos Maurício F., Marvila Markssuel, Azevedo Afonso R.G., Franco De Carvalho José Maria, Ribeiro José Carlos L.: Application of eco-friendly alternative activators in alkali-activated materials: A review. *Journal of Building Engineering*, Vol. 35, 102010, 2021, doi: 10.1016/j.jobe.2020.102010

[31] Mohapatra Smruti Sudeshna, Mishra Jyotirmoy, Nanda Bharadwaj, Patro Sanjaya K.: A review on waste-derived alkali activators for preparation of geopolymer composite. *International Conference on Materials, Machines and Information Technology-2022*, Vol. 56, 440–446, 2022, doi: 10.1016/j.matpr.2022.01.400

[32] Vassilev Stanislav V., Baxter David, Andersen Lars K., Vassileva Christina G.: An overview of the composition and application of biomass ash. Part 1. Phase–mineral and chemical composition and classification. *Fuel*, Vol. 105, 40–76, 2013, doi: 10.1016/j.fuel.2012.09.041

[33] Munawar Muhammad Assad, Khoja Asif Hussain, Naqvi Salman Raza, Mehran Muhammad Taqi, Hassan Muhammad, Liaquat Rabia, Dawood Usama Fida: Challenges and opportunities in biomass ash management and its utilization in novel applications. *Renewable and Sustainable Energy Reviews*, Vol. 150, 111451, 2021, doi: https://doi.org/10.1016/j.rser.2021.111451

[34] Odzijewicz Joanna Irena, Wołejko Elżbieta, Wydro Urszula, Wasil Mariola, Jabłońska-Trypuć Agata: Utilization of Ashes from Biomass Combustion. *Energies*, Vol. 15, No. 24, 9653, 2022, doi: 10.3390/en15249653

[35] Tosti Lorenzo, Zomeren André van, Pels Jan R., Comans Rob N. J.: Evaluating Biomass Ash Properties as Influenced by Feedstock and Thermal Conversion Technology towards Cement Clinker Production with a Lower Carbon Footprint. *Waste and Biomass Valorization*, Vol. 12, No. 8, 4703–4719, 2021, doi: 10.1007/s12649-020-01339-0

[36] Marathe Shriram, Sadowski Łukasz: Developments in biochar incorporated geopolymers and alkali activated materials: A systematic literature review. *Journal of Cleaner Production*, Vol. 469, 143136, 2024, doi: 10.1016/j.jclepro.2024.143136

[37] Bernal Susan A, Rodríguez Erich D, Kirchheim Ana Paula, Provis John L: Management and valorisation of wastes through use in producing alkali-activated cement materials. *Journal of Chemical Technology & Biotechnology*, Vol. 91, No. 9, 2365–2388, 2016, doi: 10.1002/jctb.4927

[38] Hills Colin D., Tripathi Nimisha, Singh Raj S., Carey Paula J., Lowry Florence: Valorisation of agricultural biomass-ash with CO2. *Scientific Reports*, Vol. 10, No. 1, 13801, 2020, doi: 10.1038/s41598-020-70504-1

[39] United States Department of Agriculture, Foreign Agricultural Service. Production – Sunflower seed. Available at: https://www.fas.usda.gov/data/production/2224000

[40] Production and market of sunflower in 2022 – report. Available at https://data.stat.gov.rs/?caller=SDDB&languageCode=sr-Latn.

[41] Victoriaoil, Victoria Group, available at: https://www.victoriaoil.rs/

[42] Maj Grzegorz, Krzaczek Paweł, Kuranc Andrzej, Piekarski Wiesław: Energy Properties of Sunflower Seed Husk as Industrial Extrusion Residue. *Agricultural Engineering*, Vol. 21, No. 1, 77–84, 2017, doi: 10.1515/agriceng-2017-0008

[43] Agrela Francisco, Cabrera Manuel, Morales María Martín, Zamorano Montserrat, Alshaaer Mazen: Biomass fly ash and biomass bottom ash.

[44] Šupić Slobodan, Malešev Mirjana, Radonjanin Vlastimir, Bulatović Vesna, Milović Tiana: Reactivity and Pozzolanic Properties of Biomass Ashes Generated by Wheat and Soybean Straw Combustion. *Materials*, Vol. 14, No. 4, 1004, 2021, doi: 10.3390/ma14041004

[45] Šupić Slobodan, Malešev Mirjana, Radonjanin Vlastimir: Harvest residues ash as a pozzolanic additive for engineering applications: a review and the catalogue. *Building Materials and Structures*, Vol. 64, 1–18, 2021, doi: 10.5937/GRMK2101001S

[46] Barišić Ivana, Netinger Grubeša Ivanka, Dokšanović Tihomir, Marković Berislav: Feasibility of Agricultural Biomass Fly Ash Usage for Soil Stabilisation of Road Works. *Materials*, Vol. 12, No. 9, 1375, 2019, doi: 10.3390/ma12091375

[47] Grubeša Ivanka N., Radeka Miroslava, Malešev Mirjana, Radonjanin Vlastimir, Gojević Anita, Siddique Rafat: Strength and microstructural analysis of concrete incorporating ash from sunflower seed shells combustion. *Structural Concrete*, Vol. 20, No. 1, 396–404, 2019, doi: 10.1002/suco.201800036

[48] Ramagiri Kruthi Kiran, Kar Arkamitra: Environmental impact assessment of alkali-activated mortar with waste precursors and activators. *Journal of Building Engineering*, Vol. 44, 103391, 2021, doi: 10.1016/j.jobe.2021.103391

[49] Zhu Zhijing, Li Xiuhao, Liu Rentai, Wang Zhiheng, Zhang Huasheng, Zhao Dukun, Bai Jiwen, Chen Mengjun, Li Wei: Workability and Environmental Evaluation of Using Sunflower Stalk Ash as an Alkali Activator with Blast Furnace Slag and Black Rice Hull Ash to Prepare Geopolymer Grouts. *Waste and Biomass Valorization*, Vol. 16, No. 4, 1609–1626, 2025, doi: 10.1007/s12649-024-02686-y

[50] Adesanya Elijah, Perumal Priyadharshini, Luukkonen Tero, Yliniemi Juho, Ohenoja Katja, Kinnunen Paivo, Illikainen Mirja: Opportunities to improve sustainability of alkali-activated materials: A review of side-stream based activators. *Journal of Cleaner Production*, Vol. 286, 125558, 2021, doi: 10.1016/j.jclepro.2020.125558

[51] Mendes Beatryz C., Pedroti Leonardo G., Vieira Carlos Maurício F., Marvila Markssuel, Azevedo Afonso R.G., Franco De Carvalho José Maria, Ribeiro José Carlos L.: Application of eco-friendly alternative activators in alkali-activated materials: A review. *Journal of Building Engineering*, Vol. 35, 102010, 2021, doi: font

[52] Industrial production by products. Republic of Serbia: Statistical Office of the Republic of Serbia; 2024.

[53] Nodehi Mehrab, Taghvaee Vahid Mohamad: Alkali-Activated Materials and Geopolymer: a Review of Common Precursors and Activators Addressing Circular Economy. *Circular Economy and Sustainability*, Vol. 2, No. 1, 165–196, 2022, doi: 10.1007/s43615-021-00029-w

[54] Provis John L.: Geopolymers and other alkali activated materials: why, how, and what?. *Materials and Structures*, Vol. 47, No. 1, 11–25, 2014, doi: 10.1617/s11527-013-0211-5

[55] Gruskovnjak A., Lothenbach B., Holzer L., Figi R., Winnefeld F.: Hydration of alkali-activated slag: comparison with ordinary Portland cement. *Advances in Cement Research*, Vol. 18, No. 3, 119–128, 2006, doi: 10.1680/adcr.2006.18.3.119

[56] Ben Haha M., Le Saout G., Winnefeld F., Lothenbach B.: Influence of activator type on hydration kinetics, hydrate assemblage and microstructural development of alkali activated blast-furnace slags. *Cement and Concrete Research*, Vol. 41, No. 3, 301–310, 2011, doi: 10.1016/j.cemconres.2010.11.016

[57] Qin Yongjun, Qu Changwei, Ma Cailong, Zhou Lina: One-Part Alkali-Activated Materials: State of the Art and Perspectives. *Polymers*, Vol. 14, No. 22, 5046, 2022, doi: 10.3390/polym14225046

[58] Font A., Soriano L., Moraes J.C.B., Tashima M.M., Monzó J., Borrachero M.V., Payá J.: A 100% waste-based alkali-activated material by using olive-stone biomass ash (OBA) and blast furnace slag (BFS). *Materials Letters*, Vol. 203, 46–49, 2017, doi: 10.1016/j.matlet.2017.05.129

[59] Soriano Lourdes, Font Alba, Tashima Mauro M., Monzó José, Borrachero Maria Victoria, Bonifácio Thaís, Payá Jordi: Almond-shell biomass ash (ABA): A greener alternative to the use of commercial alkaline reagents in alkali-activated cement. *Construction and Building Materials*, Vol. 290, 123251, 2021, doi: 10.1016/j.conbuildmat.2021.123251

[60] Hu Hecheng, Zhou Tuo, Li Ye, Xia Bing, Zhang Man, Hu Nan, Yang Hairui: Review of Research Progress on Dry Granulation Technology for Blast Furnace Slag. *Materials*, Vol. 18, No. 12, 2802, 2025, doi: 10.3390/ma18122802

[61] Blast furnace slag granulation | Climate Technology Centre & Network | Tue, 11/08/2016. https://www.ctc-n.org/technologies/blast-furnace-slag-granulation (2026-February-25)

[62] Marvila Markssuel Teixeira, Azevedo Afonso Rangel Garcez de, Vieira Carlos Maurício Fontes: Reaction mechanisms of alkali-activated materials. *Revista IBRACON de Estruturas e Materiais*, Vol. 14, e14309, 2021, doi: https://doi.org/10.1590/S1983-41952021000300009

[63] SRPS EN 197-1: 2011 - Cement - Part 1: Composition specification and conformity criteria for common cements. *Institute for Standardization of Serbia*, Belgrade, 2011

[64] Garcia-Lodeiro I., Palomo A., Fernández-Jiménez A.: Crucial insights on the mix design of alkali-activated cement-based binders.

[65] Shi Zhenguo, Shi Caijun, Wan Shu, Li Ning, Zhang Zuhua: Effect of alkali dosage and silicate modulus on carbonation of alkali-activated slag mortars. *Cement and Concrete Research*, Vol. 113, 55–64, 2018, doi: 10.1016/j.cemconres.2018.07.005

[66] Zhang Jian, Shi Caijun, Zhang Zuhua: Carbonation induced phase evolution in alkali-activated slag/fly ash cements: The effect of silicate modulus of activators. *Construction and Building Materials*, Vol. 223, 566–582, 2019, doi: 10.1016/j.conbuildmat.2019.07.024

[67] Reddy A Narender, Anitha D, Tilak U Venkat: Performance of Alkali Activated Slag and Alkali Activated Slag + Fly Ash with various Alkali Activators. Vol. 2, No. 1, 2014

[68] Davidovits Joseph: Geopolymeric coating system for fiber cement products.

[69] Moraes Pinheiro Sayonara Maria de, Font Alba, Soriano Lourdes, Tashima Mauro M., Monzó José, Borrachero Maria Victoria, Payá Jordi: Olive-stone biomass ash (OBA): An alternative alkaline source for the blast furnace slag activation. *Construction and Building Materials*, Vol. 178, 327–338, 2018, doi: 10.1016/j.conbuildmat.2018.05.157

[70] Koloušek David, Brus Jiri, Urbanova Martina, Andertova Jana, Hulinsky Vaclav, Vorel Jindřich: Preparation, structure and hydrothermal stability of alternative (sodium silicate-free) geopolymers. *Journal of Materials Science*, Vol. 42, No. 22, 9267–9275, 2007, doi: 10.1007/s10853-007-1910-5

[71] Zhang Gui-Yu, Lin Run-Sheng, Wang Yi-Sheng, Wang Xiao-Yong: Influence of K+ and CO32− in activator on high-temperature performance of alkali-activated slag-ceramic powder binary blends. *Case Studies in Construction Materials*, Vol. 17, e01306, 2022, doi: 10.1016/j.cscm.2022.e01306

[72] Sitarz Mateusz, Castro-Gomes João, Hager Izabela: Strength and Microstructure Characteristics of Blended Fly Ash and Ground Granulated Blast Furnace Slag Geopolymer Mortars with Na and K Silicate Solution. *Materials*, Vol. 15, No. 1, 211, 2022, doi: 10.3390/ma15010211

[73] Cong Peiliang, Du Ruyan, Gao Huanlin, Chen Zhihui: Comparison and assessment of carbon dioxide emissions between alkali-activated materials and OPC cement concrete. *Journal of Traffic and Transportation Engineering (English Edition)*, Vol. 11, No. 5, 918–938, 2024, doi: 10.1016/j.jtte.2023.07.011

[74] Khan Md Ikramullah, Ram V. Vinayaka, Patel Vipulkumar Ishvarbhai: Strength, Environmental Impact and Cost Assessment of Alkali-Activated Concrete with Pre-treated Coarse Recycled Aggregates. *International Journal of Concrete Structures and Materials*, Vol. 19, No. 1, 29, 2025, doi: 10.1186/s40069-025-00768-2

[75] Bondar Dali, Ma Qianmin, Soutsos Marios, Basheer Muhammed, Provis John L., Nanukuttan Sreejith: Alkali activated slag concretes designed for a desired slump, strength and chloride diffusivity. *Construction and Building Materials*, Vol. 190, 191–199, 2018, doi: 10.1016/j.conbuildmat.2018.09.124

[76] Wang Shao-Dong, Scrivener Karen L., Pratt P.L.: Factors affecting the strength of alkali-activated slag. *Cement and Concrete Research*, Vol. 24, No. 6, 1033–1043, 1994, doi: 10.1016/0008-8846(94)90026-4

[77] Taghvayi Hamed, Behfarnia Kiachehr, Khalili Mohammadbagher: The Effect of Alkali Concentration and Sodium Silicate Modulus on the Properties of Alkali-Activated Slag Concrete. *Journal of Advanced Concrete Technology*, Vol. 16, No. 7, 293–305, 2018, doi: 10.3151/jact.16.293

[78] Provis John L., Arbi Kamel, Bernal Susan A., Bondar Dali, Buchwald Anja, Castel Arnaud, Chithiraputhiran Sundararaman, Cyr Martin, Dehghan Alireza, Dombrowski-Daube Katja, Dubey Ashish, Ducman Vilma, Gluth Gregor J. G., Nanukuttan Sreejith, Peterson Karl, Puertas Francisca, Riessen Arie van, Torres-Carrasco Manuel, Ye Guang, Zuo Yibing: RILEM TC 247-DTA round

robin test: mix design and reproducibility of compressive strength of alkali-activated concretes. *Materials and Structures*, Vol. 52, No. 5, 99, 2019, doi: 10.1617/s11527-019-1396-z

[79] Neville A.M., Brooks J.J.: Concrete Technology.

[80] Li Ning, Shi Caijun, Zhang Zuhua, Zhu Deju, Hwang Hyeon-Jong, Zhu Yuhan, Sun Tengjiao: A mixture proportioning method for the development of performance-based alkali-activated slag-based concrete. *Cement and Concrete Composites*, Vol. 93, 163–174, 2018, doi: 10.1016/j.cemconcomp.2018.07.009

[81] Thomas Robert J, Ye Hailong, Radlińska Aleksandra, Peethamparan Sulapha: Alkali-Activated Slag Cement Concrete.

[82] SRPS EN 12350-2:2019 - Testing fresh concrete - Part 2: Slump test. *Institute for Standardization of Serbia, Belgrade*, 2019

[83] Fang Guohao, Ho Wing Kei, Tu Wenlin, Zhang Mingzhong: Workability and mechanical properties of alkali-activated fly ash-slag concrete cured at ambient temperature. *Construction and Building Materials*, Vol. 172, 476–487, 2018, doi: 10.1016/j.conbuildmat.2018.04.008

[84] Da Silva Micael Rubens Cardoso, De Castro Carvalho Ivo, Silvestro Laura, Lei Lei, Kirchheim Ana Paula, Walkley Brant: Advances in Understanding the Mechanisms of Particle Dispersion and Performance of Superplasticisers in Alkali-Activated Materials – a Systematic Literature Review. *Cement and Concrete Composites*, 106360, 2025, doi: 10.1016/j.cemconcomp.2025.106360

[85] Cartwright Christopher, Rajabipour Farshad, Radlińska Aleksandra: Shrinkage Characteristics of Alkali-Activated Slag Cements. *Journal of Materials in Civil Engineering*, Vol. 27, No. 7, B4014007, 2015, doi: 10.1061/(ASCE)MT.1943-5533.0001058

[86] Hojati Maryam, Rajabipour Farshad, Radlińska Aleksandra: Creep of alkali-activated cement mixtures. *Case Studies in Construction Materials*, Vol. 16, e00954, 2022, doi: 10.1016/j.cscm.2022.e00954

[87] Collins Frank, Sanjayan J.G: Cracking tendency of alkali-activated slag concrete subjected to restrained shrinkage. *Cement and Concrete Research*, Vol. 30, No. 5, 791–798, 2000, doi: 10.1016/S0008-8846(00)00243-X

[88] Lee N.K., Jang J.G., Lee H.K.: Shrinkage characteristics of alkali-activated fly ash/slag paste and mortar at early ages. *Cement and Concrete Composites*, Vol. 53, 239–248, 2014, doi: 10.1016/j.cemconcomp.2014.07.007

[89] Ye Hailong, Cartwright Christopher, Rajabipour Farshad, Radlińska Aleksandra: Understanding the drying shrinkage performance of alkali-activated slag mortars. *Cement and Concrete Composites*, Vol. 76, 13–24, 2017, doi: 10.1016/j.cemconcomp.2016.11.010

[90] Kumarappa Darshan Ballekere, Peethamparan Sulapha: Stress-strain characteristics and brittleness index of alkali-activated slag and class C fly ash mortars. *Journal of Building Engineering*, Vol. 32, 101595, 2020, doi: 10.1016/j.jobe.2020.101595

[91] Robayo-Salazar R., Gutiérrez R. Mejía de, Puertas F.: Alkali-activated binary concrete based on a natural pozzolan: physical, mechanical and microstructural characterization. *Materiales de Construcción*, Vol. 69, No. 335, e191–e191, 2019, doi: 10.3989/mc.2019.06618

[92] Adesanya Elijah, Ohenoja Katja, Yliniemi Juho, Illikainen Mirja: Mechanical transformation of phyllite mineralogy toward its use as alkali-activated binder precursor. *Minerals Engineering*, Vol. 145, 106093, 2020, doi: 10.1016/j.mineng.2019.106093

[93] Prinsse Silke, Hordijk Dick A., Ye Guang, Lagendijk Paul, Luković Mladena: Time-dependent material properties and reinforced beams behavior of two alkali-activated types of concrete. *Structural Concrete*, Vol. 21, No. 2, 642–658, 2020, doi: 10.1002/suco.201900235

[94] Law David W., Adam Andi Arham, Molyneaux Thomas K., Patnaikuni Indubhushan: Durability assessment of alkali activated slag (AAS) concrete. *Materials and Structures*, Vol. 45, No. 9, 1425–1437, 2012, doi: 10.1617/s11527-012-9842-1

[95] Collins Frank, Sanjayan J.G: Microcracking and strength development of alkali activated slag concrete. *Cement and Concrete Composites*, Vol. 23, No. 4–5, 345–352, 2001, doi: 10.1016/S0958-9465(01)00003-8

[96] Yang Kai, Yang Changhui, Magee Bryan, Nanukuttan Sreejith, Ye Jianxiong: Establishment of a preconditioning regime for air permeability and sorptivity of alkali-activated slag concrete. *Cement and Concrete Composites*, Vol. 73, 19–28, 2016, doi: 10.1016/j.cemconcomp.2016.06.019

[97] Ismail Idawati, Bernal Susan A., Provis John L., San Nicolas Rackel, Brice David G., Kilcullen Adam R., Hamdan Sinin, Deventer Jannie S.J. van: Influence of fly ash on the water and chloride permeability of alkali-activated slag mortars and concretes. *Construction and Building Materials*, Vol. 48, 1187–1201, 2013, doi: 10.1016/j.conbuildmat.2013.07.106

[98] Puertas F., Palacios M., Manzano H., Dolado J.S., Rico A., Rodríguez J.: A model for the C-A-S-H gel formed in alkali-activated slag cements. *Journal of the European Ceramic Society*, Vol. 31, No. 12, 2043–2056, 2011, doi: 10.1016/j.jeurceramsoc.2011.04.036

[99] Morandeau A., Thiéry M., Dangla P.: Investigation of the carbonation mechanism of CH and C-S-H in terms of kinetics, microstructure changes and moisture properties. *Cement and Concrete Research*, Vol. 56, 153–170, 2014, doi: 10.1016/j.cemconres.2013.11.015

[100] Zhang Xuanhan, Long Kaidi, Liu Wei, Li Lixiao, Long Wu-Jian: Carbonation and Chloride Ions' Penetration of Alkali-Activated Materials: A Review. *Molecules*, Vol. 25, No. 21, 5074, 2020, doi: 10.3390/molecules25215074

[101] Nguyen Thi Nhan, Phung Quoc Tri, Yu Ziyou, Frederickx Lander, Jacques Diederik, Sakellariou Dimitrios, Dauzeres Alexandre, Elsen Jan, Pontikes Yiannis: Alteration in molecular structure of alkali activated slag with various water to binder ratios under accelerated carbonation. *Scientific Reports*, Vol. 12, No. 1, 5524, 2022, doi: 10.1038/s41598-022-09491-4

[102] Bernal Susan A., Provis John L.: Durability of Alkali-Activated Materials: Progress and Perspectives. *Journal of the American Ceramic Society*, Vol. 97, No. 4, 997–1008, 2014, doi: 10.1111/jace.12831

[103] Bernal Susan A., San Nicolas Rackel, Myers Rupert J., Mejía de Gutiérrez Ruby, Puertas Francisca, Deventer Jannie S.J. van, Provis John L.: MgO content of slag controls phase evolution and structural changes induced by accelerated carbonation in alkali-activated binders. *Cement and Concrete Research*, Vol. 57, 33–43, 2014, doi: 10.1016/j.cemconres.2013.12.003

[104] McCaslin Eric R., White Claire E.: A parametric study of accelerated carbonation in alkali-activated slag. *Cement and Concrete Research*, Vol. 145, 106454, 2021, doi: 10.1016/j.cemconres.2021.106454

[105] Bernal Susan A., Provis John L., Myers Rupert J., San Nicolas Rackel, Van Deventer Jannie S. J.: Role of carbonates in the chemical evolution of sodium carbonate-activated slag binders. *Materials and Structures*, Vol. 48, No. 3, 517–529, 2015, doi: 10.1617/s11527-014-0412-6

[106] Bernal Susan A., Provis John L., Brice David G., Kilcullen Adam, Duxson Peter, Deventer Jannie S.J. van: Accelerated carbonation testing of alkali-activated binders significantly underestimates service life: The role of pore solution chemistry. *Cement and Concrete Research*, Vol. 42, No. 10, 1317–1326, 2012, doi: 10.1016/j.cemconres.2012.07.002

[107] Bernal Susan A., Provis John L., Brice David G., Kilcullen Adam, Duxson Peter, Deventer Jannie S. J. van: Accelerated carbonation testing of alkali-activated binders significantly underestimates service life: The role of pore solution chemistry. *Cement and Concrete Research*, Vol. 42, No. 10, 1317–1326, 2012, doi: 10.1016/j.cemconres.2012.07.002

[108] Bernal Susan A., Mejía de Gutiérrez Ruby, Pedraza Alba L., Provis John L., Rodriguez Erich D., Delvasto Silvio: Effect of binder content on the performance of alkali-activated slag concretes. *Cement and Concrete Research*, Vol. 41, No. 1, 1–8, 2011, doi: 10.1016/j.cemconres.2010.08.017

[109] Bernal Susan A.: Effect of the activator dose on the compressive strength and accelerated carbonation resistance of alkali silicate-activated slag/metakaolin blended materials. *Construction and Building Materials*, Vol. 98, 217–226, 2015, doi: 10.1016/j.conbuildmat.2015.08.013

[110] Zhang Xuanhan, Long Kaidi, Liu Wei, Li Lixiao, Long Wu-Jian: Carbonation and Chloride Ions' Penetration of Alkali-Activated Materials: A Review. *Molecules*, Vol. 25, No. 21, 5074, 2020, doi: 10.3390/molecules25215074

[111] Jing Li, Chaofan Yi, Zheng Chen, Wenxiang Cao, Suhong Yin, Haoliang Huang, Jie Hu, Qijun Yu: Relationships between reaction products and carbonation performance of alkali-activated slag with similar pore structure. Vol. 45, 2022, doi: 10.1016/j.jobe.2021.103605

[112] Charitha V, Athira G, Bahurudeen A, Shekhar Shivang: Carbonation of alkali activated binders and comparison with the performance of Ordinary Portland cement and blended cement binders. *Journal of Building Engineering*, Vol. 53, 2022

[113] Huyen Vu Tran, Dang Liet Chi, Kang Gyeongo, Sirivivatnanon Vute: Chloride induced corrosion of steel reinforcement in alkali activated slag concretes: A critical review. *Case Studies in Construction Materials*, Vol. 16, e01112, 2022, doi: 10.1016/j.cscm.2022.e01112

[114] Xu Qiulang, Liu Bin, Dai Lin, Yao Maogui, Pang Xijun: Factors Influencing Chloride Ion Diffusion in Reinforced Concrete Structures. *Materials*, Vol. 17, No. 13, 3296, 2024, doi: 10.3390/ma17133296

[115] Transport Properties of Engineered Cementitious Composites under Chloride Exposure. *ACI Materials Journal*, Vol. 104, No. 6, 2007, doi: 10.14359/18964

[116] Honglei Chang, Zuquan Jin, Tiejun Zhao, Benzhen Wang, Zhe Li, Jian Liu: Capillary suction induced water absorption and chloride transport in non-saturated concrete: The influence of humidity, mineral admixtures and sulfate ions. *Construction and Building Materials*, Vol. 236, 117581, 2020, doi: 10.1016/j.conbuildmat.2019.117581

[117] Runci Antonino, Provis John, Serdar Marijana: Microstructure as a key parameter for understanding chloride ingress in alkali-activated mortars. *Cement and Concrete Composites*, Vol. 134, 104818, 2022, doi: 10.1016/j.cemconcomp.2022.104818

[118] Yang Tao, Zhang Zuhua, Zhang Feng, Gao Yanan, Wu Qisheng: Chloride and heavy metal binding capacities of hydrotalcite-like phases formed in greener one-part sodium carbonate-activated slag cements. *Journal of Cleaner Production*, Vol. 253, 120047, 2020, doi: 10.1016/j.jclepro.2020.120047

[119] Runci Antonino, Serdar Marijana: Effect of curing time on the chloride diffusion of alkali-activated slag. *Case Studies in Construction Materials*, Vol. 16, e00927, 2022, doi: 10.1016/j.cscm.2022.e00927

[120] Haha M. Ben, Lothenbach B., Le Saout G., Winnefeld F.: Influence of slag chemistry on the hydration of alkali-activated blast-furnace slag — Part I: Effect of MgO. *Cement and Concrete Research*, Vol. 41, No. 9, 955–963, 2011, doi: 10.1016/j.cemconres.2011.05.002

[121] Rathod Nikhil, Chippagiri Ravijanya, Ralegaonkar Rahul V.: Cleaner production of geopolymer materials: A critical review of waste-derived activators. *Materials Today: Proceedings*, 2023, doi: 10.1016/j.matpr.2023.03.502

[122] Bernal Susan A., Rodríguez Erich D., Mejia De Gutiérrez Ruby, Provis John L., Delvasto Silvio: Activation of Metakaolin/Slag Blends Using Alkaline Solutions Based on Chemically Modified Silica Fume and Rice Husk Ash. *Waste and Biomass Valorization*, Vol. 3, No. 1, 99–108, 2012, doi: 10.1007/s12649-011-9093-3

[123] Vassilev Stanislav V., Vassileva Christina G.: Water-Soluble Fractions of Biomass and Biomass Ash and Their Significance for Biofuel Application. *Energy & Fuels*, Vol. 33, No. 4, 2763–2777, 2019, doi: 10.1021/acs.energyfuels.9b00081

[124] Athira VS, Charitha V, Athira G, Bahurudeen A: Agro-waste ash based alkali-activated binder: Cleaner production of zero cement concrete for construction. *Journal of Cleaner Production*, Vol. 286, 125429, 2021, doi: 10.1016/j.jclepro.2020.125429

[125] Matalkah Faris, Soroushian Parviz, Balchandra Anagi, Peyvandi Amirpasha: Characterization of Alkali-Activated Nonwood Biomass Ash–Based Geopolymer Concrete. *Journal of Materials in Civil Engineering*, Vol. 29, No. 4, 04016270, 2017, doi: 10.1061/(ASCE)MT.1943-5533.0001801

[126] Yurt Ümit, Bekar Fatih: Comparative study of hazelnut-shell biomass ash and metakaolin to improve the performance of alkali-activated concrete: A sustainable greener alternative. *Construction and Building Materials*, Vol. 320, 126230, 2022, doi: 10.1016/j.conbuildmat.2021.126230

[127] Cheah Chee Ban, Part Wei Ken, Ramli Mahyuddin: The hybridizations of coal fly ash and wood ash for the fabrication of low alkalinity geopolymer load bearing block cured at ambient temperature. *Construction and Building Materials*, Vol. 88, 41–55, 2015, doi: 10.1016/j.conbuildmat.2015.04.020

[128] Jurado-Contreras S., Bonet-Martínez E., Sánchez-Soto P. J., Gencel O., Eliche-Quesada D.: Synthesis and characterization of alkali-activated materials containing biomass fly ash and metakaolin: effect of the soluble salt content of the residue. *Archives of Civil and Mechanical Engineering*, Vol. 22, No. 3, 121, 2022, doi: 10.1007/s43452-022-00444-2

[129] Piotr Prochon: Geopolymer composites based on fly ash from co-combustion of coal and biomass. Doctoral dissertation, Warshaw University of Technology, 2020.

[130] Bernal S. A., Rodríguez E. D., Gutiérrez R. Mejía de, Provis J. L.: Performance at high temperature of alkali-activated slag pastes produced with silica fume and rice husk ash based activators. *Materiales de Construcción*, Vol. 65, No. 318, e049–e049, 2015, doi: 10.3989/mc.2015.03114

[131] Soriano Lourdes, Font Alba, Tashima Mauro M., Monzó José, Borrachero Maria Victoria, Bonifácio Thaís, Payá Jordi: Almond-shell biomass ash (ABA): A

greener alternative to the use of commercial alkaline reagents in alkali-activated cement. *Construction and Building Materials*, Vol. 290, 123251, 2021, doi: 10.1016/j.conbuildmat.2021.123251

[132] Peys Arne, Rahier Hubert, Pontikes Yiannis: Potassium-rich biomass ashes as activators in metakaolin-based inorganic polymers. *Applied Clay Science*, Vol. 119, 401–409, 2016, doi: 10.1016/j.clay.2015.11.003

[133] Soriano L., Font A., Borrachero M. V., Monzó J. M., Payá J., Tashima M. M.: Biomass ashes to produce an alternative alkaline activator for alkali-activated cements. *Materials Letters*, Vol. 308, 131198, 2022, doi: 10.1016/j.matlet.2021.131198

[134] Alonso M.M., Gascó C., Morales M. Martín, Suárez-Navarro J.A., Zamorano M., Puertas F.: Olive biomass ash as an alternative activator in geopolymer formation: A study of strength, radiology and leaching behaviour. *Cement and Concrete Composites*, Vol. 104, 103384, 2019, doi: 10.1016/j.cemconcomp.2019.103384

[135] Mejía J. M., Gutiérrez R. Mejía de, Puertas F.: Rice husk ash as a source of silica in alkali-activated fly ash and granulated blast furnace slag systems. *Materiales de Construcción*, Vol. 63, No. 311, 361–375, 2013, doi: 10.3989/mc.2013.04712

[136] Moraes J.C.B., Font A., Soriano L., Akasaki J.L., Tashima M.M., Monzó J., Borrachero M.V., Payá J.: New use of sugar cane straw ash in alkali-activated materials: A silica source for the preparation of the alkaline activator. *Construction and Building Materials*, Vol. 171, 611–621, 2018, doi: 10.1016/j.conbuildmat.2018.03.230

[137] Gomonsirisuk Khemmakorn, Thavorniti Parjaree: Use of Water Glass from Rice Husk and Bagasse Ashes in the Preparation of Fly Ash Based Geopolymer. *Key Engineering Materials*, Vol. 798, 364–369, 2019, doi: 10.4028/www.scientific.net/KEM.798.364

[138] Tchakouté Hervé K., Rüscher Claus H., Kong Sakeo, Kamseu Elie, Leonelli Cristina: Geopolymer binders from metakaolin using sodium waterglass from waste glass and rice husk ash as alternative activators: A comparative study. *Construction and Building Materials*, Vol. 114, 276–289, 2016, doi: 10.1016/j.conbuildmat.2016.03.184

[139] Tchakouté Hervé Kouamo, Rüscher Claus Henning, Kong Sakeo, Ranjbar Navid: Synthesis of sodium waterglass from white rice husk ash as an activator to produce metakaolin-based geopolymer cements. *Journal of Building Engineering*, Vol. 6, 252–261, 2016, doi: 10.1016/j.jobe.2016.04.007

[140] Villaquirán-Caicedo Mónica A.: Studying different silica sources for preparation of alternative waterglass used in preparation of binary geopolymer binders from metakaolin/boiler slag. *Construction and Building Materials*, Vol. 227, 116621, 2019, doi: 10.1016/j.conbuildmat.2019.08.002

[141] Tchakouté Hervé Kouamo, Rüscher Claus Henning, Hinsch Malte, Djobo Jean Noël Yankwa, Kamseu Elie, Leonelli Cristina: Utilization of sodium waterglass from sugar cane bagasse ash as a new alternative hardener for producing metakaolin-based geopolymer cement. *Geochemistry*, Vol. 77, No. 2, 257–266, 2017, doi: 10.1016/j.chemer.2017.04.003

[142] Tong Kien T., Vinai Raffaele, Soutsos Marios N.: Use of Vietnamese rice husk ash for the production of sodium silicate as the activator for alkali-activated binders. *Journal of Cleaner Production*, Vol. 201, 272–286, 2018, doi: 10.1016/j.jclepro.2018.08.025

[143] Font Alba, Soriano Lourdes, Moraes Pinheiro Sayonara Maria de, Tashima Mauro M., Monzó José, Borrachero Maria Victoria, Payá Jordi: Design and properties of 100% waste-based ternary alkali-activated mortars: Blast furnace slag, olive-stone biomass ash and rice husk ash. *Journal of Cleaner Production*, Vol. 243, 118568, 2020, doi: 10.1016/j.jclepro.2019.118568

[144] Omur Tarik, Kanat Derya, Kabay Nihat: Innovative use of hazelnut shell ash as an alkali activator: A comparative analysis with commercial activators. *Journal of Building Engineering*, Vol. 90, 109466, 2024, doi: 10.1016/j.jobe.2024.109466

[145] Zhu Zhijing, Zhang Chunyu, Liu Rentai, Li Shucai, Wang Meng: Sunflower straw ash as an alternative activator in alkali-activated grouts: A new 100% waste-based material. *Ceramics International*, Vol. 49, No. 19, 32308–32312, 2023, doi: 10.1016/j.ceramint.2023.06.306

[146] Efeovbokhan Vincent Enontiemonria, Omoleye James Abiodun, Kalu Egwu Eric: Extraction and Use of Potassium Hydroxide from Ripe Plantain Peels Ash for Biodiesel Production. Vol. 10, 2016

[147] Font Alba, Soriano Lourdes, Moraes Pinheiro Sayonara Maria de, Tashima Mauro M., Monzó José, Borrachero Maria Victoria, Payá Jordi: Design and properties of 100% waste-based ternary alkali-activated mortars: Blast furnace slag, olive-stone biomass ash and rice husk ash. *Journal of Cleaner Production*, Vol. 243, 118568, 2020, doi: 10.1016/j.jclepro.2019.118568

[148] Zhu Zhijing, Xu Xianjie, Liu Rentai, Liu Peng, Tang Haotian, Gong Yu'an, Zhang Chunyu, Li Xiuhao, Liu Yankai, Bai Jiwen, Chen Mengjun: Feasibility study of highly alkaline biomass ash to activate alkali-activated grouts. *Construction and Building Materials*, Vol. 393, 132067, 2023, doi: 10.1016/j.conbuildmat.2023.132067

[149] Lima F.S., Gomes T.C.F., Moraes J.C.B.: Effect of coffee husk ash as alkaline activator in one-part alkali-activated binder. *Construction and Building Materials*, Vol. 362, 129799, 2023, doi: 10.1016/j.conbuildmat.2022.129799

[150] Soriano Lourdes, Font Alba, Tashima Mauro M., Monzó José, Borrachero María Victoria, Payá Jordi: One-part blast furnace slag mortars activated with almond-shell biomass ash: A new 100% waste-based material. *Materials Letters*, Vol. 272, 127882, 2020, doi: 10.1016/j.matlet.2020.127882

[151] Bedov Olivera, Andabaka Ana, Draganić Suzana: Turning Agricultural Biomass Ash into a Valuable Resource in the Construction Industry—Exploring the Potential of Industrial Symbiosis. *Buildings*, Vol. 15, No. 2, 273, 2025, doi: 10.3390/buildings15020273

[152] Nikolov Aleksandar, Kostov Vladislav, Petrova Nadia, Tsvetanova Liliya, Vassilev Stanislav V., Titorenkova Rositsa: Sunflower Shells Biomass Fly Ash as Alternative Alkali Activator for One-Part Cement Based on Ladle Slag. *Ceramics*, Vol. 8, No. 3, 79, 2025, doi: 10.3390/ceramics8030079

[153] BSI: Construction materials – Alkali-activated cementitious material and concrete – Specification.

[154] SRPS EN 1936:2009 - Metode ispitivanja prirodnog kamena - Određivanje stvarne i prividne zapreminske mase i ukupne i otvorene poroznosti. *Institute for Standardization of Serbia*, Belgrade, 2009

[155] SRPS EN 196-6:2019 - Metode ispitivanja cementa – Deo 6: Određivanje finoće mliva. *Institute for Standardization of Serbia*, Belgrade, 2019

[156] SRPS EN 1015-3:2008 - Methods of test for mortar for masonry - Part 3: Determination of consistence of fresh mortar (by flow table). *Institute for Standardization of Serbia*, Belgrade, 2008

[157] SRPS EN 196-1: 2017 - Methods of testing cement - Part 1: Determination of strength. *Institute for Standardization of Serbia*, Belgrade, 2017

[158] SRPS EN 196-3:2017 - Methods of testing cement - Part : Determination of setting times and soundness. *Institute for Standardization of Serbia*, Belgrade, 2017

[159] SRPS EN 12350-1:2019 - Testing fresh concrete - Part 1: Sampling and common apparatus. *European Committee for Standardisation - CEN*, 2019

[160] SRPS EN 12350-2:2019 - Testing fresh concrete - Part 2: Slump test. *European Committee for Standardisation - CEN*, 2019

[161] SRPS EN 12350-7:2019 - Testing fresh concrete - Part 7: Air content - Pressure methods. *European Committee for Standardisation - CEN*, 2019

[162] SRPS EN 12350-6:2019 - Testing fresh concrete - Part 6: Density. *European Committee for Standardisation - CEN*, 2019

[163] SRPS EN 12390-7:2019 - Testing hardened concrete - Part 7: Density of hardened concrete. *European Committee for Standardisation - CEN*, 2019

[164] ASTM C 1585-04 - Standard Test Method for Measurement of Rate of Absorption of Water by Hydraulic Cement Concretes. 2004

[165] SRPS EN 12390-16:2019 - Testing hardened concrete - Part 16: Determination of the shrinkage of concrete. *Institute for Standardization of Serbia*, Belgrade, 2019

[166] SRPS EN 12390-3:2019 - Testing hardened concrete – Part 3: Compressive strength of test specimens. *European Committee for Standardisation - CEN*, 2019

[167] SRPS EN 12390-5:2019 - Testing hardened concrete - Part 5: Flexural strength of test specimens. *Institute for Standardization of Serbia*, Belgrade, 2019

[168] SRPS EN 12390-8: 2019 - Testing hardened concrete - Part 8: Depth of penetration of water under pressure. *Institute for Standardization of Serbia*, Belgrade, 2019

[169] SRPS EN12390-12: 2020 - Testing hardened concrete - Part 12: Determination of the carbonation resistance of concrete - Accelerated carbonation method. *Institute for Standardization of Serbia*, Belgrade, 2020

[170] NT build 492 - Concrete mortar and cement-based repair materials: Chloride migration coefficient from non-steady-state migration experiments. *NORDTEST*, Espoo, Finland, 1999

[171] Ke Xinyuan, Bernal Susan A., Provis John L.: Uptake of chloride and carbonate by Mg-Al and Ca-Al layered double hydroxides in simulated pore solutions of alkali-activated slag cement. *Cement and Concrete Research*, Vol. 100, 1–13, 2017, doi: 10.1016/j.cemconres.2017.05.015

[172] SRPS EN 206: 2014 - Concrete - Specification, performance, production and conformity. *Institute for Standardization of Serbia*, Belgrade, 2014

[173] Mehta Povindar K., Monteiro Paulo J. M., Monteiro Paulo J.: Concrete: microstructure, properties, and materials. *McGraw-Hill*, New York, 2006

[174] HRN 1128: 2023 - Concrete - National requirements to HRN EN 206:2021. *Croatian Standards Institute*, Zagreb, Croatia, 2023

[175] Ghorbani Saeid, Stefanini Laura, Sun Yubo, Walkley Brant, Provis John L., De Schutter Geert, Matthys Stijn: Characterisation of alkali-activated stainless steel slag and blast-furnace slag cements. *Cement and Concrete Composites*, Vol. 143, 105230, 2023, doi: 10.1016/j.cemconcomp.2023.105230

[176] Lecomte I., Henrist C., Liégeois M., Maseri F., Rulmont A., Cloots R.: (Micro)-structural comparison between geopolymers, alkali-activated slag cement and Portland cement. *Journal of the European Ceramic Society*, Vol. 26, No. 16, 3789–3797, 2006, doi: 10.1016/j.jeurceramsoc.2005.12.021

[177] Sun Yubo, De Lima Luiz Miranda, Rossi Laura, Jiao Dengwu, Li Zhenming, Ye Guang, De Schutter Geert: Interpretation of the early stiffening process in alkali-activated slag pastes. *Cement and Concrete Research*, Vol. 167, 107118, 2023, doi: 10.1016/j.cemconres.2023.107118

[178] Ismail Idawati, Bernal Susan A., Provis John L., San Nicolas Rackel, Hamdan Sinin, Deventer Jannie S. J. van: Modification of phase evolution in alkali-activated blast furnace slag by the incorporation of fly ash. *Cement and*

Concrete Composites, Vol. 45, 125–135, 2014, doi: 10.1016/j.cemconcomp.2013.09.006

[179] Li Botao, Sun Qi, Chen Xiaoxiao, Xu Ziming, Yang Liang: Preparation and microstructure analysis of alkali-activated ground granulated blast furnace slag-steel slag grouting materials. *Case Studies in Construction Materials*, Vol. 20, e03235, 2024, doi: 10.1016/j.cscm.2024.e03235

[180] Bílek Vlastimil, Švec Jiří, Másilko Jiří, Sedlačík Martin, Materak Kalina, Wieczorek Alicja, Koniorczyk Marcin, Hajzler Jan, Kucharczyková Barbara: Comparison of thermogravimetry response of alkali-activated slag and Portland cement pastes after stopping their hydration using solvent exchange method. *Journal of Thermal Analysis and Calorimetry*, Vol. 150, No. 2, 1013–1037, 2025, doi: 10.1007/s10973-024-13552-3

[181] Moraes J.C.B., Font A., Soriano L., Akasaki J.L., Tashima M.M., Monzó J., Borrachero M.V., Payá J.: New use of sugar cane straw ash in alkali-activated materials: A silica source for the preparation of the alkaline activator. *Construction and Building Materials*, Vol. 171, 611–621, 2018, doi: 10.1016/j.conbuildmat.2018.03.230

[182] Krieger Irvin M., Dougherty Thomas J.: A Mechanism for Non-Newtonian Flow in Suspensions of Rigid Spheres. *Transactions of the Society of Rheology*, Vol. 3, No. 1, 137–152, 1959, doi: 10.1122/1.548848

[183] Westerholm Mikael, Lagerblad Björn, Silfwerbrand Johan, Forssberg Eric: Influence of fine aggregate characteristics on the rheological properties of mortars. *Cement and Concrete Composites*, Vol. 30, No. 4, 274–282, 2008, doi: 10.1016/j.cemconcomp.2007.08.008

[184] Bakharev T., Sanjayan J.G., Cheng Y.-B.: Effect of elevated temperature curing on properties of alkali-activated slag concrete. *Cement and Concrete Research*, Vol. 29, No. 10, 1619–1625, 1999, doi: 10.1016/S0008-8846(99)00143-X

[185] Aliabdo Ali A., Abd Elmoaty Abd Elmoaty M., Emam Mohammed A.: Factors affecting the mechanical properties of alkali activated ground granulated blast furnace slag concrete. *Construction and Building Materials*, Vol. 197, 339–355, 2019, doi: 10.1016/j.conbuildmat.2018.11.086

[186] Tibbetts Caitlin M., Tao Chengcheng, Paris Jerry M., Ferraro Christopher C.: Mercury intrusion porosimetry parameters for use in concrete penetrability qualification using the Katz-Thompson relationship. *Construction and Building Materials*, Vol. 263, 119834, 2020, doi: 10.1016/j.conbuildmat.2020.119834

[187] Park S. M., Jang J. G., Lee H. K.: Unlocking the role of MgO in the carbonation of alkali-activated slag cement. *Inorganic Chemistry Frontiers*, Vol. 5, No. 7, 1661–1670, 2018, doi: 10.1039/C7QI00754J

[188] Gao Hailiang, Yu Ranran, Liu Jun, Zhang Wei, Li Mengmeng, Jia Yuyue, Ye Yongbin, Zhong Shunjie, Zhuang Can, Zhu Hong, Su Qunyong, Huang Bo-Tao, Wu Hao, Sun Jia, Hou Dongshuai: Study on the molecular structure and mechanical properties of potassium ion uptake in calcium silicate hydrate.

Construction and Building Materials, Vol. 481, 141651, 2025, doi: 10.1016/j.conbuildmat.2025.141651

[189] Sant Gaurav, Kumar Aditya, Patapy Cedric, Le Saout Gwenn, Scrivener Karen: The influence of sodium and potassium hydroxide on volume changes in cementitious materials. *Cement and Concrete Research*, Vol. 42, No. 11, 1447–1455, 2012, doi: 10.1016/j.cemconres.2012.08.012

[190] Ye Hailong, Radlińska Aleksandra: Shrinkage mechanisms of alkali-activated slag. *Cement and Concrete Research*, Vol. 88, 126–135, 2016, doi: 10.1016/j.cemconres.2016.07.001

[191] Bernal Susan A., Provis John L.: Durability of Alkali-Activated Materials: Progress and Perspectives. *Journal of the American Ceramic Society*, Vol. 97, No. 4, 997–1008, 2014, doi: 10.1111/jace.12831

[192] Sadeghian Golnaz, Behfarnia Kiachehr, Teymouri Mohammad: Drying shrinkage of one-part alkali-activated slag concrete. *Journal of Building Engineering*, Vol. 51, 104263, 2022, doi: 10.1016/j.jobe.2022.104263

[193] Thomas R.J., Lezama Diego, Peethamparan Sulapha: On drying shrinkage in alkali-activated concrete: Improving dimensional stability by aging or heat-curing. *Cement and Concrete Research*, Vol. 91, 13–23, 2017, doi: 10.1016/j.cemconres.2016.10.003

[194] ACI224R-01 Control of Cracking in Concrete Structures. 2001, doi: doi:10.14359/10632.

[195] Granger L., Torrenti J. -M., Acker P.: Thoughts about drying shrinkage: Experimental results and quantification of structural drying creep. *Materials and Structures*, Vol. 30, No. 10, 588–598, 1997, doi: 10.1007/BF02486900

[196] Li Zhenming, Zhang Shizhe, Liang Xuhui, Ye Guang: Cracking potential of alkali-activated slag and fly ash concrete subjected to restrained autogenous shrinkage. *Cement and Concrete Composites*, Vol. 114, 103767, 2020, doi: 10.1016/j.cemconcomp.2020.103767

[197] McCaslin Eric R., White Claire E.: A parametric study of accelerated carbonation in alkali-activated slag. *Cement and Concrete Research*, Vol. 145, 106454, 2021, doi: 10.1016/j.cemconres.2021.106454

[198] Ye Hailong, Huang Le, Chen Zhijian: Influence of activator composition on the chloride binding capacity of alkali-activated slag. *Cement and Concrete Composites*, Vol. 104, 103368, 2019, doi: 10.1016/j.cemconcomp.2019.103368

APPENDECES

APPENDIX 1 - Properties of aggregates

Properties of crushed limestone aggregate used in Phase 2

Grading of the aggregate fractions 0/4, 4/8 and 8/16 (Phase 2)

Retention mass Ri [g]										
	P	**0.125**	**0.25**	**0.5**	**1**	**2**	**4**	**8**	**16**	**31.5**
0/4	4	78.1	80	117	190.7	305	47.2	1.9	0	0
4/8	1	1	0.5	0.8	2.6	35.1	745.9	48.2	0	0
8/16	0.9	0.1	0.2	0.2	0.6	0.4	18.2	1219.5	70.4	0
Retention percentage [%]										
0/4	0.5	9.5	9.7	14.2	23.1	37.0	5.7	0.2	0.0	0.0
4/8	0.1	0.1	0.1	0.1	0.3	4.2	89.3	5.8	0.0	0.0
8/16	0.1	0.0	0.0	0.0	0.0	0.0	1.4	93.1	5.4	0.0
Cumulative retention percentage, Zi [%]										
0/4	100.0	99.5	90.0	80.3	66.1	43.0	6.0	0.2	0.0	0.0
4/8	100.0	99.9	99.8	99.7	99.6	99.3	95.1	5.8	0.0	0.0
8/16	100.0	99.9	99.9	99.9	99.9	99.8	99.8	98.4	5.4	0.0
Cumulative passes, Yi [%]										
0/4	0.0	0.5	10.0	19.7	33.9	57.0	94.0	99.8	100.0	100.0
4/8	0.0	0.1	0.2	0.3	0.4	0.7	4.9	94.2	100.0	100.0
8/16	0.0	0.1	0.1	0.1	0.1	0.2	0.2	1.6	94.6	100.0

Modulus of fineness of the fraction 0/4:

$$M = \frac{\sum Z_i}{100} = 3.15$$

Water absorption of the aggregate fractions (data provided by the manufacturer)

Fraction	**0/4**	**4/8**	**8/16**
WA [%]	1.3	0.6	0.4

Properties of crushed limestone aggregate used in Phase 4

Grading of the aggregate fractions 0/4, 4/8 and 8/16 (Phase 4)

	Retain mass Ri [g]									
	P	**0.125**	**0.25**	**0.5**	**1**	**2**	**4**	**8**	**16**	**31.5**
0/4	78.2	33	44.7	72.6	135.8	277.5	112.3	0	0	0
4/8	4	0.1	0.1	0.1	0.3	2.2	808.1	43.5	0	0
8/16	4.6	0.1	0.1	0.1	0.1	0.3	38.9	2761.2	90.5	0
	Retention percentage [%]									
0/4	10.4	4.4	5.9	9.6	18.0	36.8	14.9	0.0	0.0	0.0
4/8	0.5	0.0	0.0	0.0	0.0	0.3	94.2	5.1	0.0	0.0
8/16	0.2	0.0	0.0	0.0	0.0	0.0	1.3	95.3	3.1	0.0
	Cumulative retention percentage, Zi [%]									
0/4	100.0	89.6	85.3	79.3	69.7	51.7	14.9	0.0	0.0	0.0
4/8	100.0	99.6	99.6	99.6	99.5	99.5	99.3	5.1	0.0	0.0
8/16	100.0	99.8	99.8	99.8	99.8	99.8	99.8	98.5	3.1	0.0
	Cumulative passes, Yi [%]									
0/4	0.0	10.4	14.7	20.7	30.3	48.3	85.1	100.0	100.0	100.0
4/8	0.0	0.4	0.4	0.4	0.5	0.5	0.7	94.9	100.0	100.0
8/16	0.0	0.2	0.2	0.2	0.2	0.2	0.2	1.5	96.9	100.0

Modulus of fineness of the fraction 0/4:

$$M = \frac{\sum Z_i}{100} = 3.34$$

Water absorption of the aggregate fractions (data provided by the manufacturer)

Fraction	**0/4**	**4/8**	**8/16**
WA [%]	0.8	0.7	0.6

APPENDIX 2 - Fresh-state properties of AACs (Phase 2)

Results of entrained air, fresh-state density and slump of ten AAC mixes

	Mix									
	R1	**R2**	**R3**	**R4**	**R5**	**R6**	**R7**	**R8**	**R9**	**R10**
Temperature [˚C]	24.8	23.9	24.7	24.3	24.2	21.8	21.4	20.3	21.3	21.4
Δp [%]	1.5	2.4	2.0	1.3	1.4	1.3	1.5	1.2	2.0	1.6
γ [kg/m3]	2490	2480	2474	2468	2500	2460	2520	2460	2490	2530
Slump [mm]	130	10	30	50	55	78	75	120	157	212
Slump class	S3	S1	S1	S2	S2	S2	S2	S3	S3	S4

APPENDIX 3 - Compressive strength of AACs (Phase 2)

The compressive strength of the mixes R1, R2, and R3 after 2, 7 and 28 days of curing

Mix	Day of testing	Sample	γ [kg/m^3]	γ_{avg} [kg/m^3]	P [kN]	f_c [MPa]	$f_{c,avg}$ [MPa]
R1	2	R1/1	2448	2441	374.85	16.66	16.66
		R1/2	2432		361.50	16.07	
		R1/3	2443		375.81	16.69	
	7	R1/4	2461	2470	603.51	26.82	26.80
		R1/5	2477		608.29	27.04	
		R1/6	2461		597.22	26.54	
	28	R1/7	2491	2483	866.28	38.50	38.32
		R1/8	2486		854.60	37.98	
		R1/9	2472		858.77	38.17	
R2	2	R2/1	2514	2441	591.98	26.31	26.09
		R2/2	2506		579.15	25.74	
		R2/3	2510		589.95	26.22	
	7	R2/4	2490	2502	892.80	39.68	39.42
		R2/5	2508		876.38	38.95	
		R2/6	2509		891.68	39.63	
	28	R2/7	2512	2510	1287.90	57.24	56.92
		R2/8	2511		1268.55	56.38	
		R2/9	2507		1285.65	57.14	
R3	2	R3/1	2484	2480	350.55	15.58	15.41
		R3/2	2476		342.23	15.21	
		R3/3	2480		347.40	15.44	
	7	R3/4	2474	2470	543.38	24.15	23.89
		R3/5	2466		530.33	23.57	
		R3/6	2470		538.88	23.95	
	28	R3/7	2474	2470	757.58	33.67	33.31
		R3/8	2466		739.57	32.87	
		R3/9	2470		751.27	33.39	

The compressive strength of the mixes R4, R5, and R6 after 2, 7 and 28 days of curing

Mix	Day of testing	Sample	γ [kg/m^3]	γ_{avg} [kg/m^3]	P [kN]	f_c [MPa]	$f_{c,avg}$ [MPa]
R4	2	R4/1	2484	2480	314.55	13.98	13.83
		R4/2	2476		307.12	13.65	
		R4/3	2480		311.85	13.86	
	7	R4/4	2479	2475	504.90	22.44	22.20
		R4/5	2471		492.98	21.91	
		R4/6	2475		500.62	22.25	
	28	R4/7	2444	2440	738.90	32.84	32.49
		R4/8	2436		721.35	32.06	
		R4/9	2440		732.83	32.57	
R5	2	R5/1	2516	2512	774.45	34.42	34.05
		R5/2	2508		756.00	33.60	
		R5/3	2512		767.93	34.13	
	7	R5/4	2504	2500	1080.00	48.00	47.49
		R5/5	2496		1054.35	46.86	
		R5/6	2500		1071.22	47.61	
	28	R5/7	2510	2506	1427.40	63.44	62.76
		R5/8	2502		1393.42	61.93	
		R5/9	2506		1415.47	62.91	
R6	2	R6/1	2494	2490	554.85	24.66	24.40
		R6/2	2486		541.80	24.08	
		R6/3	2490		550.35	24.46	
	7	R6/4	2484	2480	1140.08	50.67	50.13
		R6/5	2476		1113.08	49.47	
		R6/6	2480		1130.62	50.25	
	28	R6/7	2491	2487	1236.15	54.94	54.35
		R6/8	2483		1206.67	53.63	
		R6/9	2487		1225.80	54.48	

The compressive strength of the mixes R7, R8, and R9 after 2, 7 and 28 days of curing

Mix	Day of testing	Sample	γ[kg/m^3]	γ_{avg} [kg/m^3]	P [kN]	f_c [MPa]	$f_{c,avg}$ [MPa]
R7	2	R7/1	2479	2475	951.30	42.28	41.83
		R7/2	2471		928.80	41.28	
		R7/3	2475		943.42	41.93	
	7	R7/4	2492	2488	1451.92	64.53	63.84
		R7/5	2484		1417.50	63.00	
		R7/6	2488		1439.78	63.99	
	28	R7/7	2483	2479	1708.88	75.95	75.14
		R7/8	2475		1668.38	74.15	
		R7/9	2479		1694.70	75.32	
R8	2	R8/1	2488	2484	597.60	26.56	26.28
		R8/2	2480		583.42	25.93	
		R8/3	2484		592.88	26.35	
	7	R8/4	2483	2479	1140.08	50.67	50.13
		R8/5	2475		1113.08	49.47	
		R8/6	2479		1130.62	50.25	
	28	R8/7	2485	2481	1454.63	64.65	63.96
		R8/8	2477		1420.20	63.12	
		R8/9	2481		1442.47	64.11	
R9	2	R9/1	2504	2500	799.87	35.55	35.17
		R9/2	2496		780.98	34.71	
		R9/3	2500		793.12	35.25	
	7	R9/4	2476	2472	1318.72	58.61	57.98
		R9/5	2468		1287.22	57.21	
		R9/6	2472		1307.70	58.12	
	28	R9/7	2487	2483	1585.12	70.45	69.70
		R9/8	2479		1547.55	68.78	
		R9/9	2483		1572.08	69.87	

The compressive strength of the mixes R10 after 2, 7 and 28 days of curing

Mix	Day of testing	Sample	γ[kg/m^3]	γ_{avg} [kg/m^3]	P [kN]	f_c [MPa]	$f_{c,avg}$ [MPa]
R10	2	R10/1	2499	2495	974.70	43.32	42.86
		R10/2	2491		951.52	42.29	
		R10/3	2495		966.82	42.97	
	7	R10/4	2492	2488	1498.72	66.61	65.90
		R10/5	2484		1463.17	65.03	
		R10/6	2488		1486.35	66.06	
	28	R10/7	2485	2481	1671.75	74.30	73.51
		R10/8	2477		1632.15	72.54	
		R10/9	2481		1658.02	73.69	

APPENDIX 4 - Durability properties of selected AACs (Phase 2)

Depth of water penetration under pressure: concrete mixes R2, R5, and R7

	R2/1	R2/2	R2/3	R5/1	R5/2	R5/3	R7/1	R7/2	R7/3
d [mm]	20	19	17.5	9.8	15	11.3	75.6	87.3	72.2

Measured carbonation depths of concrete mixes R2, R5 and R7 after 7 and 28 days of exposure to accelerated carbonation

R2		R5		R7	
		d_k [mm]			
7d	28d	7d	28d	7d	28d
10.86	17.78	6.9	18.9	9.5	17.64
9.52	16.85	6.87	18.2	10.31	20.04
8.37	17.83	9.0	17.6	4.54	20.1
8.22	19.93	7.43	20.1	5.0	22.19
8.2	19.86	6.91	18	9.14	19.66
8.5	17.21	8.05	19	8.7	18.22
8.4	19.47	8.8	17.3	8.21	19.2
9.11	18.13	8.14	18.5	8.43	20.16
7.92	19.5	7.02	18.4	8.49	21.29
8.66	19.14	9.85	17.1	9.97	20.93
8.24	19.35	6.21	19.8	6.95	18.76
7.79	19.62	7.69	16.5	10.11	18.96
11.0	20.0	7.38	17.1	7.82	18.91
8.88	22.28	9.8	13.6	7.1	18.25
11.32	19.8	8.26	17.7	8.37	19.84
10.18	20.8	7.11	2.33	7.24	18.17
Average carbonation depths [mm]					
9.1	19.1	6.7	17.1	8.1	19.4

Test parameters, chloride penetration depths, and coefficients after 28 days of curing for the mix R2, R5, and R7

Mix R2		**Sample**		
		1	**2**	**3**
Test parameters	L [mm]	50.88	50.8	51.1
	T_{avg} (°C)	23.45	23.09	23.09
	U [V]	60	60	60
	Test duration [h]	48	48	48
Chloride penetration depths [mm]	D6	19.39	3.02	2.18
	D4	10.54	2.07	1.78
	D2	5.05	0	2.04
	D1	4.75	2.57	1.64
	D3	5.67	3.52	2.83
	D5	10.21	0	3.3
	D7	9.17	3.39	2.46
	D_{avg} [mm]	9.3	2.1	2.3
	E [V/m]	1139.937107	1141.732283	1135.029354
	α	0.008392	0.008381	0.008405
	$D_{nssm,avg}$ [10^{-12} m^2/s]	0.109	0.332	0.684
	$D_{nssm,avg}$ [10^{-12} m^2/s]		**0.70**	
Mix R5		**Sample**		
		1	**2**	**3**
Test parameters	L [mm]	50.5	50.8	51.1
	T_{avg} (°C)	23.09	23.09	23.09
	U [V]	6	60	60
	Test duration [h]	24	24	24
Chloride penetration depths [mm]	D6	0	3.02	2.18
	D4	3.71	2.07	1.78
	D2	2.58	0	2.04
	D1	1.9	2.57	1.64
	D3	1.89	3.52	2.83
	D5	0	0	3.3
	D7	2.06	3.39	2.46
	D_{avg} [mm]	1.7	2.1	2.3
	E [V/m]	1148.514851	1141.732283	1135.029354
	α	0.008356	0.008381	0.008405
	$D_{nssm,avg}$ [10^{-12} m^2/s]	0.356	0.439	0.0498
	$D_{nssm,avg}$ [10^{-12} m^2/s]		**0.43**	

Mix R7		**Sample**		
		1	**2**	**3**
Test parameters	L [mm]	50.67	50.881	50.81
	T_{avg} (°C)	24.72	24.72	24.72
	U [V]	60	60	60
	Test duration [h]	24	24	24
Chloride penetration depths [mm]	D6	10.53	6.87	12.53
	D4	0.1	8.26	11.55
	D2	7.18	9.27	11.66
	D1	8.52	12.73	8.67
	D3	7.58	13.08	11.41
	D5	8.41	8.88	9.85
	D7	8.4	8.31	11.1
	D_{avg} [mm]	7.2	9.6	11.0
	E [V/m]	1144.661535	1139.914703	1141.507577
	α	0.008393	0.008410	0.008405
	$D_{nssm,avg}$ [10^{-12} m^2/s]	0.1.694	2.293	2.624
	$D_{nssm,avg}$ [10^{-12} m^2/s]		**2.20**	

APPENDIX 5 - Workability of mortar mixes (Phase 3)

Flow diameter of mortar mixes with different SHA content and w/b

SHA content	w/b	D_1 [mm]	D_2 [mm]	D_{avg} [mm]
SHA15	0.42	130	132	131
	0.45	156	155	156
	0.50	182	183	182
SHA25	0.42	129	127	128
	0.45	153	155	154
	0.50	180	182	181
SHA35	0.42	120	120	120
	0.45	152	152	152
	0.50	173	175	174

Flow diameter of samples mixed with different SHA immersion durations

Mix	w/b	D_1 [mm]	D_2 [mm]	D_{avg} [mm]
M25	0.45	153	155	154
M25/0h		153	151	152
M25/1h		143	143	143
M25/6h		129	131	130
M25/24h		134	137	136

Flow diameter of trial mortar mixes

Mix	w/b	D_1 [mm]	D_2 [mm]	D_{avg} [mm]
SHA25/0.45	0.45	118	120	119
SHA25/0.47	0.47	126	125	125
SHA25/0.5	0.50	132	134	133
SHA-S/0.45	0.45	126	128	127
SHA-S/0.47	0.47	130	130	130
SHA-S/0.50	0.50	161	160	160

APPENDIX 6 - Compressive strength of mortar mixes (Phase 3)

Compressive strength of mortar mixes with different SHA content and w/b

SHA content	w/b	F [kN]		$f_{c,7d}$ [MPa]		$f_{c,7d,avg}$ [MPa]
SHA15	0.42	46.18	46.45	28.86	29.03	29.96
		49.65	49.6	31.03	31.00	
		47.30	48.39	29.56	30.24	
	0.45	42.00	43.50	26.25	27.19	26.61
		42.00	43.00	26.25	26.88	
		43.00	42.00	26.88	26.25	
	0.5	39.26	38.93	24.54	24.33	23.80
		38.34	39.78	23.96	24.86	
		35.50	36.65	22.19	22.91	
SHA25	0.42	66.22	65.23	41.39	40.77	41.02
		65.61	65.59	41.01	40.99	
		64.16	66.98	40.10	41.86	
	0.45	52.00	53.00	32.50	33.13	33.33
		54.00	53.50	33.75	33.44	
		54.00	53.50	33.75	33.44	
	0.5	48.18	48.12	30.11	30.08	30.03
		49.51	47.64	30.94	29.78	
		47.57	47.23	29.73	29.52	
SHA35	0.42	70.49	72.07	44.06	45.04	45.19
		72.72	71.18	45.45	44.49	
		73.32	74.02	45.83	46.26	
	0.45	59.00	59.00	36.88	36.88	36.15
		58.00	58.00	36.25	36.25	
		55.50	57.50	34.69	35.94	
	0.5	57.71	56.26	36.07	35.16	36.07
		57.58	56.41	35.99	35.26	
		58.21	60.12	36.38	37.58	

Compressive strength of mortar mixes with different SHA content, after 7 and 28 days of curing at TA and T65

Day of testing	Mix	F [kN]		$f_{c,}$ [MPa]		$f_{c,\ avg}$ [MPa]
7	M15_T65	55.10	55.70	34.44	34.81	26.61
		57.30	57.10	35.81	35.69	
		56.80	57.80	35.50	36.13	
	M25_T65	76.00	77.00	47.50	48.13	43.85
		72.00	69.00	45.00	43.13	
		77.00	69.00	48.13	43.13	
	M35_T65	83.00	80.50	51.88	50.31	50.36
		85.00	85.00	53.13	53.13	
		82.00	68.00	51.25	42.50	
28	M15_TA	73.00	74.00	45.63	46.25	46.15
		74.00	75.00	46.25	46.88	
		72.50	74.50	45.31	46.56	
	M15_T65	62.00	66.00	38.75	41.25	39.90
		64.50	66.50	40.31	41.56	
		62.00	62.00	38.75	38.75	
	M25_TA	87.50	85.00	54.69	53.13	54.43
		89.00	87.00	55.63	54.38	
		88.00	86.00	55.00	53.75	
	M25_T65	77.50	82.00	48.44	51.25	50.57
		78.00	83.00	48.75	51.88	
		83.00	82.00	51.88	51.25	
	M35_TA	88.50	84.00	55.31	52.50	55.05
		89.00	92.00	55.63	57.50	
		84.00	91.00	52.50	56.88	
	M35_T65	82.00	79.00	51.25	49.38	51.20
		81.00	83.00	50.63	51.88	
		82.50	84.00	51.56	52.50	

Compressive strength of M25 samples mixed with different SHA immersion durations, after 7 days of curing

Mix	F [kN]		$f_{c,}$ [MPa]		$f_{c,\ avg}$ [MPa]
M25	52.00	53.00	32.50	33.13	26.61
	54.00	53.50	33.75	33.44	
	54.00	53.50	33.75	33.44	
M25/0h	56.00	57.00	35.00	35.63	35.31
	57.00	56.50	35.63	35.31	
	56.00	56.50	35.00	35.31	
M25/1h	55.50	53.50	34.69	33.44	34.01
	55.00	54.50	34.38	34.06	
	54.00	54.00	33.75	33.75	
M25/6h	59.00	60.00	36.88	37.50	37.45
	62.00	61.00	38.75	38.13	
	59.00	58.50	36.88	36.56	
M25/24h	61.50	60.50	38.44	37.81	38.23
	60.50	63.50	37.81	39.69	
	60.00	61.00	37.50	38.13	

Compressive strength of trial mortar mixes after 7 days of curing

Mix	F [kN]		$f_{c,}$ [MPa]		$f_{c,\ avg}$ [MPa]
SHA25/0.45	35.00	35.00	21.88	21.88	21.41
	34.00	34.50	21.25	21.56	
	34.00	33.00	21.25	20.63	
SHA25/0.47	36.00	37.00	22.50	23.13	22.34
	35.00	35.50	21.88	22.19	
	36.00	35.00	22.50	21.88	
SHA25/0.5	31.50	31.00	19.69	19.38	19.69
	31.50	32.00	19.69	20.00	
	31.50	31.00	19.69	19.38	
SHA-S/0.45	67.00	69.00	41.88	43.13	40.99
	63.50	66.50	39.69	41.56	
	64.00	63.50	40.00	39.69	
SHA-S/0.47	61.50	60.00	38.44	37.50	39.58
	65.00	66.00	40.63	41.25	
	63.00	64.50	39.38	40.31	
SHA-S/0.5	61.50	59.00	38.44	36.88	36.56
	58.00	56.00	36.25	35.00	
	57.50	59.00	35.94	36.88	

APPENDIX 7 - Fresh-state properties of mixes R, SHA 25 and SHA-S (Phase 4)

Results of entrained air and fresh-state density of the mixes R, SHA-S, and SHA25

Mix	R	SHA-S	SHA 25
Temperature [˚C]	25.2	23.2	21.7
Δp [%]	1.2	1.3	1.7
γ [kg/m3]	2348	2352	2234
Slump [mm]	66	27	10
Slump class	S2	S1	S1

APPENDIX 8 - Mechanical properties of mixes SHA 25, R, and SHA-S (Phase 4)

Compressive strength of mix SHA25 after 2, 7, and 28 days of curing

Mix	Day of testing	Sample	γ [kg/m^3]	γ_{avg} [kg/m^3]	P [kN]	f_c [MPa]	$f_{c,avg}$ [MPa]
SHA25	2	SHA25/1	2223	2329	300.40	13.35	13.27
		SHA25/2	2227		290.60	12.92	
		SHA25/3	2232		304.80	13.55	
	7	SHA25/4	2204	2202	439.60	19.54	19.16
		SHA25/5	2206		418.70	18.61	
		SHA25/6	2198		435.20	19.34	
	28	SHA25/7	2194	2195	635.10	28.23	27.62
		SHA25/8	2198		596.50	26.51	
		SHA25/9	2192		632.80	28.12	

Compressive strength of mix R after 2, 7, 28, 56 and 90 days of curing

Mix	Day of testing	Sample	γ [kg/m^3]	γ_{avg} [kg/m^3]	P [kN]	f_c [MPa]	$f_{c,avg}$ [MPa]
R	2	R/1	2311	2326	618.30	27.48	27.55
		R/2	2329		621.30	27.61	
		R/3	2339		619.70	27.54	
	7	R/4	2348	2346	739.40	32.86	33.07
		R/5	2332		748.70	33.28	
		R/6	2360		743.80	33.06	
	28	R/7	2342	2353	1054.40	46.86	46.88
		R/8	2347		1042.80	46.35	
		R/9	2371		1067.10	47.43	
	56	R/10	2349	2351	1212.30	53.88	54.46
		R/11	2350		1209.00	53.73	
		R/12	2354		1255.00	55.78	
	90	R/13	2342	2341	1316.20	58.50	57.39
		R/14	2339		1261.10	56.05	
		R/15	2342		1296.20	57.61	

Compressive strength of mix SHA-S after 2, 7, 28, 56 and 90 days of curing

Mix	Day of testing	Sample	γ [kg/m^3]	γ_{avg} [kg/m^3]	P [kN]	f_c [MPa]	$f_{c,avg}$ [MPa]
SHA-S	2	SHA-S/1	2338	2329	620.20	27.56	27.55
		SHA-S/2	2335		617.20	27.43	
		SHA-S/3	2329		618.00	27.47	
	7	SHA-S/4	2338	2334	875.70	38.92	38.52
		SHA-S/5	2335		884.30	39.30	
		SHA-S/6	2329		839.80	37.32	
	28	SHA-S/7	2338	2348	1099.60	48.87	50.06
		SHA-S/8	2358		1122.00	49.87	
		SHA-S/9	2348		1157.70	51.45	
	56	SHA-S/10	2316	2316	1261.6	56.07	57.24
		SHA-S/11	2308		1255.5	55.80	
		SHA-S/12	2324		1346.7	59.85	
	90	SHA-S/13	2343	2342	1280.70	56.92	57.39
		SHA-S/14	2342		1302.80	57.90	
		SHA-S/15	2340		1290.00	57.33	

Tensile strength of mixes R and SHA-S after 28 and 56 days of curing

Mix	Day of testing	P [kN]	f_t [MPa]	$f_{t,avg}$ [MPa]
R	28	7.90	3.56	4.23
		10.20	4.59	
		10.10	4.55	
	56	12.50	5.63	5.36
		11.70	5.27	
		11.50	5.18	
SHA-S	28	11.50	5.18	4.89
		11.50	5.18	
		9.60	4.32	
	56	11.00	4.95	5.34
		12.80	5.76	
		11.80	5.31	

Modulus of elasticity of mix R after 28 days of curing

Measured compressive strength at 28 days, dimensions, masses and calculated forces and stresses for preloading and loading, mix R

P_{cube} [kN]	$f_{c,cube,avg}$ [MPa]	$f_{c,cyl,calc}$ [MPa]	Sample	m [kg]	H [mm]	D [mm]	A [mm^2]	$P_{cyl,28,calc}$ [kN]	σ_p [MPa]	P_p [kN]	σ_b [MPa]	P_b [kN]	σ_a [MPa]	P_a [kN]
1054.40			R/1/28d	12.52	298	150.15	17706.82	671.82		8.85		67.18		223.94
1042.80	47.43	37.94	R/2/28d	12.55	299	150.29	17739.85	673.07	0.50	8.87	3.79	67.31	12.65	224.36
1067.10			R/3/28d	12.51	298	150.06	17685.60	671.02		8.84		67.10		223.67

Preloading, loading measurements and calculated stresses, strains and modulus of elasticity at 28 days

		Preloading			Loading				Calculated $\Delta\sigma$, $\Delta\epsilon_s$ and E					
Sample	Cycle	P_b [kN]	ΔL_b [mm]	P_p [kN]	P_a [kN]	ΔL_a [mm]	P_b [kN]	ΔL_b [mm]	$\sigma_{a,m}$ [MPa]	$\sigma_{b,m}$ [MPa]	$\Delta\sigma$ [MPa]	$\Delta\epsilon_s$	E [GPa]	E_{avg} [GPa]
	1	66.68	-	8.44	222.13	0.204	67.37	0.082						
R/1/28d	2	68.33	0.049	8.12	222.06	0.209	69.51	0.087	12.77	3.93	8.84	0.000640	27.64	
	3	66.43	0.05	9.07	226.11	0.214	67.34	0.087						
	1	68.31	-	9.84	225.85	0.206	68.53	0.083						
R/2/28d	2	68.32	0.047	10.15	225.76	0.213	68.8	0.088	12.69	3.88	8.81	0.000635	27.76	27.97
	3	68.33	0.047	9.1	225.13	0.215	68.05	0.086						
	1	69.17	-	8.96	223.22	0.205	67.97	0.080						
R/3/28d	2	67.51	0.044	9.65	224.52	0.207	67.36	0.084	12.72	3.81	8.91	0.000625	28.51	
	3	68.03	0.044	8.64	224.9	0.209	67.62	0.088						

Modulus of elasticity of mix R after 56 days of curing

Measured compressive strength at 56 days, dimensions, masses and calculated forces and stresses for preloading and loading, mix R

P_{cube} [kN]	$f_{c,cube,avg}$ [MPa]	$f_{c,cyl,calc}$ [MPa]	Sample	m [kg]	H [mm]	D [mm]	A [mm^2]	$P_{cyl,28,calc}$ [kN]	σ_p [MPa]	P_p [kN]	σ_b [MPa]	P_b [kN]	σ_a [MPa]	P_a [kN]
1212.30			R/1/56d	12.41	297.0	150.32	17746.94	773.25		8.87		77.33		257.75
1209.00	54.46	43.57	R/2/56d	12.52	298.5	150.21	17720.97	772.12	0.50	8.86	4.36	77.21	14.52	257.37
1255.00			R/3/56d	12.45	297.5	150.08	17690.31	770.78		8.85		77.08		256.93

Preloading, loading measurements and calculated stresses, strains and modulus of elasticity at 56 days, mix R

		Preloading			Loading				Calculated $\Delta\sigma$, $\Delta\epsilon_s$ and E					
Sample	Cycle	P_b [kN]	ΔL_b [mm]	P_p [kN]	P_a [kN]	ΔL_a [mm]	P_b [kN]	ΔL_b [mm]	$\sigma_{a,m}$ [MPa]	$\sigma_{b,m}$ [MPa]	$\Delta\sigma$ [MPa]	$\Delta\epsilon_s$	E [GPa]	E_{avg} [GPa]
	1	77.89	-	9.41	257.75	0.254	78.54	0.101						
R/1/56d	2	77.64	0.058	9.43	257.59	0.258	78.02	0.107	14.59	4.40	10.19	0.000785	25.97	
	3	77.95	0.057	8.64	258.93	0.261	78.55	0.109						
	1	78.02	-	8.88	257.87	0.235	78.31	0.092						
R/2/56d	2	78.26	0.058	9.56	257.53	0.242	78.54	0.101	14.52	4.43	10.09	0.000730	27.65	26.71
	3	77.78	0.058	9.05	257.38	0.247	77.55	0.099						
	1	77.47	-	9.49	257.18	0.244	77.60	0.096						
R/3/56d	2	78.08	0.058	9.46	257.95	0.25	77.31	0.100	14.58	4.37	10.21	0.000770	26.51	
	3	77.45	0.059	9.07	257.88	0.254	77.60	0.103						

Modulus of elasticity of mix SHA-S after 28 days of curing

Measured compressive strength at 28 days, dimensions, masses and calculated forces and stresses for preloading and loading, mix SHA-S

P_{cube} [kN]	$f_{c,cube,avg}$ [MPa]	$f_{c,cyl,calc}$ [MPa]	Sample	m [kg]	H [mm]	D [mm]	A [mm^2]	$P_{cyl,28,calc}$ [kN]	σ_p [MPa]	P_p [kN]	σ_b [MPa]	P_b [kN]	σ_a [MPa]	P_a [kN]
1122.00			SHA-S/1/28d	12.41	298	150.32	17746.94	719.2		8.87		71.92		239.75
1157.70	50.66	40.53	SHA-S/2/28d	12.37	297	150.00	17672.64	716.2	0.5	8.84	4.05	71.62	13.51	238.75
1139.85			SHA-S/3/28d	12.69	298	150.06	17685.60	716.8		8.84		71.68		238.92

Preloading, loading measurements and calculated stresses, strains and modulus of elasticity at 28 days, SHA-S

		Preloading			Loading				Calculated $\Delta\sigma$, $\Delta\epsilon_s$ and E					
Sample	Cycle	P_b [kN]	ΔL_b [mm]	P_p [kN]	P_a [kN]	ΔL_a [mm]	P_b [kN]	ΔL_b [mm]	$\sigma_{a,m}$ [MPa]	$\sigma_{b,m}$ [MPa]	$\Delta\sigma$ [MPa]	$\Delta\epsilon_s$	E [GPa]	E_{avg} [GPa]
	1	72.79	-	7.36	245.20	0.23	71.91	0.077						
SHA-S/1/28d	2	71.76	0.053	5.89	240.41	0.228	71.12	0.079	13.77	4.01	9.76	0.000780	25.03	
	3	76.16	0.057	6.45	244.34	0.234	70.66	0.079						
	1	72.5	-	8.70	239.38	0.234	73.24	0.079						
SHA-S/2/28d	2	71.91	0.055	10.47	240.79	0.239	72.02	0.081	13.51	4.08	9.43	0.000790	23.89	24.50
	3	72.22	0.056	9.14	238.76	0.239	69.56	0.081						
	1	72.04	-	10.47	238.69	0.245	72.48	0.093						
SHA-S/3/28d	2	72.27	0.058	8.04	240.78	0.258	72.47	0.100	13.56	4.10	9.47	0.000770	24.59	
	3	71.41	0.06	13.14	239.89	0.254	72.47	0.101						

Modulus of elasticity of mix SHA-S after 56 days of curing

Measured compressive strength at 56 days, dimensions, masses and calculated forces and stresses for preloading and loading, SHA-S

P_{cube} [kN]	$f_{c,cube,avg}$ [MPa]	$f_{c,cyl,calc}$ [MPa]	Sample	m [kg]	H [mm]	D [mm]	A [mm^2]	$P_{cyl,28,calc}$ [kN]	σ_p [MPa]	P_p [kN]	σ_b [MPa]	P_b [kN]	σ_a [MPa]	P_a [kN]
1261.6			SHA-S/1/56d	12.37	296	149.97	17663.21	808.9		8.83		80.89		269.62
1255.5	57.24	45.79	SHA-S/2/56d	12.33	297	150.01	17674.99	809.4	0.5	8.84	4.58	80.94	15.26	269.80
1346.7			SHA-S/3/56d	12.25	298	149.80	17624.37	807.1		8.81		80.71		269.03

Preloading, loading measurements and calculated stresses, strains and modulus of elasticity at 28 days, SHA-S

		Preloading			Loading				Calculated $\Delta\sigma$, $\Delta\epsilon_s$ and E					
Sample	Cycle	P_b [kN]	ΔL_b [mm]	P_p [kN]	P_a [kN]	ΔL_a [mm]	P_b [kN]	ΔL_b [mm]	$\sigma_{a,m}$ [MPa]	$\sigma_{b,m}$ [MPa]	$\Delta\sigma$ [MPa]	$\Delta\epsilon_s$	E [GPa]	E_{avg} [GPa]
	1	81.56	-	8.98	271.69	0.307	80.41	0.123						
SHA-S/1/56d	2	81.33	0.073	8.38	270.58	0.312	81.83	0.127	15.32	4.63	10.69	0.000935	22.87	
	3	80.71	0.073	8.18	270.64	0.314	82.52	0.131						
	1	80.94	-	8.84	272.08	0.303	82.07	0.127						
SHA-S/2/56d	2	80.76	0.079	9.85	270.56	0.312	81.21	0.130	15.31	4.59	10.71	0.000940	22.79	22.92
	3	80.76	0.077	8.79	270.52	0.318	81.84	0.133						
	1	81.57	-	8.88	270.30	0.301	81.30	0.122						
SHA-S/3/56d	2	81.28	0.073	9.67	269.75	0.308	81.48	0.125	15.36	4.62	10.74	0.00093	23.09	
	3	81.52	0.073	9.02	270.73	0.311	81.15	0.129						

APPENDIX 9 - Physical properties of mixes R and SHA-S (Phase 4)

Results of water absorption measurements of the mix R

Time [min)	Time [s]	√Time [$s^{0.5}$]	SHA-S/1	SHA-S/2	SHA-S/3	Average [$mm/s^{0.5}$]
Initial absorption						
0	0	0	0.0000	0.0000	0.0000	0.0000
1	60	8	0.1490	0.1514	0.1379	0.1461
5	300	17	0.1925	0.2316	0.2081	0.2107
10	600	24	0.2268	0.2549	0.2484	0.2434
20	1200	35	0.2598	0.2743	0.2783	0.2708
30	1800	42	0.2769	0.2989	0.3069	0.2942
60	3600	60	0.3217	0.3403	0.3446	0.3356
120	7200	85	0.3732	0.3856	0.4006	0.3864
180	10800	104	0.4061	0.4257	0.4370	0.4229
240	14400	120	0.4378	0.4503	0.4604	0.4495
300	18000	134	0.4641	0.4710	0.4877	0.4743
360	21600	147	0.4879	0.4891	0.5137	0.4969
Secondary absorption						
1440	86400	294	0.7292	0.7763	0.7920	0.7658
2880	172800	416	0.9454	1.0532	1.0690	1.0226
4320	259200	509	1.1340	1.2667	1.2719	1.2242
5760	345600	588	1.2474	1.3961	1.3500	1.3311
7200	432000	657	1.2817	1.4659	1.3994	1.3823
8640	518400	720	1.3160	1.5190	1.4111	1.4153
10080	604800	778	1.3265	1.5578	1.4540	1.4461
11520	691200	831	1.3384	1.5811	1.4865	1.4687
12960	777600	882	1.3713	1.6031	1.5060	1.4935
14400	864000	930	1.3331	1.4582	1.4579	1.4935

Results of water absorption measurements of the mix SHA-S

Time [min)	Time [s]	√Time [$s^{0.5}$]	SHA-S/1	SHA-S/2	SHA-S/3	Average [$mm/s^{0.5}$]
Initial absorption						
0	0	0	0.0000	0.0000	0.0000	0.0000
1	60	8	0.2533	0.2286	0.2237	0.2352
5	300	17	0.2900	0.3122	0.2835	0.2952
10	600	24	0.3490	0.3540	0.3147	0.3393
20	1200	35	0.3950	0.3958	0.3550	0.3819
30	1800	42	0.4370	0.4219	0.3850	0.4146
60	3600	60	0.5091	0.4807	0.4500	0.4799
120	7200	85	0.6115	0.5682	0.5423	0.5740
180	10800	104	0.6863	0.6322	0.6243	0.6476
240	14400	120	0.7335	0.6714	0.6828	0.6959
300	18000	134	0.7847	0.7249	0.7387	0.7494
360	21600	147	0.8306	0.7602	0.7881	0.7930
Secondary absorption						
1440	86400	294	1.4093	1.3232	1.4111	1.3812
2880	172800	416	1.5300	1.5021	1.4787	1.5036
4320	259200	509	1.5589	1.5348	1.5164	1.5367
5760	345600	588	1.5786	1.5688	1.5333	1.5602
7200	432000	657	1.6048	1.5975	1.5632	1.5885
8640	518400	720	1.6166	1.6171	1.5893	1.6076
10080	604800	778	1.6205	1.6184	1.5971	1.6120
11520	691200	831	1.6284	1.6184	1.6062	1.6177
12960	777600	882	1.6652	1.6197	1.6348	1.6399
14400	864000	930	1.6612	1.6014	1.6192	1.6273

Shrinkage of the mix R after 90 days

Sample	Testing time [days]									
	t_0	t_{0+1}	t_{0+3}	t_{0+7}	t_{0+14}	t_{0+21}	t_{0+28}	t_{0+42}	t_{0+56}	t_{0+90}
Stud gauges										
R1	0	-0.254	-1.058	-0.619	-0.831	-0.930	-0.972	-1.041	-1.133	-1.328
R2	0	-0.220	-1.047	-0.580	-0.684	-0.836	-0.869	-0.943	-1.024	-1.229
R3	0	-0.512	-1.442	-0.953	-1.122	-1.217	-1.267	-1.312	-1.424	-1.634
$\varepsilon_{cs,1}$ [mm/m]	0	-0.329	-0.623	-0.718	-0.879	-0.994	-1.036	-1.098	-1.194	-1.397
Strain gauges										
R1	0	-0.257	-0.324	-0.443	-0.538	-0.597	-0.618	-0.637	-0.699	-0.777
R2	0	0.007	-0.013	-0.082	-0.171	-0.212	-0.269	-0.292	-0.361	-0.430
R3	0	-0.380	-0.426	-0.543	-0.664	-0.716	-0.770	-0.802	-0.863	-0.943
$\varepsilon_{cs,2}$ [mm/m]	0	-0.210	-0.287	-0.356	-0.457	-0.508	-0.552	-0.577	-0.641	-0.716

Shrinkage of the mix SHA-S after 90 days

Sample	Testing time [days]									
	t_0	t_{0+1}	t_{0+3}	t_{0+7}	t_{0+14}	t_{0+21}	t_{0+28}	t_{0+42}	t_{0+56}	t_{0+90}
Stud gauges										
SHA-S1	0	-0.742	-1.589	-1.975	-2.322	-2.496	-2.610	-2.753	-2.822	-3.119
SHA-S2	0	-0.883	-1.322	-2.052	-2.382	-2.566	-2.677	-2.788	-2.878	-3.170
SHA-S3	0	-1.009	-1.696	-2.016	-2.296	-2.359	-2.531	-2.672	-2.787	-3.049
$\varepsilon_{cs,1}$ [mm/m]	0	-0.878	-1.536	-2.014	-2.270	-2.474	-2.606	-2.738	-2.829	-3.112
Strain gauges										
SHA-S1	0	-0.336	-0.668	-0.856	-1.043	-1.169	-1.270	-1.379	-1.462	-1.608
SHA-S2	0	-0.408	-0.782	-0.971	-1.161	-1.286	-1.356	-1.457	-1.514	-1.632
SHA-S3	0	-0.440	-0.790	-0.957	-1.109	-1.221	-1.306	-1.399	-1.469	-1.518
$\varepsilon_{cs,2}$ [mm/m]	0	-0.395	-0.747	-0.928	-1.104	-1.225	-1.311	-1.412	-1.482	-1.586

Cumulative mass loss of the R mix samples

Sample	Mass loss [kg]									
	t_0	t_{0+1}	t_{0+3}	t_{0+7}	t_{0+14}	t_{0+21}	t_{0+28}	t_{0+42}	t_{0+56}	t_{0+90}
R1	0	0.042	0.064	0.084	0.105	0.118	0.125	0.139	0.151	0.168
R2	0	0.045	0.070	0.092	0.113	0.126	0.133	0.148	0.160	0.178
R3	0	0.048	0.071	0.093	0.114	0.128	0.135	0.149	0.160	0.177
avg. cumulative	0	0.045	0.068	0.090	0.111	0.124	0.131	0.145	0.157	0.174

Cumulative mass loss of the SHA-S mix samples

Sample	Mass loss [kg]									
	t_0	t_{0+1}	t_{0+3}	t_{0+7}	t_{0+14}	t_{0+21}	t_{0+28}	t_{0+42}	t_{0+56}	t_{0+90}
SHA-S1	0	0.131	0.179	0.21	0.239	0.26	0.273	0.29	0.302	0.324
SHA-S2	0	0.136	0.182	0.212	0.242	0.262	0.276	0.291	0.303	0.324
SHA-S3	0	0.108	0.153	0.184	0.212	0.233	0.246	0.261	0.271	0.293
avg. cumulative	0	0.125	0.171	0.202	0.231	0.252	0.265	0.281	0.292	0.314

APPENDIX 10 - Durability properties of mixes R and SHA-S (Phase 4)

Depth of water penetration under pressure: concrete mixes R and SHA-S

Sample	R/1	R/2	R/3	SHA-S/1	SHA-S/2	SHA-S/3
d [mm]	21.8	25.5	34.0	33.6	35.3	28.5

Measured carbonation depths of concrete mixes R and SHA-S, after 7, 28, and 56 days of exposure to accelerated carbonation

R			SHA-S		
d_k [mm]					
7d	**28d**	**56d**	**7d**	**28d**	**56d**
6.0	14.0	27.1	5.9	16.8	27.6
7.8	15.2	24.2	7.6	16.6	25.2
8.3	16.6	22.6	8.1	16.6	25.2
9.1	17.7	24.9	8.2	17.0	26.9
6.6	15.9	25.6	9.0	18.1	25.9
7.1	16.8	25.6	6.4	16.6	28.1
7.3	16.1	24.2	7.0	15.9	24.3
5.8	15.1	26.5	12.5	17.3	25.4
4.6	14.7	27.0	8.8	16.8	25.8
5.3	14.8	23.7	7.4	17.3	25.4
4.8	14.8	22.7	7.2	16.4	24.7
6.3	14.0	25.3	8.6	16.4	26.8
7.1	15.6	24.4	6.5	17.5	27.0
7.6	15.3	21.9	7.3	18.6	27.6
9.2	14.6	22.9	7.1	16.5	27.1
7.2	14.2	25.0	6.2	17.7	26.7
Average carbonation depths [mm]					
6.9	15.3	24.6	7.7	17.0	26.2

Test parameters, chloride penetration depths, and coefficients of the mix R, after 28 and 56 days of curing

Mix R, 28d		**Sample**		
		1	**2**	**3**
Test parameters	L [mm]	50.22	50.4	50.7
	T_{avg} (°C)	23	22.9	25
	U [V]	50	50	50
	Test duration [h]	24	24	24
Chloride penetration depths [mm]	D6	4.6	5.9	3.8
	D4	4.7	4.2	4.6
	D2	3.6	4.5	4.9
	D1	2.7	4.3	5.4
	D3	5.5	4	6.8
	D5	6.3	4.5	6.3
	D7	7.5	3	5.2
	D_{avg} [mm]	5.0	4.3	5.3
	E [V/m]	955.794504	952.380952	946.745562
	α	0.009158	0.009173	0.009233
	$D_{nssm,avg}$ [10^{-12} m^2/s]	1.34	1.158	1.449
	$D_{nssm,avg}$ [10^{-12} m^2/s]		**1.32**	

Mix R, 56d		**Sample**		
		1	**2**	**3**
Test parameters	L [mm]	51.6	50.47	50.2
	T_{avg} (°C)	28.3	28.3	28.3
	U [V]	60	60	60
	Test duration [h]	24	24	24
Chloride penetration depths [mm]	D6	0	4.83	6.9
	D4	3.07	6	7.96
	D2	4.94	6.33	6.64
	D1	5.2	5.72	5.83
	D3	4.91	4.75	5.74
	D5	4.24	4.29	5.73
	D7	2.57	6.44	4.93
	D_{avg} [mm]	3.6	5.5	6.2
	E [V/m]	1124.031008	1149.197543	1155.378486
	α	0.008520	0.008427	0.008404
	$D_{nssm,avg}$ [10^{-12} m^2/s]	0.816	1.270	1.452
	$D_{nssm,avg}$ [10^{-12} m^2/s]		**1.18**	

Test parameters, chloride penetration depths, and coefficients of the mix SHA-S, after 28 and 56 days of curing

Mix SHA-S, 28d		**Sample**		
		1	**2**	**3**
Test parameters	L [mm]	50.61	50.45	51.18
	T_{avg} (°C)	21.05	20.88	22.73
	U [V]	30	30	30
	Test duration [h]	24	24	24
Chloride penetration depths [mm]	D6	4.1	2.7	4.5
	D4	4.43	2.8	8.8
	D2	3.34	3.8	5.9
	D1	3.93	4	6.6
	D3	2.62	3.8	4.8
	D5	5.02	4.8	4.8
	D7	4.04	4.2	6
	D_{avg} [mm]	3.9	3.7	5.9
	E [V/m]	553.250346	555.004955	547.088707
	α	0.011998	0.011975	0.012099
	$D_{nssm,avg}$ [10^{-12} m^2/s]	1.683	1.583	2.687
	$D_{nssm,avg}$ [10^{-12} m^2/s]		**1.98**	
Mix SHA-S, 56d		**Sample**		
		1	**2**	**3**
Test parameters	L [mm]	50.61	50.45	51.18
	T_{avg} (°C)	29.41	29.41	30.42
	U [V]	35	35	35
	Test duration [h]	24	24	24
Chloride penetration depths [mm]	D6	1.11	1.36	1.64
	D4	2.66	6.96	2.72
	D2	5.24	1.78	2.71
	D1	3.93	3.12	3.64
	D3	2.08	2.04	3.21
	D5	3.88	0	2.22
	D7	0	0	4.51
	D_{avg} [mm]	2.7	2.2	3.0
	E [V/m]	652.045050	654.112983	644.783118
	α	0.011207	0.011190	0.011289
	$D_{nssm,avg}$ [10^{-12} m^2/s]	0.98	0.764	1.097
	$D_{nssm,avg}$ [10^{-12} m^2/s]		**0.95**	

LIST OF PUBLICATIONS

Journal Publications

1. **Bedov, O.** Draganić, S.; Vučetić, S.; Serdar, M. Optimisation of Sunflower Husk Ash-Activated Slag Binder. *Buildings,* 2025, 15(23), 4210. https://doi.org/10.3390/buildings15234210
2. **Bedov, O.**; Andabaka, A.; Draganić, S. Turning Agricultural Biomass Ash into a Valuable Resource in the Construction Industry - Exploring the Potential of Industrial Symbiosis. *Buildings,* 2025, 15(2), 273. https://doi.org/10.3390/buildings15020273

Conference publications

1. **Bedov, O.**; Draganić, S.; Serdar, M. Biomass ash in alkali-activated materials technology - a scoping review. *International Conference Synergy of Architecture and Civil Engineering SINARG* 2025,2(1):695-705, September 11-12, 2025, Niš, Serbia. https://doi.org/10.62683/SINARG2025.097
2. **Bedov, O.**; Draganić, S.; Serdar, M.; Malešev, M. Compressive strength of alkali-activated mortars with conventional hydroxide activators and sunflower husk ash – comparative analysis. *XXIX congress DIMK and X congress SIGP with International Symposium on researching and application of modern achievements in Civil Engineering in the Field of Materials and Structures*, May 21-23, 2025, Sokobanja, Serbia. https://doi.org/10.46793/29DIMK.100B
3. **Bukvić O.**; Malešev M.; Draganić S.; Serdar M.; Radonjanin V. Valorisation of sunflower husk ash: the influence on microstructure and compressive strength of alkali-activated slag mortars, *16th International Scientific Conference iNDiS - Proceedings*, 2023 pp. 606-612, ISBN 978-86-6022-615-2, Novi Sad, Serbia
4. **Bukvić O.**; Malešev M.; Serdar M., Draganić S.; Radonjanin V. Feasibility of using sunflower husk ash as an alternative activator for alkali-activated slag, *International Symposium MASE – Proceedings*, 2023, ISBN 978-608-66946-3-0, Skopje, Republic of North Macedonia
5. Flegar M.; Bašić A.D.; **Bukvić O.**; Serdar M. Carbonation of concretes with different binder chemistry – a comparative analysis, *The International RILEM Conference on Synergising expertise towards sustainability and robustness of cement-based materials and concrete structures, Conference Proceedings*, 2023, ISBN 978-3-031-33186-2, Milos, Greece

6. **Bukvić O.**; Serdar M.. Influence of pre-saturation regime on the scaling resistance of alkali-activated slag concrete, *DuRSAAM Symposium Proceedings*, 2023, ISBN 978-9-082-52684-4 pp. 106-108, Ghent, Belgium.
7. **Bukvić O.**; Serdar M. Influence of alkali content and silica modulus on the carbonation kinetics of alkali-activated slag concrete, *6th International Conference on Concrete Repair, Rehabilitation and retrofitting*, MATEC Web Conferences 364, 2022, Cape Town, South Africa, https://doi.org/10.1051/matecconf/202236405004
8. **Bukvić O.**; Ye G.; Serdar M. Durability performance of slag-based alkali-activated concretes of different compressive strength class, *76th RILEM Annual Week*, 2022, Kyoto, Japan
9. **Bukvić O.**; Serdar M. Freeze-thaw resistance with de-icing salts of alkali-activated slag concrete: the influence of activator type and dosage and comparison to the ordinary Portland cement concrete, *8th Doctoral Symposium in Civil Engineering - Proceedings*, 2022, pp. 213-224, doi:10.5592/CO/PhDSym.2022.17, Zagreb, Croatia
10. **Bukvić O.;** Runci A.; Serdar M. Critical parameters for the mix design of slag-based alkali-activated concrete, *15th International Conference on planning, design, construction and building renewal - iNDiS 2021*, 2021, pp. 569-576, ISBN 978-86-6022-253-6, Novi Sad, Serbia

BIOGRAPHY

Olivera Bedov was born in 1993 in Novi Sad. She completed her undergraduate and master's studies in Civil Engineering at the Faculty of Technical Sciences, University of Novi Sad.

She enrolled in a doctoral programme in 2018 at the Faculty of Technical Sciences and was appointed to the academic position of Teaching Associate and, subsequently, Teaching Assistant in the scientific field of Building Materials, Assessment and Repair of Structures. She is engaged in teaching activities within the study programmes of Civil Engineering, Architecture, and Disaster Risk Management and Fire Safety.

She has participated in national research projects supported by the Ministry of Education, Science and Technological Development of the Republic of Serbia, as well as in international research projects, including ERASMUS+ and COST projects. Within the ERASMUS+ programme, she spent five months as a visiting researcher at the Division of Fire Safety Engineering, Faculty of Engineering, Lund University, Sweden, during her doctoral studies.

As a recipient of the Marie Skłodowska-Curie fellowship, she carried out research at the Faculty of Civil Engineering, University of Zagreb, participating in the international research project "The PhD Training Network on Durable, Reliable and Sustainable Structures with Alkali-Activated Materials – DuRSAAM", funded under the Horizon 2020 programme.

She has authored and co-authored 29 scientific papers published in international and national journals and scientific conference proceedings. She is a member of the Fire Safe Europe organisation.

План третмана података

Назив пројекта/истраживања
Possibilities of sunflower husk ash utilization as an alternative activator for slag-based alkali-activated materials (Могућности примене пепела сунцокретове љуске као алтернативног активатора за алкално-активиране материјале на бази згуре)
Назив институције/институција у оквиру којих се спроводи истраживање
а) Универзитет у Новом Саду, Факултет техничких наука, Департман за грађевинарство и геодезију б) Универзитет у Загребу, Грађевински факултет, Завод за материјале
Назив програма у оквиру ког се реализује истраживање
Истраживање је реализовано у оквиру међународног двојног доктората, на студијском програму Грађевинарство, на Факултету техничких наука Универзитета у Новом Саду и на Грађевинском факултету Универзитета у Загребу.
1. Опис података
1.1 Врста студије *Укратко описати тип студије у оквиру које се подаци прикупљају* Докторска дисертација 1.2 Врсте података **а) квантитативни** **б) квалитативни** 1.3. Начин прикупљања података а) анкете, упитници, тестови б) клиничке процене, медицински записи, електронски здравствени записи в) генотипови: навести врсту _____ г) административни подаци: навести врсту _____ д) узорци ткива: навести врсту_____ ђ) снимци, фотографије: навести врсту_____ **е) текст, актуелна литература у области истраживања, грађевински стандарди** ж) мапа, навести врсту _____ **з) остало: сопствена лабораторијска експериментална истраживања**

1.3 Формат података, употребљене скале, количина података

1.3.1 Употребљени софтвер и формат датотеке:

а) **Excel фајл, датотека .xlsx**

b) SPSS фајл, датотека _____

c**) PDF фајл, датотека .pdf**

d) Текст фајл, датотека .docx

e) JPG фајл, датотека .jpg, .png

f) Spectragryf, датотека .sgd, Origin, датотека .opju

1.3.2. Број записа (код квантитативних података)

а) број варијабли **седам**

б) број мерења (испитаника, процена, снимака и сл.) **велики број**

1.3.3. Поновљена мерења

а) да

б) не

Уколико је одговор да, одговорити на следећа питања:

а) временски размак између поновљених мера је _____

б) варијабле које се више пута мере односе се на _____

в) нове верзије фајлова који садрже поновљена мерења су именоване као _____

Напомене: _____

Да ли формати и софтвер омогућавају дељење и дугорочну валидност података?

а) Да

б) Не

Ако је одговор не, образложити _____

_____

2. Прикупљање података

2.1 Методологија за прикупљање/генерисање података

2.1.1. У оквиру ког истраживачког нацрта су подаци прикупљени?

а) експеримент, <u>лабораторијски</u>

б**) корелационо истраживање, <u>компаративна анализа</u>**

<u>ц) анализа текста, систематски преглед актуалне литературе из области истраживања, грађевински стандарди</u>

д) остало, навести шта _____

2.1.2 Навести врсте мерних инструмената или стандарде података специфичних за одређену научну дисциплину (ако постоје).

Инструменти за хемијску и физичку карактеризацију материјала (уређај за испитивање хемијског састава материјала методом рендгенске флуоресцентне спектрометрије - XRF, уређај за термогравиметријску и деривациону термогравиметријску анализу - TGA/DTG, уређај за спектроскопију инфрацрвеном радијацијом са Фуријеовом трансформацијом - FTIR, уређај за рендгенску дифракциону анализу - XRD, скенирајући електронски микроскоп са уређајем за енергетски дисперзивну спектроскопију X-зрака - EDX, уређај за анализу величине честица ласерскомд дифракцијом), Бленов апарат, инструмент за јонску хроматографију); инструменти за одређивање механичких својстава (хидрауличне пресе за испитивање чврстоће при притиску малтера и бетона, хидраулична преса за испитивање чврстоће бетона на затезање савијањем, хидраулична преса за одређивање модула еластичности бетона); уређај за одређивање расподеле величине пора и укупне порозности методом живине порозиметрије (MIP); инструмент за мерење pH вредности раствора; опрема за испитивање отпорности бетона на продор хлорида методом миграције у нестационарном стању; инструменти за линеарна мерења и аквизицију података (дигитални компаратер, аквизициони уређаји, дигитално помично мерило); дигиталне ваге; термометар; порозиметар за бетон.

2.2 Квалитет података и стандарди

2.2.1. Третман недостајућих података

а) Да ли матрица садржи недостајуће податке? Да **Не**

Ако је одговор да, одговорити на следећа питања:

а) Колики је број недостајућих података? _____

б) Да ли се кориснику матрице препоручује замена недостајућих података? Да Не

в) Ако је одговор да, навести сугестије за третман замене недостајућих података

_____

2.2.2. На који начин је контролисан квалитет података? Описати

Квалитет података је контролисан анализом и поређењем резултата измерених при експерименталном испитивању са резултатима из анализиране литературе.

2.2.3. На који начин је извршена контрола уноса података у матрицу?

Валидација података је реализована од стране ментора истраживања.

3. Третман података и пратећа документација

3.1. Третман и чување података

*3.1.1. Подаци ће бити депоновани у **Репозиторијуму докторских дисертација на Универзитету у Новом Саду**.*

3.1.2. URL адреса https://cris.uns.ac.rs/searchDissertations.jsf

3.1.3. DOI _____

3.1.4. Да ли ће подаци бити у отвореном приступу?

а) ***Да***

б) *Да, али после ембарга који ће трајати до* _____

в) *Не*

Ако је одговор не, навести разлог _____

3.1.5. Подаци неће бити депоновани у репозиторијум, али ће бити чувани.

Образложење

_____

_____

3.2 Метаподаци и документација података

-

3.3 Стратегија и стандарди за чување података

3.3.1. До ког периода ће подаци бити чувани у репозиторијуму? **Неограничено.**

3.3.2. Да ли ће подаци бити депоновани под шифром? Да **Не**

3.3.3. Да ли ће шифра бити доступна одређеном кругу истраживача? Да Не

3.3.4. Да ли се подаци морају уклонити из отвореног приступа после извесног времена?

Да **Не**

Образложити

_____

_____

4. Безбедност података и заштита поверљивих информација

Овај одељак МОРА бити попуњен ако ваши подаци укључују личне податке који се односе на учеснике у истраживању. За друга истраживања треба такође размотрити заштиту и сигурност података.

4.1 Формални стандарди за сигурност информација/података

Истраживачи који спроводе испитивања с људима морају да се придржавају Закона о заштити података о личности *(https://www.paragraf.rs/propisi/zakon_o_zastiti_podataka_o_licnosti.html)* и одговарајућег институционалног кодекса о академском интегритету.

4.1.2. Да ли је истраживање одобрено од стране етичке комисије? Да **Не**

Ако је одговор Да, навести датум и назив етичке комисије која је одобрила истраживање

_____

4.1.2. Да ли подаци укључују личне податке учесника у истраживању? Да **Не**

Ако је одговор да, наведите на који начин сте осигурали поверљивост и сигурност информација везаних за испитанике:

а) Подаци нису у отвореном приступу

б) Подаци су анонимизирани

ц) Остало, навести шта

_____

_____

5. Доступност података

5.1. Подаци ће бити

а) јавно доступни

б) доступни само уском кругу истраживача у одређеној научној области

ц) затворени

Ако су подаци доступни само уском кругу истраживача, навести под којим условима могу да их користе:

_____

_____

Ако су подаци доступни само уском кругу истраживача, навести на који начин могу приступити подацима:

_____

_____

5.4. Навести лиценцу под којом ће прикупљени подаци бити архивирани.

Ауторство – некомерцијално – без прераде

6. Улоге и одговорност

6.1. Навести име и презиме и мејл адресу власника (аутора) података

Оливера Бедов, olivera.bukvic@uns.ac.rs

6.2. Навести име и презиме и мејл адресу особе која одржава матрицу с подацима

Оливера Бедов, olivera.bukvic@uns.ac.rs

6.3. Навести име и презиме и мејл адресу особе која омогућује приступ подацима другим истраживачима

Оливера Бедов, olivera.bukvic@uns.ac.rs